

AD-A058 631

OHIO STATE UNIV COLUMBUS ELECTROSCIENCE LAB

F/G 17/5

A STUDY OF WATER VAPOR ABSORPTION AT CO2 LASER FREQUENCIES USIN--ETC(U)

JUN 78 J C PETERSON

DAAG29-77-C-0010

UNCLASSIFIED

ESL-784701-2

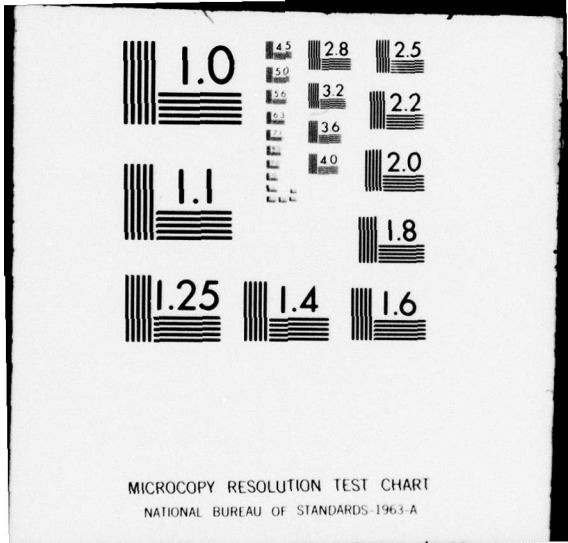
ARO-14702.1-65

NL

1 of 3

AD
4058631





MICROCOPY RESOLUTION TEST CHART
NATIONAL BUREAU OF STANDARDS-1963-A

ARO 14702.1-GS

12

A STUDY OF WATER VAPOR ABSORPTION AT CO₂ LASER
FREQUENCIES USING A DIFFERENTIAL SPECTROPHONE
AND WHITE CELL

Interim Technical Report for Period 1/1/78 - 6/30/78

John C. Peterson

LEVEL II

The Ohio State University

ElectroScience Laboratory

Department of Electrical Engineering
Columbus, Ohio 43212

June 1978

U. S. Army Research Office

Contract DAAG29-77-C-0010

DDC
SEP 14 1978
F

Approved for Public Release
Distribution Unlimited

78 09 05 202

AD A058631

AD No. _____
DDC FILE COPY



NOTICES

When Government drawings, specifications, or other data are used for any purpose other than in connection with a definitely related Government procurement operation, the United States Government thereby incurs no responsibility nor any obligation whatsoever, and the fact that the Government may have formulated, furnished, or in any way supplied the said drawings, specifications, or other data, is not to be regarded by implication or otherwise as in any manner licensing the holder or any other person or corporation, or conveying any rights or permission to manufacture, use, or sell any patented invention that may in any way be related thereto.

UNCLASSIFIED

SECURITY CLASSIFICATION OF THIS PAGE (When Data Entered)

REPORT DOCUMENTATION PAGE		READ INSTRUCTIONS BEFORE COMPLETING FORM
1. REPORT NUMBER	2. GOVT ACCESSION NO.	3. RECIPIENT'S CATALOG NUMBER
4. TITLE (and Subtitle) A STUDY OF WATER VAPOR ABSORPTION AT CO ₂ ⁷ LASER FREQUENCIES USING A DIFFERENTIAL SPECTROPHONE AND WHITE CELL.		5. TYPE OF REPORT & PERIOD COVERED Interim Technical Report for Period 1/1/78 - 6/30/78
7. AUTHOR(s) John C. Peterson		6. PERFORMING ORG. REPORT NUMBER ESL-784701-2
9. PERFORMING ORGANIZATION NAME AND ADDRESS The Ohio State University ElectroScience Laboratory Department of Electrical Engineering Columbus, Ohio 43212		8. CONTRACT OR GRANT NUMBER(s) Contract DAAG29-77-C-001A
11. CONTROLLING OFFICE NAME AND ADDRESS U. S. Army Research Office Post Office Box 12211 Research Triangle Park, NC 27709		10. PROGRAM ELEMENT, PROJECT, TASK AREA & WORK UNIT NUMBERS
14. MONITORING AGENCY NAME & ADDRESS (if different from Controlling Office) ARO 14702.1-GS		12. REPORT DATE June 1978
16. DISTRIBUTION STATEMENT (of this Report) Approved for public release; distribution unlimited. Interim technical rept. 1 Jan - 30 Jun 78,		13. NUMBER OF PAGES 245
17. DISTRIBUTION STATEMENT (of the abstract entered in Block 20, if different from Report) NA		15. SECURITY CLASS. (of this report) Unclassified
18. SUPPLEMENTARY NOTES The findings in this report are not be construed as an official Department of the Army position, unless so designated by other authorized documents. The material contained in this report was also used as a dissertation submitted to the Ohio State University.		15a. DECLASSIFICATION/DOWNGRADING SCHEDULE NA
19. KEY WORDS (Continue on reverse side if necessary and identify by block number)		
20. ABSTRACT (Continue on reverse side if necessary and identify by block number) Water vapor absorption at CO ₂ laser frequencies has been studied using a differential spectrophone and a long path multiple traversal cell. The results of these measurements have been analyzed in terms of the Lorentz line shape and the far wing model for continuum absorption in the 9-10 μm wavelength region. micrometers An electronically stabilized, grating tunable cw CO ₂ laser with a nominal output power of 2 watts was used in performing measurements of water vapor ab-		

DD FORM 1 JAN 73 1473

EDITION OF 1 NOV 65 IS OBSOLETE

UNCLASSIFIED
SECURITY CLASSIFICATION OF THIS PAGE (When Data Entered)

402251

LB

20.

micrometers

sorption as a function of both pressure and temperature. Pressure broadened studies of H_2O in N_2 at a total pressure of 1 atm. were performed at 27 CO_2 laser lines in the 9.4 and 10.4 μm bands. The experimental data indicates that the continuum absorption (in this region) is a slowly varying function of frequency which can be modeled by the semi-empirical equation

$$k(\nu) = 1.72 \times 10^5 \nu^{-2} + 2.47 \times 10^{-2}$$

for a water vapor partial pressure of 14.3 Torr, where k is the absorption coefficient in km^{-1} and ν is the frequency in cm^{-1} .

Temperature dependence of (continuum) H_2O in artificial air absorption at a total pressure of 760 Torr was studied in the spectrophone at the 10.4 μm P(16) and P(20) laser lines. The temperature range covered was from 289 to 300.6°K. Results of these measurements indicate an approximate temperature dependence of -1.7% per degree Kelvin at 295°K. Near line center temperature dependence was also examined for the R(20) laser line at 975.930 cm^{-1} . The experimental data indicate a significant positive temperature coefficient of $\sim +2\%$ per degree Kelvin which is in close agreement with that predicted from the Lorentz line shape model.

The influence of oxygen and nitrogen as components of the buffer gas were studied for four different mixtures; pure N_2 , 80-20 air, 60-40 air and pure O_2 . Results at 975.93 cm^{-1} verify that O_2 is a less effective broadening gas than N_2 . This difference was less pronounced (though discernible at frequencies where the continuum is the dominant absorption mechanism. *micrometers*

→ A technique for pure (low pressure) H_2O measurements using the spectrophone is presented together with some preliminary results at the 10.6 μm P(20) laser line. White cell measurements of pure water vapor were performed at seven laser lines in the 9.4 and 10.4 μm bands; these data also indicate a significant negative temperature dependence for continuum absorption.

ACCESSION for	
NTIS	White Section <input checked="" type="checkbox"/>
DDC	Buff Section <input type="checkbox"/>
UNANNOUNCED	<input type="checkbox"/>
JUSTIFICATION	
BY	
DISTRIBUTION/AVAILABILITY CODES	
Dist.	AVAIL. and/or SPECIAL
A	

TABLE OF CONTENTS

		Page
LIST OF TABLES.		vi
LIST OF FIGURES.		viii
 Chapter		
I	INTRODUCTION.	1
II	MOLECULAR ABSORPTION.	4
	A. Introduction	5
	B. The Absorption Coefficient	8
	1. Line shape	8
	2. Line strength	11
	C. Temperature and Pressure Dependence	13
	1. Near line center behavior	14
	2. Far wing behavior	15
	D. Water Vapor Dimers	19
III	PRINCIPLES AND PROBLEMS OF SPECTROPHONE AND WHITE CELL ABSORPTION MEASUREMENTS.	20
	A. Transmittance Measurements	20
	1. Calculation of absorption coefficient	21
	a. error sensitivity	21
	b. optimum path length	22
	2. Background stability	24
	a. mechanical	24
	b. optical (mirror reflectivity)	24
	B. Optoacoustic Measurements	25
	1. Basic theory	26
	a. introduction	26
	b. rate-equation description	26
	c. heat flow description	30
	d. comparison of descriptions	33
	e. limitations of sensitivity	38
	1. window signal (noise)	38
	2. wall signal (noise)	39
	3. transducer noise	39
	f. low pressure measurements	40
	1. introduction	40
	2. previous work	42
	3. a technique	42
	2. The O.S.U. differential spectrophone	44
	a. theory of operation	44
	b. construction details	48
	c. temperature control system	50

IV	THE EXPERIMENTS.	53
	A. The experimental apparatus	53
	1. CO ₂ laser	53
	2. Power meters	57
	3. Data acquisition system	57
	4. Spectrophone instrumentation	60
	a. pressure transducer	60
	b. lock-in amplifier	60
	c. dew point hygrometer	60
	d. gas handling manifold	60
	e. accessory equipment	60
	5. Multiple traversal cell	64
	B. The Experimental Procedures and Tests	64
	1. Calibration tests of data system	64
	a. dc amplifiers and the A/D	64
	2. Spectrophone measurements	66
	a. introduction	66
	b. instrument response tests	67
	1. lock-in amplifier	67
	2. linearity	67
	c. sample handling	72
	d. optical alignment	76
	3. White cell measurements	78
	a. optical alignment	78
	b. stability tests	78
	C. Sample Handling	82
V	RESULTS.	84
	A. Spectrophone Study of Water Vapor	84
	1. Artificial air broadened samples	84
	a. 100% N ₂ results	84
	b. calibration for N ₂ -O ₂ mixtures	84
	1. 80% N ₂ and 20% O ₂ results	109
	2. 60% N ₂ and 40% O ₂ results	109
	3. 100% O ₂ results	109
	2. Temperature studies	136
	a. calibration vs. temperature	136
	b. results	136
	3. Pure H ₂ O studies	136
	a. calibration vs. pressure	136
	b. results	144
	B. White Cell Data and a Comparison with Spectrophone Results	144
	1. Artificial air broadened samples	147
	a. 100% N ₂ results	147
	b. 80% N ₂ and 20% O ₂ results	147
	c. 60% N ₂ and 40% O ₂ results	147
	2. Pure H ₂ O studies	178

VI	ANALYSIS OF RESULTS.	186
	A. Pressure Broadened Water Vapor Measurements	186
	1. Introduction	186
	2. Room temperature data	187
	a. curve fit coefficients	187
	b. comparison of results	194
	1. this study	194
	2. previous studies	195
	c. effects of oxygen	203
	3. Temperature studies	211
	a. curve fit coefficients	211
	b. temperature coefficient	219
	1. near line center	219
	2. far wings	219
	c. influence of lower state energy level	225
	B. Pure Water Vapor Measurements	227
	1. Introduction	227
	2. Ambient and Elevated Temperature Data	227
	a. curve fit coefficients	227
	b. comparison of spectrophone and White cell data	229
	c. temperature dependence	230
	C. The Continuum	232
VII	SUMMARY AND CONCLUSIONS.	239
	REFERENCES.	241

LIST OF TABLES

Table		Table
1	Approximate spectral regions for the electronic, vibrational and rotational transitions. From lecture notes given by K. Narahari Rao.	7
2	Values of D_m in the heat flow solution. After Kerr and Atwood.	36
3	Experimental results of White cell measurements of pressure broadened H_2O at 944.194 cm^{-1} . This data was obtained using a path length of 1.46 km.	80
4	Ratios of specific volumes, \bar{v} (at 70°F and 1 atm) to specific heat at constant volume, C_v for nitrogen and oxygen.	109
5	List of spectrophone and White cell curve fit coefficients for H_2O in N_2 measurements at a total pressure of 760 torr.	188
6	List of spectrophone and White cell curve fit coefficients for H_2O in 80% N_2 and 20% O_2 absorption measurements at a total pressure of 760 Torr.	189
7	List of spectrophone and White cell curve fit coefficients for H_2O in 60% N_2 and 40% O_2 absorption measurements at a total pressure 760 Torr.	189
8	List of spectrophone curve fit coefficients for H_2O in O_2 absorption measurements at a total pressure of 760 Torr.	190
9	List of spectrophone and White cell curve fit coefficients for H_2O in N_2 measurements at a total pressure of 760 Torr.	191
10	List of spectrophone and White cell curve fit coefficients for H_2O in 80% N_2O and 20% O_2 absorption measurements at a total pressure of 760 Torr.	192
11	List of spectrophone and White cell curve fit coefficients for H_2O in 60% N_2 , and 40% O_2 absorption measurements at a total pressure of 760 Torr.	192

12	List of spectrophone curve fit coefficients for H_2O in O_2 absorption measurements at a total pressure of 760 Torr.	193
13	Comparison of measured values of the self broadening coefficient for the P(20) CO_2 laser line at 944.194.	202
14	Comparison of measured values of A for the R(20) CO_2 laser line at 975.93 cm^{-1}	202
15	List of figures where the indicated pressure broadened water vapor absorption data may be found.	203
16	List of curve fit coefficients for spectrophone measurements of H_2O in 80-20 air at the sample temperatures indicated.	218
17	List of curve fit coefficients, C_s^0 and γ for spectrophone measurements of H_2O in 80-20 air at the sample temperatures indicated.	218
18	Curve fit coefficients for pure water vapor absorption measurements at the temperature indicated in column five.	227
19	Curve fit coefficients for pure water vapor absorption measurements at 975.930 cm^{-1}	228
20	List of measured temperature coefficient, θ as defined in Equation (128), for the pure water vapor absorption measurements.	231
21	List of the coefficients, A^R and $A^{\nu 2}$ which appear in Equation (135) of the text.	235

78 09 05 202

LIST OF FIGURES

Figure		Page
1	Energy level diagram explaining the fine structure of a rotation-vibration band	7
2	Percentage change in k^{LC} with temperature, relative to the absorption coefficient at $300^{\circ}K$	16
3	Percentage change in k^{FW} with temperature relative to the absorption coefficient of $300^{\circ}K$	18
4	Percentage error in absorption coefficient plotted versus percentage error in transmittances. After Trusty.	23
5	Schematic diagram of the physical situation which will be described using the rate equation approximate of Kreuzer and the heat flow solutions of Kerr and Atwood.	27
6	Energy level diagram for the rate equation description given by Kreuzer.	27
7	Schematic plot of laser power vs time when chopped by a rotating mechanical blade.	29
8	Plot of the theoretical pressure signal given by the rate equation approximation of Equation (66), with $\tau_T=0.2$ sec and $T=0.125$ sec.	31
9	Normalized step response of a cylindrical spectrophone to a Gaussian beam as predicted by the heat flow analysis of Kerr and Atwood.	34
10	An RC circuit analog to the spectrophone.	36
11	Pressure variations produced by induced temperature variation of the sample cell.	41
12a	Normalized optoacoustic signal vs pressure with $\omega\tau^0$ as a parameter.	45
12b	Phase shift of the optoacoustic signal as a function of pressure with $\omega\tau^0$ as a parameter.	46
13	A basic differential spectrophone.	47

14	Schematic drawing of the Brewster angle differential spectrophone.	49
15	The stainless steel spectrophone.	51
16	Block diagram of the temperature control system for the spectrophone.	52
17	Schematic diagram of CO ₂ laser optics.	54
18	Block diagram of the electronic stabilizer for the CO ₂ laser.	56
19	Photograph of the CO ₂ laser.	58
20	Block diagram of data acquisition system.	59
21	Block diagram of spectrophone instrumentation.	62
22	Manifold.	63
23	Calibration data for the signal and reference channels.	65
24	Block diagram of lock-in amplifier calibration experiment.	68
25a	Calibration data on the 1 mV scale.	68
25b	Calibration data on the 2.5 mV scale.	69
25c	Calibration data on the 10 mV scale.	69
26	Schematic diagram of optical system for spectrophone experiment.	70
27	Plot of normalized response of reduced low power vs normalized response at "full" power.	71
28	An illustration of the problems caused by incomplete sample mixing in the spectrophone.	73
29	Sectional view at one end of the spectrophone.	75
30	Schematic diagram of spectrophone alignment optics.	77
31	Entrance optics for the White cell experiments.	79
32	Normalized stability test results for the White cell at 1.1 km path length.	81

33	Measured H ₂ O in N ₂ absorption coefficient at a total pressure of 760 Torr for the P(30) CO ₂ laser line at 934.894 cm ⁻¹	86
34	Measured H ₂ O in N ₂ absorption coefficient at a total pressure of 760 Torr for the P(28) CO ₂ laser line at 936.804 cm ⁻¹	87
35	Measured H ₂ O in N ₂ absorption coefficient at a total pressure of 760 Torr for the P(26) CO ₂ laser line at 938.688 cm ⁻¹	88
36	Measured H ₂ O in N ₂ absorption coefficient at a total pressure of 760 Torr for the P(24) CO ₂ laser line at 940.548 cm ⁻¹	89
37	Measured H ₂ O in N ₂ absorption coefficient at a total pressure of 760 Torr for the P(22) CO ₂ laser line at 942.383 cm ⁻¹	90
38	Measured H ₂ O in N ₂ absorption coefficient at a total pressure of 760 Torr for the P(20) CO ₂ laser line at 944.194 cm ⁻¹	91
39	Measured H ₂ O in N ₂ absorption coefficient at a total pressure of 760 Torr for the P(18) CO ₂ laser line at 945.980 cm ⁻¹	92
40	Measured H ₂ O in N ₂ absorption coefficient at a total pressure of 760 Torr for the P(12) CO ₂ laser line at 951.192 cm ⁻¹	93
41	Measured H ₂ O in N ₂ absorption coefficient at a total pressure of 760 Torr for the P(10) CO ₂ laser line at 952.881 cm ⁻¹	94
42	Measured H ₂ O in N ₂ absorption coefficient at a total pressure of 760 Torr for the R(10) CO ₂ laser line at 969.140 cm ⁻¹	95
43	Measured H ₂ O in N ₂ absorption coefficient at a total pressure of 760 Torr for the R(12) CO ₂ laser line at 970.547 cm ⁻¹	96
44	Measured H ₂ O in N ₂ absorption coefficient at a total pressure of 760 Torr for the R(14) CO ₂ laser line at 971.930 cm ⁻¹	97
45	Measured H ₂ O in N ₂ absorption coefficient at a total pressure of 760 Torr for the R(16) CO ₂ laser line at 973.288 cm ⁻¹	98

46	Measured H ₂ O in N ₂ absorption coefficient at a total pressure of 760 Torr for the R(20) CO ₂ laser line at 975.930 cm ⁻¹	99
47	Measured H ₂ O in N ₂ absorption coefficient at a total pressure of 760 Torr for the R(22) CO ₂ laser line at 977.215 cm ⁻¹	100
48	Measured H ₂ O in N ₂ absorption coefficient at a total pressure of 760 Torr for the R(28) CO ₂ laser line at 980.913 cm ⁻¹	101
49	Measured H ₂ O in N ₂ absorption coefficient at a total pressure of 760 Torr for the P(16) CO ₂ laser line at 1050.441 cm ⁻¹	102
50	Measured H ₂ O in N ₂ absorption coefficient at a total pressure of 760 Torr for the P(14) CO ₂ laser line at 1052.196 cm ⁻¹	103
51	Measured H ₂ O in N ₂ absorption coefficient at a total pressure of 760 Torr for the P(12) CO ₂ laser line at 1053.924 cm ⁻¹	104
52	Measured H ₂ O in N ₂ absorption coefficient at a total pressure of 760 Torr for the R(12) CO ₂ laser line at 1073.278 cm ⁻¹	105
53	Measured H ₂ O in N ₂ absorption coefficient at a total pressure of 760 Torr for the R(18) CO ₂ laser line at 1077.303 cm ⁻¹	106
54	Measured H ₂ O in N ₂ absorption coefficient at a total pressure of 760 Torr for the R(22) CO ₂ laser line at 1079.852 cm ⁻¹	107
55	Measured H ₂ O in N ₂ absorption coefficient at a total pressure of 760 Torr for the R(24) CO ₂ laser line at 1081.087 cm ⁻¹	108
56	Measured H ₂ O in 80% N ₂ and 20% O ₂ absorption coefficient at a total pressure of 760 Torr for the P(28) CO ₂ laser line at 936.804 cm ⁻¹	110
57	Measured H ₂ O in 80% N ₂ and 20% O ₂ absorption coefficient at a total pressure of 760 Torr for the P(20) CO ₂ laser line at 944.194 cm ⁻¹	111

58	Measured H ₂ O in 80% N ₂ and 20% O ₂ absorption coefficient at a total pressure of 760 Torr for the R(20) CO ₂ laser line at 975.930 cm ⁻¹	112
59	Measured H ₂ O in 80% N ₂ and 20% O ₂ absorption coefficient at a total pressure of 760 Torr for the R(28) CO ₂ laser line at 980.913 cm ⁻¹	113
60	Measured H ₂ O in 80% N ₂ and 20% O ₂ absorption coefficient at a total pressure of 760 Torr for the P(20) CO ₂ laser line at 1046.854 cm ⁻¹	114
61	Measured H ₂ O in 80% N ₂ and 20% O ₂ absorption coefficient at a total pressure of 760 Torr for the P(18) CO ₂ laser line at 1048.661 cm ⁻¹	115
62	Measured H ₂ O in 80% N ₂ and 20% O ₂ absorption coefficient at a total pressure of 760 Torr for the P(16) CO ₂ laser line at 1050.441 cm ⁻¹	116
63	Measured H ₂ O in 80% N ₂ and 20% O ₂ absorption coefficient at a total pressure of 760 Torr for the R(18) CO ₂ laser line at 1077.303 cm ⁻¹	117
64	Measured H ₂ O in 80% N ₂ and 20% O ₂ absorption coefficient at a total pressure of 760 Torr for the R(26) CO ₂ laser line at 1082.296 cm ⁻¹	118
65	Measured H ₂ O in 60% N ₂ and 40% O ₂ absorption coefficient at a total pressure of 760 Torr for the P(28) CO ₂ laser line at 936.804 cm ⁻¹	119
66	Measured H ₂ O in 60% N ₂ and 40% O ₂ absorption coefficient at a total pressure of 760 Torr for the P(20) CO ₂ laser line at 944.194 cm ⁻¹	120
67	Measured H ₂ O in 60% N ₂ and 40% O ₂ absorption coefficient at a total pressure of 760 Torr for the R(20) CO ₂ laser line at 975.930 cm ⁻¹	121
68	Measured H ₂ O in 60% N ₂ and 40% O ₂ absorption coefficient at a total pressure of 760 Torr for the R(28) CO ₂ laser line at 980.913 cm ⁻¹	122
69	Measured H ₂ O in 60% N ₂ and 40% O ₂ absorption coefficient at a total pressure of 760 Torr for the P(20) CO ₂ laser line at 1046.854 cm ⁻¹	123
70	Measured H ₂ O in 60% N ₂ and 40% O ₂ absorption coefficient at a total pressure of 760 Torr for the P(18) CO ₂ laser line at 1048.661 cm ⁻¹	124

71	Measured H ₂ O in 60% N ₂ and 40% O ₂ absorption coefficient at a total pressure of 760 Torr for the P(16) CO ₂ laser line at 1050.441 cm ⁻¹	125
72	Measured H ₂ O in 60% N ₂ and 40% O ₂ absorption coefficient at a total pressure of 760 Torr for the R(18) CO ₂ laser line at 1077.303 cm ⁻¹	126
73	Measured H ₂ O in 60% N ₂ and 40% O ₂ absorption coefficient at a total pressure of 760 Torr for the R(26) CO ₂ laser line at 1082.296 cm ⁻¹	127
74	Measured H ₂ O in O ₂ absorption coefficient at a total pressure of 760 Torr for the P(28) CO ₂ laser line at 936.804 cm ⁻¹	128
75	Measured H ₂ O in O ₂ absorption coefficient at a total pressure of 760 Torr for the P(20) CO ₂ laser line at 944.194 cm ⁻¹	129
76	Measured H ₂ O in O ₂ absorption coefficient at a total pressure of 760 Torr for the R(20) CO ₂ laser line at 975.930 cm ⁻¹	130
77	Measured H ₂ O in O ₂ absorption coefficient at a total pressure of 760 Torr for the R(28) CO ₂ laser line at 980.913 cm ⁻¹	131
78	Measured H ₂ O in O ₂ absorption coefficient at a total pressure of 760 Torr for the P(20) CO ₂ laser line at 1046.854 cm ⁻¹	132
79	Measured H ₂ O in O ₂ absorption coefficient at a total pressure of 760 Torr for the P(18) CO ₂ laser line at 1048.661 cm ⁻¹	133
80	Measured H ₂ O in O ₂ absorption coefficient at a total pressure of 760 Torr for the P(16) CO ₂ laser line at 1050.441 cm ⁻¹	134
81	Measured H ₂ O in O ₂ absorption coefficient at a total pressure of 760 Torr for the R(18) CO ₂ laser line at 1077.303 cm ⁻¹	135
82	Measured H ₂ O in 80% N ₂ and 20% O ₂ absorption coefficient at a total pressure of 760 Torr for the P(20) CO ₂ laser line at 944.194 cm ⁻¹	137
83	Measured H ₂ O in 80% N ₂ and 20% O ₂ absorption coefficient at a total pressure of 760 Torr for the P(20) CO ₂ laser line at 944.194 cm ⁻¹	138

84	Measured H ₂ O in 80% N ₂ and 20% O ₂ absorption coefficient at a total pressure of 760 Torr for the P(16) CO ₂ laser line at 947.743 cm ⁻¹	139
85	Measured H ₂ O in 80% N ₂ and 20% O ₂ absorption coefficient at a total pressure of 760 Torr for the P(16) CO ₂ laser line at 947.743 cm ⁻¹	140
86	Measured H ₂ O in 80% N ₂ and 20% O ₂ absorption coefficient at a total pressure of 760 Torr for the R(20) CO ₂ laser line at 975.930 cm ⁻¹	141
87	Measured H ₂ O in 80% N ₂ and 20% O ₂ absorption coefficient at a total pressure of 760 Torr for the R(20) CO ₂ laser line at 975.930 cm ⁻¹	142
88	Plot of the calibration function vs relative pressure. .	145
89	Measured water vapor absorption coefficient plotted as a function of the total pressure squared for the P(20) CO ₂ laser line at 944.194 cm ⁻¹	146
90	Measured H ₂ O in N ₂ absorption coefficient at a total pressure of 760 Torr for the P(30) CO ₂ laser line at 934.894 cm ⁻¹	148
91	Measured H ₂ O in N ₂ absorption coefficient at a total pressure of 760 Torr for the P(28) CO ₂ laser line at 936.804 cm ⁻¹	149
92	Measured H ₂ O in N ₂ absorption coefficient at a total pressure of 760 Torr for the P(26) CO ₂ laser line at 938.688 cm ⁻¹	150
93	Measured H ₂ O in N ₂ absorption coefficient at a total pressure of 760 Torr for the P(24) CO ₂ laser line at 940.548 cm ⁻¹	151
94	Measured H ₂ O in N ₂ absorption coefficient at a total pressure of 760 Torr for the P(22) CO ₂ laser line at 942.383 cm ⁻¹	152
95	Measured H ₂ O in N ₂ absorption coefficient at a total pressure of 760 Torr for the P(20) CO ₂ laser line at 944.194 cm ⁻¹	153
96	Measured H ₂ O in N ₂ absorption coefficient at a total pressure of 760 Torr for the P(18) CO ₂ laser line at 945.980 cm ⁻¹	154

97	Measured H ₂ O in N ₂ absorption coefficient at a total pressure of 760 Torr for the P(12) CO ₂ laser line at 951.192 cm ⁻¹	155
98	Measured H ₂ O in N ₂ absorption coefficient at a total pressure of 760 Torr for the P(10) CO ₂ laser line at 952.881 cm ⁻¹	156
99	Measured H ₂ O in N ₂ absorption coefficient at a total pressure of 760 Torr for the R(12) CO ₂ laser line at 970.547 cm ⁻¹	157
100	Measured H ₂ O in N ₂ absorption coefficient at a total pressure of 760 Torr for the R(18) CO ₂ laser line at 974.622 cm ⁻¹	158
101	Measured H ₂ O in N ₂ absorption coefficient at a total pressure of 760 Torr for the R(20) CO ₂ laser line at 975.930 cm ⁻¹	159
102	Measured H ₂ O in N ₂ absorption coefficient at a total pressure of 760 Torr for the R(22) CO ₂ laser line at 977.215 cm ⁻¹	160
103	Measured H ₂ O in N ₂ absorption coefficient at a total pressure of 760 Torr for the R(28) CO ₂ laser line at 980.913 cm ⁻¹	161
104	Measured H ₂ O in N ₂ absorption coefficient at a total pressure of 760 Torr for the P(18) CO ₂ laser line at 1048.661 cm ⁻¹	162
105	Measured H ₂ O in N ₂ absorption coefficient at a total pressure of 760 Torr for the P(16) CO ₂ laser line at 1050.441 cm ⁻¹	163
106	Measured H ₂ O in N ₂ absorption coefficient at a total pressure of 760 Torr for the P(14) CO ₂ laser line at 1052.196 cm ⁻¹	164
107	Measured H ₂ O in N ₂ absorption coefficient at a total pressure of 760 Torr for the R(18) CO ₂ laser line at 1077.303 cm ⁻¹	165
108	Measured H ₂ O in N ₂ absorption coefficient at a total pressure of 760 Torr for the R(24) CO ₂ laser line at 1081.087 cm ⁻¹	166
109	Measured H ₂ O in N ₂ absorption coefficient at a total pressure of 760 Torr for the R(26) CO ₂ laser line at 1082.296 cm ⁻¹	167

110	Measured H ₂ O in 80% N ₂ and 20% O ₂ absorption coefficient at a total pressure of 760 Torr for the P(28) CO ₂ laser line at 936.804 cm ⁻¹	168
111	Measured H ₂ O in 80% N ₂ and 20% O ₂ absorption coefficient at a total pressure of 760 Torr for the P(20) CO ₂ laser line at 944.194 cm ⁻¹	169
112	Measured H ₂ O in 80% N ₂ and 20% O ₂ absorption coefficient at a total pressure of 760 Torr for the R(20) CO ₂ laser line at 975.930 cm ⁻¹	170
113	Measured H ₂ O in 80% N ₂ and 20% O ₂ absorption coefficient at a total pressure of 760 Torr for the R(22) CO ₂ laser line at 977.214 cm ⁻¹	171
114	Measured H ₂ O in 80% N ₂ and 20% O ₂ absorption coefficient at a total pressure of 760 Torr for the R(28) CO ₂ laser line at 980.913 cm ⁻¹	172
115	Measured H ₂ O in 60% N ₂ and 40% O ₂ absorption coefficient at a total pressure of 760 Torr for the P(28) CO ₂ laser line at 936.804 cm ⁻¹	173
116	Measured H ₂ O in 60% N ₂ and 40% O ₂ absorption coefficient at a total pressure of 760 Torr for the P(20) CO ₂ laser line at 944.194 cm ⁻¹	174
117	Measured H ₂ O in 60% N ₂ and 40% O ₂ absorption coefficient at a total pressure of 760 Torr for the R(20) CO ₂ laser line at 975.930 cm ⁻¹	175
118	Measured H ₂ O in 60% N ₂ and 40% O ₂ absorption coefficient at a total pressure of 760 Torr for the R(22) CO ₂ laser line at 977.214 cm ⁻¹	176
119	Measured H ₂ O in 60% N ₂ and 40% O ₂ absorption coefficient at a total pressure of 760 Torr for the R(28) CO ₂ laser line at 980.913 cm ⁻¹	177
120	Measured pure water vapor absorption coefficient for the P(28) CO ₂ laser line at 936.804 cm ⁻¹	179
121	Measured pure water vapor absorption coefficient for the P(20) laser line at 944.194 cm ⁻¹	180
122	Measured pure water vapor absorption coefficient for the R(20) laser line at 975.930 cm ⁻¹	181
123	Measured pure water vapor absorption coefficient for the R(22) laser line at 977.214 cm ⁻¹	182

124	Measured pure water vapor absorption coefficient for the R(28) laser line at 980.913 cm^{-1}	183
125	Measured pure water vapor absorption coefficient for the P(14) laser line at 1052.196 cm^{-1}	184
126	Measured pure water vapor absorption coefficient for the R(18) laser line at 1077.303 cm^{-1}	185
127	Measured H_2O in N_2 absorption as a function of the CO_2 laser line wavenumber.....	196
128	Measured H_2O in 80-20 air absorption in km^{-1} as a function of wavenumber for a water vapor partial pressure of 14.3 Torr.....	197
129	Measured absorption coefficient (in km^{-1}) of CO_2 laser radiation as a function of frequency (in cm^{-1}) for a water vapor partial pressure of 14.3 Torr.....	199
130	Comparison of measured water vapor absorption coefficient (in km^{-1}) for the R(22) CO_2 laser line at 977.214 cm^{-1} and a total sample gas pressure of 760 Torr.....	200
131	Measured absorption in km^{-1} as a function of water vapor partial pressure in Torr for the P(20) CO_2 laser line at 944.194 cm^{-1}	201
132	Plot of Equation (113) as a function of the variable (1-ax). Where x gives the fraction of oxygen in the buffer gas.....	205
133	Measured water vapor absorption coefficient at a total pressure of 760 Torr, for the P(28) CO_2 laser line at 936.804 cm^{-1}	206
134	Measured water vapor absorption coefficient at a total pressure of 760 Torr, for the P(20) CO_2 laser line at 944.194 cm^{-1}	207
135	Measured water vapor absorption coefficient at a total pressure of 760 Torr, for the R(28) CO_2 laser line at 980.913 cm^{-1}	208
136	Measured water vapor absorption coefficient at a total pressure of 760 Torr, for the P(20) CO_2 laser line at 1046.854 cm^{-1}	209

137	Measured water vapor absorption coefficient at a total pressure of 760 Torr, for the P(18) CO ₂ laser line at 1048.661 cm ⁻¹	210
138	Measured water vapor absorption coefficient at a total pressure of 760 Torr, for the R(20) CO ₂ laser line at 975.930 cm ⁻¹	212
139	Measured water vapor absorption coefficient at a total pressure of 760 Torr, for the P(28) CO ₂ laser line at 936.804 cm ⁻¹	213
140	Measured water vapor absorption coefficient at a total pressure of 760 Torr, for the P(20) CO ₂ laser line at 944.194 cm ⁻¹	214
141	Measured water vapor absorption coefficient at a total pressure of 760 Torr, for the R(20) CO ₂ laser line at 975.930 cm ⁻¹	215
142	Measured water vapor absorption coefficient at a total pressure of 760 Torr, for the R(22) CO ₂ laser line at 977.214 cm ⁻¹	216
143	Measured water vapor absorption coefficient at a total pressure of 760 Torr, for the R(28) CO ₂ laser line at 980.913 cm ⁻¹	217
144	Measured absorption coefficient of H ₂ O in 80-20 air for the R(20) CO ₂ laser line at 975.930 cm ⁻¹ ...	220
145	Percentage change in the measured H ₂ O in air absorption coefficient with temperature, relative to the absorption at 300°K for the R(20) laser line at 975.930 cm ⁻¹	221
146	Measured absorption coefficient of H ₂ O in 80-20 air for the P(20) CO ₂ laser line at 944.194 cm ⁻¹ ...	222
147	Measured absorption coefficient of H ₂ O in 80-20 air for the P(16) CO ₂ laser line at 947.743 cm ⁻¹ ...	223
148	Measured values of the self broadening coefficient, C _S (ν) as a function of temperature near 10.6 μm for pure water vapor samples.....	230

149	Measured absorption coefficient of 14.3 Torr H_2O_1 in N_2 as a function of CO_2 laser frequency in cm^{-1} .. 233
150	Measured absorption coefficient of 14.3 Torr H_2O_1 in N_2 as a function of CO_2 laser frequency in cm^{-1} .. 234
151	Plot of "corrected" spectrophone absorption coefficient results (as defined in the text) vs. CO_2 laser frequency in cm^{-1} for 14.3 Torr of H_2O in N_2 at a total pressure of 760 Torr and a nominal temperature of $24^{\circ}C$ 236
152	Plot of "corrected" White cell absorption coefficient results (as defined in the test) vs. CO_2 laser frequency in cm^{-1} for 14.3 Torr of H_2O in N_2 at a total pressure of 760 Torr and a nominal temperature of $22.5^{\circ}C$ 237

CHAPTER I INTRODUCTION

Radiation from the CO₂ laser has the useful property of residing within the 8-12 μm atmospheric window. This fortunate situation makes the laser extremely useful for applications such as communications, remote sensing, etc. However, these applications require accurate modeling of the small absorption that does exist. An atmospheric transmission model for this spectral region is also vital to broadband measurements concerned with IR transfer through the atmosphere. The purpose of this study is to investigate one aspect of this problem - the molecular absorption of CO₂ laser radiation by water vapor.

In the atmosphere, molecular absorption of CO₂ laser radiation can be attributed principally to carbon dioxide and water vapor.* Absorption by the carbon dioxide molecule is relatively well understood and its contribution can be accurately predicted¹. However, an accurate model for water vapor absorption for the 8-12 μm window does not exist² and this is a source of great concern to systems designers. The contribution of H₂O to total molecular absorption in this wavelength region is comparable to that of carbon dioxide at CO₂ laser frequencies, and nearly an order of magnitude greater for broadband radiation propagation.

Traditional (i.e., Lorentz) line shape models of far wing water vapor absorption fail (by nearly an order of magnitude) to correctly predict the absorption which is experimentally observed. This failure includes an inability to model both the pressure and temperature dependence of water vapor absorption. To compensate for this deficiency, workers have given a name to this phenomenon, calling it the water vapor continuum, which simply means there exists an anomalous additional contribution to absorption that is attributable to water vapor. The word continuum is used to imply that this source of absorption is a slowly varying function of frequency as opposed to the normal situation at a frequency in a vibration-rotation band consisting of many closely spaced narrow absorption lines.

Studies of atmospheric transmittance in the 8-12 μm region were reported as early as 1881³ and the existence of a water vapor continuum in this spectral region was first suggested in 1938 by Elsasser⁴. Since then, numerous low resolution (broad band) studies of IR transmittance through the atmosphere have reported this phenomenon⁵⁻⁹. Although there is a long standing agreement on its existence, there is no definitive explanation for the origin of the water vapor continuum.

*Ozone also has some strong, but narrow, absorption lines in this spectral region.

More recently, McCoy¹⁰ has performed accurate laboratory (multiple traversal cell) measurements to examine water vapor absorption at the 10.59 μm P(20) CO_2 laser line, for which the principal contribution to absorption arise from the continuum. Because a laser measurement obtains information at only one (narrow) position, it cannot provide frequency dependence information unless a large number of laser lines are examined. A second limitation of many reported laser studies is that they were performed at a single temperature. Bignell¹¹ has performed broad band measurements of the continuum temperature dependence which indicated a negative temperature coefficient of approximately -2% near 30°C but Trusty¹² using a CO_2 laser and spectrophone, measured a positive coefficient. (More will be said concerning Trusty's results later.)

Burch¹³ has resolved this question in favor of Bignell by demonstrating a negative temperature coefficient for water vapor samples studied at elevated (nearly 388°K) temperatures. This negative temperature dependence has been used to substantiate two new theories -- the water dimer¹⁴ (H_2O_2), and clusters¹⁵, which attribute continuum absorption to mechanisms other than the far wings of strong water vapor lines⁴. However, the data available is insufficient to definitely support one mechanism in favor of another; in particular, a refined far wing line profile may be equally capable of explaining continuum absorption and the observed temperature dependence⁴.

In this study we conducted both optoacoustic (spectrophone) and long path (multiple traversal cell) measurements of water vapor absorption at several CO_2 laser lines in the 9.4 μm and 10.4 μm bands. These studies were performed with the goal of obtaining highly accurate pressure, temperature and frequency dependence data on the continuum absorption. The analysis of the results has been made in terms of the well known, widely used (and simplistic) Lorentz line shape, with the full knowledge that this procedure does not provide an accurate model in this region. We have attempted to examine the near line center and far wing behavior of this model in terms of the experimental results in hopes of clearly showing where and how this model fails. The results from this study are then used to provide an empirical description of the frequency and temperature dependence of water vapor continuum absorption in the atmosphere near 295°K and one atm. pressure.

In Chapter II selective ideas and principles from the theory of molecular absorption are presented together with an analytic formulation of the absorption coefficient in terms of the Lorentz line shape. The discussion includes an analysis of the temperature and pressure dependence of the absorption coefficient predicted by this model. Chapter III contains a fundamental as well as detailed description of the spectrophone and White¹⁶ cell used to perform absorption measurements in this study. Also considered are the limitations and experimental difficulties which are typically encountered in the application of these two techniques. Analysis of the spectrophone includes a review of two theoretical descriptions of the pressure signal response for a nonresonant instrument.

In Chapter IV the experimental apparatus and procedures are described. Chapter V contains computer plots of the pressure broadened and pure water vapor absorption data which is then analyzed in Chapter VI. The results of this analysis are summarized in Chapter VII.

CHAPTER II MOLECULAR ABSORPTION

Absorption of radiation by the atmosphere is most readily described in terms of an extinction or attenuation constant, $\alpha(\nu', T, P)$, which gives the fractional energy lost per unit length in the direction of propagation. In its most general form $\alpha(\nu', T, P)$ will contain contributions from all of the mechanisms which are active in attenuating an electromagnetic beam as it passes through the atmosphere. In this study, the only contributions considered come from the phenomenon of molecular absorption. Under controlled laboratory conditions it will be assumed that scattering and turbulence are not present. In this case it is more appropriate to write $\alpha = k(\nu', T, P)$ where k is defined as the absorption coefficient and will have units of km^{-1} for this study. With Lambert's law we can relate the transmitted intensity, I , to the incident intensity, I_0 , by the expression

$$I = I_0 e^{-k(\nu', T, P) \ell} \quad (1)$$

where ℓ is the path length in km of the absorbing medium. The transmittance of this medium is defined by the ratio I/I_0 and from Equation (1) it is observed that

$$T \equiv \frac{I}{I_0} = e^{-k(\nu', T, P) \ell} \quad (2)$$

When the only contributions under consideration come from molecular absorption, the parameter k together with Equation (2) describe the transmission characteristics of the atmosphere.

The arguments, ν' , T and P of the absorption coefficient are included to explicitly show the dependence of k on both the frequency, ν' of the radiation and certain intensive properties of the gaseous medium such as pressure and temperature. In order to analyze these functional dependences it will be more convenient and conventional to express k in a different fashion. It is customary to define the absorption coefficient as a product of two functions, the line shape, $g(\nu' - \nu'_0)$ with line center ν'_0 and line strength S , so that

$$k = \sum_{i=1}^N S_i g_i(\nu' - \nu_{0i}) \quad (3)$$

The summation is included here to indicate that contributions from more than one absorption line, g_i with strength S_i are required to determine k at the frequency ν' . This discrete sum arises from the fact that photon absorption is a quantum process in which the internal energy of the absorbing molecule is raised from a lower state E_i'' to an upper state E_i' . Equation (3) gives the macroscopic parameter k as a sum of products which describe the interaction

of the photon flux with molecules active in the absorption process. The line strength function, S_i , provides a quantum mechanical description giving the probability that a photon, ν'_o will be absorbed at the center frequency, also ν'_o , of a particular transition, i.e.,

$$E''_i + h\nu'_{oi} \rightarrow E'_i \quad (4)$$

The line shape, $g_i(\nu' - \nu'_{oi})$ relates this probability of the transition at line center, ν'_{oi} , given by the line strength, S_i , to that at any other frequency, ν' which is removed from line center. Also contained in the expressions for S_i and $g_i(\nu' - \nu'_{oi})$ are the temperature and pressure dependence of the absorption process.

This formulation of the absorption coefficient (given in Equation (3)) will serve as the basis on which the theoretical discussion of this chapter will follow. The first section contains a qualitative description of the photon-matter interaction and some comments concerning the subject of molecular absorption. This is followed by an analysis of the analytic expressions used to describe molecular absorption, i.e., the equations for line strength and line shape. In the third section the temperature and pressure dependence contained in these two functions is considered. Finally, the results of this chapter are connected with continuum absorption; in particular the concept of the water vapor dimer(s) is discussed.

A. Introduction

The analytic description given in Equation (4) provides the most fundamental picture of the absorption process. Implicit in this equation is the description of the event where a molecule in the lower energy state E'' absorbs one photon (we will only treat single photon processes here) of energy $h\nu'_o$ and thereby increases its total energy to E' . The energy levels, E , which appear in this picture represent a sum of the internal energy contribution provided by electronic, vibrational and rotational "motions" of the molecule. These energy levels are discrete which is to say that not all values of the internal energy are possible. Only those energy levels which correspond to eigenvalues of the Hamiltonian for the particular molecule are allowed, i.e.,

$$\hat{H}_M | E \rangle = E | E \rangle \quad (5)$$

where \hat{H}_M is the Hamiltonian operator for the molecule

$| E \rangle$ is the energy eigenstate,

and E is the energy eigenvalue for the state $| E \rangle$.

Equation (4) can be re-written

$$E' - E'' = h\nu'_o \quad (6)$$

to show that the energy of the molecule must increase by an amount $h\nu'_o$. The internal form (electronic, vibration and/or rotation) by which this additional energy manifests itself will be determined by the photon energy under

consideration. Table 1 gives a list of the three fundamental transitions and the relative photon energies which are encountered in each case. In this study we shall only be concerned with the absorption of photons with wavelengths between 9 and 11 μm . This corresponds to the near infrared and vibration-rotation transitions, see Table 1. A set of such transitions is shown in Figure 1 which was taken from Herzberg¹⁷. In this figure a set of rotational energy levels for each (upper and lower) vibrational energy level are drawn and labeled with their appropriate rotational quantum numbers, J' for the higher level and J'' for the lower. The allowed transitions (indicated by the vertical lines) are also shown and labeled. The energy levels at $J'=0$ and $J''=0$ correspond to the pure vibrational energy states of this hypothetical molecule. The adjacent rotational energy levels are more closely spaced than the vibrational energies and correspond to smaller changes of the internal energy. The vibration-rotation energy levels (shown in Figure 1) correspond to allowed energy eigenstates (interactions are ignored in this zero order approximation) which have been formed by simply superimposing the rotational energy structure on the vibration levels. In this simplified description the Hamiltonian of Equation (5) is given by

$$\hat{H}_M = \hat{H}_{\text{Rot}} + \hat{H}_{\text{Vib}} \quad (7)$$

and Equation (5) becomes

$$\hat{H}_M |E\rangle = (E_{\text{Rot}} + E_{\text{Vib}}) |E\rangle = E |E\rangle \quad (8)$$

where E_{Rot} is the rotational energy eigenvalue,
 E_{Vib} is the vibrational energy eigenvalue

and the model being considered here is the vibrating rotator. The quantum numbers J which appear in Figure 1 provide a label for the rotational energy eigenstates since they appear explicitly in the analytic expression for the eigenvalue, E_{Rot} .

For each allowed energy (level) eigenvalue, E , there exists an eigenstate $|E\rangle$ which contains a complete description of the molecule. In wave-mechanical terms this description is given by the wavefunction $\psi(\underline{r})$, i.e.,

$$\psi(\underline{r}) = \langle \underline{r} | E \rangle \quad (9)$$

It is important to realize that not all of the processes described by Equation (4) will readily occur, i.e., not all transitions are allowed. Note in particular that only certain energy levels in Figure 1 are connected by the vertical lines which indicate the allowed transitions. The probability that a molecule in the energy state E'' will absorb a photon with energy $h\nu'$ is determined by the relative nature of the upper and lower eigenstates. In quantum mechanical terms the transition probability is determined by applying Fermi's golden rule which essentially calls for the evaluation of the dipole matrix element

$$M_{\nu} = \langle E' | \underline{r} | E'' \rangle \quad (10)$$

Table 1
 Approximate spectral regions for the electronic, vibrational and rotational transitions. From lecture notes given by K. Narahari Rao.

Transition	Wavelength μm	Region
Electronic	less than 0.7	Optical
Vibration	0.7 - 50 50 - 1000	Near IR Far IR
Rotation	greater than 1000	Microwave

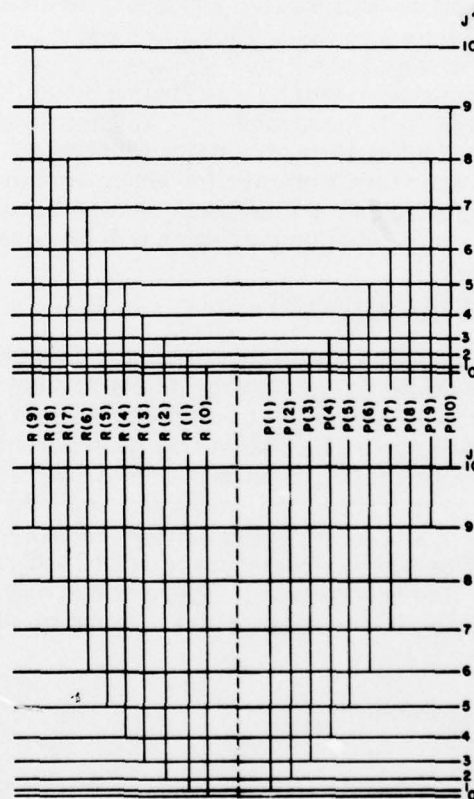


Figure 1. Energy level diagram explaining the fine structure of a rotation-vibration band. In general, the separation of the two vibrational levels is considerably larger compared to the spacing of the rotational levels than shown in the figure indicated by the broken parts of the vertical lines representing the transitions.

when $|M| \neq 0$, the transition is called an "allowed transition"; if $|M| = 0$, it is "not allowed". For the vibrating rotator model which has its energy levels drawn in Figure 1, $|M|$ in Equation (10) will be nonzero only for $J'-J''=-1$. $+1$ corresponds to the R branch lines, -1 to the P branch.

The rigid rotator described here provides a useful but crude model for predicting the basic structure of near infrared molecular absorption. Its failures arise from the extremely simplistic formulation which ignores the consequences of interaction energies, motion by the center of mass (doppler broadening), external perturbation (pressure broadening), etc. These effects have a significant influence on the molecule-photon interaction. They result in a continuous range of photon frequencies which can be active in any of the transitions, such as those shown in Figure 1. In the earlier description only a photon with energy $h\nu' = E'-E''$ could be active in the transition between the two states $|E''\rangle$ and $|E'\rangle$. The point made here is that in a "real" molecule this transition will involve a range of photon frequencies, centered about ν'_0 which can be absorbed. This gives rise to a description of the transition in terms of a "line shape" $g(\nu'-\nu'_0)$ which gives the probability that a photon with frequency ν' will be absorbed relative to the absorption of a line center photon with frequency ν'_0 . Absolute levels in the absorption coefficient are arrived at through a determination of the line strength which is proportional to the transition rate for absorption at line center. In the next section these concepts will be brought together and analytic expressions for both line shape and line strength will be considered.

B. The Absorption Coefficient

Perturbations of the absorbing molecules increase the number of transitions which contribute to the absorption coefficient $k(\nu')$ from a single line centered at the frequency ν' to all those lines in a neighborhood of ν' . In the case of water vapor absorption this neighborhood may be quite large. The size of each contribution is determined by the "strength" of the line, given here in a function S and the frequency dependence or shape, given by a function $g(\nu'-\nu'_0)$, where ν'_0 is the center frequency, see Equation (3). Because the absorption line no longer has a delta function frequency dependence, one says that the line is broadened. There are several mechanisms which produce a broadening of the spectral line. Some of the most notable are:

1. natural
2. collision (pressure)
3. Doppler.

1. Line shape

Natural line width is produced by an interaction of the molecule with a radiation field. This perturbation distorts the upper and lower energy levels of the transition and thereby produces a molecular line width on the order of 10^{-8} cm^{-1} . This mechanism results in a homogeneous broadened line and therefore establishes a lower limit for spectral line width. Weisskopf and Wigner¹⁸ have shown that this natural line shape, $g_N(\nu-\nu_0)$, is Lorentzian, so that

$$g_N(\nu - \nu_0) = \frac{1}{\pi} \frac{\alpha_N}{(\nu - \nu_0)^2 + \alpha_N^2} \quad (11)$$

where ν_0 is the line center frequency in wavenumbers,
 α_N is the halfwidth in wavenumbers, i.e., one half the width of
the line at one half its maximum amplitude

and¹⁹

$$\alpha_N = \frac{1}{2\pi c\tau} \quad (12)$$

where c is the speed of light
and τ is the spontaneous life time.

Of the three broadening mechanisms listed above collision broadening will prove to be the most relevant to this study. This effect also produces a homogeneously broadened line and is usually referred to as pressure broadening. It is the dominant mechanism in gas samples with a pressure greater than about 30 Torr. A rigorous and complete quantum mechanical treatment of collision broadening does not exist; the problem requires treatment of a very large number of mutually interacting systems all of which must be treated at once. Hence, this is a multibody problem which has not proved tractable. Approximate solutions to the problem indicate that this line shape is also Lorentzian²⁰

$$g_L(\nu - \nu_0) = \frac{1}{\pi} \frac{\alpha_L}{(\nu - \nu_0)^2 + \alpha_L^2} \quad (13)$$

where α_L is the Lorentz half width.

From the kinetic theory of gases²¹ it can be shown that

$$\alpha_L = \frac{F}{2\pi} = \frac{1}{4\pi} \sum_i N_i (D_{a,i})^2 \left[2\pi kT \left(\frac{1}{m_a} + \frac{1}{m_i} \right) \right]^{\frac{1}{2}} \quad (14)$$

where F is the collision frequency,
 N_i is the number of molecules of the i th type per unit volume,
 $D_{a,i}$ is the sum of the optical collision diameters of the absorbing molecule and a molecule of the i th type,
 k is the Boltzmann's constant,
 T is the temperature,
 m_a is the mass of the absorbing molecule,
and m_i is the mass of a molecule of the i th type.

The most general form of Equation (14) required for this study involves a mixture of three gases - water vapor (the absorber), nitrogen and oxygen. Substituting the ideal gas law into this equation and redefining terms permits the Lorentz half width to be expressed as²¹

$$\alpha_L = \frac{1}{(8\pi kT)^{\frac{1}{2}}} C_{H_2O, N_2} [P_{H_2O}^B + P_{O_2} F_{O_2} + P_{N_2}] \quad (15)$$

or

$$\alpha_L = \frac{1}{(8\pi kT)^{\frac{1}{2}}} C_{H_2O, N_2} P_e \quad (16)$$

where

$$P_e = P_{H_2O}^B + P_{O_2} F_{O_2} + P_{N_2} \quad (17)$$

and is referred to as the effective pressure. In Equation (15) the variables are defined as follows

$$C_{H_2O, N_2} = (D_{H_2O, N_2})^2 \left(\frac{m_{H_2O} + m_{N_2}}{m_{H_2O} m_{N_2}} \right)^{\frac{1}{2}} \quad (18)$$

where P_{H_2O} is the partial pressure of H_2O ,
 P_{O_2} is the partial pressure of oxygen,
 P_{N_2} is the partial pressure of nitrogen,
 B is the self-broadening coefficient,
of H_2O with respect to N_2 ,
and F_{O_2} is the foreign broadening coefficient of oxygen
with respect to N_2 .

At frequencies near line center the Lorentz line shape gives reasonable results. However, when strong interactions (collisions) are significant, i.e., in the far wings, its description does not accurately model water vapor absorption. As a result, other line shapes²² have been proposed to model the far wing line profile. One such line shape is given by

$$g(\nu - \nu_0) = \frac{a}{2\pi} \sin \frac{\pi}{a} \frac{\alpha^{a-1}}{|\nu - \nu_0|^a + \alpha^a} \quad 1 < a < 2 \quad (19)$$

which accentuates the contributions in the far wings. For the present discussions the Lorentz line shape of Equation (13) will be adequate to describe the central features. Equation (19) can provide an empirical fit to experimental results.

As the name implies, the third source of broadening (Doppler) is produced by the relative motion of molecules while they absorb (or emit) photons. This produces an inhomogeneously broadened line, i.e., since the molecules are traveling with different velocities, they will have their respective line center frequencies shifted by different amounts relative to the laboratory reference frame. The Doppler line shape is given by²³

$$g_D(\nu - \nu_0) = \frac{1}{\alpha_D} \left(\frac{\ln 2}{\pi} \right)^{\frac{1}{2}} e^{-[\ln 2 (\nu - \nu_0)^2 / \alpha_D^2]} \quad (20)$$

which represents a line shape produced by the Maxwellian velocity distribution of the molecules. Here α_D is the Doppler half width which can be found from

$$\alpha_D = \nu_0 \left(\frac{2kT}{mc^2 \ln 2} \right)^{\frac{1}{2}} \quad (21)$$

where ν_0 is the line center frequency,
 T is the temperature,
 k is the Boltzmann's constant,
 m is the molecular mass,
and c is the speed of light.

At pressures between ~ 1 and ~ 30 Torr both Doppler and collision broadening are important mechanisms and jointly determine the shape of the spectral lines. Under these conditions it is necessary to combine the two descriptions. This amounts to a convolution of the Doppler line, Equation (20) with the Lorentz line, Equation (13), which produces the Voigt profile, given by²⁴

$$g_V(\nu - \nu_0) = \frac{\alpha_L}{\pi^{3/2}} \int_{-\infty}^{\infty} \frac{e^{-x^2} dx}{\left[(\nu - \nu_0) - \frac{2\alpha_D x}{\ln 2} \right]^2 + \alpha_L^2} \quad (22)$$

where α_L is the Lorentz half width given by Equation (16)
and α_D is the Doppler half width given by Equation (21).

2. Line strength

The line strength provides a measure of the transition probability at the line center frequency. The frequency dependence of the absorption coefficient appears in the line shape functions which we have required to satisfy

$$\int_{-\infty}^{\infty} g(\nu - \nu_0) d\nu = 1 \quad (23)$$

by multiplying with the appropriate constants. This normalization is motivated by the definition of line strength

$$S_i = \int_{-\infty}^{\infty} k_i(\nu) d\nu \quad (24)$$

i.e., the integral of the absorption coefficient over all wavenumbers. Substituting from Equation (3) and using only the contribution from a single (the *i*th) absorption line

$$S_i(\nu_{0i}, T, p_a) = \int_{-\infty}^{\infty} S_i g_i(\nu - \nu_{0i}) d\nu \quad (25)$$

where the arguments of S_i are included to emphasize the dependence of S_i on ν_{0i} , the line center frequency, the temperature, T and the absorber partial pressure, p_a . An equation for the line strength can be derived from Lambert's law and an expression for the induced transition rate²⁵

$$S = \frac{p_a}{kT} \frac{g_u}{8\pi \nu_0^2} \frac{A_{u\ell}}{Q_V Q_R Q_E} (1 - e^{-hc \nu_0/kT}) e^{-E_\ell/kT} \quad (26)$$

where p_a is the absorber partial pressure,
 T is the temperature,
 ν_0 is the line center frequency of the transition in wavenumbers,
 $A_{u\ell}$ is the Einstein transition probability of spontaneous emission,
 Q_V is the vibrational partition function,
 Q_R is the rotational partition function,
 Q_E is the electronic partition function,
 k is the Boltzmann's constant,
 E_ℓ is the energy of the lower energy state,
 i.e., $(E_u - E_\ell)/hc = \nu_0$,

and g_u is the degeneracy of the upper energy level.

In the case of a transition between two degenerate levels with degeneracies g_ℓ and g_u , the Einstein coefficient of spontaneous emission is given by¹⁷

$$A_{u\ell} = \frac{64 \pi^4 \nu_0^3}{3h g_u} \frac{g_\ell g_u}{\sum_{i,j} |M_{u,j,\ell,i}|^2} \quad (27)$$

In this discussion we can set $Q_F = 1$. It remains to express the temperature dependence found in Q_V and Q_R . The vibrational partition function can be easily calculated in the harmonic oscillator approximation and is given by²¹

$$Q_V = \frac{1}{1 - e^{-\omega_e hc/kT}} \quad (28)$$

where ω_e is a vibration constant.

For the range of temperatures considered here Q_V is essentially unity and will also be eliminated. For water vapor (asymmetric top) the rotational partition function is given approximately by¹⁷

$$Q_R = \sqrt{\frac{\pi}{ABC} \left(\frac{kT}{hc} \right)^3} \quad (29)$$

where A, B and C are the rotational constants, i.e., $h/(8\pi^2 cT)$.

C. Temperature and Pressure Dependence

From the results given in the previous section it is now possible to find an expression for the temperature and pressure dependence of the absorption coefficient. Starting with Equation (3) and substituting in the expressions for the pressure broadened line shape, Equation (13) and line strength, Equation (26) we obtain the desired result

$$k(\nu) = \frac{1}{\pi} \frac{p_a}{p_a^0} \frac{T^0}{T} \frac{Q_R^0}{Q_R} \sum_i \frac{\alpha_{L_i}}{(\nu - \nu_{oi})^2 + \alpha_{L_i}^2} \frac{1 - e^{-hc\nu_{oi}/kT}}{1 - e^{-hc\nu_{oi}/kT^0}} e^{-\frac{E_{l_i}}{k} \left(\frac{1}{T} - \frac{1}{T^0} \right)} S_i^0 \quad (30)$$

where

$$S_i^0 = \frac{p_a^0}{kT^0} \frac{g_{u_i}}{8\pi\nu_{oi}^2} \frac{A_{u_{l_i}}}{Q_R^0} (1 - e^{-hc\nu_{oi}/kT^0}) e^{-E_{l_i}/kT^0} \quad (31)$$

and

$$Q_R^0 = \sqrt{\frac{\pi}{ABC} \left(\frac{kT^0}{hc} \right)^3} \quad (32)$$

for some reference temperature, T^0 and absorber partial pressure p_a^0 . The absorption coefficient can be rewritten using Equations (32) and (29) as

$$k(\nu) = \frac{1}{\pi} \frac{p_a}{p_a} \left(\frac{T^0}{T} \right)^{5/2} \sum_i \frac{\alpha_{L_i}}{(\nu - \nu_{oi})^2 + \alpha_{L_i}^2} \frac{1 - e^{-hc \nu_{oi}/kT}}{1 - e^{-hc \nu/kT}} e^{-\frac{E_{\ell_i}}{K} \left(\frac{1}{T} - \frac{1}{T^0} \right)} S_i^0 \quad (33)$$

Equation (33) will be used in the analysis of the pressure broadened water vapor absorption data with α_L given by Equation (16). A similar expression for $k(\nu)$ can be used for the pure water vapor studies, except that the Lorentz line shape must be replaced with the Voigt line profile which appears in Equation (22).

There are two cases of special interest in our analysis of Equation (32)

1. near line center absorption
- and 2. far wing absorption.

These conditions are specified by a comparison of the ratio $(\nu - \nu_0)^2 / \alpha_L^2$ with unity, i.e.,

$$\left(\frac{\nu - \nu_0}{\alpha_L} \right)^2 \begin{cases} < 1 \text{ near line center} \\ > 1 \text{ far wings.} \end{cases} \quad (34)$$

Examination of the Lorentz line shape shows that when $[(\nu - \nu_0) / \alpha_L]^2 < 1$

$$g_L^{NL,C}(\nu - \nu_{oi}) \simeq \frac{1}{\pi \alpha_L} \left[1 - \left(\frac{\nu - \nu_{oi}}{\alpha_L} \right)^2 \right] \quad (35)$$

and for the other extreme, $[(\nu - \nu_0) / \alpha_L]^2 > 1$

$$g_L^{FW}(\nu - \nu_{oi}) \simeq \frac{\alpha_L}{\pi(\nu - \nu_{oi})^2} \left[1 - \left(\frac{\alpha_L}{\nu - \nu_{oi}} \right)^2 \right] \quad (36)$$

1. Near line center behavior

The first case to be considered is a near line center contribution to $k(\nu)$. Substituting Equation (35) into Equation (33) we obtain

$$k^{NL,C}(\nu) = \frac{1}{\pi \alpha_L} \frac{p_a}{p_a} \left(\frac{T^0}{T} \right)^{5/2} \left[1 - \left(\frac{\nu - \nu_0}{\alpha_L} \right)^2 \right] \frac{1 - e^{-hc \nu_0/kT}}{1 - e^{-hc \nu/kT}} e^{-\frac{E_{\ell}}{K} \left(\frac{1}{T} - \frac{1}{T^0} \right)} S^0 \quad (37)$$

It is possible to simplify this equation by making several good approximations which apply to a water vapor absorption line in the 10 μm region that permit Equation (37) to be rewritten

$$k^{LC} \approx \frac{S^0}{\pi \alpha_L^0} \frac{P_e^0}{P_e} \frac{p_a}{p_a^0} \left(\frac{T^0}{T} \right)^2 e^{\frac{E_\ell}{kT^0} \left(1 - \frac{T^0}{T} \right)} \quad (38)$$

where P_e^0 is a reference effective pressure defined by Equation (17)
 T^0 is the reference temperature
 p_a^0 is the reference absorber partial pressure
 α_L^0 is the reference Lorentz half width under the conditions that
 $P_e = P_e^0$ and $T = T^0$.

It has also been assumed that $\left(\frac{\nu - \nu_0}{\alpha_L} \right)^2 = 0$. The temperature dependence of k^{LC} as given by Equation (38) is shown in Figure (2) where k^{LC}/k^0 is plotted vs. temperature and k^0 is defined as $\frac{S^0}{\pi \alpha_L^0}$. This plot shows that k^{LC} has a positive temperature coefficient, i.e., the absorption increases with increasing temperature. The curve shown in Figure 2 is based on a typical value of E_ℓ ($\sim 2000 \text{ cm}^{-1}$) for a water vapor line in the $10 \mu\text{m}$ region.

The dependence of k^{LC} on the absorber partial pressure can be displayed by substituting for P_e , as given by Equation (17), into Equation (38), with the result that

$$k^{LC} \approx \frac{S^0}{\pi \alpha_L^0} \left(\frac{T^0}{T} \right)^2 e^{\frac{E_\ell}{kT^0} \left(1 - \frac{T^0}{T} \right)} \frac{[(B-1)p_a^0 + 760]}{p_a^0 760} \left[p_a - \frac{(B-1)}{760} p_a^2 \right] \quad (39)$$

where only nitrogen is being considered as a broadening gas. This equation shows that for near line center absorption K will have both a linear and a quadratic pressure dependence.

2. Far wing behavior

For most CO_2 laser lines the contributions from the far wings of water vapor lines to the absorption coefficient will be significant. A notable exception is the R(20) line at 975.9 cm^{-1} which is nearly coincident with a rotational water line. The contributions to $k(\nu)$ from far wing absorption can be examined by using the line shape of Equation (36) in Equation (33) with the result that

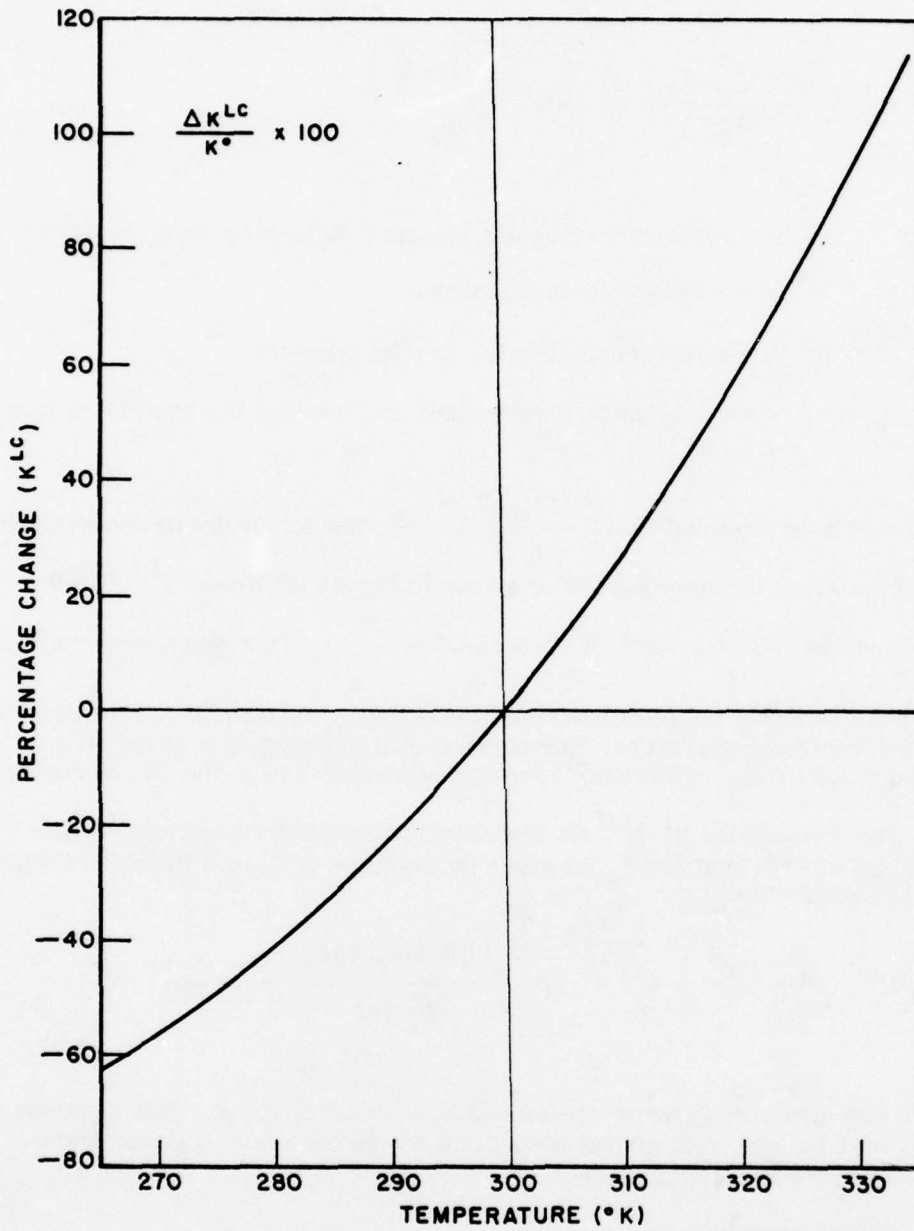


Figure 2. Percentage change in k^{LC} with temperature, relative to the absorption coefficient at 300°K . Curve is based on the line center model given by Equation (38).

$$k^{FW}(\nu) = \frac{1}{\pi} \frac{p_a}{p_a^0} \left(\frac{T^0}{T} \right)^{5/2} \sum_i \frac{\alpha_{L_i}}{(\nu - \nu_{oi})^2} \left[1 - \left(\frac{\alpha_{L_i}}{\nu - \nu_{oi}} \right)^2 \right] \times \frac{1 - e^{-hc \nu_{oi}/kT}}{1 - e^{-hc \nu_{oi}/kT^0}} e^{\frac{E_{\ell_i}}{kT^0} - \frac{T - T^0}{T}} S_i^0 \quad (40)$$

Again it is possible to simplify this expression by making some reasonable approximations which will allow the pressure and temperature dependence to be explicitly displayed, i.e.

$$k^{FW} \sim \frac{p_a}{p_a^0} \frac{p_e}{p_e^0} \left(\frac{T^0}{T} \right)^3 \sum_i \frac{S_i^0}{\pi \alpha_{L_i}^0} \left[\frac{\alpha_{L_i}^0}{(\nu - \nu_{oi})} \right]^2 e^{\frac{E_{\ell_i}}{kT^0} - \left(\frac{T - T^0}{T} \right)} \quad (41)$$

which gives the appropriate form of the absorption coefficient under the assumption that $[\alpha_{L_i}/(\nu - \nu_{oi})]^2 \ll 1$.

The temperature dependence can be most easily considered by rewriting (41) as

$$k^{FW} \sim \sum_i \left(\frac{\alpha_{L_i}^0}{\nu - \nu_{oi}} \right)^2 \left(\frac{T^0}{T} \right)^3 e^{\frac{E_{\ell_i}}{kT^0} - \frac{T - T^0}{T}} \frac{S_i^0}{\pi \alpha_{L_i}^0} \quad (42)$$

which shows that k^{FW} can have either a positive or negative temperature coefficient depending on the value of E_{ℓ_i} , i.e., as T increases the term

$$\left(\frac{T^0}{T} \right)^3$$

will cause k^{FW} to decrease while

$$\frac{E_{\ell_i}}{kT^0} - \frac{T - T^0}{T}$$

will cause k^{FW} to increase. These two expressions appear as a product in Equation (42) so that the actual temperature dependence will be determined by which term dominates. Figure 3 shows a plot of

$$\left(\frac{T^0}{T} \right)^3 e^{\frac{E_{\ell_i}}{kT^0} - \frac{T - T^0}{T}}$$

as a function of T for $T^0 = 300^{\circ}\text{K}$ with E_{ℓ_i} as a parameter.

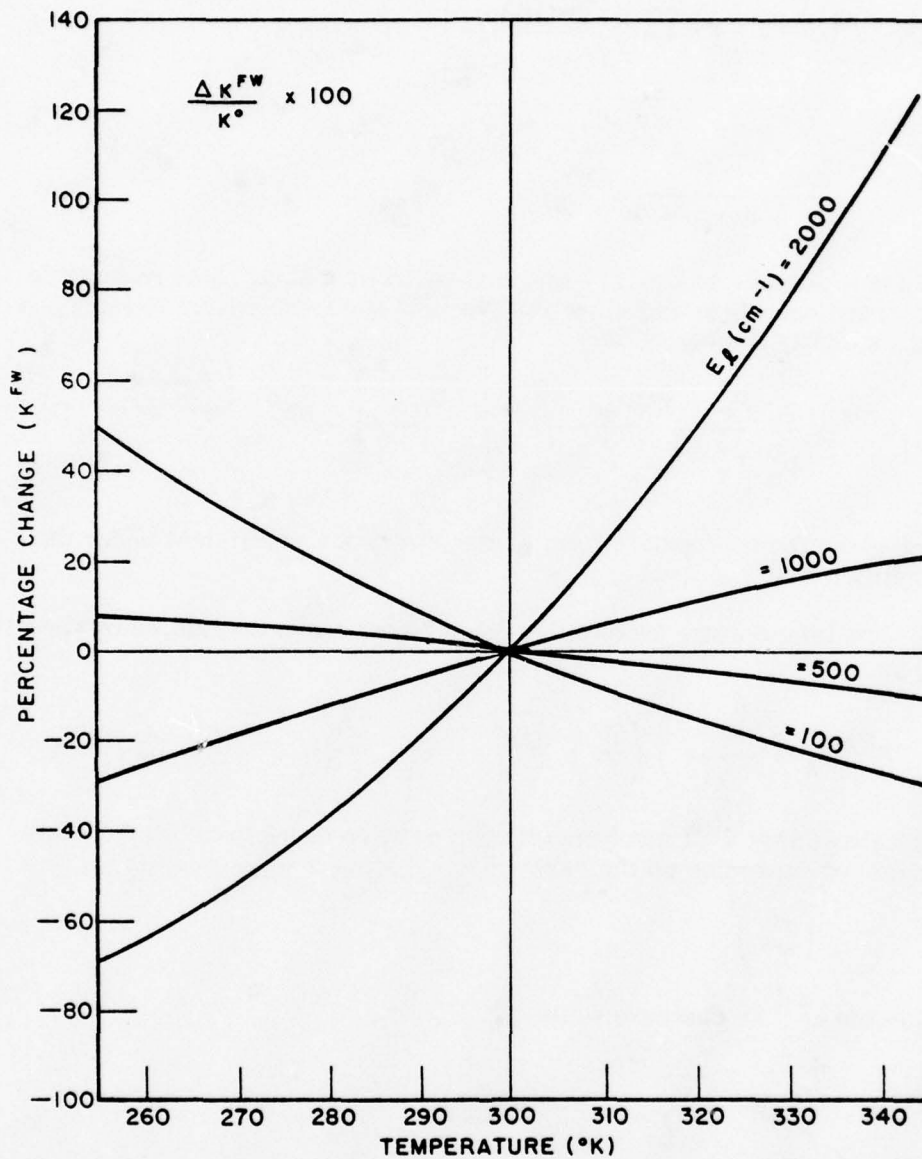


Figure 3. Percentage change in k^{FW} with temperature relative to the absorption coefficient at 300°K . Curves are based on the far wing model given by Equation (42) with E_0 in cm^{-1} as a parameter.

The pressure dependence can also be easily examined provided the expression for α_T given in Equation (16) is used together with Equation (17), which defines the effective pressure, P_e . Substituting into Equation (41) we have

$$k^{FW}(\nu) \sim \frac{(B-1)p_a^2 + 760 p_a}{(B-1)p_a^{02} + 760 p_a^0} \sum_i \left(\frac{\alpha_i^0 L_i}{\nu - \nu_{oi}} \right)^2 \left(\frac{T^0}{T} \right)^3 \times \frac{E_{\lambda i}}{e^{kT^0}} \frac{T - T^0}{T} \frac{S_i^0}{\pi \alpha_i^0 L_i} \quad (43)$$

where we have assumed that only nitrogen is being used as a buffer gas. This equation shows that the far wing contributions to k will also have a linear and quadratic pressure dependence.

D. Water Vapor Dimers

The measured values of absorption for the water vapor continuum in the 9 and 10 μm region are significantly greater than those predicted by calculations which use the Lorentz line shape to model the far wings. It should be appreciated that this is exactly the region where the Lorentz line is expected to be least accurate in modeling the true line profile²⁶. As a result of this failure to predict H_2O absorption it has been proposed that an alternative mechanism is responsible for the experimentally observed results. This theory suggests that water vapor dimer (H_2O)₂ formations are the source of the continuum absorption²⁷. The basic arguments for this mechanism follow from the temperature and pressure dependence of dimer absorption which also agrees with that observed for the continuum²⁸. At this time no experimental evidence is available to conclusively substantiate or exclude either the far wing or dimer formation models.

CHAPTER III
 PRINCIPLES AND PROBLEMS OF SPECTROPHONE
 AND WHITE CELL ABSORPTION MEASUREMENTS

The theoretical bases for both optoacoustic and White cell absorption measurements are extremely simple and fundamental in that both techniques measure the amount of energy which is lost (absorbed) in passing electromagnetic radiation through a gas sample. However, these techniques employ quite different methods. In studies which utilize the spectrophone, the sample gas is enclosed in a small rigid container with windows at each end that permit incident radiation to enter and exit the chamber. When an absorbing sample is enclosed a fraction of this incident radiation will be lost to the gas and converted into kinetic energy of the molecules. This produces an increase in both the temperature and pressure which is directly proportional to the energy absorbed by the gas. The absorption coefficient for a sample gas is obtained by measuring this pressure rise and then using a suitable calibration. The White cell technique consists of an insertion loss measurement that determines a transmittance from which the absorption coefficient is calculated. This chapter contains theoretical descriptions of these two methods and discussions on the fundamental problems which can inhibit accurate measurements.

A. Transmittance Measurements

The starting point for this discussion is Lambert's Law

$$I_{\text{out}} = I_{\text{in}} e^{-k(\nu) \ell} \quad (44)$$

where I_{in} and I_{out} are the radiation power levels incident on and exiting the White cell; ℓ is the path length in cm and $k(\nu)$ is the absorption coefficient at the frequency ν with units of cm^{-1} . The transmittance through the cell is given by the equation

$$T = \frac{I_{\text{out}}}{I_{\text{in}}} = e^{-k(\nu) \ell} \quad (45)$$

When a nonabsorbing (at the frequency ν) sample gas is present in the cell Equation (45) is rewritten

$$T^0 = \frac{I_{\text{out}}^0}{I_{\text{in}}^0} e^{-k^0(\nu) \ell} \quad (46)$$

where the superscript (0) indicates that the background transmittance of the cell is being considered. To determine the transmittance of a sample gas it is necessary to divide Equation (45) by (46), so that

$$T = \frac{T'}{T^0} = \frac{(I'_{\text{out}}/I'_{\text{in}})}{(I^0_{\text{out}}/I^0_{\text{in}})} = e^{-[k'(\nu) - k^0(\nu)]\ell} = e^{-k(\nu)\ell} \quad (47)$$

from which the absorption coefficient $k(\nu)$ of the gas can be calculated. Taking the natural logarithm of both sides we obtain

$$k(\nu) = -\frac{1}{\ell} \ln T = -\frac{1}{\ell} \ln \frac{T'}{T^0}, \quad (48)$$

which enables $k(\nu)$ to be evaluated directly from a measurement of the transmittance at the path length ℓ .

From Equation (47) it is observed that

$$k'(\nu) = k(\nu) + k^0(\nu), \quad (49)$$

but this is really a fundamental assumption for it implies that the residual background losses of the multi-traversal cell experiment remain constant. That is, to be able to calculate the absorption coefficient from Equation (48), it is necessary to assume that the difference between $k'(\nu)$ and $k^0(\nu)$ is a result of the sample gas and not a change in mirror alignment and/or reflectivity which occurred between the measurement of T' and T^0 . Otherwise we must write Equation (49) as

$$k(\nu) = k'(\nu) - k^0(\nu) \pm \delta \quad (50)$$

where δ would represent a small change in the background attenuation of the laser radiation. For this situation, it is necessary that Equation (48) be rewritten as

$$k(\nu) \mp \delta = -\frac{1}{\ell} \ln \frac{T'}{T^0} \quad (51)$$

which indicates an error in the measurement for the absorption coefficient of order $|\delta|$.

Both Equations (48) and (51) have serious implications which by themselves serve to delimit the accuracy which one can expect to realize with White cell measurements. In the next section, Equation (50) will be used to predict the relative uncertainty in the absorption coefficient as a function of error in the transmittance measurement. Section 2 deals with similar implications that are contained in Equation (51). Finally, these results are combined to predict an optimum path length as a function of $k(\nu)$.

1. Calculation of absorption coefficient

a. error sensitivity

After the transmittance has been recorded it is a simple matter to calculate the absorption coefficient using Equation (48). However, it is instructive to examine the influence which a small uncertainty in the transmittance measurement has on the calculated value of $k(\nu)$. This can be done by looking at the differential of $k(\nu)$,

$$dk(\nu) = -\frac{1}{\ell} \ln \left(1 + \frac{dT}{T} \right) \quad (52)$$

or expanding the natural logarithm we have

$$dk(\nu) = -\frac{1}{\ell} \left[\frac{dT}{T} - \frac{1}{2} \left(\frac{dT}{T} \right)^2 + \dots \right]. \quad (53)$$

If only terms of order dT are retained the result

$$\frac{dk(\nu)}{k(\nu)} = (\ln T)^{-1} \frac{dT}{T} + o(dT^2) \quad (54)$$

is obtained. This expression gives the relative change in the absorption coefficient for a small change in the transmittance, i.e., it predicts the error which can be expected when the uncertainty in the value of T is known. Figure 4 shows a plot of the percentage change in $k(\nu)$ versus the percentage change in T with $T \times 100$ as a parameter. From these results it is clear that reasonable accuracy in the absorption coefficient (1%) can only be achieved if there is substantial absorption.

b. optimum path length

Inspection of Equation (54) shows that the relative uncertainty in $k(\nu)$ can be made negligible by decreasing the value of T , i.e.,

$$\frac{dk/k}{dT/T} \sim (\ln T)^{-1} \rightarrow 0 \text{ as } T \rightarrow 0. \quad (55)$$

When sample gases with a relatively small value of $k(\nu)$ ($< 0.1 \text{ km}^{-1}$) are studied this criteria requires that large path lengths be utilized. For example, if $k(\nu) = 0.1 \text{ km}^{-1}$, a path length of 23 km is required to reduce the transmittance below 10%. Such a path length is not easily achieved so that a more realistic criterion needs to be considered. A reasonable objective would be to require that the uncertainty in absorption coefficient equal the uncertainty in the transmittance measurement; looking at Equation (54) this implies that $\ln T = -1$ or $T = 0.368$. This simply says that the optimum path length (by the above definition) should be chosen such that

$$k(\nu) \cdot \ell = 1. \quad (56)$$

In this study the maximum path length available was approximately 1.5 km so that the condition given by Equation (56) was not achieved.

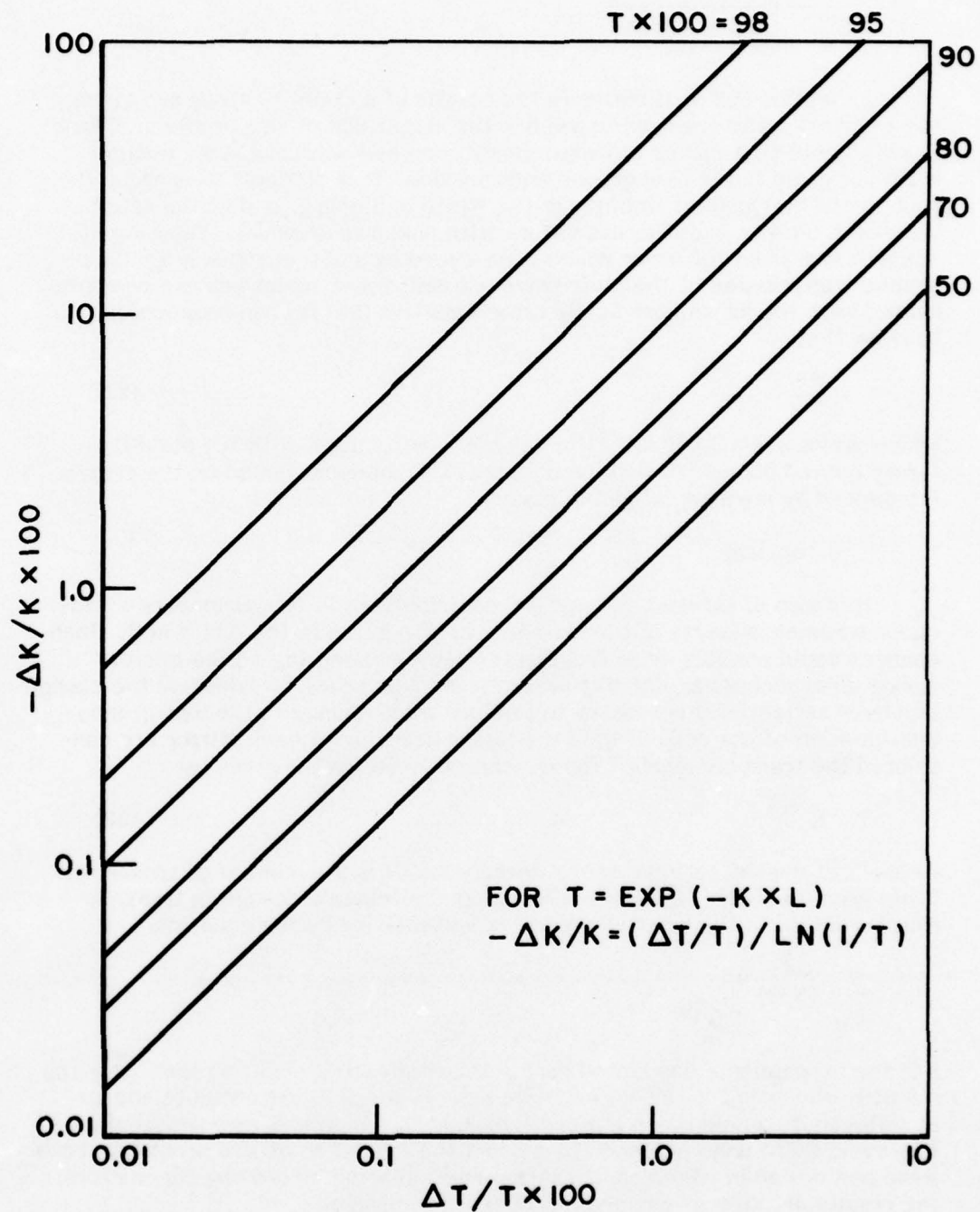


Figure 4. Percentage error in absorption coefficient plotted versus percentage error in transmittances. After Trusty.

2. Background stability

a. mechanical

In Section B.3 of Chapter IV the results of a stability study are given, see Figure 32, and are used to predict the magnitude of this problem. These data indicate that during any experiment, one can conservatively assume a 1% variation in the background transmission. It is difficult to analyze the problem of mechanical stability in the White cell optics in that the effects were of a random and discrete nature with unknown origin(s). Their significance arises from the error which is produced by small changes in the background transmission of the multitraversal cell; these variations can be represented with the parameter δ . By using Equation (51) it is an easy matter to show that

$$\delta \approx \frac{dT/T}{l} , \quad (57)$$

which yields a $\delta = 0.007 \text{ km}^{-1}$ for a 1.5 km path length with the stability figure quoted above. This value of δ provides an upper bound on the error introduced by mechanical instability.

b. optical

It is also of interest to consider contributions to the parameter δ produced by small changes in the reflectivity of mirrors in the White cell. Such changes could possibly arise from water vapor condensing on the mirrors during an experiment. For this reason it is instructive to calculate the change in mirror reflectivity necessary to produce a 1% change in the background transmission of the cell. If only the losses occurring at each mirror are considered the transmittance of the evacuated White cell is given by

$$T = R^{N-2} \quad (58)$$

where R is the reflectivity of the mirrors and N is the number of traversals. From Equation (58) it is easy to show that the relative change in transmission is related to the relative change in reflectivity by the equation

$$\frac{dT}{T} = (N-2) \frac{dR}{R} . \quad (59)$$

For the experiments conducted during this study $(N-2) \sim 10^2$ so that $\frac{dR}{R} \times 100 = 0.01\%$ when $dT/T \times 100 = 1\%$. If we assume $R = .99$, the absolute change in reflectivity would be on the order of 0.0001, which is a very small change. However, there is no evidence to support the existence of this problem. Tests were performed in which condensation was inhibited by heating the mirrors; the results of those experiments proved inconclusive.

By combining the results of these two sections it is observed that an optimum situation will exist when $K(\nu) \cdot \ell$ is large and N is small. In the case of a highly transmitting sample gas these criteria can only be satisfied in an experiment employing a cell with an extremely long base path length. Since this is not always possible, an alternate technique, the spectrophone has developed as a promising research tool which is capable of performing accurate measurements when the absorption is quite small. The next section treats the basic theory of this instrument and its unique set of problems.

B. Optoacoustic Measurements

The optoacoustic effect was discovered in 1880 by Alexander Graham Bell²⁹. It received relatively little attention until intense coherent sources of radiation became available; the first attempts at employing this effect to measure absorption in gas samples were limited by the intensity of thermal radiation sources and the sensitivity of acoustic transducers. Viengerov³⁰ made the first such measurements in 1938 using a resonant cavity. However, it was the advent of the laser which allowed Kerr and Atwood³¹ to demonstrate the potential of the spectrophone as a sensitive instrument capable of measuring extremely small levels of absorption. In 1967 they performed water vapor and CO_2 absorption measurements with a nonresonant instrument using both pulsed and cw laser sources. With their spectrophone and a capacitive manometer pressure transducer they achieved a sensitivity of 10^{-7} cm^{-1} that was limited by a false pressure signal associated with the end windows. Three years later Kreuzer³² used a nonresonant cell with a specially designed pressure sensing microphone to further study the ultimate sensitivity of the optoacoustic instrument. In that work he discussed the theoretical implications of noise in the pressure transducer electronics and Brownian motion of the microphone diaphragm. Experimentally Kreuzer observed that contaminants restricted an accurate determination of absorber concentration.

In an attempt to improve the optoacoustic technique, Dewey and co-workers³³ modulated the excitation beam at a frequency corresponding to a natural (Helmholtz) frequency of the sample cell thus producing a resonant spectrophone signal. This work demonstrated an enhancement of the pressure signal at or near the resonant frequencies of the instrument. When compared to a nonresonant spectrophone their device has a relatively large volume-to-surface area ratio which should serve to reduce the problems of contamination. However, this method requires very high acoustic "Q" values which make it extremely sensitive to variations in either the modulation frequency or speed of sound in different gas samples.

Deaton, et al.³⁴ improved the sensitivity of the basic spectrophone by designing a nonresonant differential instrument consisting of two isolated chambers connected by a single IR window. This instrument achieved a substantial reduction in the false pressure signal produced at the end windows

by a technique which will be thoroughly discussed later in this chapter when the OSU differential spectrophone is considered. Recently the optoacoustic technique has come into widespread usage in the study of common atmospheric gases and pollutants³⁵⁻³⁸. Schnell and Fischer have used a nonresonant Pyrex spectrophone to investigate the toxic gas phosgene and the isotopes of NO and water vapor at CO and CO₂ laser frequencies³⁹. Menzies and Shumate have also studied water vapor absorption at CO₂⁴⁰ and CO₂⁴¹ laser lines. The technique has been used with a tunable HeNe laser source by Zuev et al.⁴² to measure halfwidth, line strength and line center frequency of methane and its isotope ¹³CH₄. At this laboratory, we have used the spectrophone for several years in the study of molecular absorption at DF⁴³ and CO₂¹² laser frequencies. In this section the two basic theories used in formulating an analytic description of the nonresonant spectrophone will be given and the essential results discussed. (Most recently Farrow and Richton⁴⁴ have performed a numerical analysis which combines the heat flow solution of Kerr and Atwood³¹ and the rate equation approximation of Kreuzer³² and Rosengren⁴⁶.) By using those results, an analysis of the fundamental limitations on sensitivity will be given. This discussion will conclude with a derivation of the technique used in obtaining low pressure measurements in this study.

1. Basic theory

a. introduction

The situation to be analyzed is pictured schematically in Figure 5 which illustrates a laser beam that passes through a closed chamber containing the sample gas. In these initial arguments, it will be assumed that the windows are nonabsorbing and all the incident radiation except that absorbed by the gas is transmitted through the cell. We will also assume the chamber is vacuum tight and that there is no dead space, i.e., regions not illuminated by the laser beam. These assumptions are necessary to make the analytic solution tractable. However, in practical devices they are seldom true so that a realistic and complete analysis requires that they be dealt with separately, see section e.

b. rate equation description

Kruezer's³² analysis of this problem was formulated in terms of a rate equation that describes the number density n_1 of molecules which have been raised from the lower energy state E_0 to an excited state E_1 . An energy level diagram for this situation is pictured in Figure 6. In this development we consider the case in which there is only one absorption line with strength S and width $\Delta\nu$ active in removing energy from the incident laser beam. Since the excited rotational energy states relax to translational energies in just a few collisions⁴⁵ as opposed to many collisions for the excited vibrational energy states⁴⁵, it is assumed that the rotational temperature remains equal to the translation temperature of the sample gas molecules. With these restrictions the time rate of change in number density of molecules in the higher vibrational state ν' is given by the differential equation³²

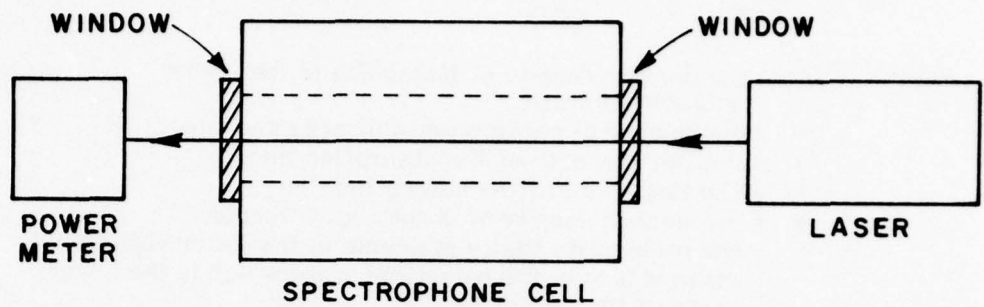


Figure 5. Schematic diagram of the physical situation which will be described using the rate equation approximation of Kreuzer and the heat flow solutions of Kerr and Atwood.

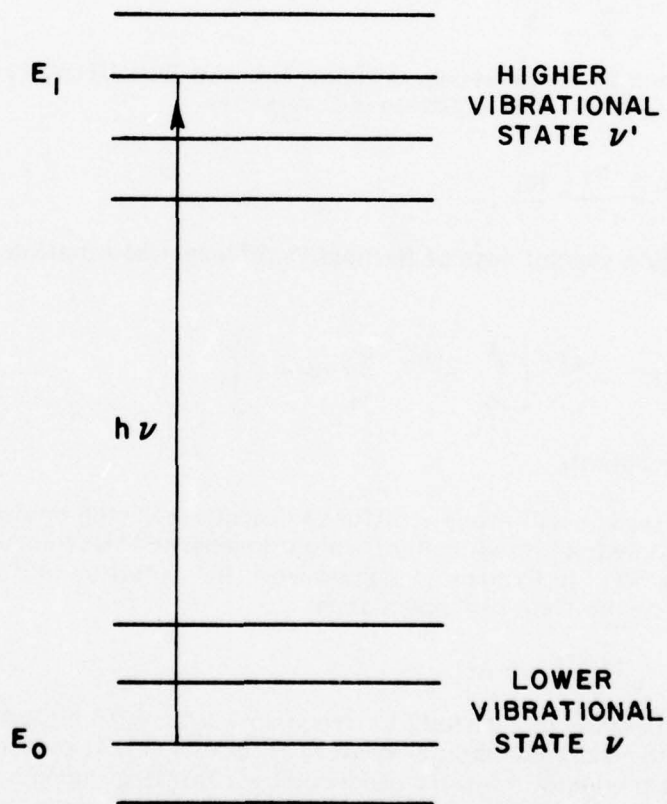


Figure 6. Energy level diagram for the rate equation description given by Kreuzer.

$$\frac{dn_1}{dt} = -n_1 \frac{IS\beta}{\pi\Delta\nu} - \frac{n_1}{\tau} + N \frac{IS\alpha}{\pi\Delta\nu} \quad (60)$$

where n_1 = the number density of molecules in the higher vibrational state,
 I = the number of photons per unit area and time,
 S = the line strength of the absorption line,
 $\Delta\nu$ = the line width of the absorption line,
 N = the number density of absorbing molecules,
 α = the probability that a molecule in the lower vibrational state is also in the rotational state which is the lower state of the transition,
 γ = the probability that a molecule in the upper vibrational state is also in the rotational state which is the upper state of the transition,
 τ_C = the collisional lifetime in the upper vibrational state,
 τ_R = the radiation lifetime in the upper vibrational state,
 $\tau' = (\tau_C^{-1} + \tau_R^{-1})^{-1}$,
 and $\beta = \alpha \mp \gamma$.

This equation can be simplified by defining two new quantities, $\tau_I = (\pi\Delta\nu)/(I_0 S)$ and $\tau = (\beta/\tau_I + 1/\tau')$ so that Equation (60) becomes

$$\frac{dn_1}{dt} = -\frac{n_1}{\tau} + \frac{N\alpha}{\tau_I} \quad (61)$$

which is merely a special case of Bernoulli's differential equation. The solution is

$$n_1(t) = e^{-t/\tau} \left[\int_0^t e^{t'/\tau} \frac{N\alpha}{\tau_I} dt' + C \right], \quad (62)$$

where C is a constant.

At this stage it will prove fruitful to deviate from the analysis proposed by Kreuzer and instead consider that which Rosengren⁴⁶ developed by also using Equation (61). In Kreuzer's original work the radiation intensity was assumed to have the time dependent form

$$I = I_0 (1 + \delta \sin \omega t), \quad (63)$$

i.e., the laser beam is modulated at a frequency $\omega/2\pi$ with a modulation depth δ . However, the most common laboratory form of I is that pictured in Figure 7, which gives the beam intensity produced by a rotating chopper wheel such as that used in the experiments performed in this study. It is assumed in this figure that the velocity of the wheel is such that the beam is switched

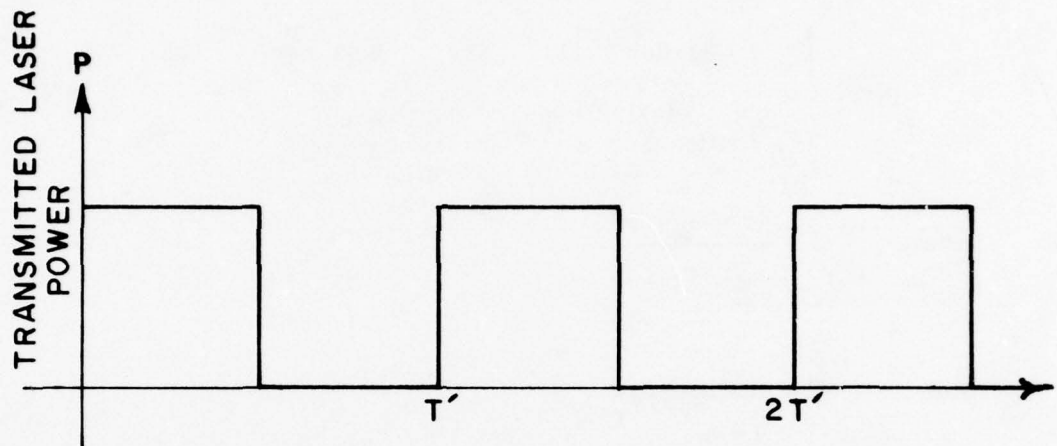


Figure 7. Schematic plot of laser power vs time when chopped by a rotating mechanical blade.

on and off in a time t_s that is much smaller than the period T' , i.e., $t_s \ll T'$. Substituting the intensity wave form shown in Figure 7 and applying the appropriate conditions at the end points yields the following solution for $n_1(t)$ in the interval $0 < t < T'$ ⁴⁶

$$n_1(t) = \begin{cases} N\alpha \frac{\tau}{\tau_T} \left[1 - e^{-t/\tau} \frac{1 - e^{-T'/2\tau}}{-\beta T'/2\tau_T - T'/\tau} \right] & 0 < t < \frac{T'}{2} \\ N\alpha \frac{\tau}{\tau_T} e^{-(t - \frac{T'}{2})/\tau} \frac{1 - e^{-T'/2\tau}}{1 - e^{-\beta T'/2\tau_T - T'/\tau}} & \frac{T'}{2} < t < T' \end{cases} \quad (64)$$

The pressure variations in the sample gas are found by using the differential equation³²

$$\frac{dP}{dt} = \frac{2}{3} E \frac{n_1(t)}{\tau_T} - \frac{(P - P_0)}{\tau_T} \quad (65)$$

together with the results given by Equation (64), where

- $P(t)$ = the time dependent pressure,
- P_0 = the equilibrium pressure,
- E^0 = the energy difference between the levels of the transition,
- τ_T = the thermal relaxation time of the sample cell.

Making the reasonable assumptions that $\tau \ll \tau_T$ and T' the pressure variations in the interval $0 \leq t \leq T'$ are given by⁴⁶

$$P(t) = \begin{cases} P_0 + A (1 - Be^{-t/\tau_T}) & 0 \leq t \leq \frac{T'}{2} \\ P_0 + AB e^{-(t-T'/2)/\tau_T} & \frac{T'}{2} \leq t \leq T' \end{cases} \quad (66)$$

where $A = \frac{2EN\alpha\tau\tau_T}{3\tau_C\tau_I}$

and $B = \frac{1}{1 + e^{-T'/2\tau_T}}$

Equation (66) is the desired result, giving an analytical expression for the pressure signal, $P(t) - P_0$, in a sample cell of arbitrary geometry when illuminated by a uniform laser beam. A normalized plot of this function is given in Figure 8; the true amplitude of this signal is directly proportional to the

radiation energy absorbed by the gas, since $\frac{\alpha}{\tau_I}$ equals $\frac{I_0 S \alpha}{\pi \Delta v}$, as would be

expected. Interaction with the walls of the spectrophone are not included in Equation (66) except as they enter through the parameter τ_T , which is a function of the cell geometry. More will be said concerning this solution when it is compared to the results of the next section where a similar expression is developed for a cylindrical spectrophone in which the sample gas is illuminated by a nonuniform Gaussian beam.

c. heat flow description

Kerr and Atwood³¹ have treated the case of a long cylindrical cell irradiated by a laser beam having a "modified" Gaussian intensity. Here, the assumption is made that α , the gas absorptivity per unit length, is much less than one so that this problem can be reduced to finding a solution for the one dimensional heat flow equation

$$\frac{\partial^2 \theta}{\partial r^2} + r^{-1} \frac{\partial \theta}{\partial r} = a^2 k^{-1} \frac{\partial \theta}{\partial t} - \frac{A(r)}{K} \quad (67)$$

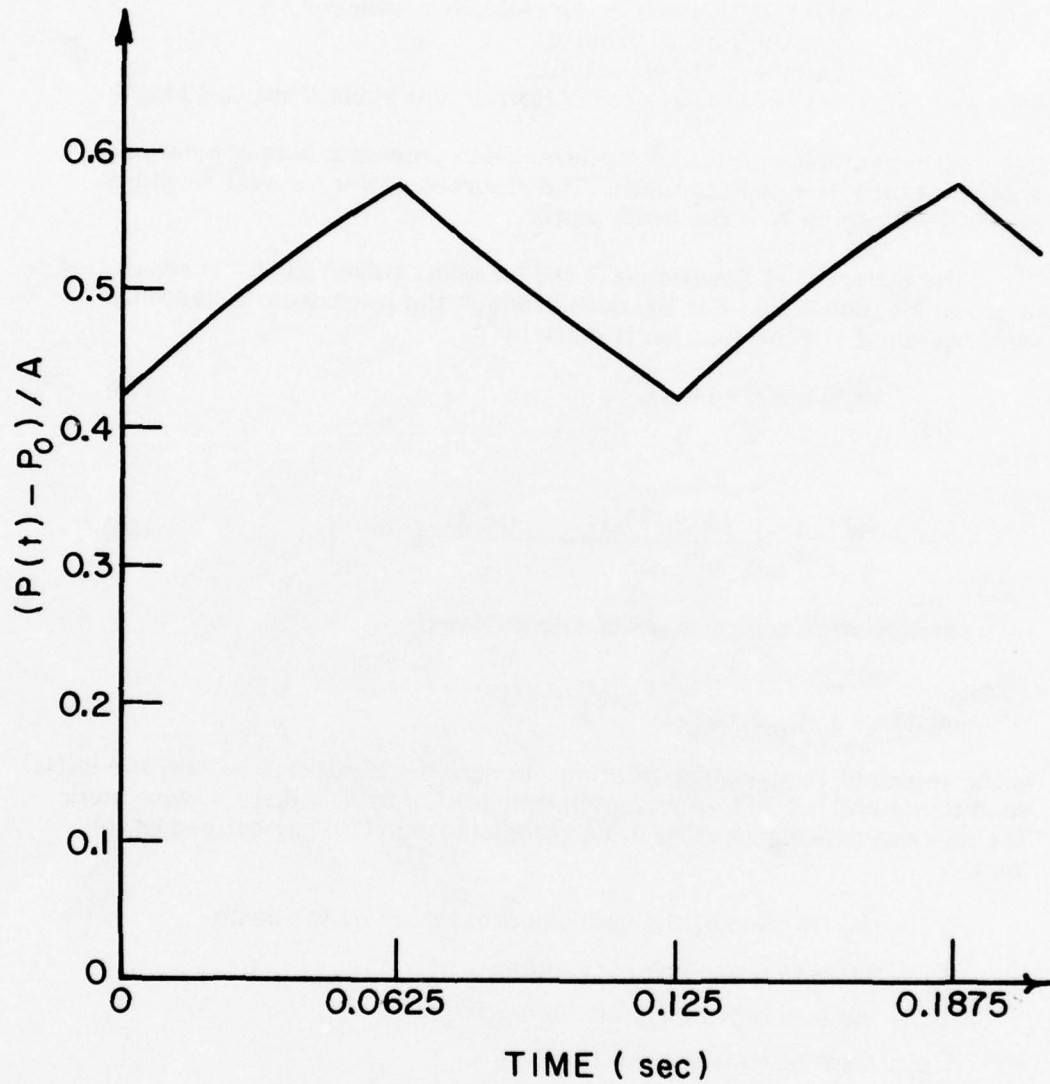


Figure 8. Plot of the theoretical pressure signal given by the rate equation approximation of Equation (66), with $\tau_T=0.2$ sec and $T=0.125$ sec.

r = a dimensionless radial coordinate,
 a = the cell radius,
 $\rho = ra$
 $\theta(r,t)$ = temperature in the cell above ambient,
 k = gas thermal diffusivity,
 K = gas thermal conductivity,
 and $A(r)$ = rate of heat generation per unit volume per unit length.

In this treatment the nature of the absorption process is simply ignored and a gas absorptivity α is introduced. The absorbed power per unit length is given by αW where W is the beam power.

The differential Equation (67) can be easily solved using the separation of variables technique. For the case in which the laser beam is suddenly switched on at $t=0$ the solution is given by³¹

$$\theta(r,t) = v(r) + u(r,t), \quad (68)$$

where

$$v(r) = \frac{\alpha W}{4\pi K} \left[\sum_{n=1}^{\infty} \frac{(-1)^n (r^{2n-1})}{b^{2n} n!} + \frac{(r^2-1)}{b^2} e^{-1/b^2} \right] \quad (69)$$

is the steady state temperature distribution and

$$u(r,t) = \sum_{m=1}^{\infty} C_m J_0(\xi_m r) e^{-(k \xi_m^2 t/a^2)} \quad (70)$$

is the transient temperature solution. In deriving these expressions, the initial condition $\theta(r,0) = 0$ and boundary conditions $\theta(1,t) = 0$, $\theta(0,t) \neq \infty$ were used. The new quantities appearing in Equations (69) and (70) are defined as follows

b = the fraction of the cell radius occupied by the beam,
 J_0 = the zero order Bessel function,
 ξ_m = the m th root of J_0 , i.e., $J_0(\xi_m) = 0$,
 and C_m = a set of constant coefficients

The relationship between the pressure rise and the temperature rise is found by taking the differential of the ideal gas law

$$\frac{dP}{P} = \frac{dT}{T} \quad (71)$$

where P = nominal pressure,
 and T = absolute ambient temperature.

The total pressure rise, $P(t)$ is found by evaluating the integral expression

$$P(t) = \frac{2P}{T} \int_0^1 \theta(r,t) dr. \quad (72)$$

The result is

$$P(t) = \frac{\alpha w P}{4\pi K T} \left[R(b) + \sum_{m=1}^{\infty} D_m e^{-k \xi_m^2 t / a^2} \right] \quad (73)$$

where $B = R(b) = \left[1 - b^2 + (b^2 - \frac{1}{2} b^{-2}) \exp(-1/b^2) \right]$
and $D_m =$ a set of constants

given by the expression

$$D_m = \frac{4}{\xi_m^2} \left\{ \frac{4e^{-1/b^2}}{b^2 \xi_m^2} + \sum_{n=1}^{\infty} \frac{(-1)^n}{n! n b^{2n}} \left[1 - (\xi_m / J_1(\xi_m)) \int_0^1 r^{2n+1} J_0(\xi_m r) dr \right] \right\} \quad (74)$$

where $J_1 =$ the first order Bessel function.

Equation (73) is more or less the desired result for it gives the pressure rise in a cylindrical spectrophone when it is suddenly illuminated by a laser beam with Gaussian intensity distribution. The cell and beam geometry enter into this solution through the dimensionless factor B , the time constant $\tau = a^2/k\xi_m^2$ and the evaluation of the constants D_m . A normalized plot of this solution with b as a parameter, is given in Figure 9. These curves indicate the effects of spot size on the magnitude and shape of the pressure signal. As with the previous analysis it is observed that the pressure rise is directly proportional to the energy, αw , absorbed by the gas. In the next section the results given by Equation (73) will be further amplified and compared with those predicted by the rate Equation analysis in Equation (66).

d. comparison of descriptions

In section b the rate equation approximation of Kreuzer³² was used to predict the pressure signal in an absorbing sample gas that is illuminated by a chopped source of radiation with uniform intensity. The result of that analysis, which is given by Equation (66), is repeated below to permit easy comparison with the expression derived by Kerr and Atwood³¹. Their solution gives an expression for the pressure rise in a cylindrical spectrophone under the assumption that a modified Gaussian beam is passing through a weak absorbing gas. That solution is also repeated below,

03/18/78 STEP RESPONSE

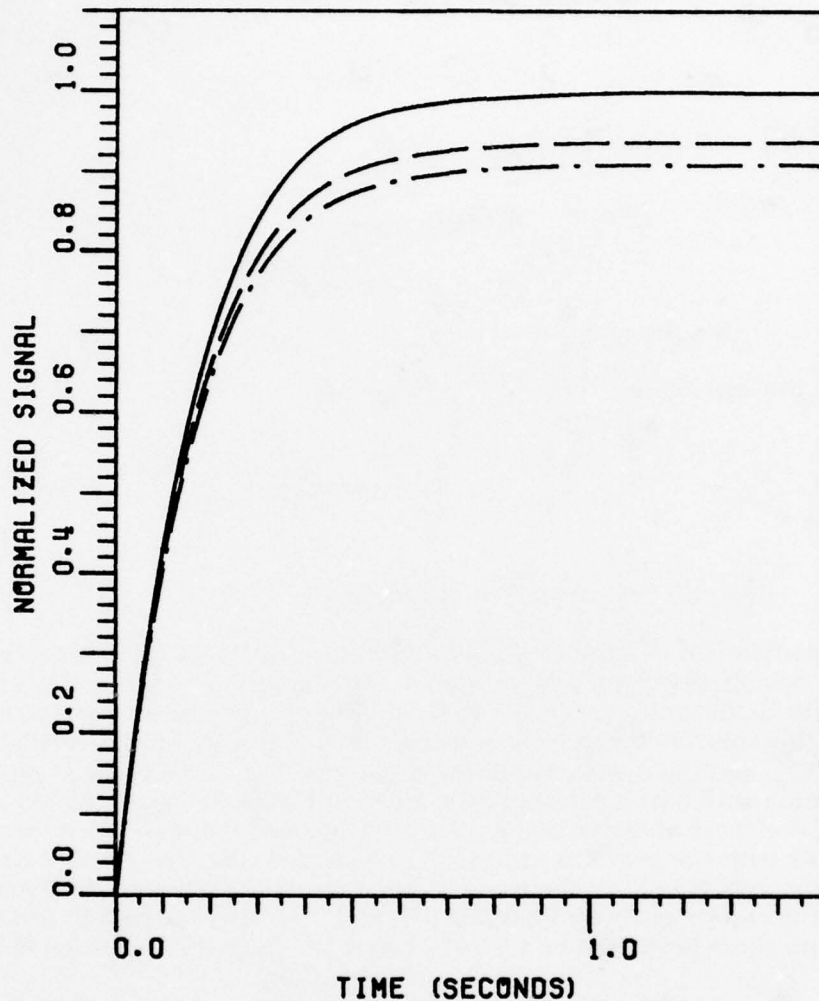


Figure 9. Normalized step response of a cylindrical spectrophone to a Gaussian beam as predicted by the heat flow analysis of Kerr and Atwood. In this figure b , the fractional illumination of the cell, serves as the parameter for these curves, i.e.,
— $b=0$, - - $b=0.25$, - · - $b=0.3$.

Rate Equation Solution:

$$P(t) = \begin{cases} P_0 + A(1 - B e^{-t/\tau_T}) & 0 \leq t \leq T/2 \\ P_0 + AB e^{-(t - T/2)/\tau_T} & T/2 \leq t \leq T \end{cases} \quad (75a)$$

(75b)

Heat Flow Solution:

$$P(t) = P_0 + \frac{\alpha WP}{4 \pi KT} \left[B(b) + \sum_{m=1}^{\infty} D_m e^{-k \xi_m^2 t/a^2} \right] \quad (76)$$

The equation (75a) corresponds to the forced response of the gas, as does Equation (76); thus, it is reasonable to compare the forms of these two equations. Before doing this it is necessary to consider the values which the various D_m assume. These values are a function of b , the fraction of the cell radius occupied by the beam, so it will also be necessary to choose b . A reasonable choice is $b=0.20$, in which case the D_m are as shown in Table 2. Equation 76 can then be rewritten

$$P(t) \sim P_0 + \frac{\alpha WP}{4 \pi KT} \left[0.96 - 1.01 e^{-t/(a^2/k\xi_1^2)} \right] \quad (77)$$

where the terms containing D_m , $m=2,3,4,\dots$ have been neglected because $D_1 \gg D_m$, $m=2,3,4,\dots$. A comparison of this expression with the corresponding one given by Equation (75a) shows they are indeed of the same form, allowing for the fact that the latter represents a part of the steady state solution for a periodic source. If the analysis of section b is repeated for a step input, the rate-equation method gives the solution

$$P(t) = P_0 + \frac{2}{3} E \alpha \frac{\tau \tau_T}{\tau_C \tau_I} (1 - e^{-t/\tau_T}), \quad (78)$$

which has exactly the same form as Equation (77). In the exact heat flow solution, see Equation (73), an infinite series of terms is required to model the response for a Gaussian beam. However, as the spot size becomes large, i.e., increasing b , the intensity becomes more uniform and fewer terms are required to describe the pressure rise, see Table 2. It is in this limit that we have made our comparison between the two approaches.

A direct analogy can be made between the equation describing the small pressure signal and those used to model the response of an RC network. Consider for example the circuit shown in Figure 10 where an RC network with a time constant $\tau = RC$ is driven by a square wave voltage input with amplitude V_0 . The output signal, V_c is given by the equation

Table 2
 Values of D_m in the heat flow solution. After Kerr and Atwood.

m	b=0.20	b=0.25	b=0.30
1	-1.0358	-1.0123	-0.9728
2	0.1045	0.08683	0.0704
3	-0.0211	-0.0141	-0.0084
4	0.0056	0.0024	0.0009
5	-0.0010	-0.0004	-0.0001
6	0.0004		

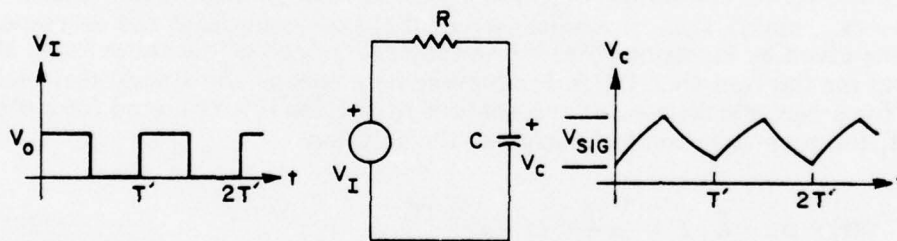


Figure 10. AnRC circuit analog to the spectrophone.

$$V_c = \begin{cases} A(1-B)e^{-t/\tau} & 0 \leq t \leq \frac{T'}{2} \\ AB e^{-(t - \frac{T'}{2})/\tau} & \frac{T'}{2} \leq t \leq T' \end{cases} \quad (79)$$

where $A = V_0$

$$\text{and } B = \frac{1 - e^{-T'/2\tau}}{1 - e^{-T'/\tau}} = \frac{1}{1 + e^{-T'/2\tau}}$$

which has exactly the same form as Equation (66).

It is interesting to explore this analogy to determine the effects which the time constant τ , period T' , and source amplitude, V_0 , have on the signal magnitude. In Figure 10 we define the signal magnitude to be the peak to peak voltage of V_c , i.e., the quantity V_{sig} . Analysis of Equation (79) shows that

$$V_{sig} = V_0 \tanh(T'/4\tau), \quad (80)$$

which simply says that it is desirable to have V_0 and $T'/4\tau$ as large as possible.

The rate at which the pressure rises to its steady state value (or decays to the equilibrium pressure) is determined by the time constant τ_T or $a^2/k\xi_1^2$, depending on which solution one applies. From Kreuzer's analysis³² $\tau_T \sim \frac{C_v(2a)^2}{10K}$, which gives a time constant of ~ 0.3 seconds for air at atmospheric pressure and room temperature in a 1 cm diameter cell. Evaluation of $a^2/k\xi_1^2$ under similar circumstances gives ~ 0.2 seconds. If we assume a value for τ of the same order as was just calculated and a chopping frequency, $f \sim 10$ Hz Equation (80) can be approximated by

$$V_{sig} \sim V_0 \frac{T'}{4\tau} \sim V_0 \frac{T'k\xi_1^2}{4a^2} \quad \forall T'/4\tau \ll 1, \quad (81)$$

which says that the signal amplitude is linear in the period T' , (this has also been observed experimentally), and falls off as the radius squared.

In the case of a cylindrical cell and a Gaussian laser beam the source amplitude, V_0 , corresponds to the coefficient $\frac{\alpha WP}{4\pi KT}$

\forall mathematical symbol "for all".

in Equation (77). The amplitude term is linear with respect to the energy absorbed, αW , and total pressure, P ; it is inversely proportional to equilibrium temperature T and the thermal conductivity, K of the gas. Combining all of these results, and noting that $k = K/\rho C_v$, Equation (81) can be written in more explicit form as

$$V_{\text{sig}} \approx \frac{\alpha W T \xi^2 R}{16\pi C_v a^2 m} \quad V \quad T/4\tau \ll 1. \quad (82)$$

where m = gram molecular weight,
 R = gas constant,
 C_v = specific heat at constant volume,
 T = the period = $1/f$,
 and f = the chopping frequency,

This equation says that the amplitude of the pressure signal is independent of temperature and pressure, i.e., it depends only upon:

1. the energy absorbed
2. the thermodynamic properties of the gas
3. the diameter of the cell
4. the chopping frequency

assuming that $T/4\tau \ll 1$ is valid.

e. limitations on sensitivity

The absorption levels measured in this study were all on the order of 0.01 km^{-1} or greater so that efforts to achieve the ultimate in sensitivity for a spectrophone were not warranted. However, the background noise attributable to window and wall effects was considered here. Window noise was reduced by the use of a Brewster angle differential spectrophone and the false signal produced by absorption at the walls was controlled by precise alignment of the laser beam through the cell. In applications where extremely low level gas concentrations are being detected both of these problems (false window and wall signals) plus noise in the pressure transducer and its associated electronics, become critical limitations on sensitivity.

1. window signal (noise)

Absorption by the end windows results in a temperature rise which heats the sample gas, producing a nearly inphase pressure signal. The optoacoustic technique has often been used to study solids; in fact A. G. Bell's original discovery²⁹ was made when he observed that modulated light incident upon a solid could produce an audible sound. In principle this window signal will remain constant in magnitude and phase, which allows it to be easily eliminated by either electronically or numerically subtracting it. However, when

the absorption signal and window noise are of the same order small variations in the background (which are experimentally observed) seriously reduce accuracy and sensitivity. Absorption by windows in an optoacoustic device has been studied by Parker⁴⁷ who concludes that the effect can be attributed to a surface layer on the window and is possibly related to surface conductivity. Parker has also shown that the magnitude of the window signal falls off with both pressure (it is linear w.r.t. P^2) and frequency.

Several approaches have been taken to reduce the window signal^{34,48,49} among which are:

1. The differential instrument, which will be described in section B.2. of this chapter.
2. The two-path detector, which attempts to produce a constant, i.e., 0 Hz, background window signal that synchronous detection would filter.
3. The baffle technique, which uses a set of obstructions (baffles) near each window to check the flow of gas and thus restrict propagation of the window signal. This is done to isolate the center section of the spectrophone where the pressure transducer is located.

2. wall signal (noise)

Heating at the cell walls can also be a very significant problem and is a second source of background noise. Relatively little work has been done to study this phenomenon but experimentally we have observed that a very large background signal results from permitting the laser beam to approach a cell wall. The magnitude of this signal is very sensitive to small changes in beam alignment so that this situation is strictly to be avoided. Two methods are available to deal with the problem. They consist of focusing the laser beam and/or increasing the diameter of the spectrophone. Equation (82) indicates that response of an instrument falls off as $1/a^2$, where a is the radius of the cell. In this work a beam-reducing telescope was used to achieve a minimum spot size inside the cell⁵⁰.

3. transducer noise

In his study on the ultimate sensitivity of spectrophones, Kreuzer³⁹ analyzed the noise produced by Brownian motion of the microphone diaphragm and Johnson noise in the amplifier electronics. He concluded that Brownian noise, which varies as A^{-2} , where A is the surface area of the microphone, may ultimately be the limiting noise source in extremely sensitive instruments. Experimentally, he observed that the microphone electronics were the most significant source of noise. Like Kreuzer, we have also found "electronic" noise to be a significant problem, however for a different reason than Johnson noise and Brownian motion.

Mechanical vibrations in the laboratory induced motion of the capacitance manometer diaphragm which produced low frequency noise in the output of the transducer electronics. We have also observed 120 Hz ripple in the dc amplifiers produced by inadequate filtering in the power supply. The vibration problem was controlled by removing all vacuum pumps from the spectrophone laboratory and mounting the limestone optical table on vibration isolators.

The last source of false background signal to be discussed is thermal instability of the spectrophone. From Charles' law we have that in a closed volume the change in pressure is proportional to the change in temperature, $\frac{\Delta P}{\Delta T} = \frac{N}{V} R$ which says that a ΔT of 4×10^{-6} °K will correspond to a $\Delta P = 10^{-5}$ Torr. This would represent a very undesirable situation since a ΔP of 10^{-5} Torr is easily on the order of signals which are measured in absorption studies.

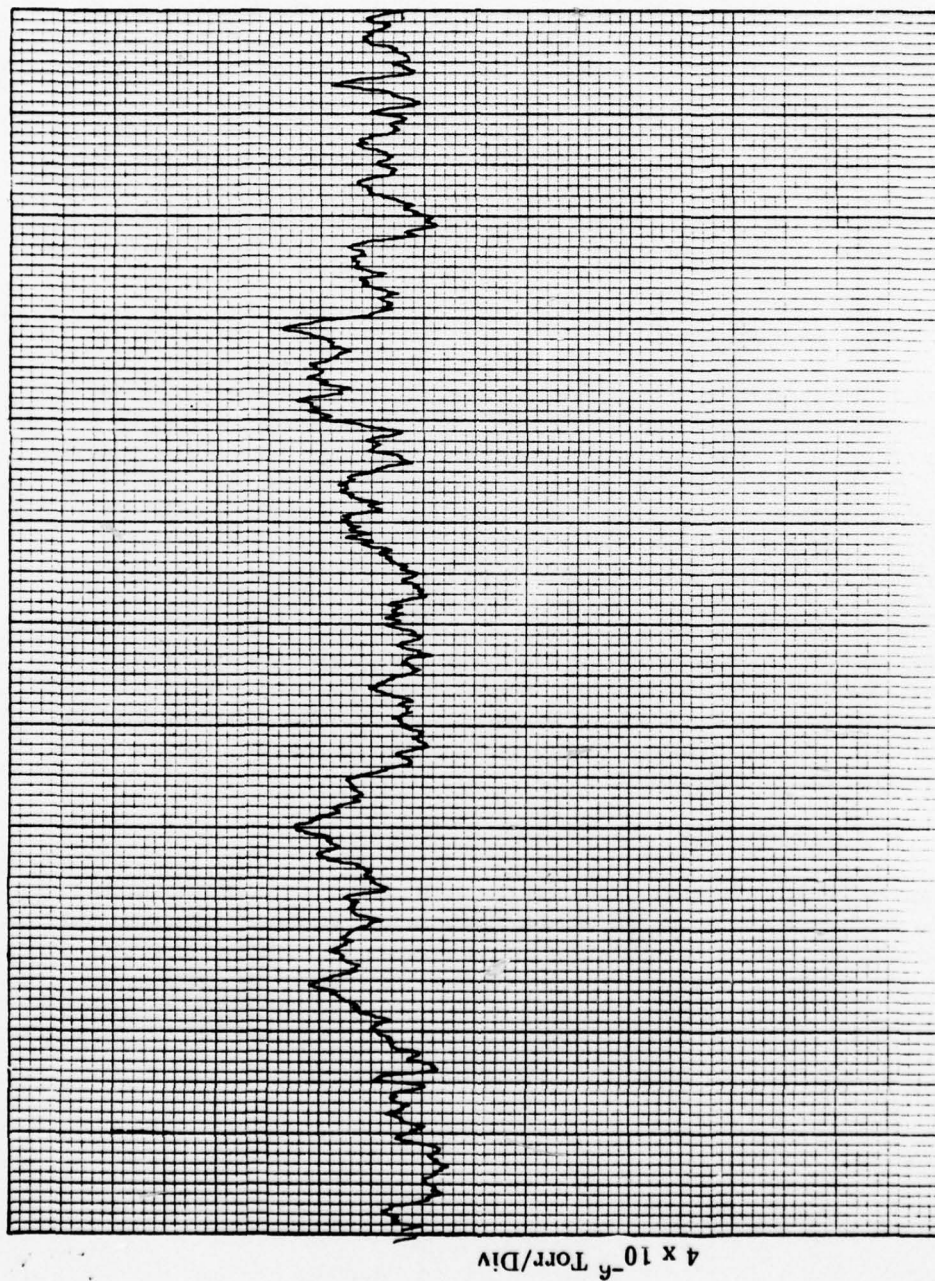
The significance of this problem can be observed by considering the plot given in Figure 11 which shows the output of the pressure transducer produced by temperature instabilities that were artificially induced in the spectrophone. This plot was obtained while the temperature controller, see section B.2., was being used to maintain the cell at a temperature 5°C above ambient. A temperature probe in the body of the spectrophone indicated that the stainless steel body of the instrument was stable to at least 1 part in 10^3 ; however, as can be seen from the figure, a sizable variation in pressure is evident. The implication here is that temperature instability could easily be one of the more significant problems in optoacoustic studies. The variations present in Figure 11 were significantly reduced for this study by employing the following measures:

1. the body of the spectrophone was covered with insulation
2. the entire apparatus, pressure transducer and spectrophone were enclosed in a plexiglass box
3. a leak valve was used to reduce the effects of long-term drifts, see section B.2
4. a more accurate temperature controller is now being employed with the circulating bath.

f. low pressure measurements

1. introduction

If the spectrophone were limited in its application to measurements at atmospheric pressure, it would still be a very useful and promising research tool but there is no reason why it should not be capable of performing meas-



2 Sec/Div

Figure 11. Pressure variations produced by induced temperature variation of the sample cell.

measurements at lower pressures. When an absorbing sample is being measured, a fraction of the incident radiation is absorbed by the gas and subsequently converted from vibration-rotational energy to translational energy. The question which must be asked here is, how do changes in the total pressure of the sample gas affect the rate at which this process occurs? Or, how is the magnitude and phase of the pressure signal influenced by the total pressure of the sample gas? Looking at Equation (82) it would appear that the magnitude will not be a function of pressure, at least to first order of the theory presented in this chapter and subject to the condition that $T/4\tau \ll 1$. The purpose of this section is to develop a simple theory based on the model given by Equation (79) which will answer these questions and justify the technique used to obtain the pure water vapor results which are described in Chapter V.

2. previous work

Nearly all applications of the optoacoustic technique have involved measurements performed at or near a total pressure of 1 atm. Recently, several workers have applied this optoacoustic technique to perform or demonstrate the feasibility of measurements at lower pressures. Abrams⁵¹ has used the spectrophone to measure the broadening coefficients for the 10 μm P(20) CO_2 laser transition. By looking at the normalized output of a spectrophone² as a waveguide CO_2 laser was tuned across the absorption line, he was able to measure both line shape and width. For this study only relative absorption levels were required. Patel⁵² has demonstrated the potential for absolute measurement at low pressures by giving a calibration procedure. Recognizing the pressure dependence in the vibrational to translational energy exchange process he has used samples with constant absorber concentration in N_2 at different pressures to give a calibration for the optoacoustic signal of his instrument.

3. a technique

The first step in finding a method for calibration is to obtain the explicit pressure dependence of the optoacoustic signal as it will be measured in the laboratory. To accomplish this it is necessary to consider how the pressure signal will be processed by the synchronous detection system, i.e., the lock-in amplifier is designed so that its output gives the phase sensitive RMS voltage at the fundamental frequency of the input signal. This requires that we examine the Fourier series representation of Equation (79) which is given by

$$V_{\text{sig}} = C_0 + \sum_{m=1}^{\infty} C_m \cos(m\omega t - \phi_m) \quad (83)$$

$$\text{where } C_0 = V_0 \left\{ 1 - \frac{2\tau/T}{1 + e^{T/2\tau}} \right\}$$

$$C_m = \begin{cases} 0 & m\text{-even} \\ \frac{2V_0}{m\pi [1 + (m\omega\tau)^2]^{\frac{1}{2}}} & m\text{-odd} \end{cases}$$

$$\text{and } \phi_m = \pi - \arctan \frac{1}{m\omega\tau}.$$

So that to first order the output from the lock-in amplifier will be given by the RMS value of the signal represented by

$$V_{\text{sig}}^F = \frac{-2V_0}{\pi [1 + (\omega\tau)^2]^{\frac{1}{2}}} \cos(\omega t + \arctan \frac{1}{\omega\tau}) \quad (84)$$

which is simply

$$(V_{\text{sig}}^F)_{\text{RMS}} = \frac{\sqrt{2} V_0}{\pi [1 + (\omega\tau)^2]^{\frac{1}{2}}} \quad (85)$$

at the phase angle

$$\phi_1 = \pi - \arctan \frac{1}{\omega\tau}. \quad (86)$$

The pressure dependence of Equations (85) and (86) resides in the amplitude, V_0 , and time constant, τ , which are given by

$$\frac{\alpha WP}{4\pi K T}$$

and $a^2/k\xi_1^2$ respectively. This permits τ and V_0 to be rewritten

$$\tau = \tau^0 \frac{P}{P_0} \quad (87)$$

and

$$V_0 = V_0^0 \frac{P}{P_0} \quad (88)$$

where $\tau^0 = \tau(P=P_0)$ and $V_0^0(P_0)$. Substitution finally yields

$$(V_{\text{sig}}^F)_{\text{RMS}} = \frac{\sqrt{2} V_0^0 (P/P_0)}{\pi [1 + (\omega \tau^0 P/P_0)^2]^{\frac{1}{2}}} \quad (89)$$

and

$$\phi_1 = \pi - \arctan \frac{1}{\omega \tau^0 (P/P_0)} \quad (90)$$

Equations (89) and (90) are the essential results which predict how the magnitude and phase of the acoustic signal will change with pressure. A plot of these equations as a function of pressure is given in Figures 12a and b. The results of the analysis reveal that, even to first order, the acoustic signal is a nontrivial function of pressure and that an accurate calibration of the spectrophone can only be obtained from a direct comparison with White cell data. The procedure for this calibration will be described in section A.3 of Chapter V.

2. The OSU differential spectrophone

The spectrophone used in this study is a stainless steel nonresonant differential instrument with ZnSe Brewster windows. It was designed with the intention of eliminating that portion of background noise caused by the absorption of laser radiation in the IR windows. The theory employed here was originally tested and developed on an aluminum spectrophone which served as the prototype for the current stainless steel instrument³³. Several refinements have been made in the construction of the new spectrophone which make it more versatile and reliable than its precursor.

The most significant improvement is the addition of temperature control capability. The stainless steel walls of the spectrophone were drilled with a spiralling series of holes that conduct a water-alcohol mixture which is used as the heat exchange fluid. Insulation has been installed around the instrument to improve the temperature range of this system and to insure a uniform temperature distribution. The ZnSe windows permit the study of samples with high relative humidities; the previous aluminum instrument was limited by the hygroscopic property of NaCl windows.

a. theory of operation

The instrument concept shown schematically in Figure 13 was conceived by Professor E. K. Damon to improve sensitivity by employing a differential technique to reduce window noise. Our experience, like that of Kerr and Atwood³¹, had shown that the principal problem associated with the optimum sensitivity of a spectrophone originates from the false pressure signal produced by absorption in the end windows. This "window noise" is observed in the form of a coherent signal that inevitably limits the signal to noise ratio and thus defines a lower limit on sensitivity.

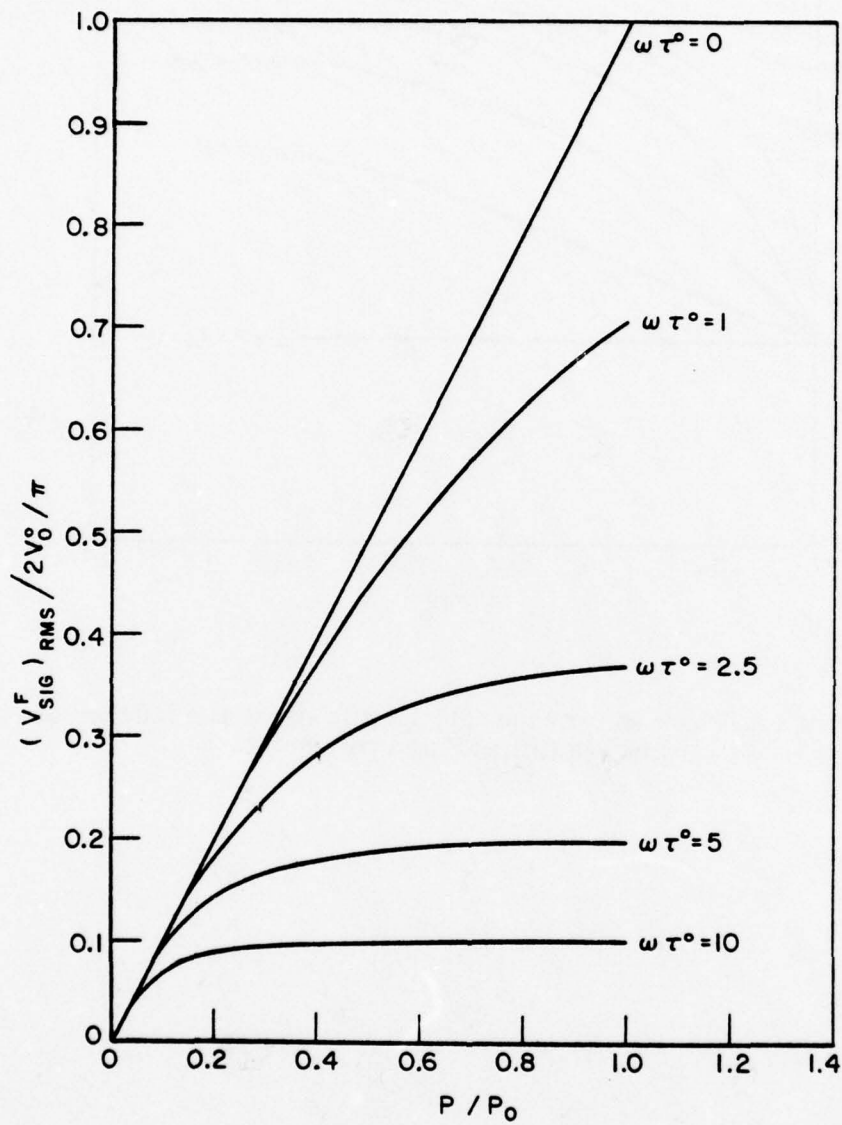


Figure 12a. Normalized optoacoustic signal vs pressure with $\omega \tau^0$ as a parameter.

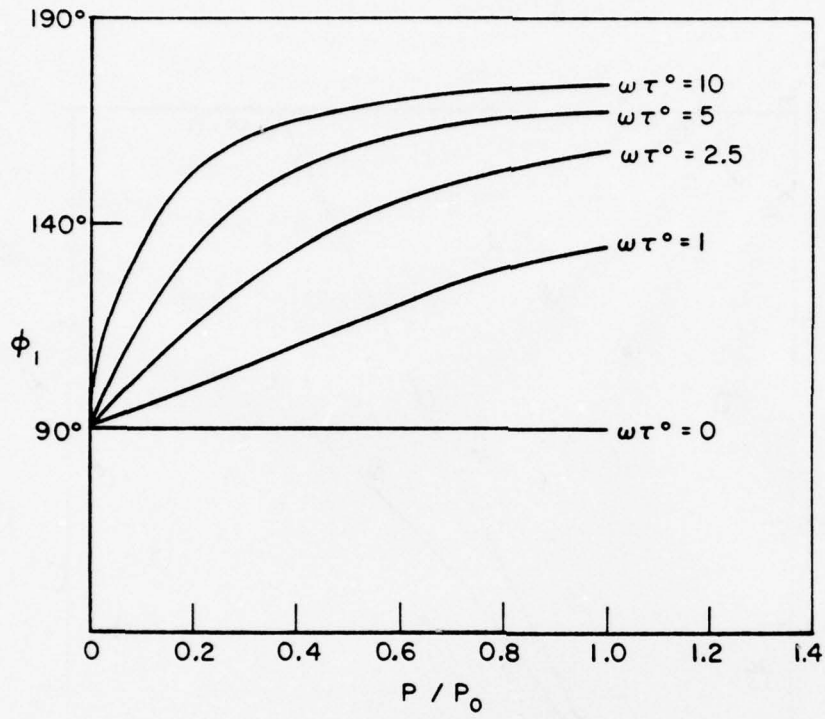


Figure 12b. Phase shift of the optoacoustic signal as a function of pressure with $\omega\tau^0$ as a parameter.

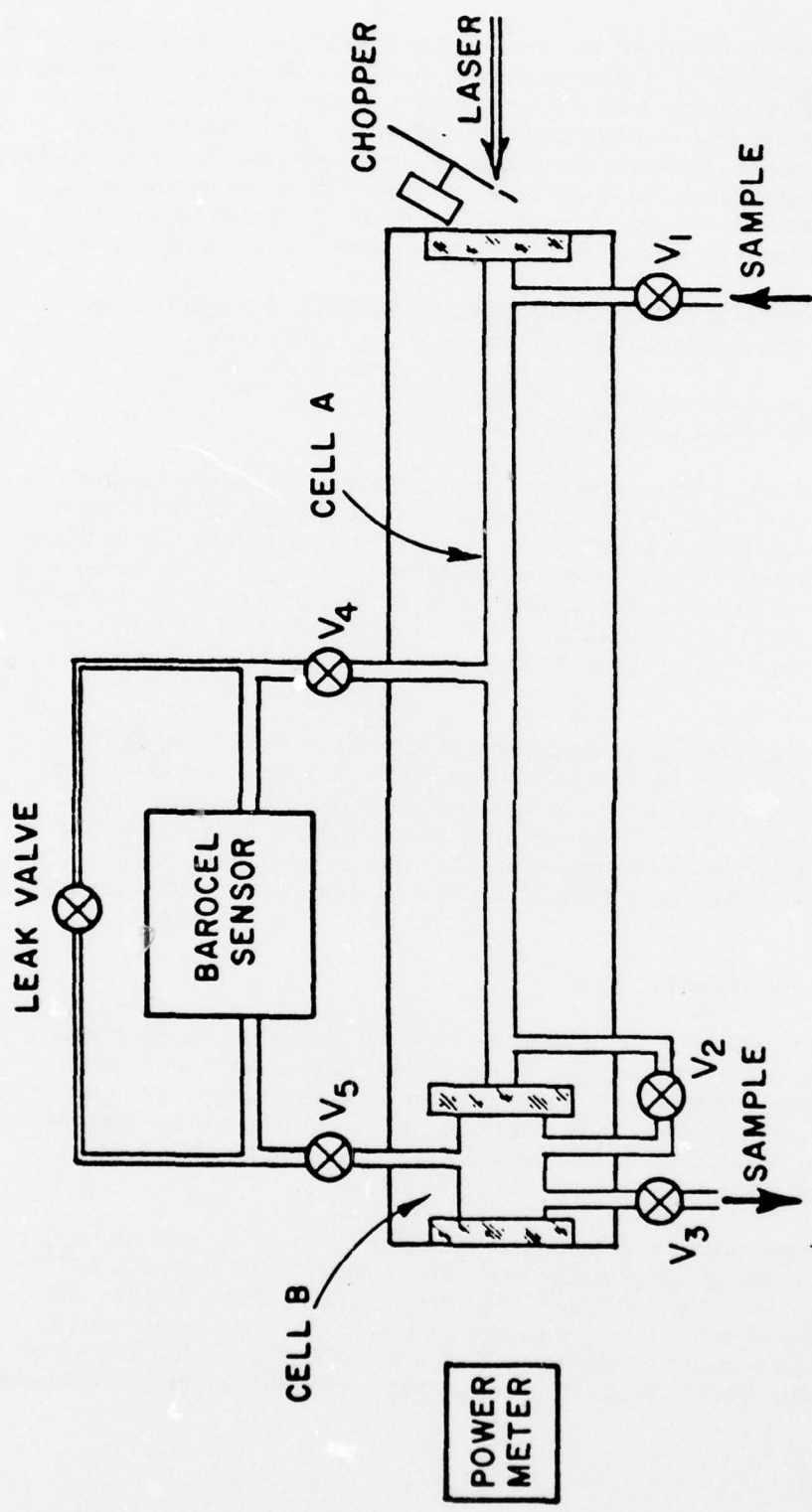


Figure 13. A basic differential spectrophotone.

The differential spectrophone which appears in Figure 13 was designed to minimize this problem. In order to accomplish this objective, two chambers of different lengths but equal volumes are joined together with a single window that serves to isolate the two sections. When the instrument contains an inert sample gas the pressure rise produced by the windows in each chamber will appear as equal signals (in magnitude and phase) on opposite sides of the pressure sensor. In theory, this should not produce any deflection of the sensor diaphragm and therefore (in theory) no "window signal" will be observed.

When an absorbing gas sample is being measured, the pressure signal in cells A and B will consist of two parts -

1. that produced by window absorption
2. that produced by molecular absorption.

Assuming that all windows and both volumes are equal, the window signal will be equal in both chambers and therefore cancel. The radiation energy absorbed by the sample gas is proportional to path length so that the molecular absorption signal will be greater in cell A than in cell B. Thus, the response of this instrument is roughly equivalent to that of a conventional spectrophone whose length is equal to the difference between that of cell A and cell B with the important difference that there should be no false window signal.

Spectrophone measurements require that pressure variations on the order of 10^{-4} - 10^{-7} Torr be detected. This makes it necessary to equalize the static pressure across the transducer head to within its working range. In the present design, this is accomplished by employing a micro-metering (leak) valve between the two chambers. With this method a balance is automatically achieved without any adjustments to system parameters such as cell volume.

b. construction details

A schematic diagram of the stainless steel differential spectrophone is shown in Figure 14. This drawing shows the two end window adapters on which the ZnSe windows are mounted at the Brewster angle. The two cells, A' and B' are separated by a third window that is also mounted at the Brewster angle. Not shown in this figure is the extensive heating-cooling capability which has been designed into this system.

The principal problem encountered in our previous work was contamination of the sample gas, especially when water vapor was being studied⁵⁴. The current instrument was designed with the objective of preventing this problem by using high vacuum technology to achieve an ultra clean system. To this end an all stainless steel instrument was built with welded joints and high vacuum ultra Torr fittings. The result was a chamber which can achieve

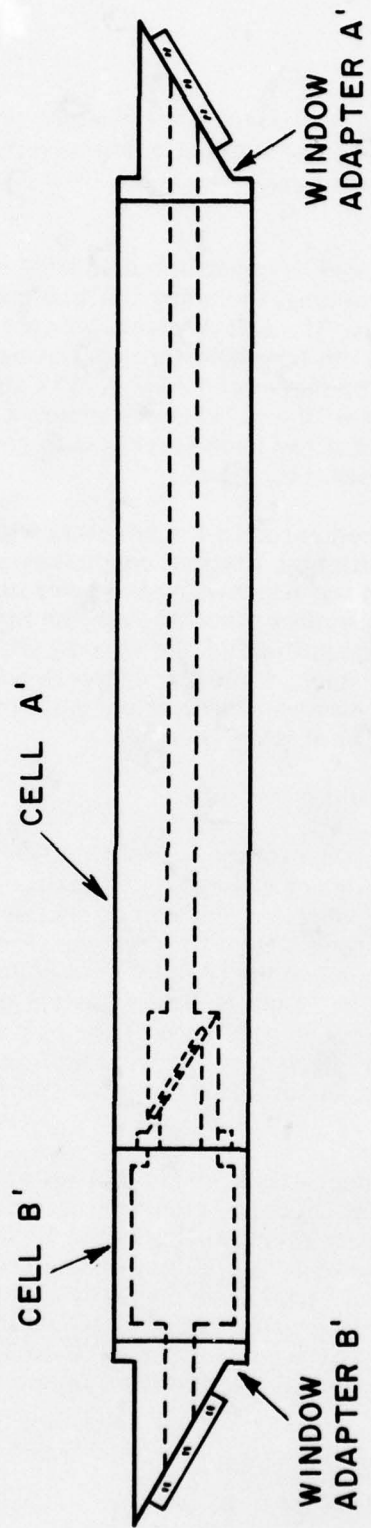


Figure 14. Schematic drawing of the Brewster angle differential spectrophone.

a vacuum on the order of 10^{-8} Torr. After final cleaning procedures were completed this instrument showed no signs of contaminants, even after circulating a water vapor sample for nearly one hour. This instrument is shown in Figure 15.

The body of the spectrophone is constructed of #304 stainless steel. The entire instrument is 62.5 cm long, including the window adapters at each end which are 13.3 cm in length. The cell A' measures approximately 5 x 5 x 29.5 cm and includes a 29.5 cm long hole through the center which was reamed and polished to a final diameter of 1.03 cm. The short section B' measures approximately 5 x 5 x 6.35 cm. This cell offers a relatively short path for the incident radiation but has been machined to comprise a volume equal to that of the long chamber, i.e., 30 cc.

The ZnSe windows were cemented to the adapters with Stycast #2850GT, a low vapor pressure sealant with high thermal conductivity. This latter property is important in that heating of windows by the laser beam will be reduced by heat transfer to the stainless steel through the Stycast. In principle, this should further reduce the magnitude of the window signal. The ZnSe windows at each end are 3 mm thick, while the center window is 1 mm thick. The 1 mm thickness was used to reduce the vertical shift in the beam as it passes from the long cell into the shorter chamber.

c. temperature control system

The spectrophone used in this work was designed to include a temperature control capability which enables absorption to be studied as a function of temperature. Both the long and short cells were drilled with a spiralling series of 0.48 cm holes that permit a fluid to circulate through the stainless steel block. The end window holders are fitted with a hollow sleeve that is brazed shut at both ends of the adapter. These sleeves permit the heat exchange fluid to pass up and around both ends of the cell and insure a uniform temperature for the sample gas near the windows. Finally, the whole spectrophone is covered with sound proofing material and 1.27 cm of thermal insulation.

The temperature of the heat exchange fluid (a water-alcohol mixture) is controlled by a Yellow Springs Model 63 temperature controller, that was adapted for use with a Lauda K-2/R circulating bath. Figure 16 shows the configuration of this control system. A stability on the order of 0.001°C for at least 1 hour was observed with a Stow Lab. temperature probe that is located in the center of the long cell. In these studies the temperature control facility was only used over a range from 16°C to 27°C ; as a consequence it was assumed unnecessary to regulate the temperature of other external plumbing.

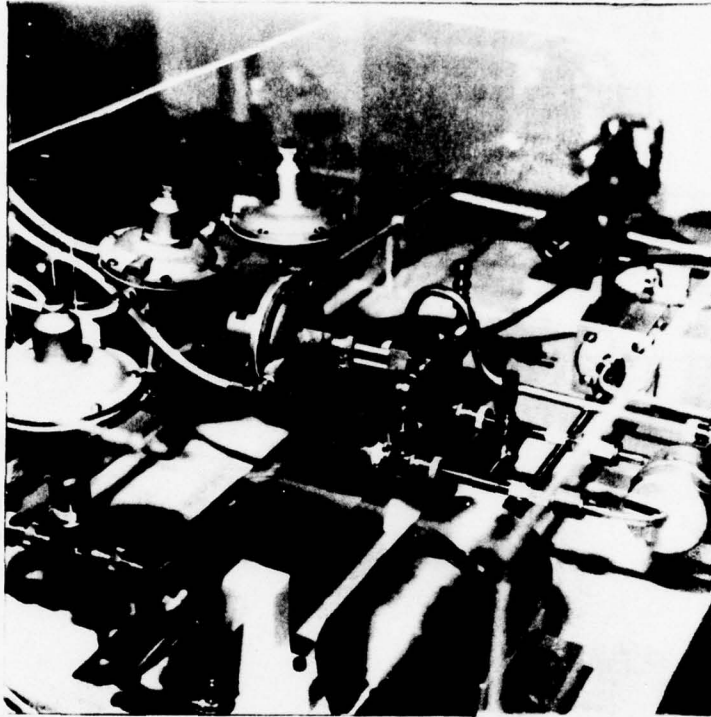


Figure 15. The stainless steel spectrophone.

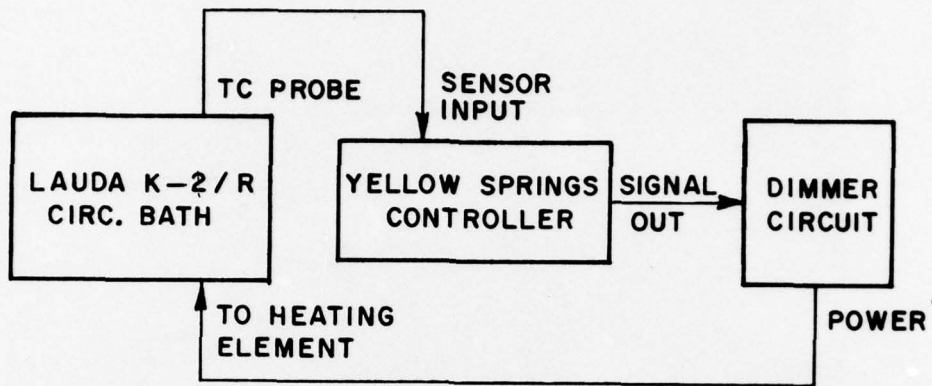


Figure 16. Block diagram of the temperature control system for the spectrophone.

CHAPTER IV THE EXPERIMENTS

This chapter serves to describe the equipment and techniques employed in obtaining the data which will be presented in Chapter V. The discussion includes a detailed account of the tests performed on the spectrophone and White cell apparatus. These tests were performed to explore and define the accuracy of each experiment in several critical areas. For instance, the results of White cell measurements at high transmittances are extremely sensitive to changes in the background, i.e., the transmission measured with a nonabsorbing sample present. Stability tests were performed to predict the magnitude of this problem by measuring these variations during the course of a typical experiment.

Spectrophone results are susceptible to quite a different set of experimental problems among which is calibration. Calibration data for the spectrophone must ultimately come from White cell measurements, which are typically most accurate and hence reliable when the transmittance is much less than 90%. However, the most useful and interesting applications for spectrophone measurements are those in which the absorption is quite low, i.e., at least an order of magnitude smaller absorption than for a desirable calibration level. Inherent in this procedure is the extrapolation of the calibration results down to the signal level at small absorption where the instrument is intended to be fruitfully employed. This requires that the response of the spectrophone as a function of signal level be accurately determined, since it would be an oversight to assume that this instrument must respond in a linear fashion. A description of this experiment as well as other significant experimental procedures and tests are included in section B. Section A contains a description of the equipment employed in this study.

A. The Experimental Apparatus

1. CO₂ Laser

The laser used in these experiments is a sealed off cw CO₂ laser which is grating tunable for single line operation and electronically stabilized to maintain a stable output power at line center. Output power for the laser lines studied varied from 1/4 to 4 watts when the laser was operating in the TEM₀₀ mode. This laser is tunable over both the 10 μm (00⁰1-10⁰0) and 9 μm (00⁰1-02⁰0) bands, however, the number of lines observed in the 9 μm band was substantially smaller and limited the frequencies studied in this region. Unique features of this laser are the configuration of the resonant cavity and an etalon output mirror which often prohibited laser operation at several lines where lasing action could normally be expected. Coping with this latter property required special consideration that will be described shortly.

The resonant cavity for the CO₂ laser, shown schematically in Figure 17, consists of a flat grating, a spherical "turning" mirror, mounted on a PZT transducer and a flat GAS output window. For this type of resonator the stability condition can be shown to be

$$0 < \left(1 - 2 \frac{L_1}{R}\right) \left(1 - 2 \frac{L_2}{R}\right) < 1 \quad (91)$$

where the distances L₁ and L₂ are illustrated in the figure and R is the radius of curvature of the spherical mirror. For the present situation we have L₁ = 1.1 m, L₂ = 0.3 m, and R = 3m, so that the inequality becomes

$$0 < 0.21 < 1 \quad (92)$$

and is satisfied. The motivation for this particular cavity configuration comes from the internal flat output mirror which was supplied by the manufacturer of the plasma tube. (This tube was supplied in a Sylvania model 948 multiline CO₂ laser.) The use of a flat grating in the cavity requires that a focusing element be included so as to achieve a stable resonant cavity; this can be seen by letting R → ∞ in Equation (91), i.e.,

$$\lim_{R \rightarrow \infty} \left(1 - 2 \frac{L_1}{R}\right) \left(1 - 2 \frac{L_2}{R}\right) = 1 \quad (93)$$

Letting R → ∞ is equivalent to making the spherical turning mirror flat which is equivalent to removing the turning mirror and placing the grating on the optic axis of the plasma tube a distance (L₁+L₂) away from the GAS window. The inequality now reads

$$0 < 1 < 1 \quad (94)$$

and is not satisfied for any distances L₁, L₂.

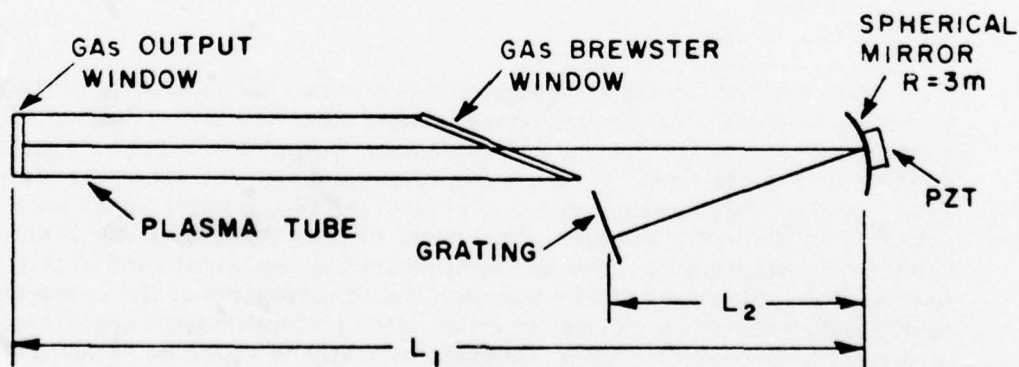


Figure 17. Schematic diagram of CO₂ laser optics.

An interesting aspect of this laser is introduced by the presence of the gallium arsenide flat, which serves as the output mirror, i.e., it is used as an etalon. This means that the output mirror is frequency selective and on cold start will not allow operation on some laser lines. However, the etalon is temperature sensitive so that its frequency properties can be temporarily altered by heating or cooling. When this difficulty arises it can generally be resolved by the two methods described below. The first consists of running the laser on a nearby "operable" line, thus heating the output window, and then quickly re-adjusting the grating for the desired laser line. The second technique involves the local heating of the air surrounding the GaAs window using heating tape connected to a variac. By combining these methods, satisfactory results were nearly always obtained. For most laser lines this problem was not significant. Also, the gallium arsenide window appeared to reach thermal equilibrium in a brief period of time so that no observable stability problems were introduced by this phenomenon.

The laser operates at a nominal power of 4 watts on the P(20) line at 944.194 cm^{-1} . Because of the large power intensities within the optical cavity, approximately 1000 w/cm^2 , an original grating, ruled with 150 lines/mm and blazed at $8.6 \text{ }\mu\text{m}$ is used. This grating was chosen for its relatively large angular dispersion, which permits precise and convenient selection of the desired lines. Fine tuning of the resonant cavity is achieved with translation of the spherical "turning" mirror by means of the PZT on which that mirror is mounted. This transducer is used for both the manual adjustments and the electronic stabilization of the laser.

Electronic tuning of the cavity length is accomplished by a frequency stabilizer which is electrically connected to the PZT. The stabilizer design was adapted from one that Thomason and Elbers⁵⁵ used with a commercial laser. In operation, the stabilizer periodically varies the cavity length by a small amount which causes a small modulation of the laser output power when operating above threshold. This variation in output power simultaneously produces oscillations in the plasma impedance which are synchronously detected by the stabilizer. This signal is then used to create a control voltage which is "added" to a manually adjusted PZT bias voltage.

The impedance of the CO_2 laser plasma varies inversely with gain. By sensing changes in plasma impedance (error signal), it is possible to maintain laser operation at line center (maximum gain) by adjusting the cavity length to continuously minimize impedance. The stabilizer correction signal is derived by integrating the output of the synchronously detected variation in plasma impedance induced by a 520 Hz voltage applied to the PZT, see Figure 18. The integrated signal is then amplified and "added" to the PZT bias voltage so as to adjust the optical cavity length to obtain a minimum error (plasma impedance) signal and thus maintain maximum gain (line center).

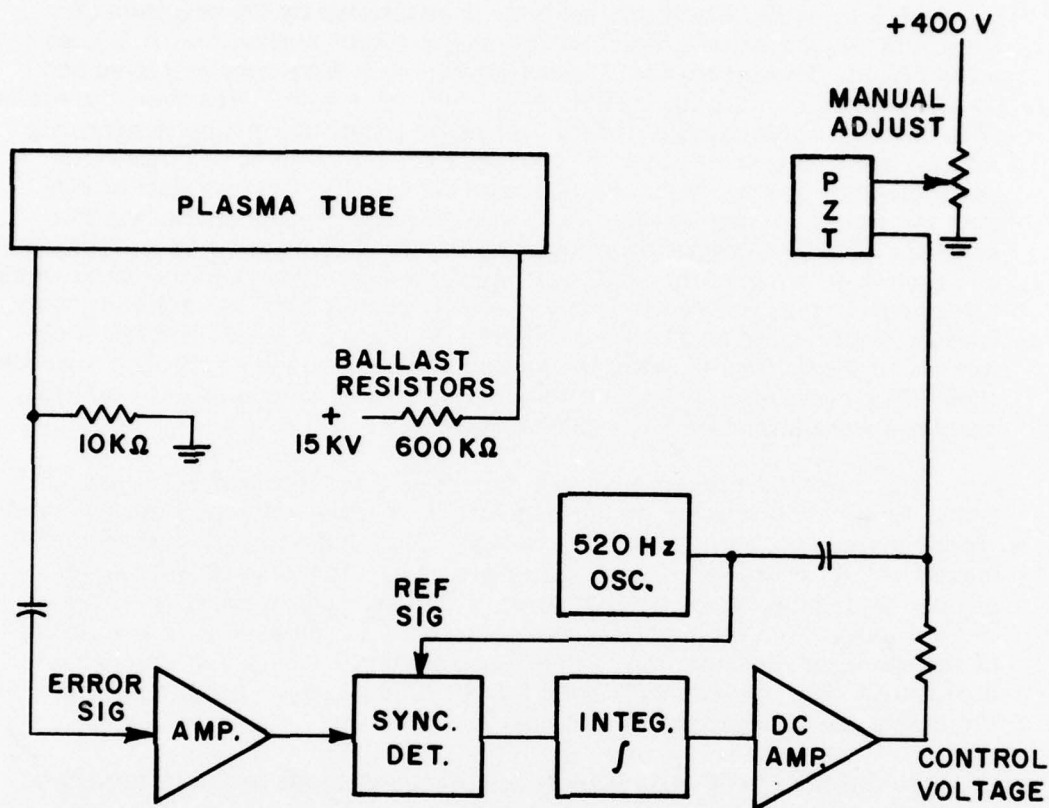


Figure 18. Block diagram of the electronic stabilizer for the CO₂ laser.

The high voltage power supply for the laser tube is the "CO₂ Laser Exciter" unit supplied by Sylvania in the model 948 CO₂ laser. The exciter consists of a variable low voltage (80-160 volts) highly regulated and filtered dc supply, the output of which is fed to a DC-DC converter that steps up the voltage through a high voltage transformer and voltage multiplying network. The high frequency AC ripple is then filtered to produce a highly regulated and highly filtered dc voltage for the laser tube. A low noise, high voltage source is essential to proper operation of the electronic stabilizer just described. The signal used by the stabilizer is derived from a small signal 520 Hz voltage in the plasma tube circuit so that ripple in the high voltage source would distort the desired signal.

A picture of the laser is shown in Figure 19. The plasma tube and cavity optics are mounted on a 7.62 cm thick limestone slab which gives the laser the mechanical stability necessary for stable operation. To assure maximum stability and cleanliness, the laser head is enclosed in a 1 cm thick plexiglass box with one small covered opening that permits adjustment of the grating micrometer. Figure 19 also shows the flexible rubber hose used in the cooling system, the ballast resistors, which are cemented to the top of the plasma tube and the DC-DC converter mounted next to the laser tube. The plasma tube, ballast resistors and power transistors (in the DC-DC converter) are all water cooled using ordinary tap water. This laser was used for both the spectrophone and white cell measurements.

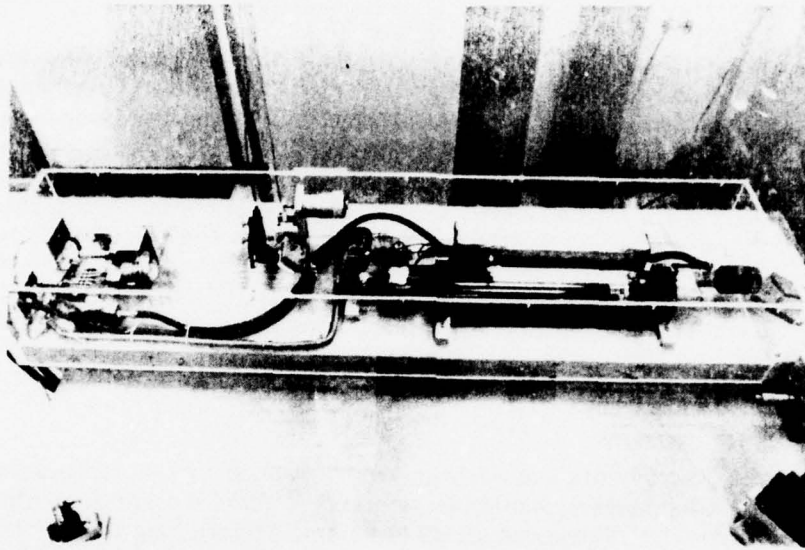
2. Power meters

In both experiments laser power was measured with Scientech model 36-0001 disc calorimeters, having an aperture of 2.54 cm and a nominal output of 100 mv/watt. These detectors have a relatively long time constant of 14 seconds, which effectively averages out any short term variations in laser power. During an experiment the detectors were enclosed in boxes so as to eliminate the fluctuations and drifts caused by laboratory air currents. As a result, the laser power signals measured by the data acquisition system had standard deviations at least three orders of magnitude less than the signal level.

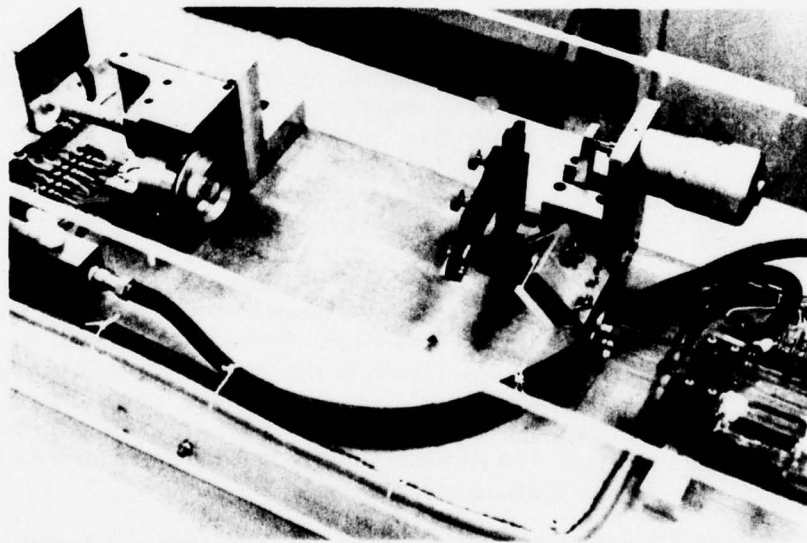
3. Data acquisition system

The computer controlled data acquisition system consists of a SDS Model 920 computer with 8K memory, a typewriter, a high speed 24 channel analog to digital converter, and dc amplifiers⁵⁶. Each measurement is performed by sampling two channels of the A/D converter 400 times each, and calculating the average and standard deviation for each channel, the ratio of the two channel readings is also calculated. The two channels, called signal and reference are sampled 10 ms. apart and there is a delay of 100 msec between the pairs of readings. In operation, the 400 samples are divided into four groups of 100 samples for which averages, standard deviations, and ratios are calculated and printed on the typewriter. These intermediate values allow the experimenter to observe trends in the data as the measuring process continues, i.e., it indicates whether the experiment was stable during the period of a measurement. The averaging process serves to filter out noise induced by room vibration, 120 Hz ripple in the various power supply electronics, and laser power fluctuations, etc.

Figure 20 shows a block diagram of the data acquisition system. Selection of the appropriate pair of A/D channels for the two experiments is accomplished by entering the desired channel numbers in the data taking program from the typewriter. The A/D converter used in both experiments is an Epsco, model 1400, with 1.25 mv resolution (14 bit system). Two different sets of dc amplifiers were used in these experiments; the amplifiers used in the spectrophone experiments are Alinco model 518A while those used in the White cell are Ectron model R516-6A. The dc amplifiers were used to keep the signal levels into the A/D between one and ten volts where they



(a)



(b)

Figure 19. Photograph of the CO₂ laser.

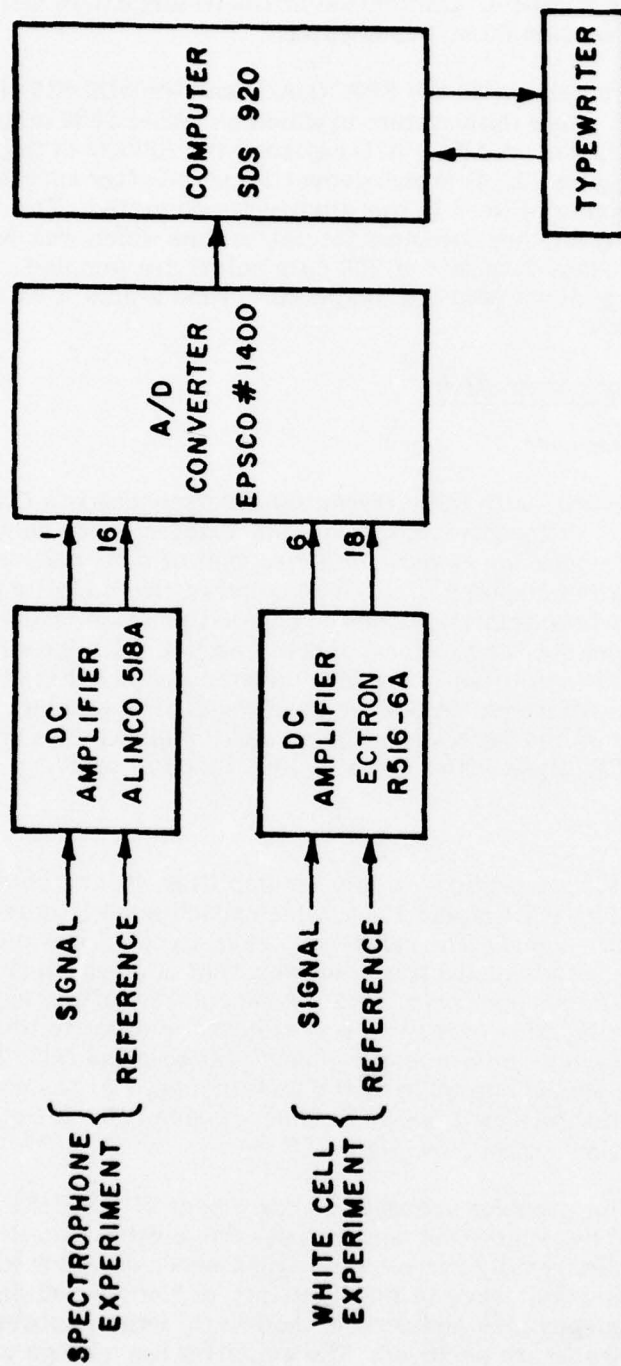


Figure 20. Block diagram of data acquisition system.

were observed to be most accurate. Calibration of the dc amplifiers and A/D is discussed later in section B3 of this chapter.

Note: Recurring problems with the EPSCO A/D and the SDS 920 prompted the implementation of a new data system in which an IMSAI 8080 micro-computer replaced the 920 and an Altair A/D replaced the EPSCO in the configuration shown in Figure 20. This changeover occurred after approximately 75% of the experimental work in this study was completed. The data taking program for this system has the same format as that which was described previously except that four sets of 256 data points are sampled. The Altair A/D is a 12 bit instrument which is jumpered to read 0-9.9974 volts with a resolution of 2.5 mv.

4. Spectrophone instrumentation

a. pressure transducer

The pressure sensor used with the differential spectrophone is a C.G.S. Datametries Model 523-15 differential electronic manometer, trade name Barocel, whose theory of operation is very similar to that of a capacitive microphone in that a flexible diaphragm is placed between two metallic plates, creating two capacitors whose relative values change with motion of the diaphragm. The capacitors are used to form opposite legs of a bridge circuit, the output of which is amplified to produce an analog signal that is proportional to the pressure difference across the diaphragm. The pressure sensor has a full scale range of one Torr, while the associated electronics unit offers a selection of higher sensitivities down to 10^{-4} Torr full scale.

b. lock-in amplifier

The pressure signal is processed by a lock-in amplifier, Princeton Applied Research Corporation, PAR Model 128A, which synchronously detects and integrates the pressure signal. The reference signal for the lock-in is obtained from an infrared diode-photo transistor pair that is mounted on a mechanical chopper. The chopper provides 100% modulation of the laser beam at a frequency of 8 Hz; this frequency was selected in order to limit the problems of DC drift while maintaining a good signal-to-noise ratio for the pressure signal. The analog output from the lock-in amplifier has a range of ± 1 volt which is fed into the signal channel (Alinco dc amplifier set at X10) of the data acquisition system, see Figure 20.

The lock-in amplifier provides accurate measurement of the RMS voltage for signals corrupted by broad-band noise, power line pickup, etc. It does this by means of an extremely narrow band synchronous detector which has the center of its pass band locked to the frequency of the desired signal. Because of the frequency lock and narrow bandwidth, large improvements in signal-to-noise ratio are achieved. The amplifier has a range of sensitivities from 1 μ V to 250 mV full scale; for this work only the 2.5 mV, 10 mV and 25 mV ranges were employed. At the output of the lock-in, ac

fluctuations from the synchronous detector stage are reduced by a low-pass filter, with a time constant that is switch adjustable from 1 msec to 100 sec. This switch on the PAR was adjusted for a 10 sec time constant to match the response of the power meter used for laser power measurements in the spectrophone experiment. Figure 21 shows a block diagram of instrumentation associated with the spectrophone experiment.

c. dew point hygrometer

The partial pressure of water vapor in the spectrophone was measured using an EG&G industrial dew point hygrometer, model 992. This instrument has an accuracy of $\pm 0.5^{\circ}\text{F}$ for dew points in the range from -60°F to 120°F , which corresponds to an uncertainty of $\pm 1.8\%$ at water vapor partial pressures near 15 Torr. The dew point hygrometer consists of an optical sensing bridge network and an inert metallic mirror that is temperature controlled by a thermoelectric cooler. In operation, a sample gas is passed over the mirror and condensation occurs. The optical bridge detects the changes in reflectivity of the mirror and generates a signal voltage that is used to control the thermoelectric cooler. An independent platinum resistance thermometer is used to measure the dew point by sensing the mirror temperature at which the optical bridge is balanced.

d. gas handling manifold

Water vapor samples and buffer gases for the spectrophone measurements were introduced from a stainless steel manifold, which is schematically pictured in Figure 22. A Wallace and Tiernan mechanical gauge, model 62B 4D 0800 with a range of 0-800 Torr and an accuracy of 0.8 Torr was used to measure the total pressure of the pressure broadened samples. Total pressure of the pure water vapor samples was measured with a 0-10" of H_2O model FA 141 Wallace and Tiernan mechanical gauge. Vacuum in the manifold was determined with a NRC model 801 thermocouple gauge.

Prior to conducting these experiments the stainless steel tubing, ultra Torr fittings and bellows seal vacuum valves of the manifold were thoroughly cleaned in spectroscopic grade carbon tetrachloride and then boiled in double distilled water. These precautions are extremely important since it has been observed that water vapor samples can "pick up" contaminants from the vacuum system walls that will cause interference with absorption measurements⁵⁷. The viton "O" rings used with Ultra Torr fittings and the pyrex test tube which holds the triple distilled liquid water sample were also boiled in H_2O . Finally, the manifold was baked out using heating tape and the Edwards model 660 mechanical pump associated with this gas handling system.

e. accessory equipment

In addition to the manifold the spectrophone is also connected to a mass spectrometer which serves as a high vacuum pumping station that was used for leak checking and outgasing the vacuum system. This pumping station consists of an air cooled diffusion pump with a liquid nitrogen cold trap that is capable of achieving pressures on the order of 10^{-8} Torr.

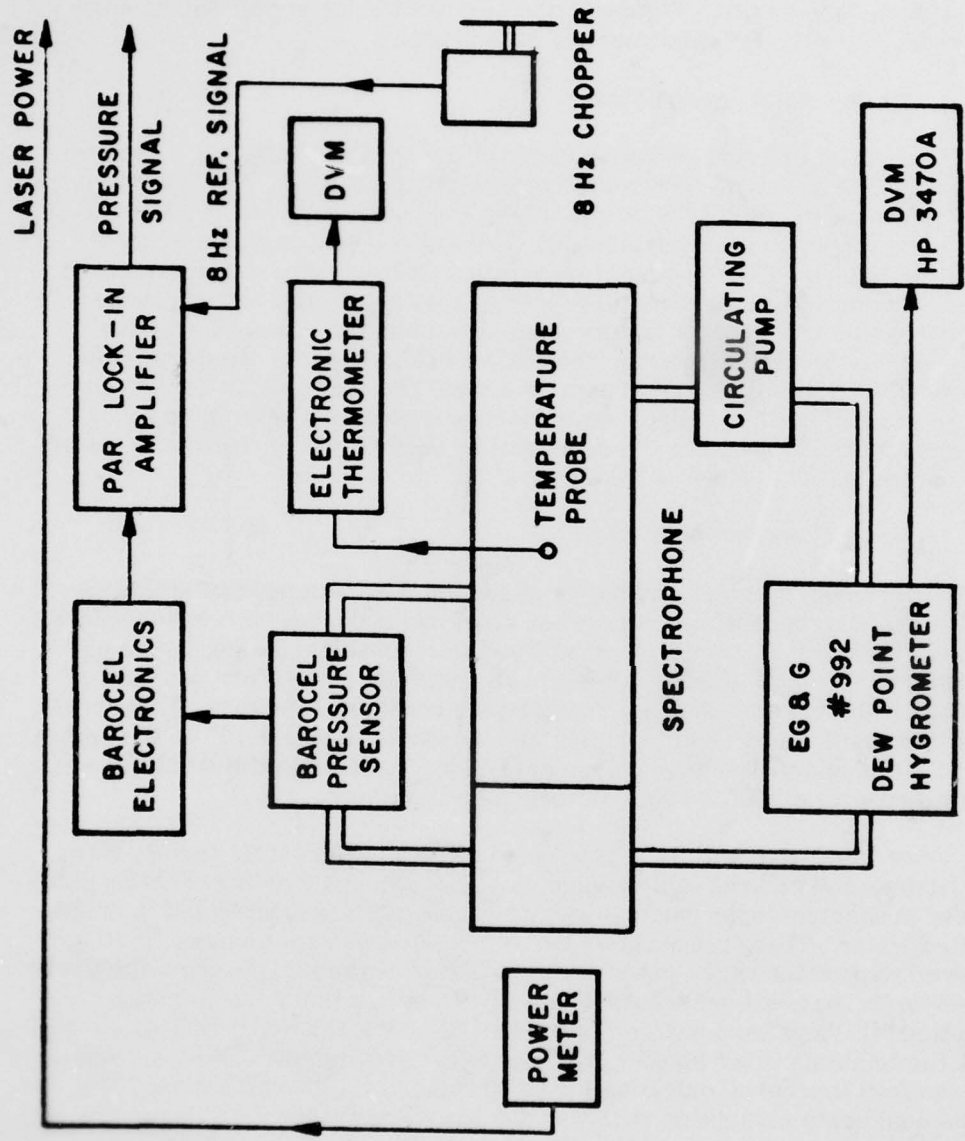


Figure 21. Block diagram of spectrophone instrumentation.

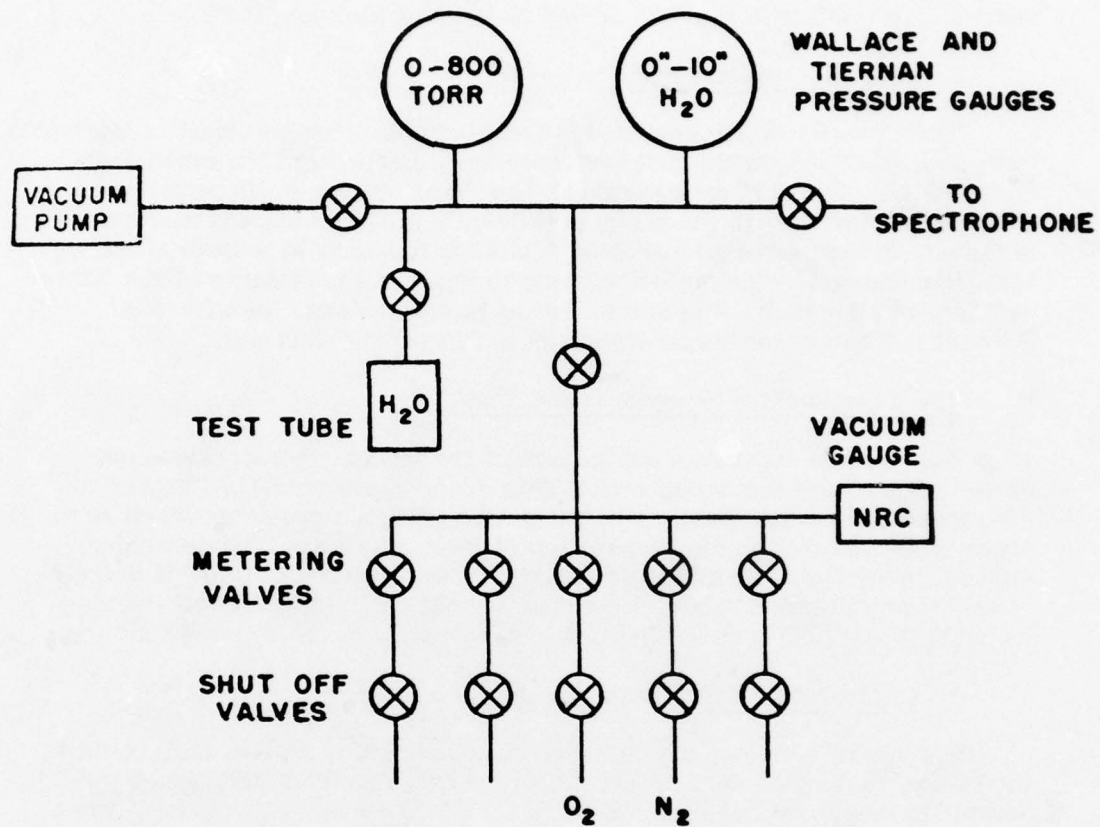


Figure 22. Manifold.

The temperature of the spectrophone was monitored by a Stow Laboratories electronic thermometer, model 911 PL. The temperature probe is located in a small hole near the center of the long stainless steel cell.

5. Multiple traversal cell

The 15 meter White cell used in this study has been previously described⁵⁸. Just prior to this study the cell was thoroughly cleaned and the mirrors re-coated with a new aluminum surface. This "new" mirror finish permitted a significant increase in the useful path length; 1.5 kilometers is now readily obtained. Recent efforts have also been made to uncouple sources of vibration from the cell -- the objective being to improve the stability of the White cell optical alignment. The author wishes to acknowledge the efforts of Michael E. Thomas for his contributions in "upgrading" this cell.

B. The Experimental Procedures and Tests

This section contains a description of the laboratory techniques employed in obtaining the experimental data which is presented in Chapter V. Also treated here is an analysis of the most significant problems which were observed in this study and a description of their solutions. This discussion includes many tests which were conducted in anticipation of possible sources of experimental error. These tests involved not only calibration of the electronic apparatus but a determination of the spectrophone response function.

1. Calibration tests of data system

The use of a computer controlled data acquisition system facilitated the task of running each experiment, however, it also made the results vulnerable to any problems in that system. This was made quite apparent when the Epsco A/D failed, i.e., a resistor in the comparator circuit opened up causing a nonlinear response from that instrument. In another instance, an electrolytic capacitor in the dc amplifier power supply failed, the amplifier continued to work, but its output was corrupted by 120 Hz noise. Fortunately both of these problems were discovered during the course of periodic calibration tests.

a. dc amplifiers and the A/D

Calibration of the dc amplifiers and A/D converter was performed both prior to and during the course of these experiments. An Analogic model AN 3100 voltage standard with a resolution of 0.1 millivolts was used to perform the calibration tests. Each of the data channels was examined separately by connecting the voltage standard directly to a DC amplifier input, see Figure 20, and initiating the data taking cycle from the Teletype. To determine accuracy and linearity, the voltage standard was stepped in 0.5 volt increments in the output of the dc amplifier and the A/D was read at each step.

02/19/78 CALIBRATION OF DATA SYSTEM

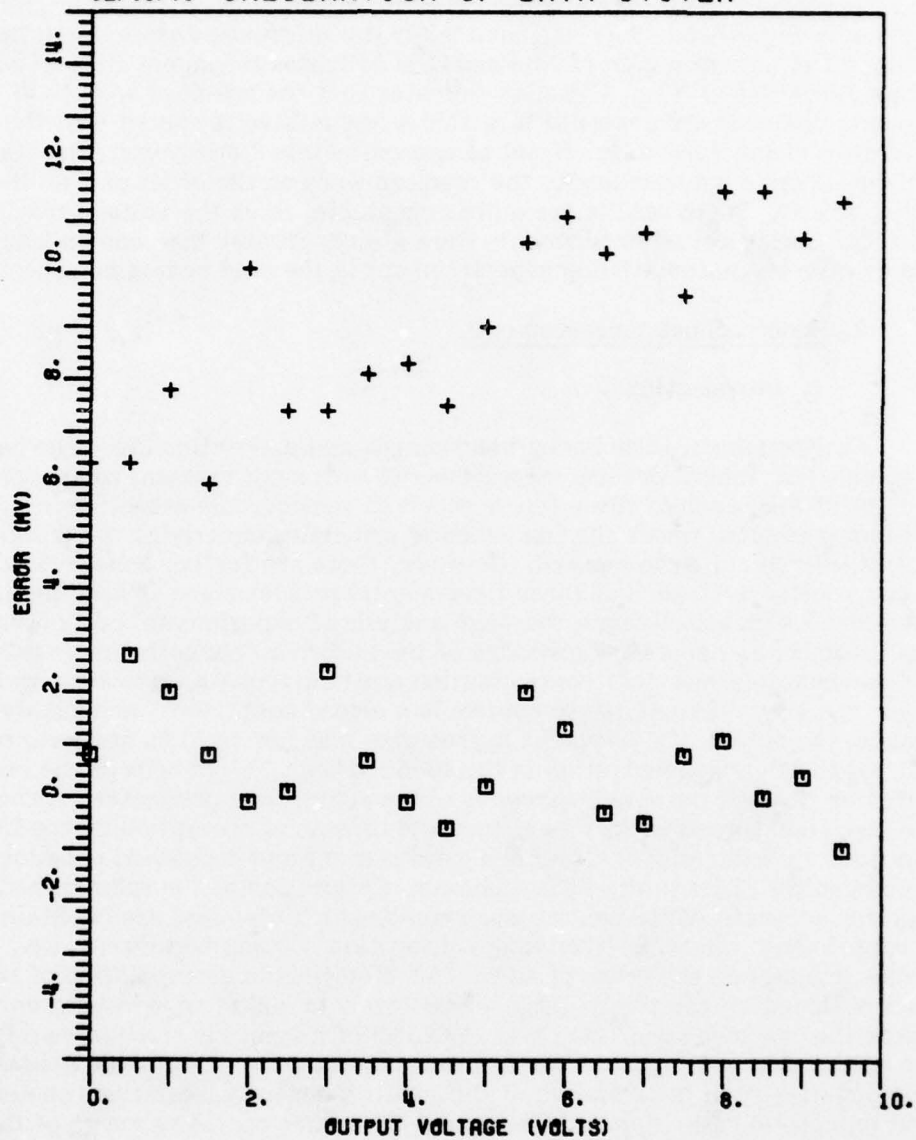


Figure 23. Calibration data for the signal and reference channels. The error in mV is plotted vs the theoretical output voltage in volts. The □ correspond to the signal channel (dc amplifier gain=X10) while the + are for the reference channel dc amplifier gain=X50).

A plot of error (MV) in the recorded voltage vs theoretical output voltage, i.e., the product of voltage standard dial setting and the dc amplifier gain, is given in Figure 23. The (+) symbol is for the reference channel with its dc amplifier set for a gain of X50 and (□) indicates the signal channel with its amplifier set at X10. This plot indicates that the readings on both of the data channels are accurate to within a few millivolts except that the reference channel has a dc off-set of approximately 6 millivolts. The standard deviations corresponding to the readings were on the order of 5 millivolts, or less. These results are quite acceptable, since the voltage levels recorded during actual experiments were always greater than one volt and the dc offset is automatically subtracted out in the data reduction process.

2. Spectrophone measurements

a. introduction

Contaminants, false background signals and calibration are three basic problems that inhibit precise measurements with a nonresonant spectrophone. In light of this, each of these topics received considerable attention in the preceding chapter where the fundamental principles underlying the design of this instrument were treated. However, there are further considerations; in conjunction with each of these fundamental problems are equally significant questions which arise from a thorough analysis of experimental procedures. For instance, an accurate knowledge of the absorber concentration is essential for the same reasons that contamination must be avoided. However, water vapor is a very difficult gas to control in a closed container⁵⁹ and simply reading the output of a dewpoint hygrometer may not yield an accurate result for the H₂O concentration in the spectrophone. Alignment of the laser radiation through the spectrophone is also a significant parameter. Although the instrument was designed to reduce the effects of absorption by the IR windows, a small residual signal is always present and dependent upon localized nonuniformities in the ZeSe windows. Calibration of the spectrophone requires accurate White cell measurements, which are most easily obtained in experiments where relatively high absorption is being considered, i.e., transmittances on the order of 40%. This requires the extrapolation of results obtained at (relatively) large signal levels to calibrate measurements where the pressure signal may be two orders of magnitude smaller than for the calibration experiment. The question raised here concerns the assumption of linearity in the response of the spectrophone; i.e., can the same calibration constant be employed throughout the entire operating range of the instrument? The first step in resolving this problem is to verify the linearity of the lock-in amplifier which is used to synchronously detect the pressure signal.

b. instrument response tests

1. lock-in amplifier

The absorption coefficients measured in this study range from 0.01 km^{-1} to 1.0 km^{-1} . For the spectrophone this corresponds to two orders of magnitude variation in the pressure signal. Only one scale of the Barocel electronics was employed in these measurements, the sensitivity switch was set at X.01 so that a full scale reading corresponds to a pressure of 0.01 Torr. The range in pressure signals required that several different sensitivity scales be utilized on the lock-in amplifier which was used to measure the analog output from the Barocel transducer. Thus, it is necessary to consider linearity and consistency of all the lock-in amplifier ranges required during these studies. This is especially important for the higher sensitivity scales (1 mv, 2.5 mv and 10 mv) which were required for a majority of the experiments.

The apparatus used to perform this calibration consisted of a Wavetek model 130 signal generator, a precision attenuation circuit and a RMS voltmeter, Hewlett Packard #3400A. The block diagram of this experiment is given in Figure 24. The procedure employed here was to measure the signal voltage with the RMS voltmeter, adjust the attenuator circuit for the desired level and then read the output of the lock-in on the signal channel with the A/D. The results of this experiment for the 1.0, 2.5 and 10 mv scales are shown in Figures 25a, b and c. In these plots the lock-in readings (ordinate) are plotted against the RMS voltage (abscissa) read on the HP voltmeter. From this data it is observed that the calibration of the PAR lock-in amplifier is satisfactory. However, it still remains to demonstrate that the response from the spectrophone is linear over the range of signals observed in this study.

2. linearity

To determine whether the spectrophone response is linear, an experiment was performed using a BaF_2 wedge to replace a conventional mirror and thus reduce the laser power incident on the spectrophone. The idea is that reduced laser power will result in a proportionately smaller pressure signal; this permits a direct comparison of the instrument response for small and large signals by simply interchanging the BaF_2 wedge with a front surface mirror while leaving the sample gas unchanged. Figure 26 shows a schematic diagram of the pertinent optics; mirror M3 represents the components which were interchanged using kinematic mirror mounts.

The experiment consisted of introducing an arbitrary amount of absorber, CO_2 in this case, into the spectrophone and measuring the response at both full and reduced laser power levels. The reduced power level was obtained by replacing mirror M3 with the BaF_2 wedge. Full power is defined as that observed with a conventional mirror located at M3. Figure 27, shows a plot of normalized spectrophone signal (pressure signal divided by laser power) at full laser power vs normalized spectrophone signal at reduced laser power with absorber concentration as a parameter. Linear response for this

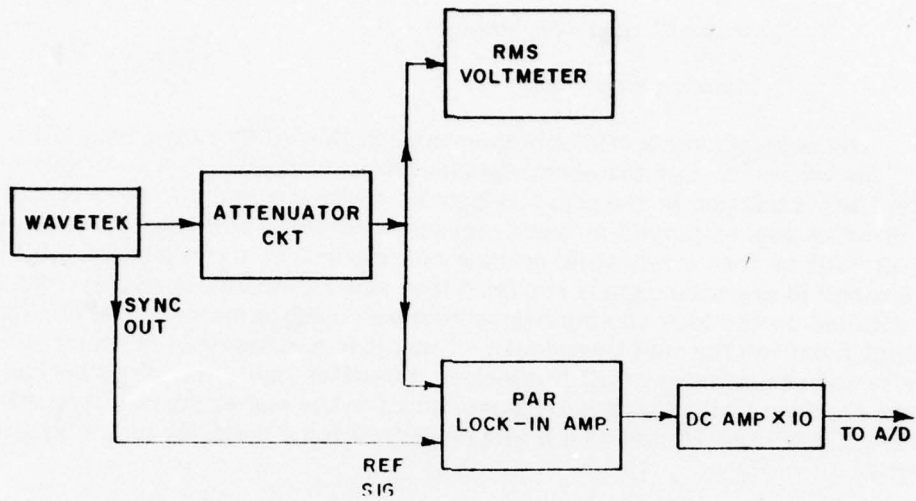


Figure 24. Block diagram of lock-in amplifier calibration experiment.

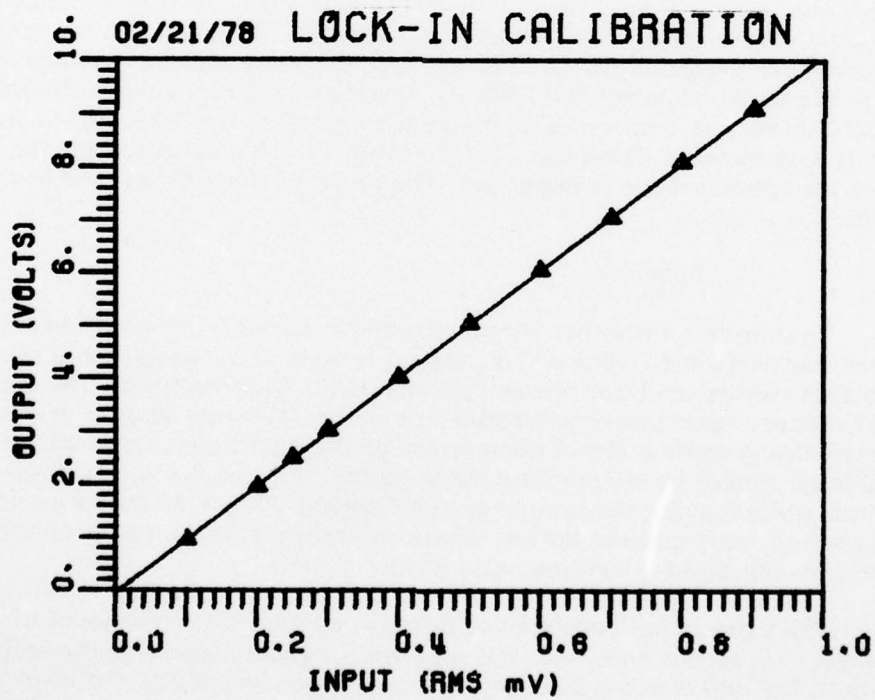


Figure 25a. Calibration data on the 1 mV scale.

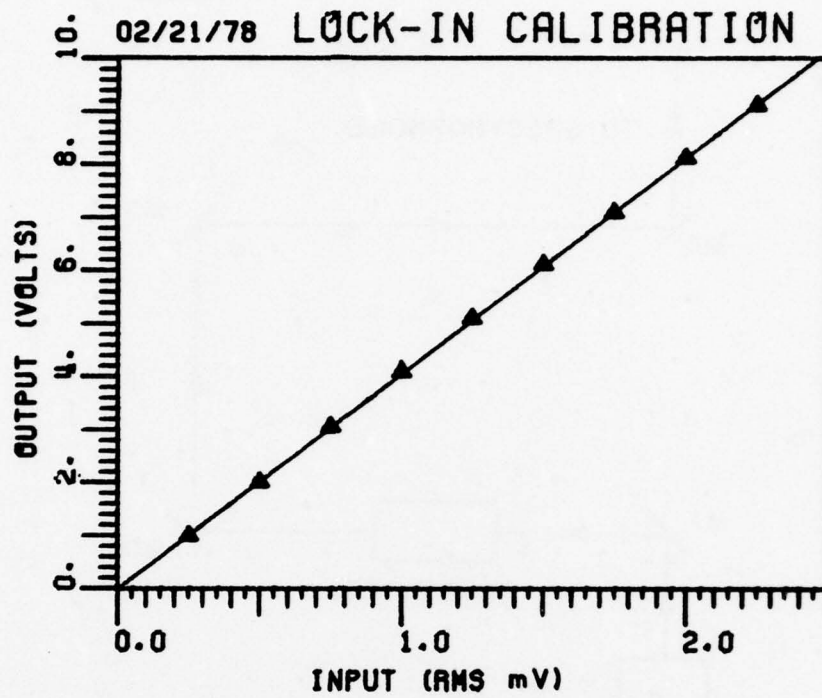


Figure 25b. Calibration data on the 2.5 mV scale.

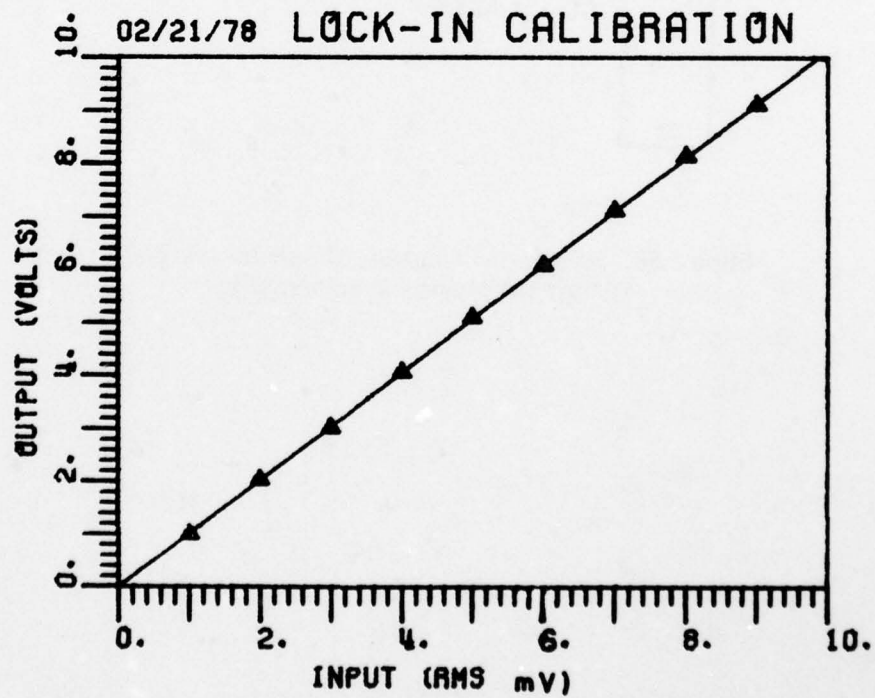


Figure 25c. Calibration data on the 10 mV scale.

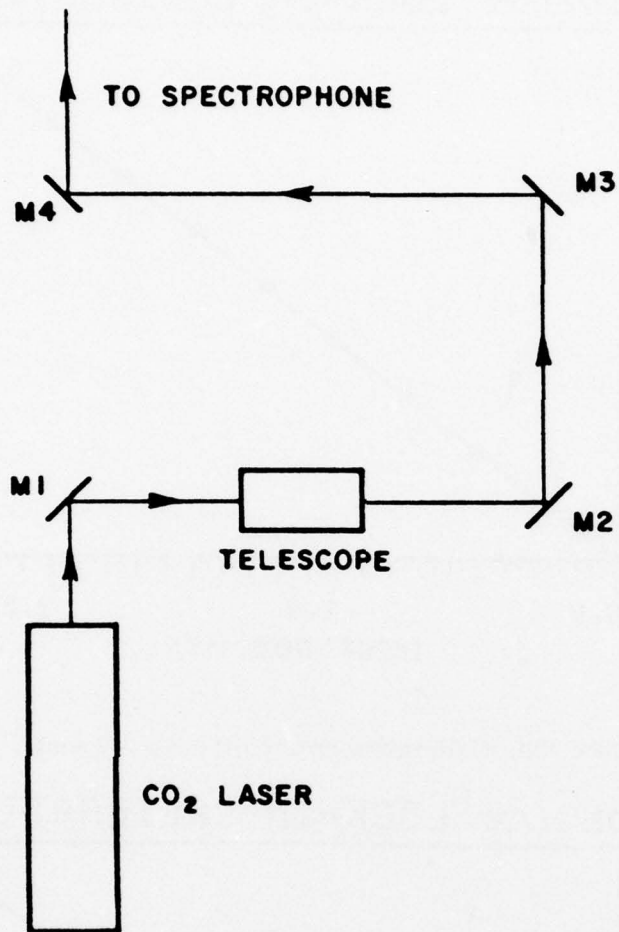


Figure 26. Schematic diagram of optical system for spectrophone experiment.

08/24/77 TEST FOR SPECTROPHONE RESPONSE

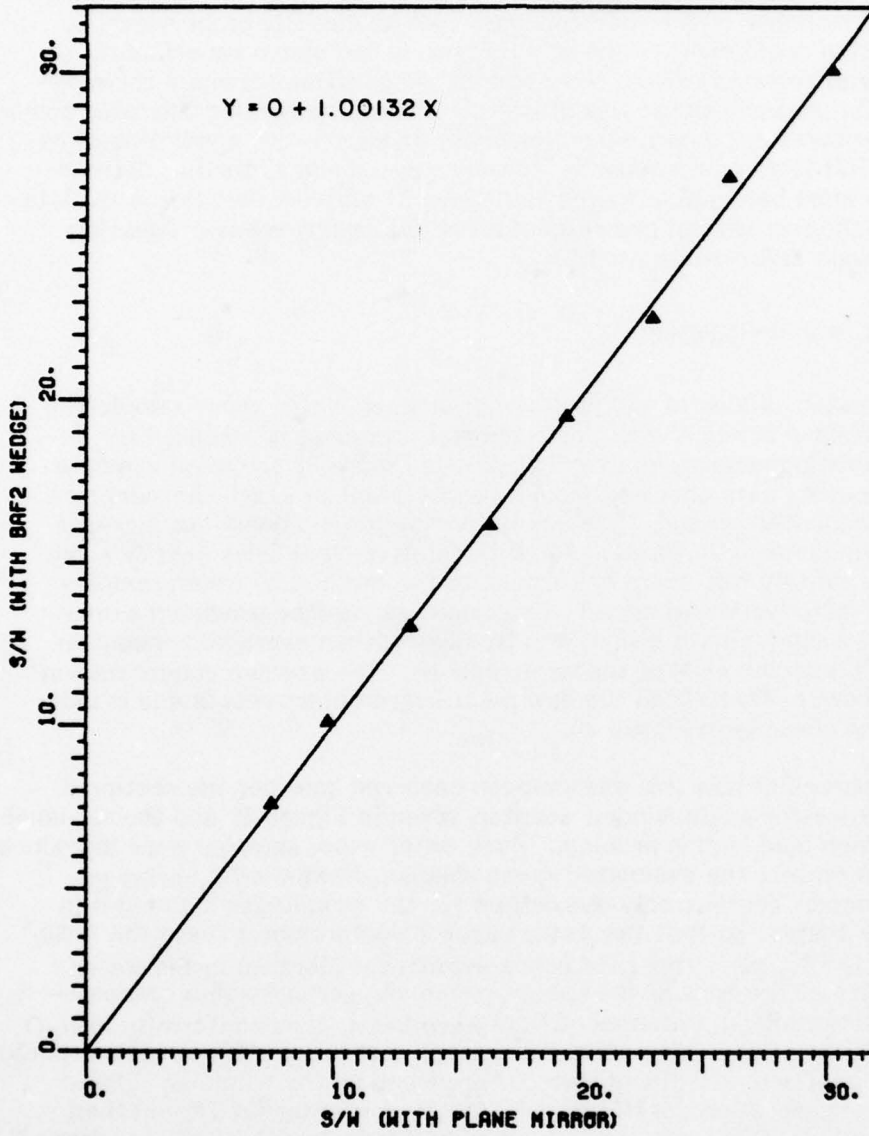


Figure 27. Plot of normalized response of reduced low power vs normalized response at "full" power.

instrument implies that, independent of the pressure signal magnitude, the normalized response of the spectrophone must be directly proportional to the absorption coefficient of the sample gas. In the above experiment, a sample was introduced (with a fixed absorption coefficient) while the magnitude of the pressure signal was discretely altered by varying the laser power. For a linear system the normalized response under the two conditions of reduced and full laser power must be linearly related and as further defined above they must be equal. The plot in Figure 27 verifies that this is the situation, i.e., the two normalized responses are related by a linear equation with unit slope and zero intercept.

c. sample handling

The proper mixing of the pressure broadened water vapor samples in the spectrophone is one of the most important procedures required for accurate absorption measurements. The plot in Figure 28 shows an example of the H_2O in N_2 data obtained from an experiment in which the samples were not adequately mixed. These results indicate an anomalous increase in absorption, especially for samples with relative humidities near 50% or higher. Ultimately this error was traced to the method by which samples were being introduced and mixed. This improper method produced a non-homogeneous sample with a significantly higher (than average) concentration of H_2O near the ends of the spectrophone. The average concentration is defined here as that which the dew point hygrometer records and is indicated by the abscissa in Figure 28.

To appreciate how this phenomenon occurred consider the sectional view of a Brewster angle window adapter, given in Figure 29 and the sequence of steps which lead to this problem. Pure water vapor samples were introduced by evaporation into the evacuated spectrophone. Next the N_2 buffer gas was introduced. There is only one orifice for the sample gas molecules in the window adapter so that the water vapor is compressed toward the ZnSe window by the N_2 gas. This results in a significant increase in the water vapor density at the ends of the spectrophone and perhaps some condensation when large initial pressures of H_2O were used. A nonuniformity in H_2O concentration could produce abnormally large absorption; this situation should be especially apparent if liquid water is produced on the windows. Liquid water has an absorption coefficient 10,000 times greater (at $10 \mu m$) than the gas phase⁶⁰. This would explain the significant departure of the "dashed" curve (anomalous data) from the solid curve (correct data) at high relative humidities, see Figure 28.

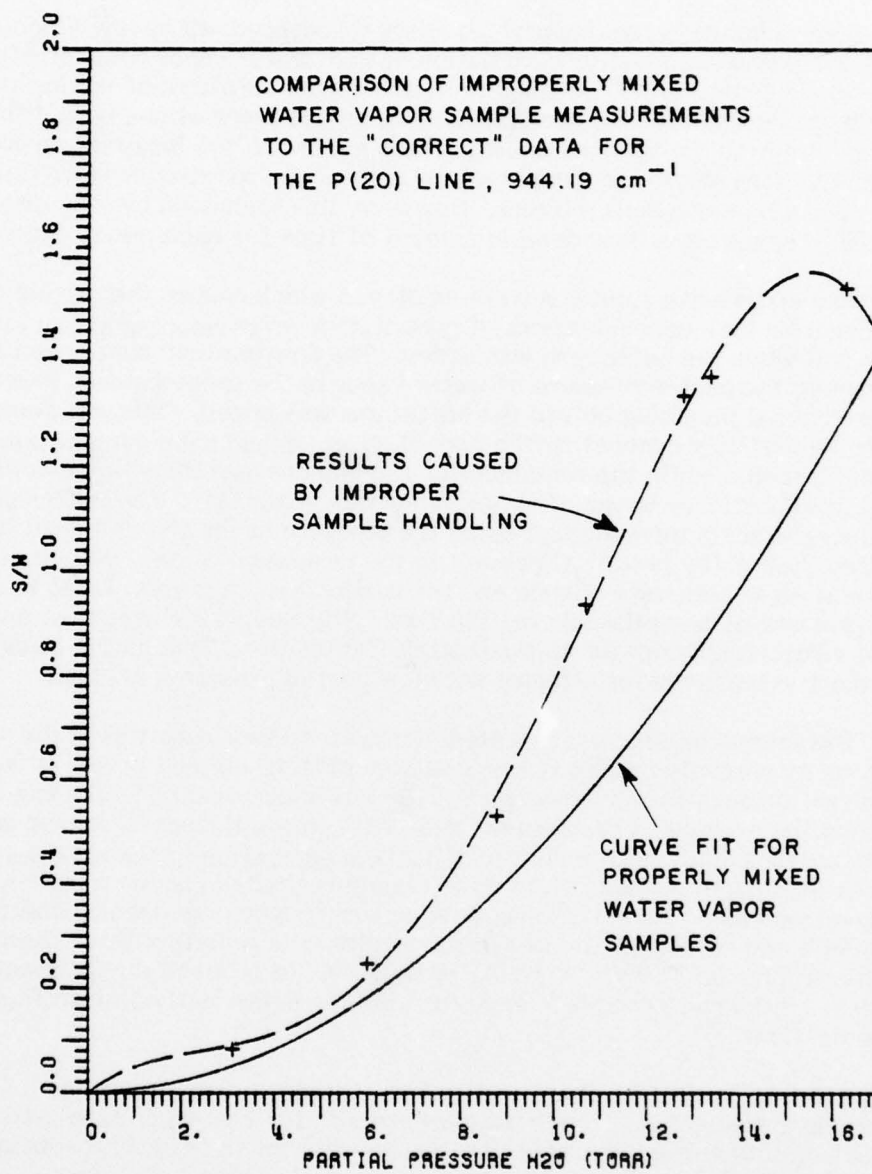


Figure 28. An illustration of the problems caused by incomplete sample mixing in the spectrophone.

Several solutions to this problem were discovered, all having a common basis - the prevention and/or elimination of high water vapor concentrations in the window adapters. The most obvious solution consisted of mixing the samples for extremely long periods of time, on the order of one hour. This resolved the problem by the simplest means available; the long mixing process eventually "stirred" up the sample at the ends of the spectrophone sufficiently to achieve a homogeneous mixture. However, this technique has the disadvantage of requiring a considerable amount of time for each measurement.

Two alternative solutions were employed which reduce the mixing time by preventing high concentrations of pure H_2O from developing at the ends of the cell when the buffer gas was added. The first method simply consisted of reducing the partial pressure of water vapor in the spectrophone, relative to the external plumbing before the buffer gas was added. This was accomplished by partially evacuating the pure H_2O which had been evaporated into the spectrophone, while the remainder of the vacuum system which contained the desired partial pressure of water vapor was valved off. The buffer gas was then gradually introduced, raising the pressure inside the cell until it equalled that of the pure H_2O present in the remainder of the system; at this point all valves were opened and the whole vacuum system filled to a total pressure of one atmosphere, 760 Torr. The sample gas was then mixed by the circulating pump for approximately 20 minutes. This method was used most extensively for samples with low partial pressures of H_2O .

The second technique prevented high water vapor densities in the spectrophone by partially mixing the new sample outside the cell before it was circulated through the spectrophone. This was accomplished by leaving the gas from the previous measurement valved off inside the spectrophone and mixing a new sample with a different H_2O concentration in the external plumbing. At this stage two uniformly mixed samples existed inside and outside the spectrophone. The final "new" sample was obtained by opening the valves to the cell and thoroughly mixing both samples by circulating them through the spectrophone. This final mixing was allowed to proceed for 20 minutes. This last method was used primarily for samples with relatively high H_2O concentrations.

After an initial set of absorption measurements were performed, the water vapor sample was frequently recirculated for 7 to 10 minutes and a new set of data taken. By repeating this process several times, it was confirmed that uniform mixing could be achieved with these techniques.

Four different buffer gases were used in this study; N_2O , 80-20 artificial air, 60-40 artificial air and O_2 . The 80% N_2 -20% O_2 and 60% N_2 -40% O_2 artificial air mixtures were obtained by mixing the appropriate percentages of pure N_2 and pure O_2 with water vapor according to methods described above. FTS spectra were taken of both the N_2 and O_2 gases as a test for the presence of contaminants. The nitrogen sample showed trace amounts of CO while the oxygen sample indicated trace amounts of both methane

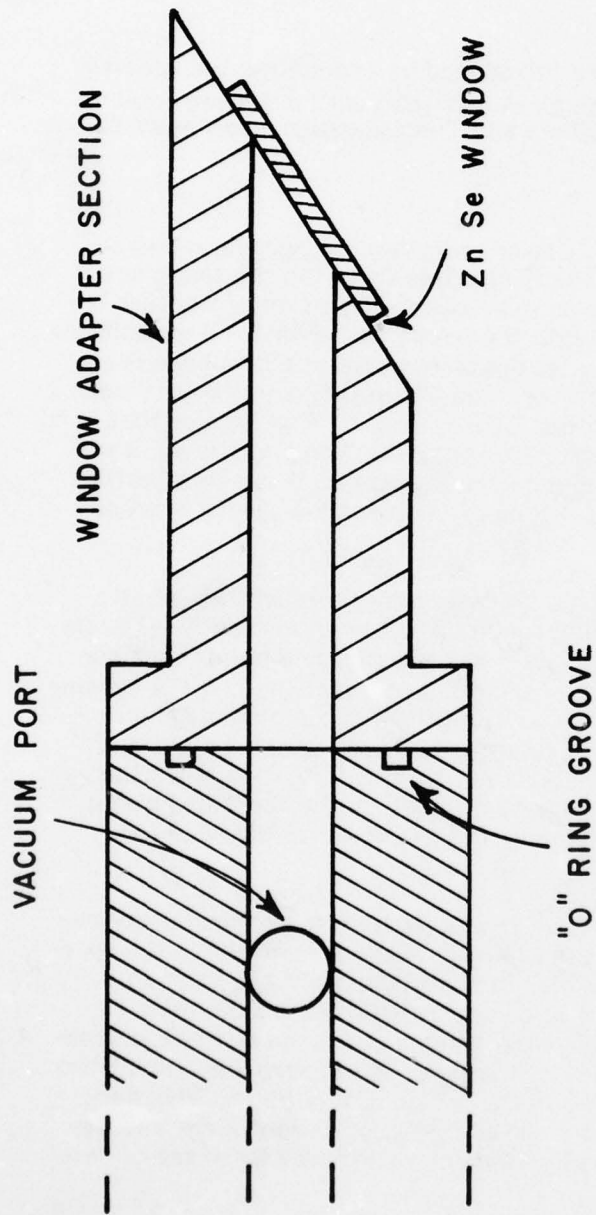


Figure 29. Sectional view at one end of the spectrophone.

AD-A058 631

OHIO STATE UNIV COLUMBUS ELECTROSCIENCE LAB

F/G 17/5

A STUDY OF WATER VAPOR ABSORPTION AT CO2 LASER FREQUENCIES USIN--ETC(U)

JUN 78 J C PETERSON

DAAG29-77-C-0010

UNCLASSIFIED

ESL-784701-2

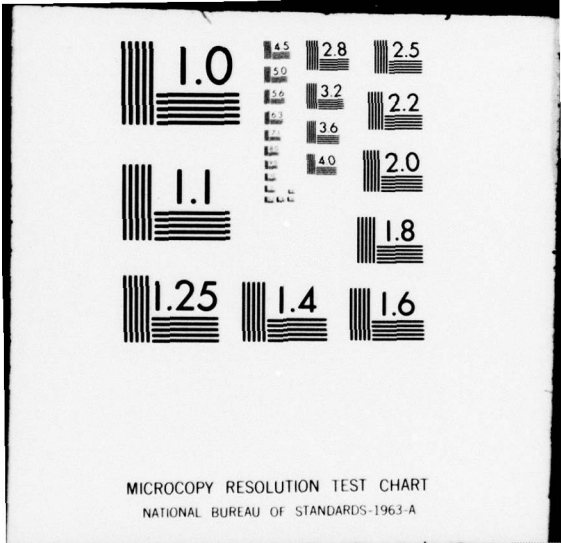
ARO-14702.1-6S

NL

2 OF 3

AD
A058631





and nitrous oxide. However, these contaminants do not have any strong absorption features in the spectral region of interest so that their presence is of no serious consequence. Previous workers⁶¹ have indicated a serious problem exists with ammonia contamination of water vapor samples; an FTS spectrum of the pure water vapor was taken to check for such contamination but the results were negative.

Pure water vapor samples were introduced by evacuating the spectrophone and evaporating H₂O from the glass test tube until a desired total pressure was read on the 0-10 " Wallace and Tiernan gauge, see Figure 22.

d. optical alignment

Accurate alignment of the CO₂ laser radiation through the spectrophone is essential for two reasons; the first arises from the relatively small diameter bore through which the beam must pass. Radiation contacting the walls will be absorbed or scattered with the result that additional undesirable background signal is produced. Finally, the differential spectrophone is essentially a very sensitive "window tester" (see Chapter III section B) which can detect small nonuniformities in the ZnSe windows. This implies that a constant and hence repeatable background window signal can be achieved only if a precision alignment technique is employed, i.e., it is essential that the laser beam pass through the same area of each window during a set of measurements.

The optical system used to align the laser beam through the spectrophone is schematically pictured in Figure 30. The two irises are fixed along the optical axis of the spectrophone and serve as reference points that define the desired path for the CO₂ laser beam. Accurate alignment is accomplished by imaging the laser radiation on a thermal screen placed behind an iris and adjusting mirrors M₃ and M₄ until the laser "spot" and iris are concentric. This condition can be determined by slowly closing down the iris diaphragm while observing the radiation image on the thermal screen; a concentric beam will produce a symmetric Fraunhofer diffraction pattern.

By using this alignment technique it was possible to perform measurements on several laser lines while the same sample was confined in the spectrophone. The procedure used here was to simply "switch" the laser to a nearby line and then fine "tune" the alignment with small adjustments to the micrometer grating drive. These adjustments consisted of small corrections for "play" in the grating mount micrometer drive mechanism and were made using the procedures described in the previous paragraph. This permitted three to four laser lines to be considered in one experiment and significantly reduced the amount of time required to obtain a large set of data at multiple frequencies.

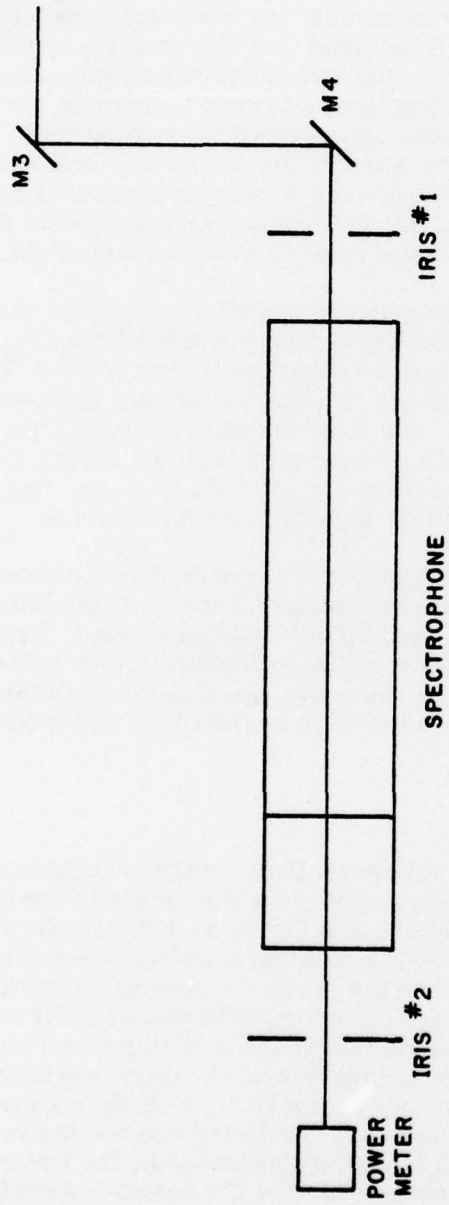


Figure 30. Schematic diagram of spectrophone alignment optics.

3. White cell measurements

a. optical alignment

The White cell measurements required that two separate alignments be maintained. The first and most difficult was the mirror alignment inside the multiple traversal cell. The mirror mounts are moderately unstable and required frequent readjustment. It is believed that this problem originates with low frequency building vibrations that induced minute displacements in the mirror mounts. A 100 mW Argon laser was used to monitor the cell alignment and to determine the adjustment required for realignment. This was accomplished by observing the location of the visible exit beam of the Argon laser on a white index card placed over the output window of the White cell. This technique provided a sensitive method for measuring even the slightest misalignment and was employed prior to every measurement.

Alignment of the CO₂ laser radiation to the White cell is the second requirement. This was accomplished by adjusting the path of the CO₂ radiation to retrace that of the Argon laser by using the thermal screen technique described in the previous section and two irises which are located along the optical path of the Argon laser. Again, it was possible to perform measurements at several frequencies (with a single sample in the absorption cell) by simply "fine tuning" the alignment of each CO₂ laser line through both irises with small adjustments to the grating drive micrometer.

Figure 31 shows a schematic drawing of external optics for these experiments. The signal disc calorimeter is located near the output window of the White cell and measures the transmitted CO₂ laser power. Before the laser beam enters the cell a portion of the incident radiation is reflected by a BaF₂ beam splitter into the Reference disk calorimeter. The transmission of each sample is proportional to the ratio of the signal and reference power meter voltages.

b. stability tests

In section A of Chapter III it was shown that a small uncertainty in the measurement of transmittance can produce a large error in the calculated value of the absorption coefficient, see Figure 4. In particular, for experiments where the transmittance is near 90%, a 1% error in the transmission measurement will produce a 10% error in the absorption coefficient. With the exception of those measurements performed at 975.9 cm⁻¹ all of the laser lines studied were highly transmitting, making the results extremely vulnerable to small experimental errors. A typical example is the nitrogen broadened water vapor data at the 10.6 μm P(20) line given in Table 3. The fourth column in this table gives relative uncertainty in the absorption coefficient as calculated from the equation (54); the last column gives the absolute error in the calculated value of the absorption coefficient for a hypothetical 1% error in the transmittance.

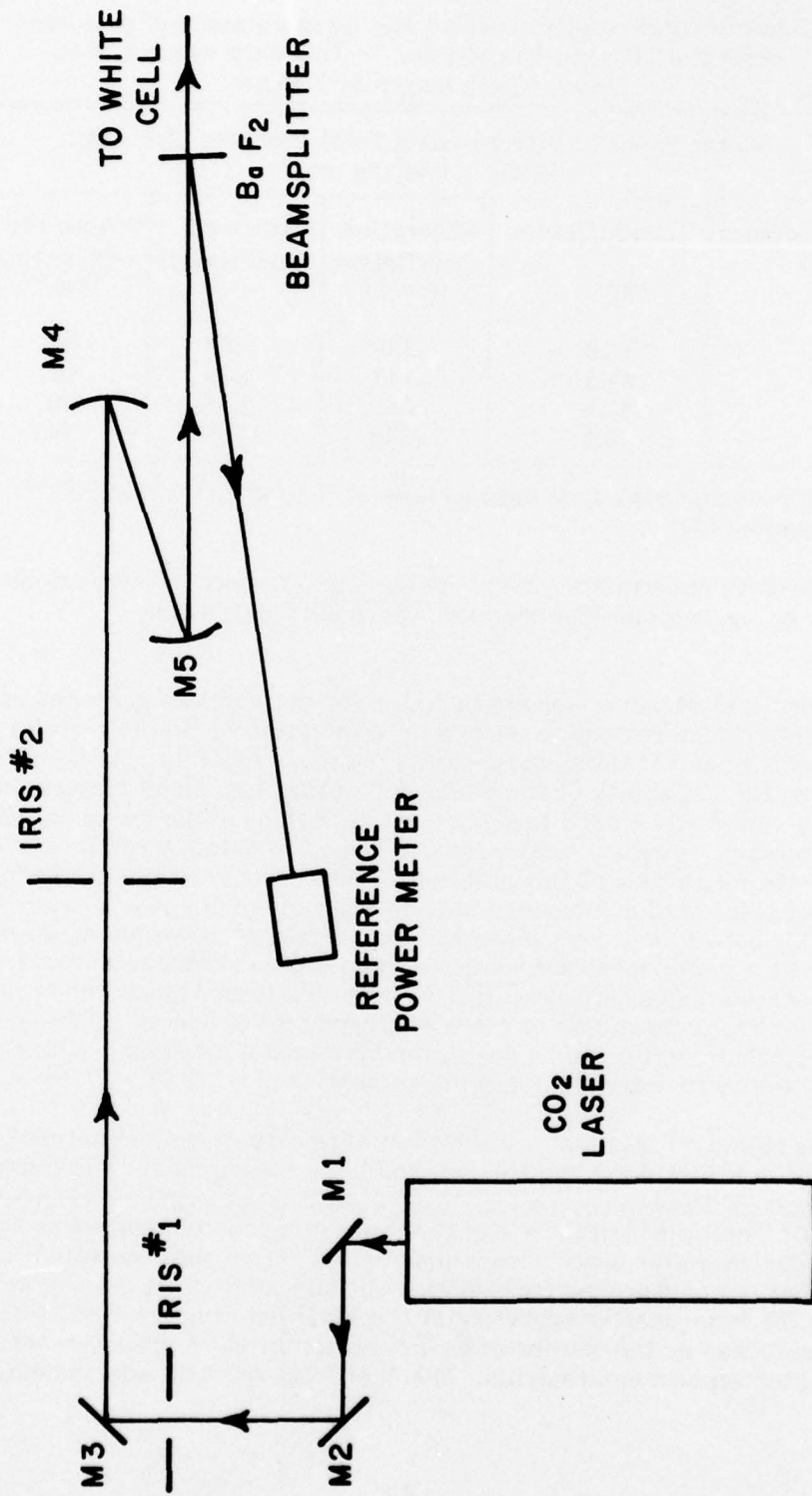


Figure 31. Entrance optics for the White cell experiments.

Table 3
 Experimental results of White cell measurements of pressure
 broadened H₂O at 944.194 cm⁻¹. This data was obtained
 using a path length of 1.46 km.

Water Vapor in Nitrogen at a Total Pressure of 1 Atm. P(20) 944.194 cm ⁻¹				
Partial Pressure of H ₂ O (Torr)	Transmittance (%)	Absorption Coefficient (km ⁻¹)	*Relative Uncertainty	**Absolute Error ($\Delta T/T \times 100 = 1.0$) (km ⁻¹)
15	71.8	.226	3.02	.007
12	80.8	.146	4.69	.007
9	87.5	.092	7.49	.007
6	94.3	.040	17.04	.007

* The relative uncertainty is defined here as $(\Delta k/k)/(\Delta T/T) = 1/\ln(T^{-1})$, see Equation (54)

** The absolute uncertainty given here assumes an error in the transmittance of 1.0%, i.e., we consider the case where $(\Delta T/T) \times 100 = 1.0$.

In order to obtain a meaningful value for the absolute accuracy of these experiments it is necessary to make a determination of the uncertainty in the transmittance. In these experiments the most apparent source of error came from the instability of the White cell optics, i.e., small changes in the alignment would correspond to significant variations in the measured value of transmission. Stability tests were performed to obtain a reasonable estimate of the magnitude of this problem. These tests consisted of performing a series of transmission measurements on a sample of N₂ over a seven-hour period; this corresponds very closely to the format of an actual experiment except that a single nonabsorbing gas sample was used for the entire test. With a nonabsorbing sample gas, the transmission values measured in this experiment are proportional to the background transmittance of the cell and therefore delimit (in some sense) the system stability and/or the experimenter's ability to maintain optical alignment.

The results of this test are shown in Figure 32 where the normalized transmission is plotted vs the time at which the measurement was performed. Five CO₂ laser lines in the 10.4 μm band were studied in the experiment. The use of "multiple" lines was employed because this technique was also used during the water vapor absorption studies. From these results it is observed that the background transmission varied less than 1% for the majority of lines; the large scatter occurring at the P(22) line (represented by the \diamond) is considered by this author to be unrepresentative of precision achieved in the water vapor measurements. The data from this test also indicated

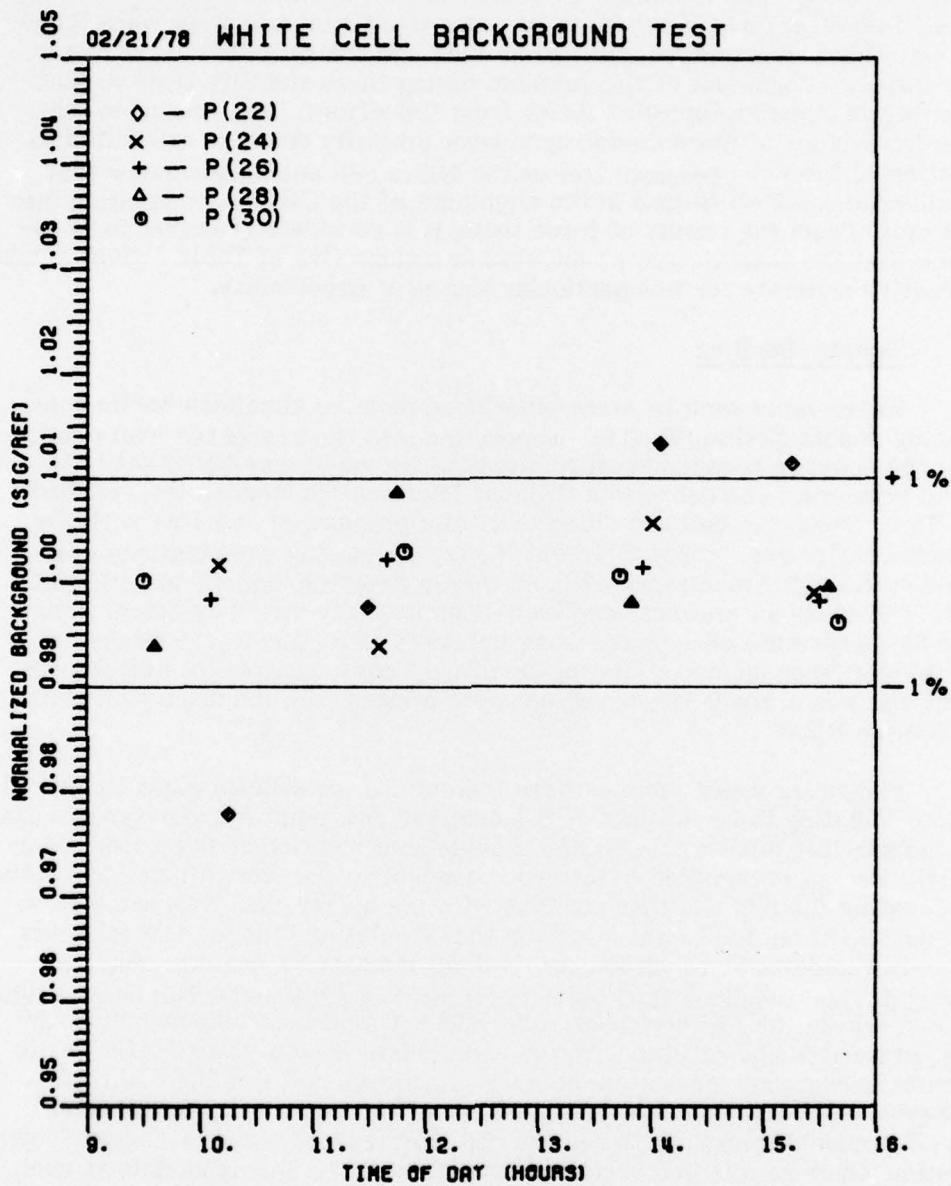


Figure 32. Normalized stability test results for the White cell at 1.1 km path length.

that the background transmission was dependent upon the intensity of a laser line. This effect was observed to be quite significant and steps were taken to maintain a constant laser power at each line during actual experiments. We were not cognizant of this problem during these stability tests so that the results given in Figure 32 suffer from this effect. It is presumed that the dependence of transmission upon laser intensity could be attributed to heating of the BaF₂ beamsplitter or the White cell entrance window that resulted in small variations in the alignment of the CO₂ laser radiation into the cell. From the results of these tests, it is considered reasonable to assume that the absolute error tabulated in column five of Table 3 gives a conservative estimate for this particular source of uncertainty.

C. Sample Handling

Water vapor samples were introduced from an aluminum bottle containing double distilled H₂O by evaporation into the evacuated White cell. For the pressure broadened experiments water vapor was added until the total pressure, recorded with a Gilmont Micrometric Manometer, reached 15 Torr. Then, the cell was filled to a total pressure of 760 Torr with the desired buffer gas. Three different N₂-O₂ broadening combinations were used in the experiments; pure N₂, 80-20 artificial air, and 60-40 artificial air. The 80-20 air was obtained from commercially mixed cylinders while the 60-40 samples were mixed using cylinders of N₂ and O₂. FTS spectra of sample gases indicated that no significant contaminants (having absorption features in the 9-10 μm region) were present, see the discussion given in section B.2.c.

The water vapor samples were then mixed for at least eight hours with two circulating fans. An E.G. & G Model 880 dew point hygrometer was used to monitor the mixing process and provide confirmation of the water vapor partial pressure. Smaller water vapor concentrations were studied by partially evacuating the cell and then refilling with the buffer gas. New samples obtained by this method were mixed by the circulating fans for several hours or until the dew point hygrometer readings indicated a homogeneous gas. By using this technique H₂O partial pressures of 12, 9 and 6 Torr were studied in addition to the 15 Torr case. After the 6 Torr measurements the White was evacuated and refilled with the appropriate nonabsorbing buffer gas to permit background measurements. This last step, refilling the cell, is extremely important because the alignment of the White cell optics varies as a function of pressure. When the cell is evacuated there is a slight "bowing" motion which results in a vertical translation of the mirror mounts at each end. This motion causes the CO₂ laser radiation to fall on entirely different areas of each mirror, so that a transmission measurement with the cell evacuated does not represent a good model for determining the background in the pressure broadened studies which were performed at 1 atmosphere.

Pure water vapor samples were also introduced by evaporation into the evacuated White cell. Before the H₂O was added, background measurements were taken with the cell under vacuum. Following these measurements water vapor was added until the White cell contained the smallest

desired pressure and at this point transmission measurements were performed on the sample. After the first set of measurements, more water was evaporated into the cell and the process repeated until the final and highest concentration was reached.

CHAPTER V RESULTS

In this chapter the results from spectrophone and White cell measurements of water vapor absorption will be presented. The first section deals exclusively with the data obtained from the stainless steel differential spectrophone. These measurements include pressure broadened studies in which four different forms of artificial air were used as a buffer gas. Also presented are the results from experiments on the temperature dependence of line and continuum absorption at the 10.4 μm R(20), P(16), and P(20) laser lines. This data was obtained by using the temperature control capability of the spectrophone which was described in Chapter III. This section concludes with the presentation of a method for spectrophone measurements of pure water vapor absorption including some of the preliminary results obtained by this new technique.

The second half of this chapter consists of a comparison, where possible, of the spectrophone results with those obtained from the White cell experiments. This includes both the pressure broadened and pure water vapor data. A comparison of all these results with data from other workers is left to Chapter VI.

A. Spectrophone Study of Water Vapor

In these studies triple distilled H_2O was evaporated from a pyrex glass test tube into the stainless steel spectrophone vacuum system. Absorber concentration for the pure H_2O samples was determined with a 0-10" H_2O mechanical pressure gauge ($1'' \text{H}_2\text{O} = 1.87 \text{ Torr}$). Pressure broadened samples were mixed with a stainless steel circulating pump and the water vapor partial pressure measured with a dew point hygrometer. Calibration of the spectrophone signal was based upon White cell data from nitrogen broadened water vapor measurements with the R(20) CO_2 laser line at 975.93 cm^{-1} .

1. Artificial Air Broadened Samples

The buffer gases for these experiments were obtained by mixing nitrogen and oxygen in the designated ratios. Different percentages of N_2 and O_2 were considered to discover whether nitrogen alone is adequate for modeling water vapor absorption as it occurs in the atmosphere. In the past⁶² it has often been assumed reasonable to simply use nitrogen as the broadening gas since it comprises nearly 80% of the atmosphere and neither it nor oxygen are infrared active. The results of these measurements indicate that a detectable difference in the $\text{H}_2\text{O}-\text{N}_2$ and $\text{H}_2\text{O}-\text{O}_2$ interactions exists. The effects of oxygen will be further analyzed in Chapter VI, where the results to be presented here are discussed. Those interested only in the final results of this study are directed to pages 188 through 193 where the curve fit coefficients for the experimental data are listed in Tables 5 through 12.

a. 100% N₂

The first set of pressure broadened data consists of H₂O in N₂ absorption measurements at a total pressure of 760 Torr. These results are presented in Figures 33 through 55 and represent measurements performed at 23 CO₂ laser lines in the 9 (centered at 9.4 μm - 1064 cm⁻¹) and 10 (centered at 10.4 μm - 962 cm⁻¹) μm bands. The appropriate frequency position is denoted at the top of each plot. The temperature of the spectrophone, recorded by a Stow Lab electronic thermometer, is also given in these figures. This temperature represents an average of the values recorded during each experiment. The spectrophone was in thermal equilibrium with the laboratory air and its temperature drifted approximately ± 0.5°C. In these plots the partial pressure of water vapor in Torr is given by the abscissa (760 Torr = 1 atm) and the absorption coefficient in km⁻¹ is given by the ordinate. The square boxes indicate the measured data points, while the dashed line represents the best fit of these data to an equation of the form $k = Ap + Bp^2$, where k is the absorption coefficient in km⁻¹ and p is the partial pressure of water in Torr. An exception is made for the R(20) line at 975.93 cm⁻¹ where the data has been fit to a linear equation $k = Ap$. These same curve fit equations will be used for all the pressure broadened data presented in this chapter. This particular choice of equations is based on the theoretical development presented in Chapter II and will be discussed further in Chapter VI.

b. Calibration for N₂-O₂ mixtures

As was previously stated, the calibration of the spectrophone is based upon nitrogen broadened water vapor absorption data at the R(20) line 975.93 cm⁻¹. In the following experiments, the nature of the buffer gas will no longer be the same as that used in the calibration measurements. This makes it necessary to investigate the possible need for corrections in the calibration constant as the percentages of nitrogen and oxygen are varied. To see what is required here, it is necessary to go back and consider Equation (85)

$$(V_{\text{sig}}^F)_{\text{RMS}} = \frac{\sqrt{2} V_o}{\pi [1 + (\omega\tau)^2]^{\frac{1}{2}}} \quad (85)$$

which describes the RMS pressure signal. Substituting into this equation the appropriate terms for V_o and τ we obtain

$$(V_{\text{sig}}^F)_{\text{RMS}} \sim V_o \frac{\bar{v}}{C_v} \quad (95)$$

where \bar{v} is the specific volume

and C_v is the specific heat at constant volume of the sample gas.

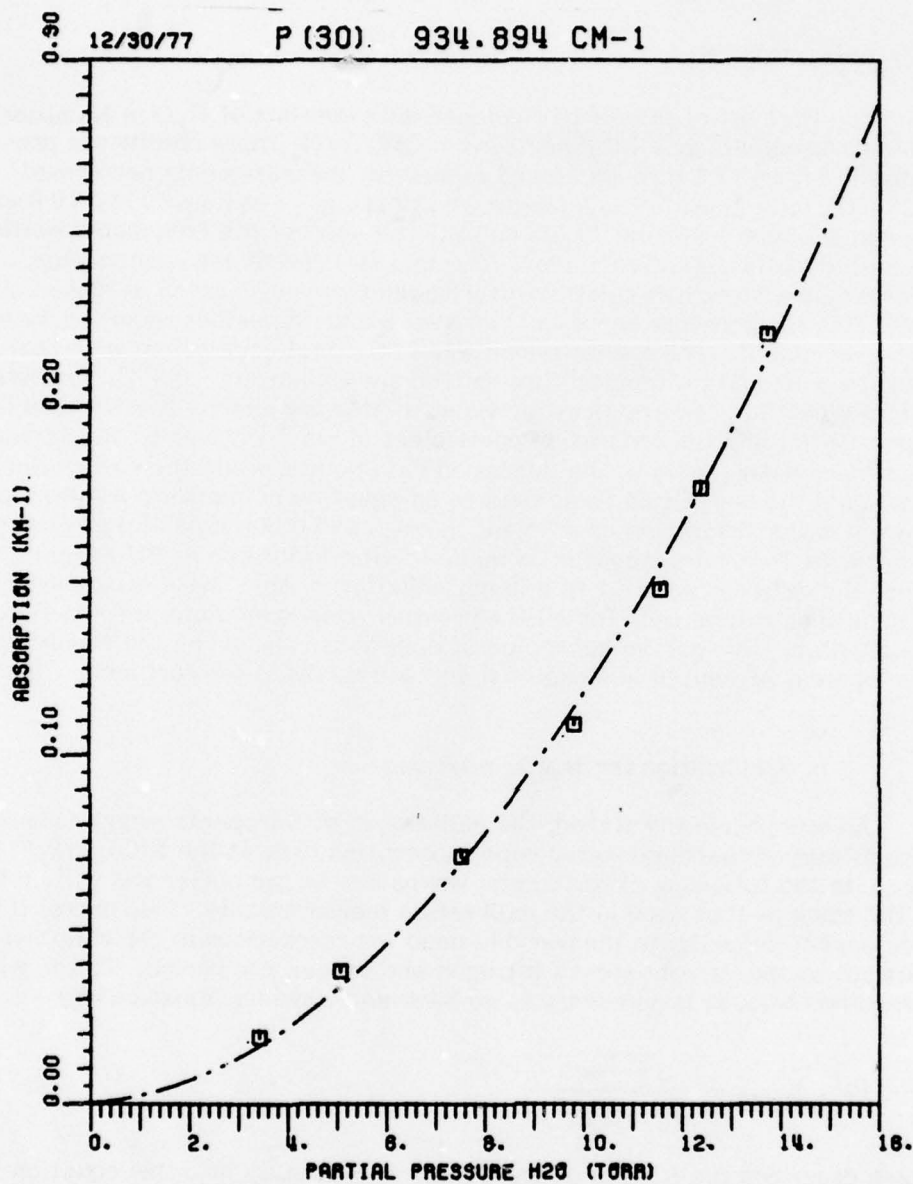


Figure 33. Measured H₂O in N₂ absorption coefficient at a total pressure of 760 Torr for the P(30) CO₂ laser line at 934.894 cm⁻¹. Average spectrophone temperature was 24.5°C.

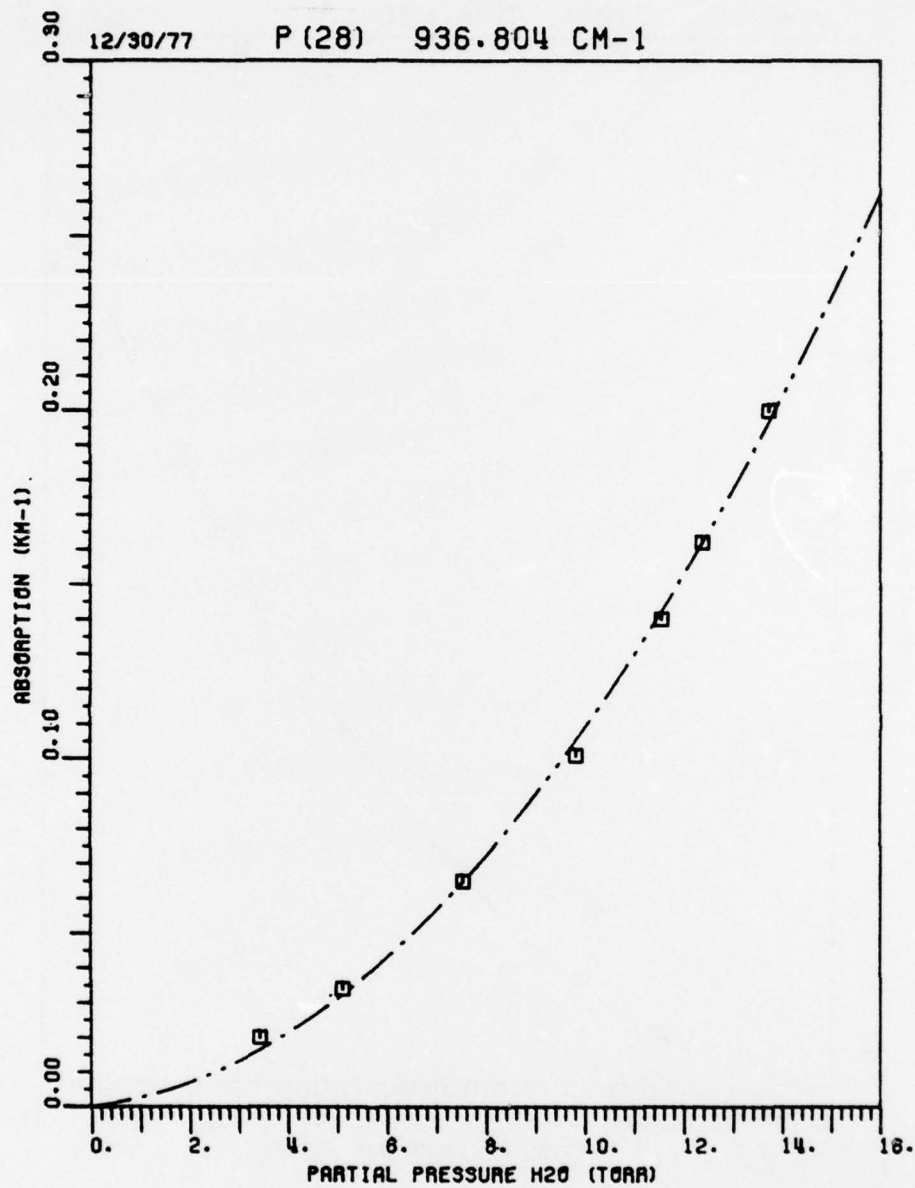


Figure 34. Measured H₂O in N₂ absorption coefficient at a total pressure of 760 Torr for the P(28) CO₂ laser line at 936.804 cm⁻¹. Average spectrophone temperature was 24.5° C.

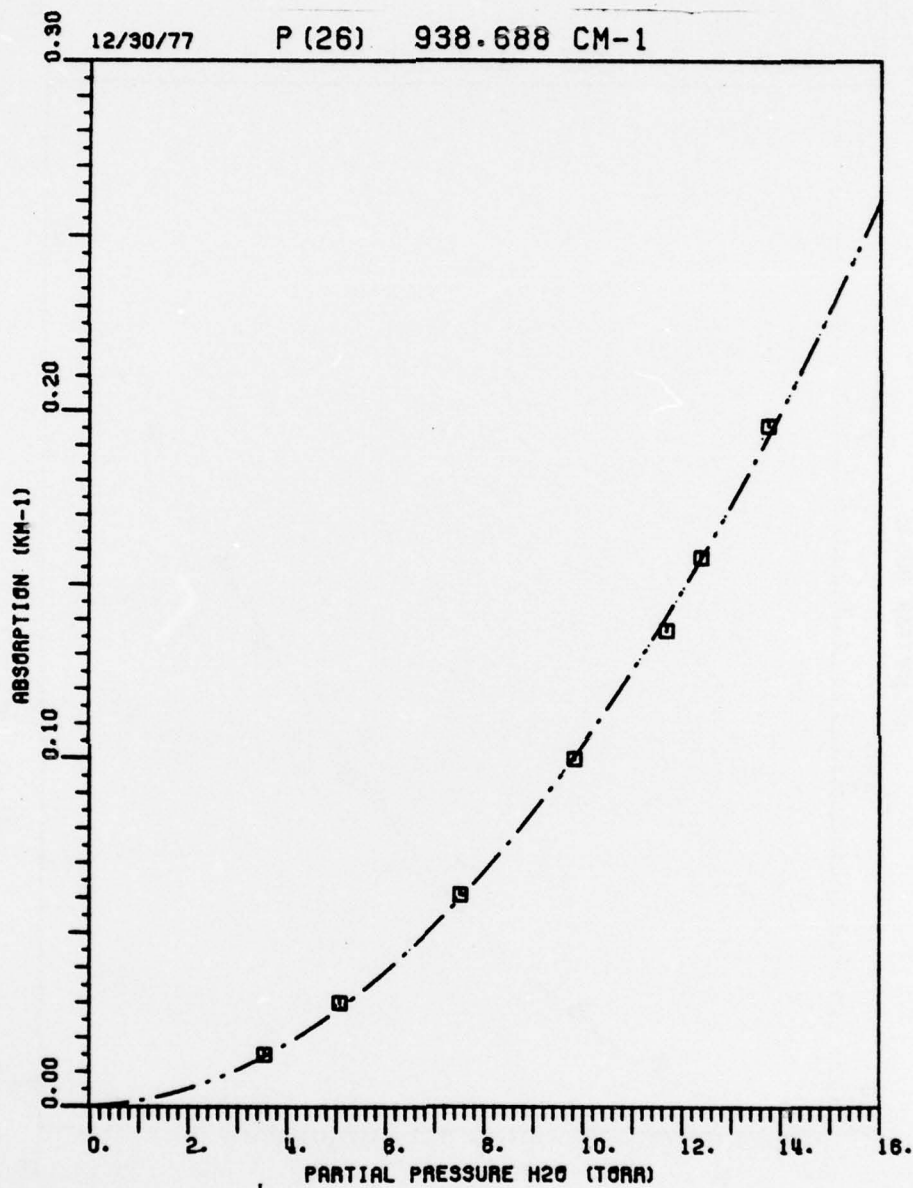


Figure 35. Measured H₂O in N₂ absorption coefficient at a total pressure of 760 Torr for the P(26) CO₂ laser line at 938.688 cm⁻¹. Average spectrophone temperature was 24.5 C.

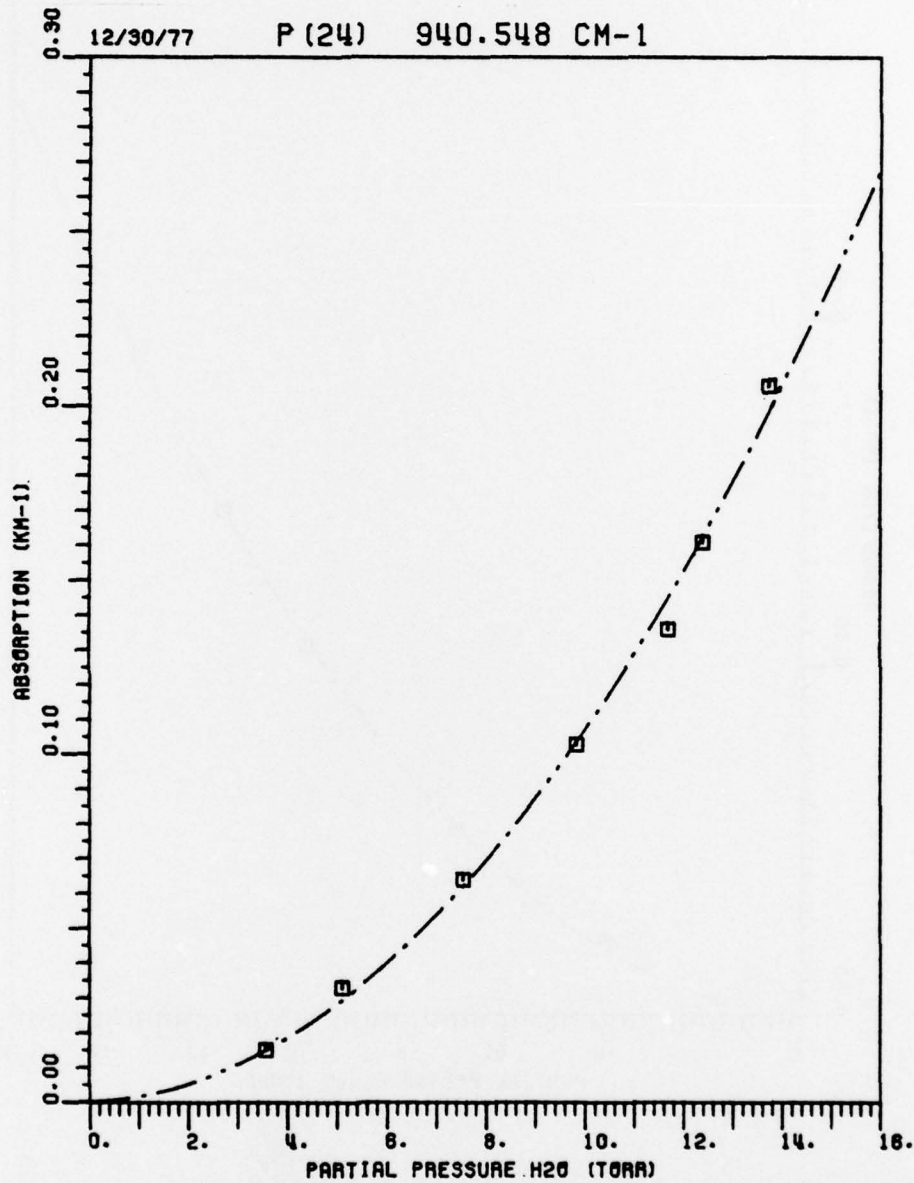


Figure 36. Measured H₂O in N₂ absorption coefficient at a total pressure of 760 Torr for the P(24) CO₂ laser line at 940.548 cm⁻¹. Average spectrophone temperature was 24.5 °C.

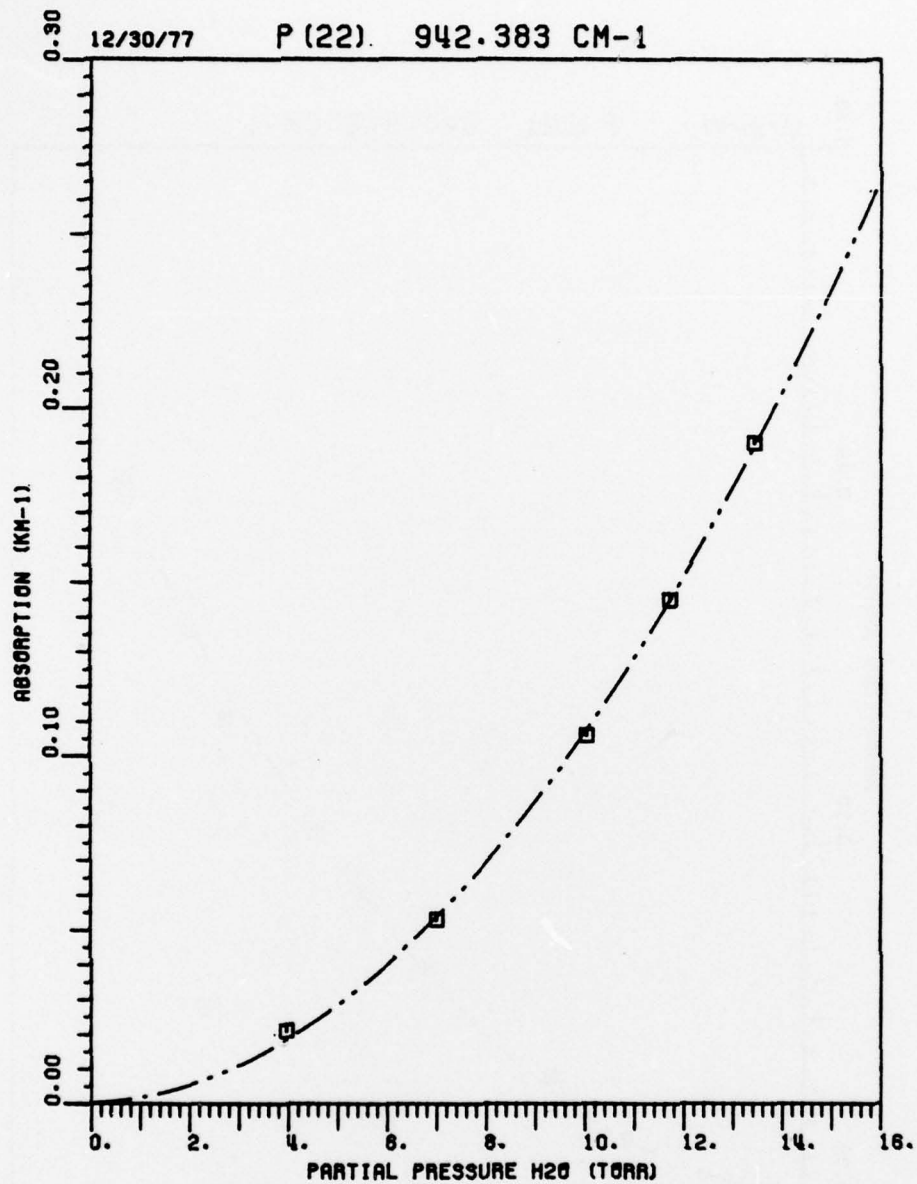


Figure 37. Measured H₂O in N₂ absorption coefficient at a total pressure of 760 Torr for the P(22) CO₂ laser line at 942.383 cm⁻¹. Average spectrophone temperature was 24.5° C.

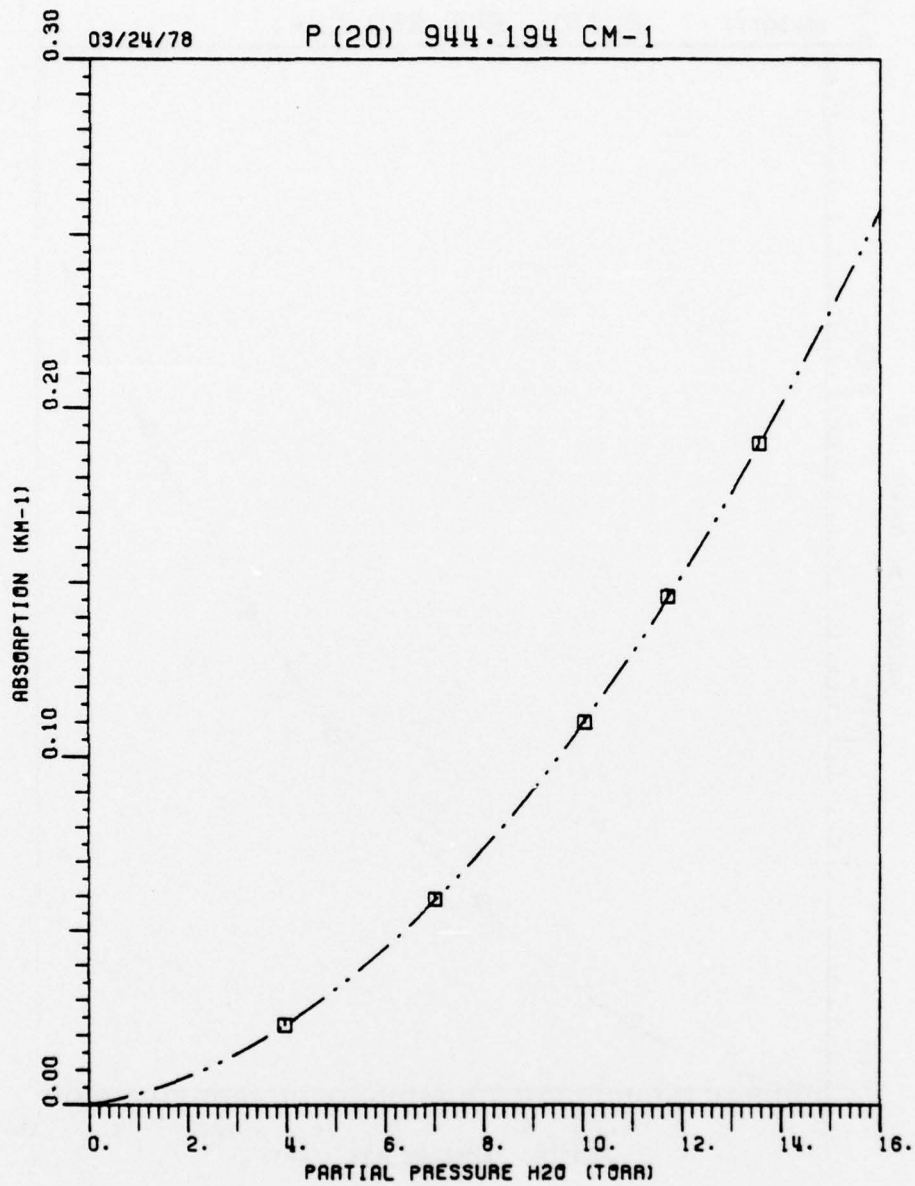


Figure 38. Measured H₂O in N₂ absorption coefficient at a total pressure of 760 Torr for the P(20) CO₂ laser line at 944.194 cm⁻¹. Average spectrophone temperature was 23.5°C.

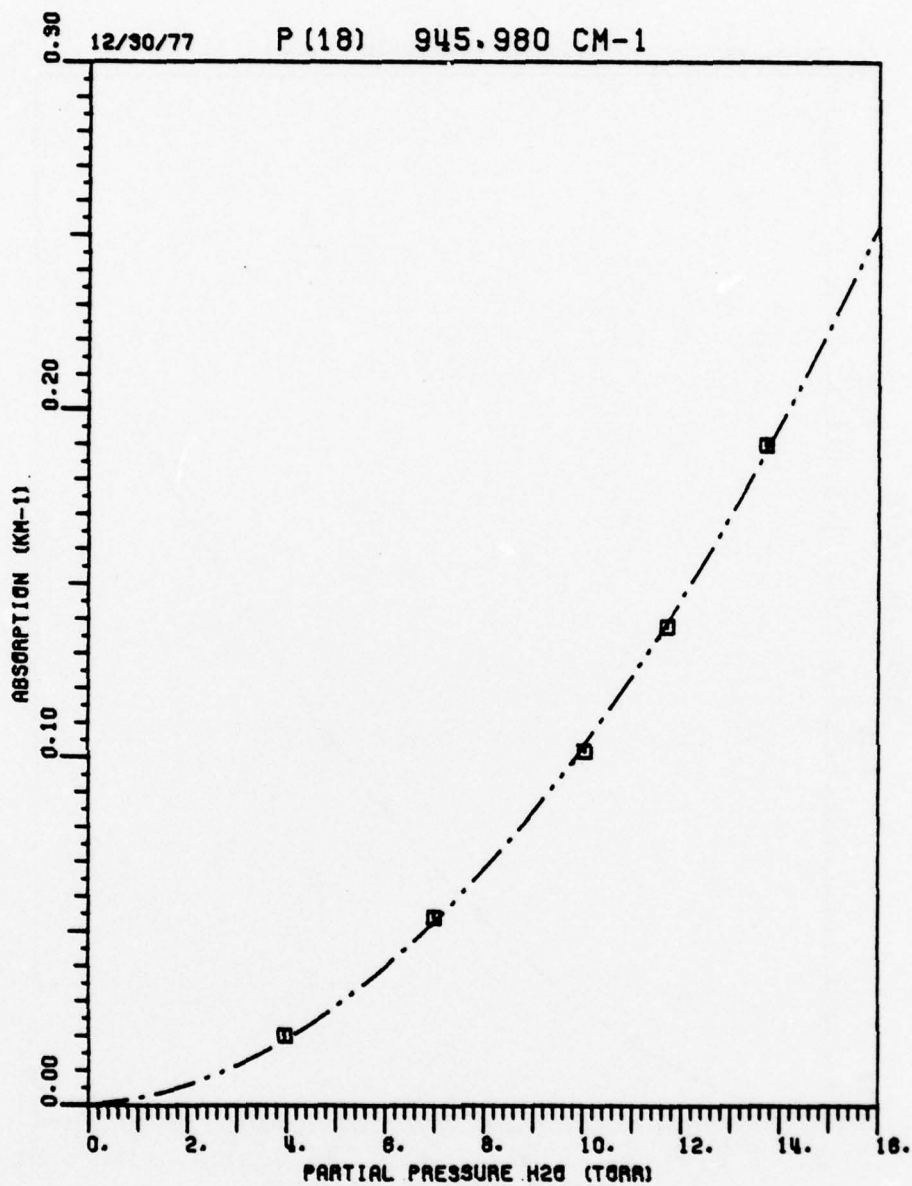


Figure 39. Measured H₂O in N₂ absorption coefficient at a total pressure of 760 Torr for the P(18) CO₂ laser line at 945.980 cm⁻¹. Average spectrophone temperature was 24.5°C.

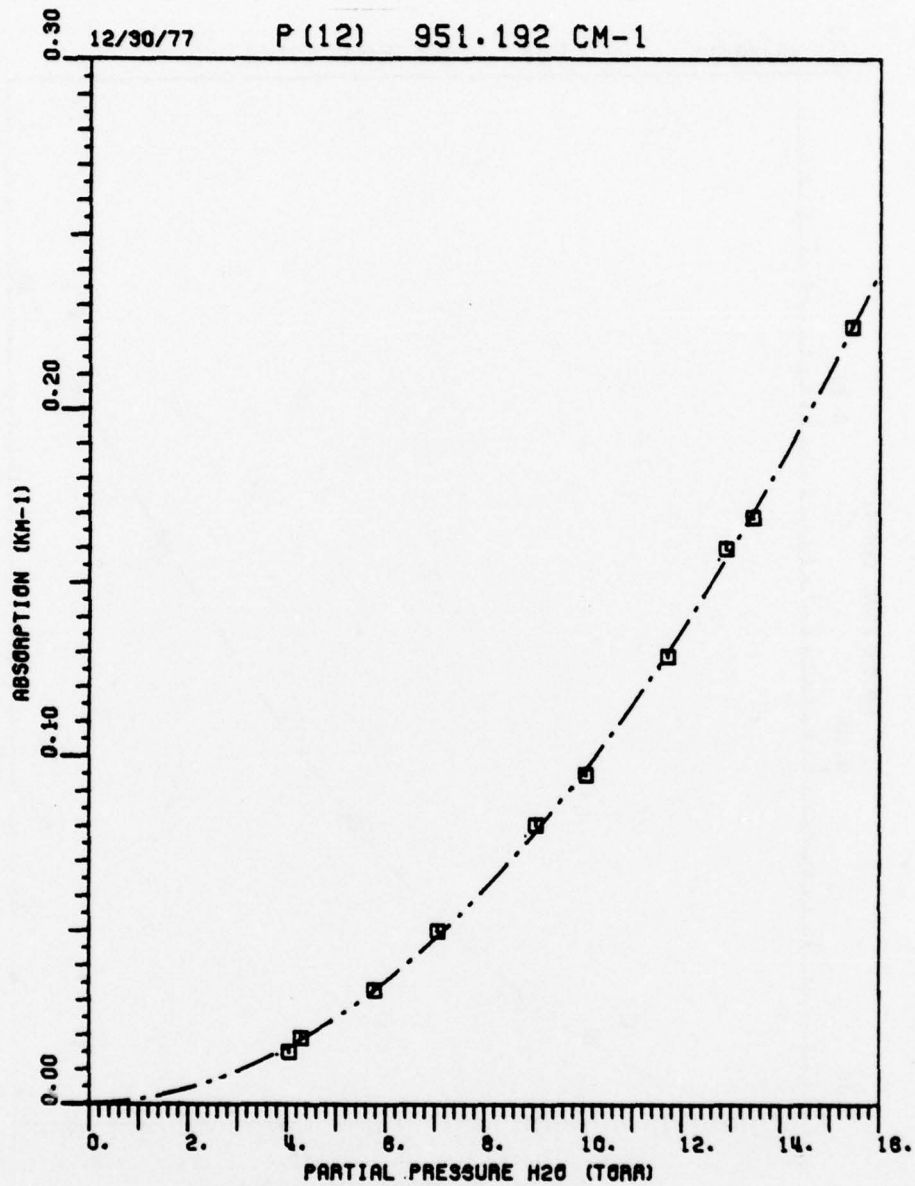


Figure 40. Measured H₂O in N₂ absorption coefficient at a total pressure of 760 Torr for the P(12) CO₂ laser line at 951.192 cm⁻¹. Average spectrophone temperature was 24.5°C.

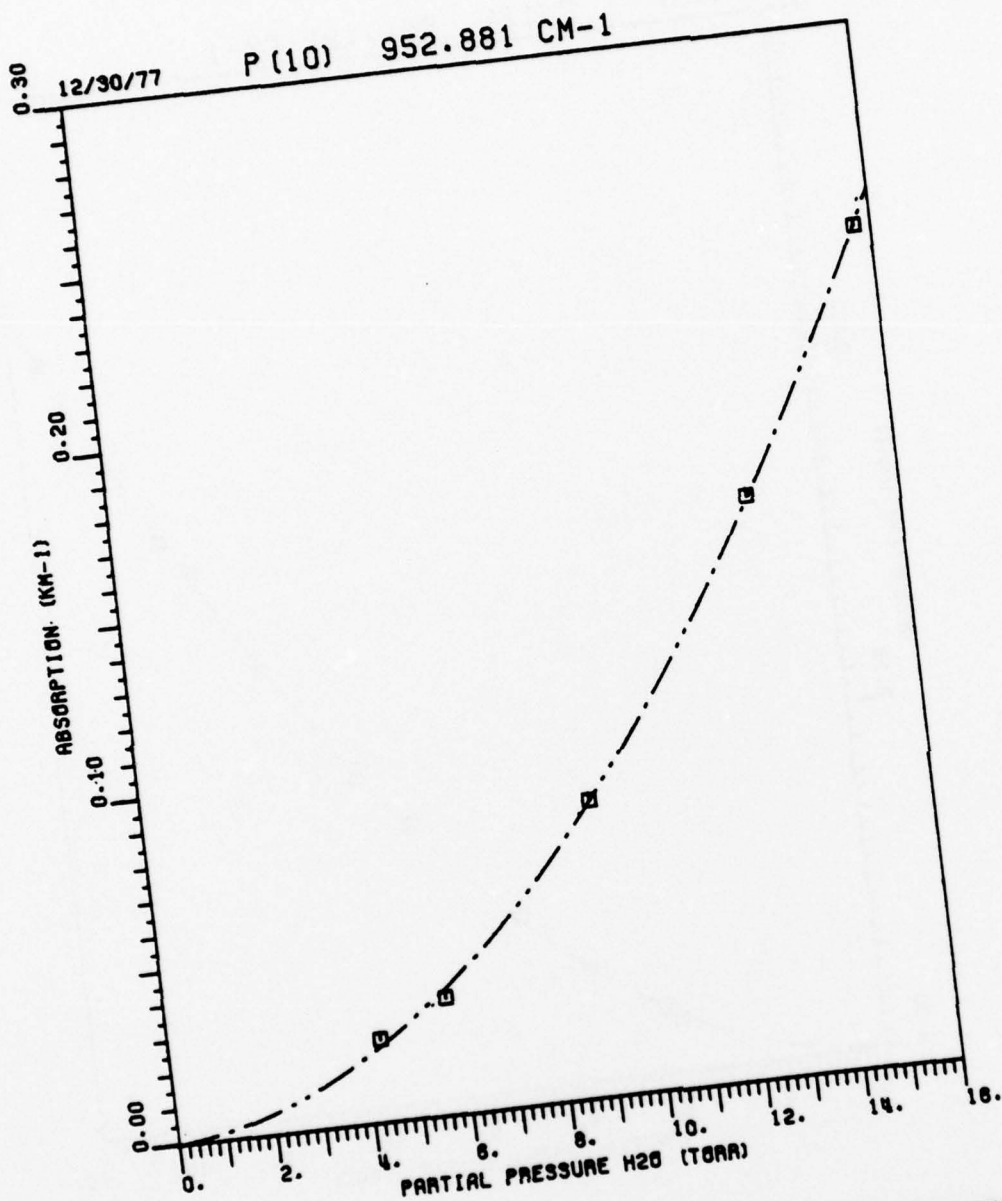


Figure 41. Measured H₂O in N₂ absorption coefficient at a total pressure of 760 Torr for the P(10) CO₂ laser line at 952.881 cm⁻¹. Average spectrophone temperature was 24.5°C.

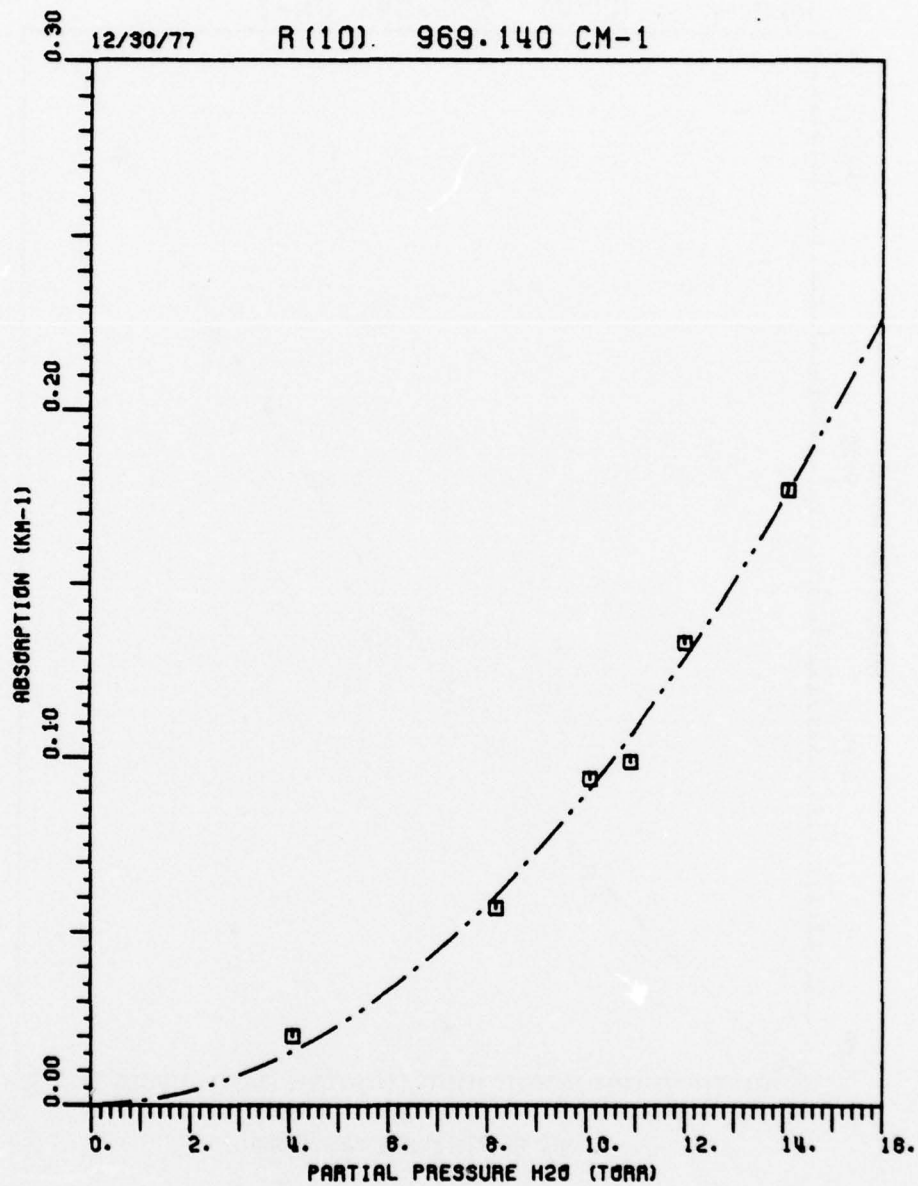


Figure 42. Measured H₂O in N₂ absorption coefficient at a total pressure of 760 Torr for the R(10) CO₂ laser line at 969.140 cm⁻¹. Average spectrophone temperature was 24.5°C.

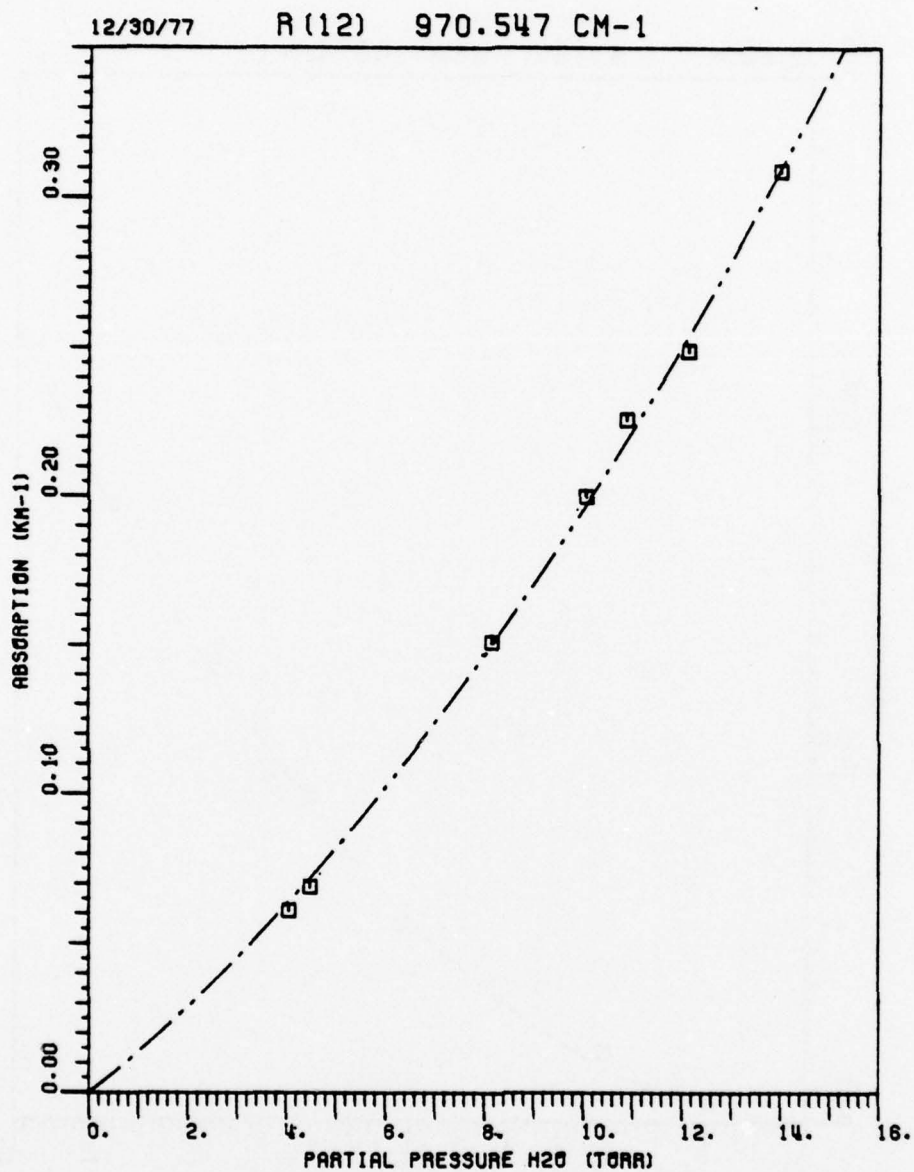


Figure 43. Measured H₂O in N₂ absorption coefficient at a total pressure of 760 Torr for the R(12) CO₂ laser line at 970.547 cm⁻¹. Average spectrophone temperature was 24.5°C.

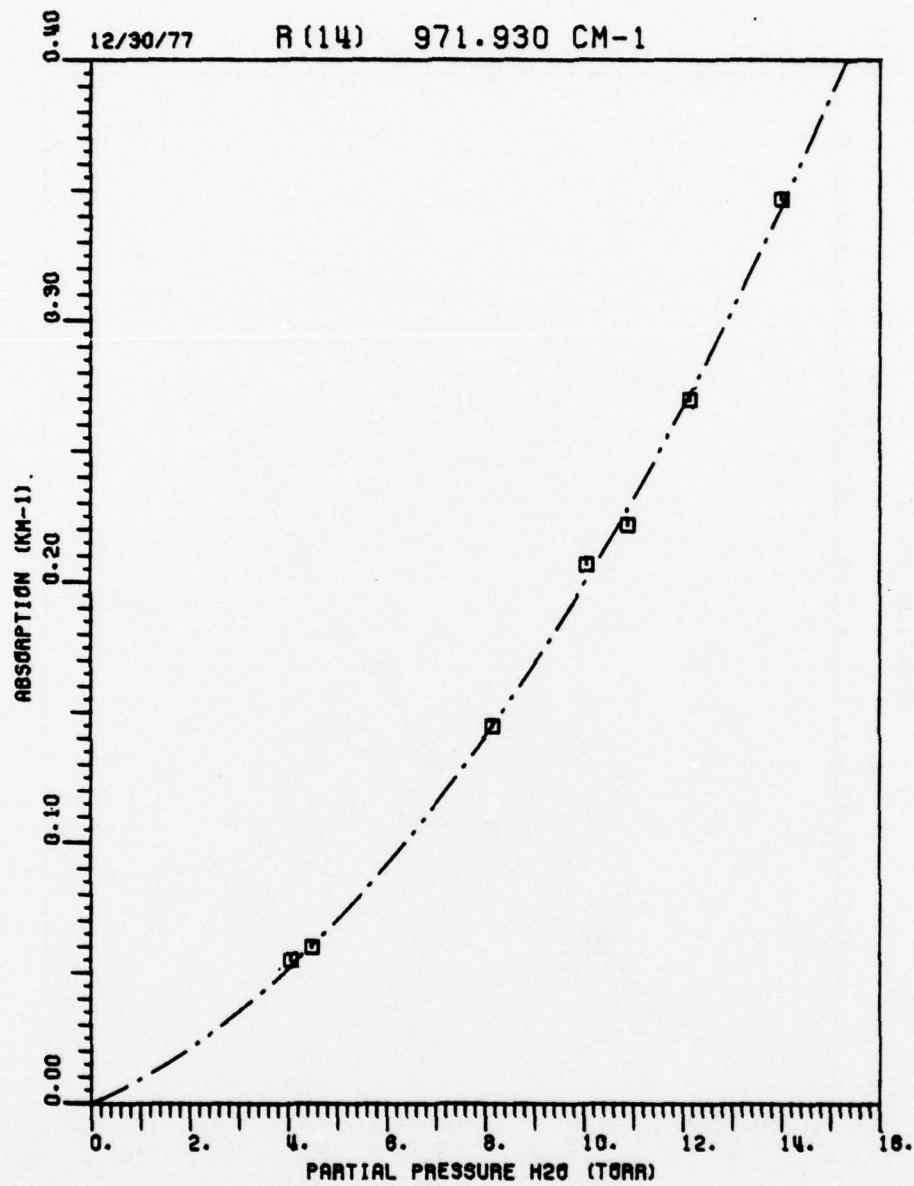


Figure 44. Measured H₂O in N₂ absorption coefficient at a total pressure of 760 Torr for the R(14) CO₂ laser line at 971.930 cm⁻¹. Average spectrophone temperature was 24.5°C.

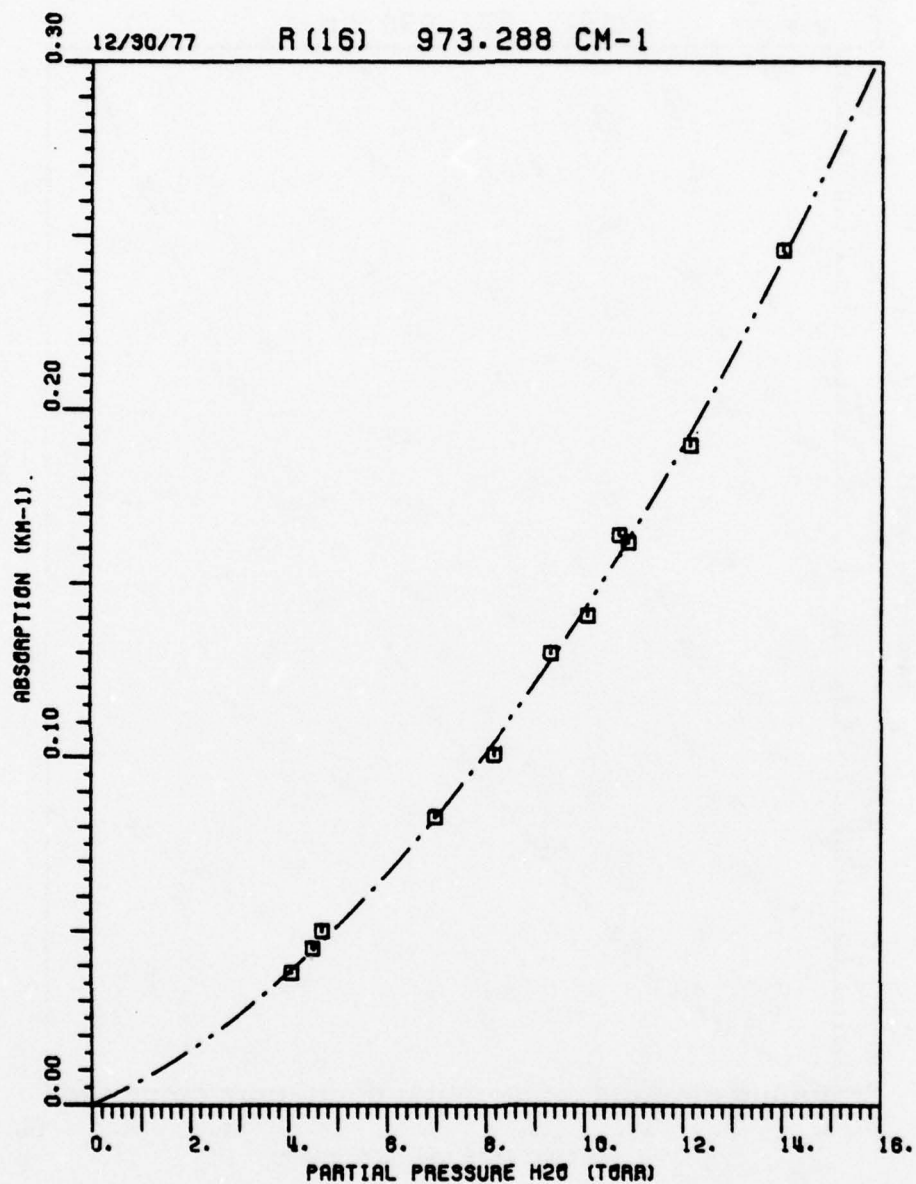


Figure 45. Measured H₂O in N₂ absorption coefficient at a total pressure of 760 Torr for the R(16) CO₂ laser line at 973.288 cm⁻¹. Average spectrophone temperature was 24.5°C.

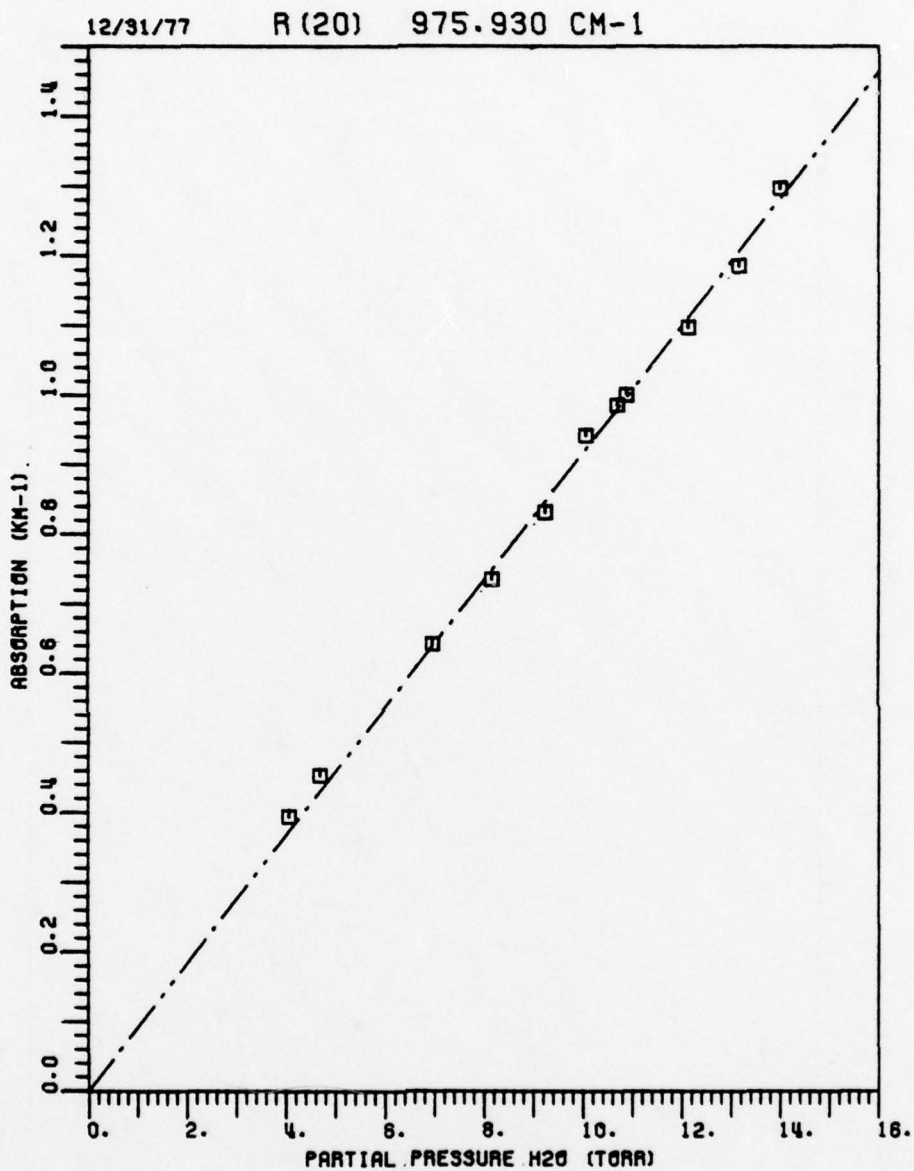


Figure 46. Measured H₂O in N₂ absorption coefficient at a total pressure of 760 Torr for the R(20) CO₂ laser line at 975.930 cm⁻¹. Average spectrophone temperature was 22.5°C.

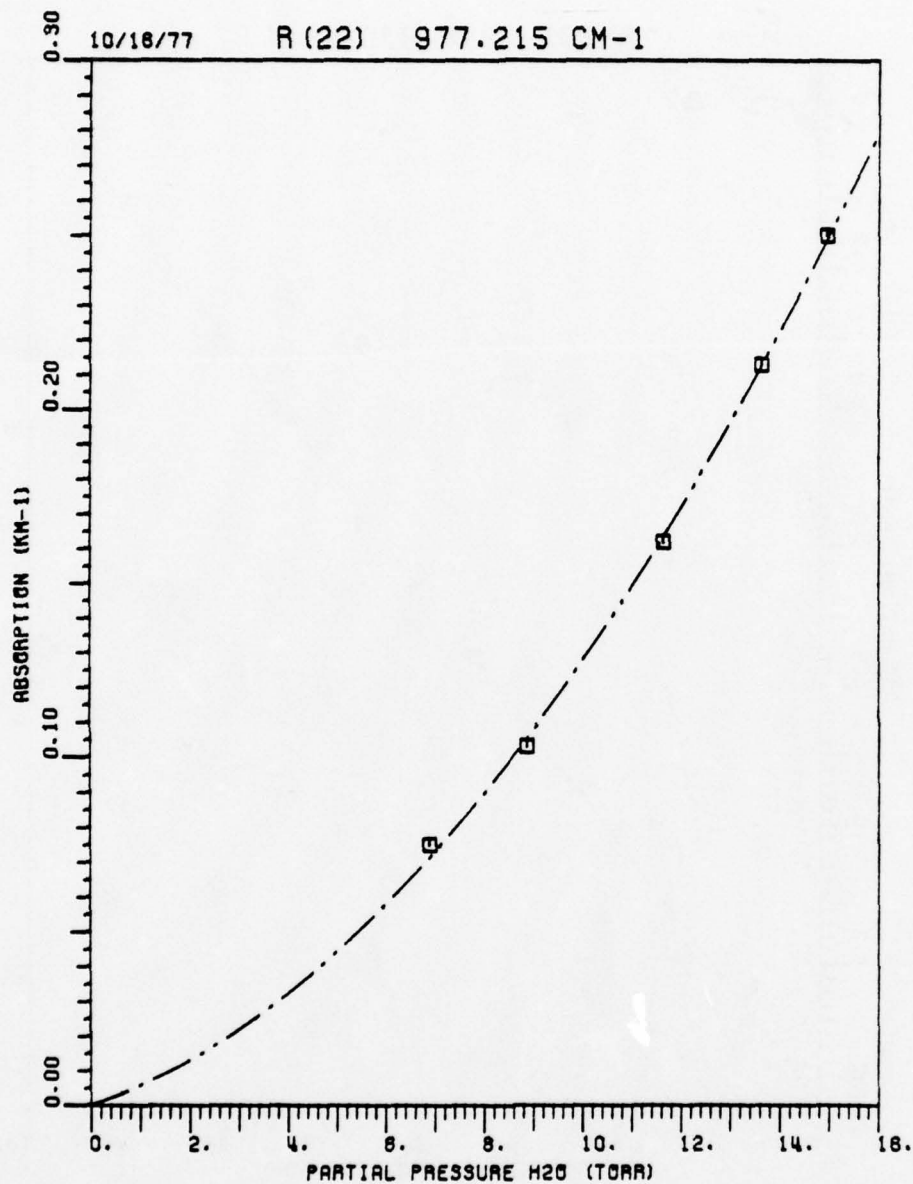


Figure 47. Measured H₂O in N₂ absorption coefficient at a total pressure of 760 Torr for the R(22) CO₂ laser line at 977.215 cm⁻¹. Average spectrophone temperature was 25°C.

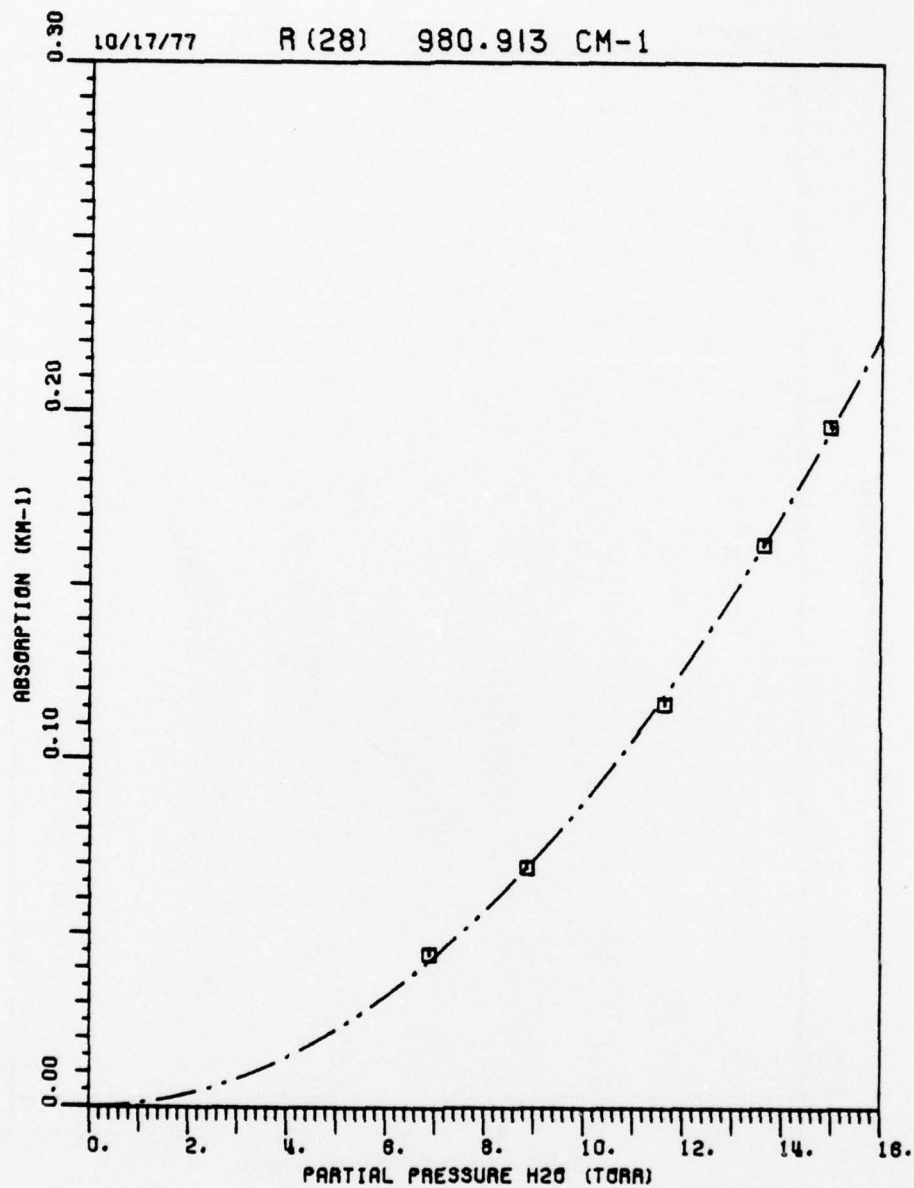


Figure 48. Measured H₂O in N₂ absorption coefficient at a total pressure of 760 Torr for the R(28) CO₂ laser line at 980.913 cm⁻¹. Average spectrophone temperature was 25°C.

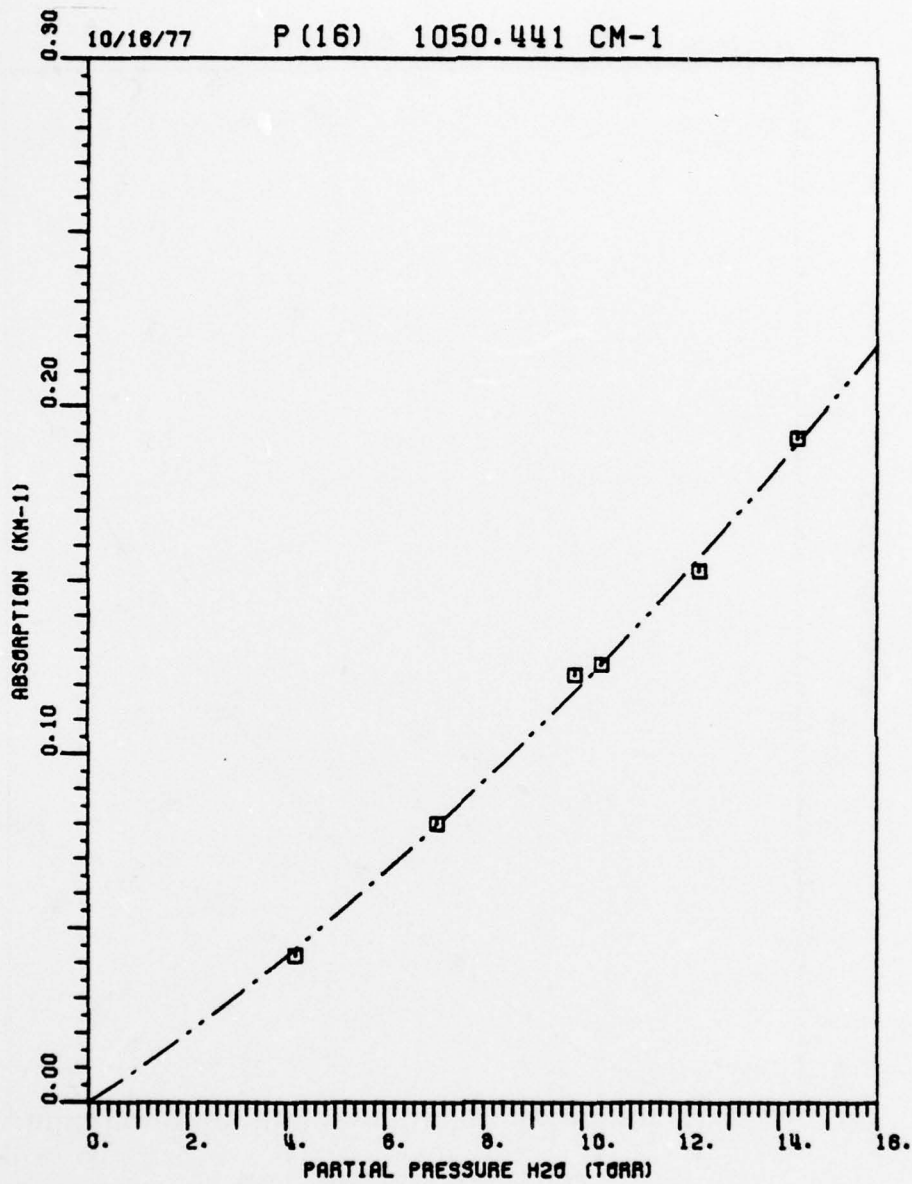


Figure 49. Measured H₂O in N₂ absorption coefficient at a total pressure of 760 Torr for the P(16) CO₂ laser line at 1050.441 cm⁻¹. Average spectrophone temperature was 23.5°C.

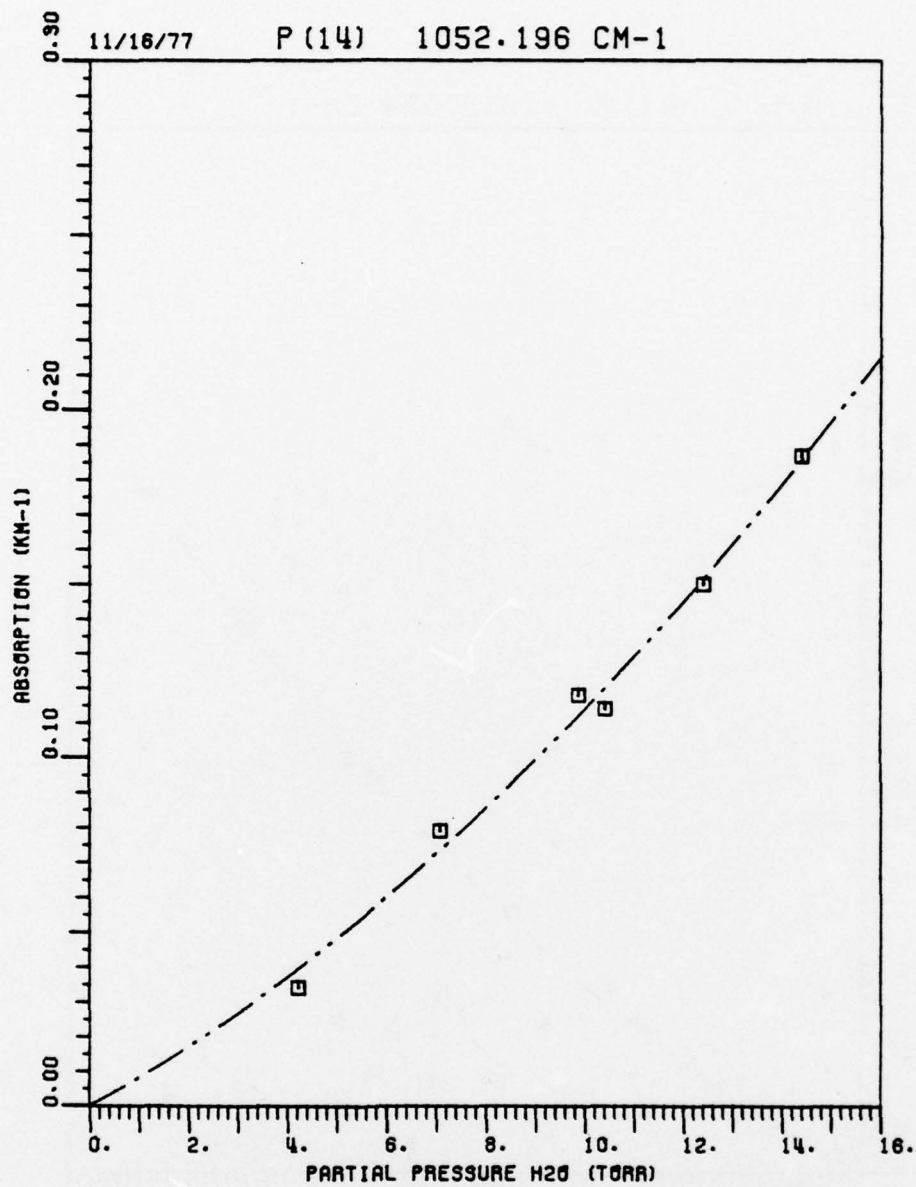


Figure 50. Measured H₂O in N₂ absorption coefficient at a total pressure of 760 Torr for the P(14) CO₂ laser line at 1052.196 cm⁻¹. Average spectrophone temperature was 23.5°C.

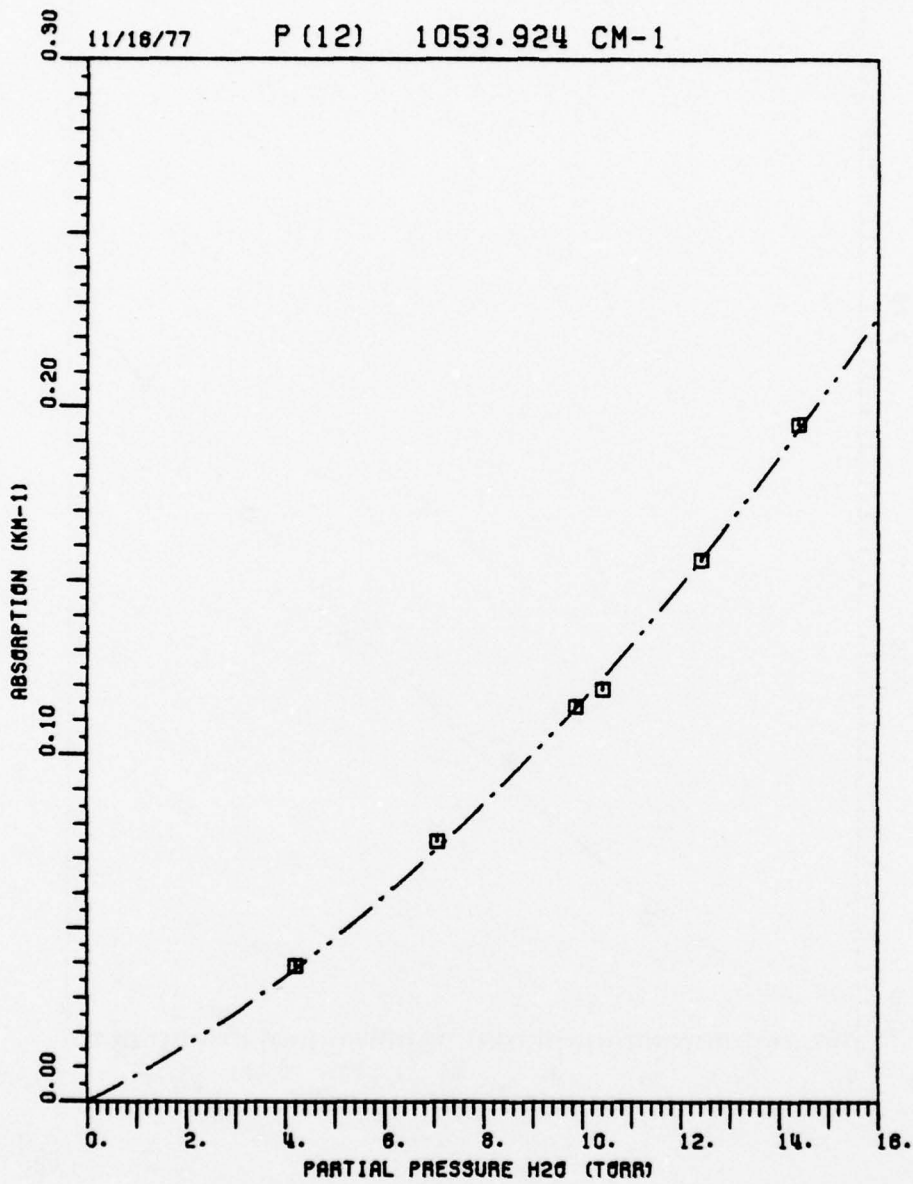


Figure 51. Measured H₂O in N₂ absorption coefficient at a total pressure of 760 Torr for the P(12) CO₂ laser line at 1053.924 cm⁻¹. Average spectrophone temperature was 23.5°C.

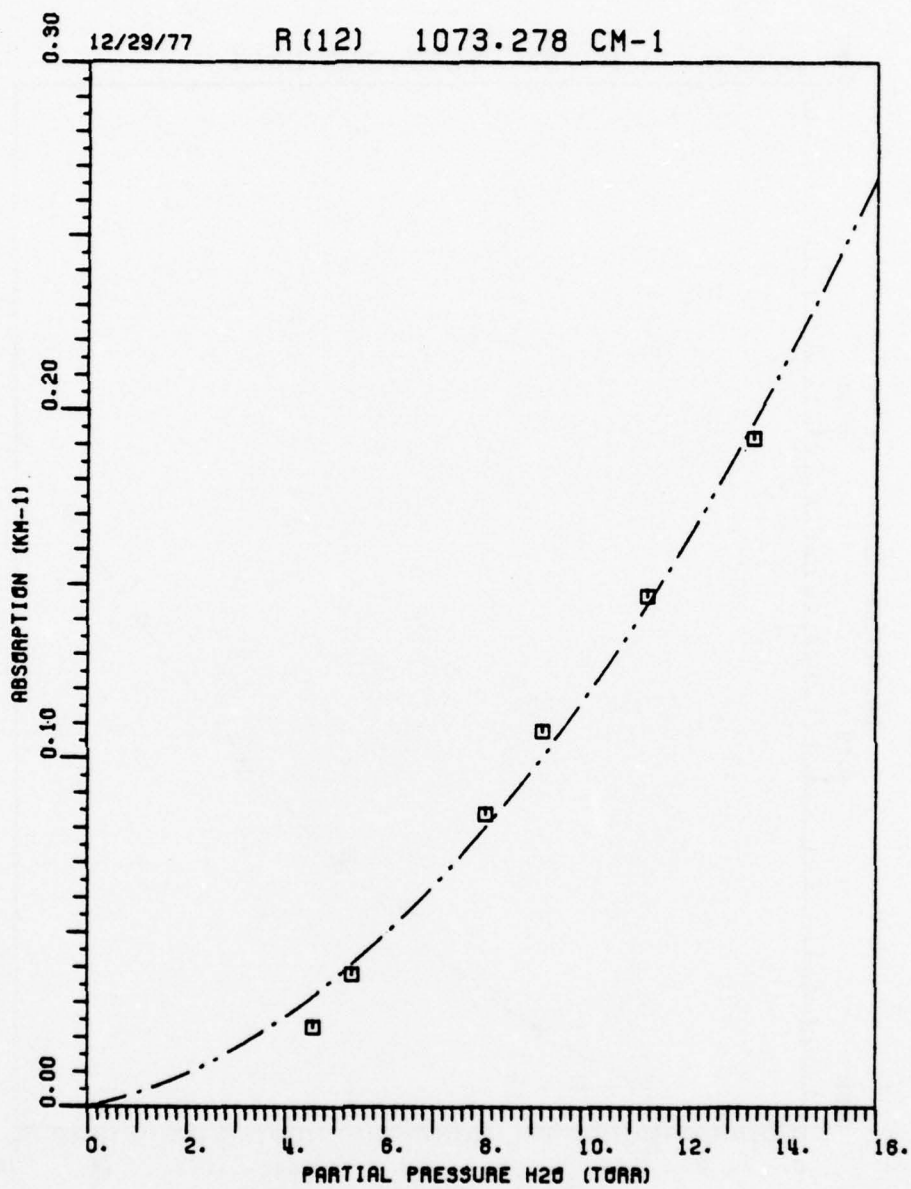


Figure 52. Measured H₂O in N₂ absorption coefficient at a total pressure of 760 Torr for the R(12) CO₂ laser line at 1073.278 cm⁻¹. Average spectrophone temperature was 24 °C.

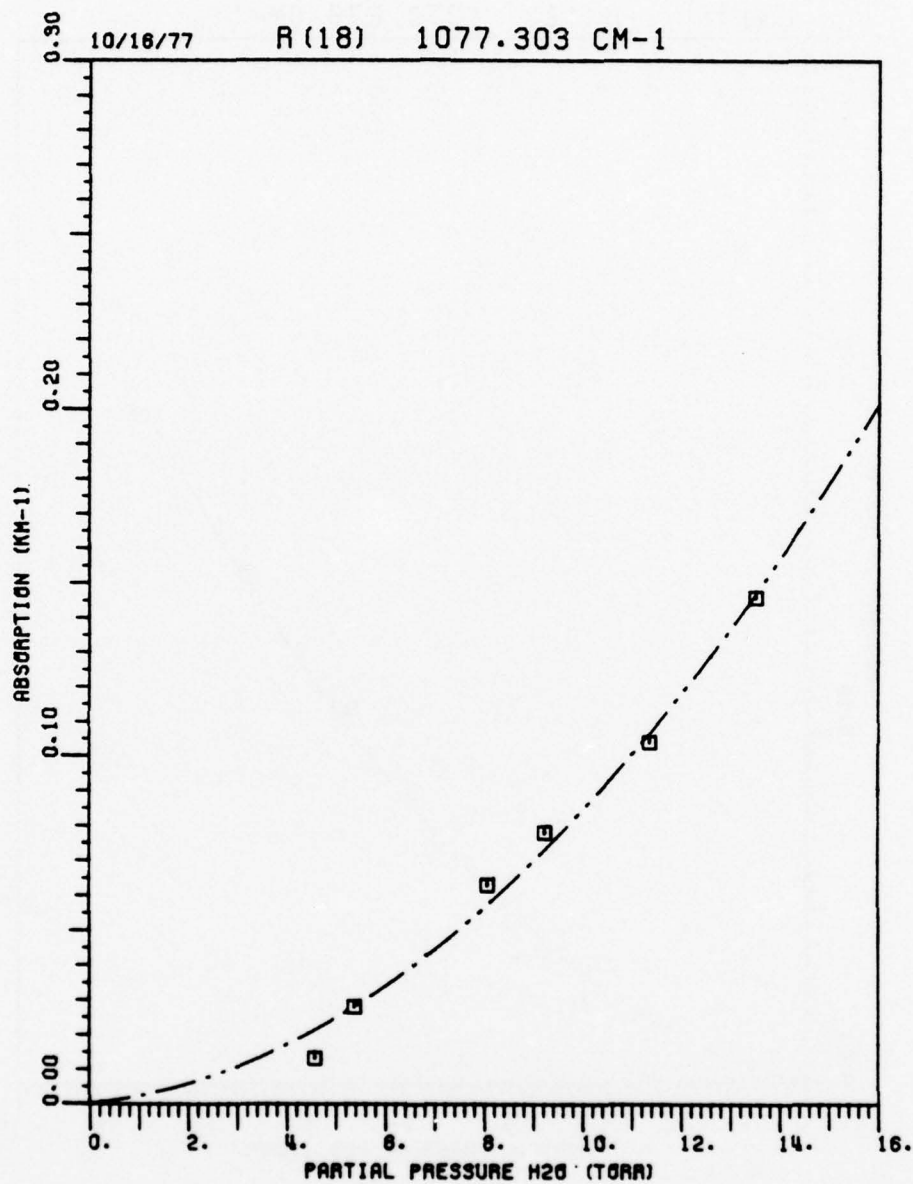


Figure 53. Measured H₂O in N₂ absorption coefficient at a total pressure of 760 Torr for the R(18) CO₂ laser line at 1077.303 cm⁻¹. Average spectrophone temperature was 24 °C.

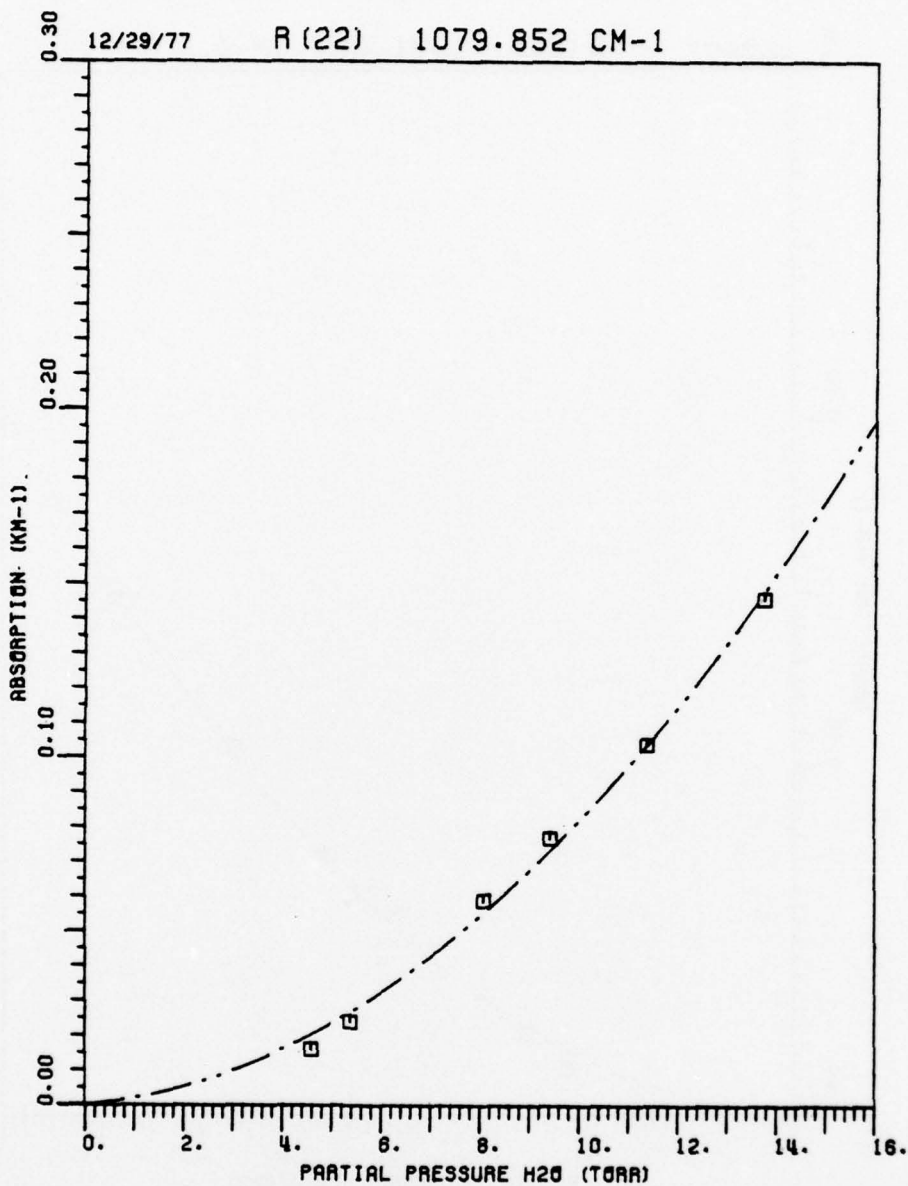


Figure 54. Measured H₂O in N₂ absorption coefficient at a total pressure of 760 Torr for the R(22) CO₂ laser line at 1079.852 cm⁻¹. Average spectrophone temperature was 24°C.

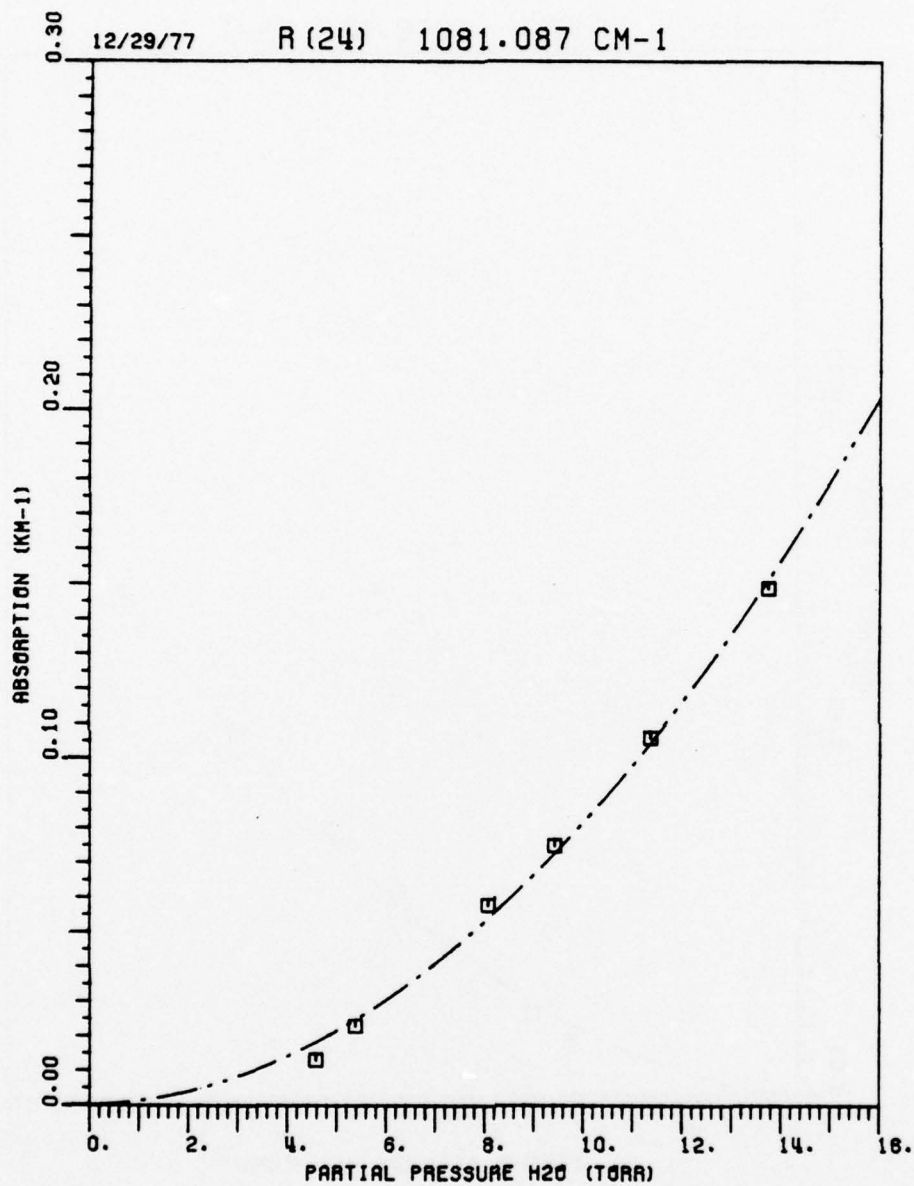


Figure 55. Measured H₂O in N₂ absorption coefficient at a total pressure of 760 Torr for the R(24) CO₂ laser line at 1081.087 cm⁻¹. Average spectrophone temperature was 24°C.

The constant V'_0 contains all the remaining variables which do not depend upon the "nature" of the sample gas.

The final step in this procedure is to see how the ratio \bar{v}/C_v changes in going from a nitrogen sample to one with pure oxygen. These ratios, shown in Table 4, indicate that there will be a very slight change in the pressure signal amplitude which can be strictly attributed to the thermodynamic properties of nitrogen and oxygen. However, the effect is so small that it has been ignored in the calibration of results for the 80% N_2 -20% O_2 and 60% N_2 -40% O_2 buffer gas mixtures. The appropriate correction was made for the studies which considered pure oxygen as a broadening gas.

Table 4
Ratios of specific volumes, \bar{v} (at 70°F and 1 atm) to specific heat at constant volume, C_v for nitrogen and oxygen⁶³.

Nitrogen	Oxygen
\bar{v}/C_v ($\text{cm}^3 \text{ } ^\circ\text{C}/\text{cal}$)	\bar{v}/C_v ($\text{cm}^3 \text{ } ^\circ\text{C}/\text{cal}$)
2.049×10^{-4}	2.057×10^{-4}

1. 80% N_2 and 20% O_2 results

In this second set of pressure broadened data, the results obtained with 80-20 air as the buffer gas are presented in Figures 56 through 64. Nine CO_2 laser lines in the 9 and 10 μm bands were studied at a total sample pressure of 760 Torr. The temperature and laser frequency are supplied in each figure.

2. 60% N_2 and 40% O_2 results

In this third set of pressure broadened data the results obtained with 60-40 air as the buffer gas are presented in Figures 65 through 73. Nine CO_2 laser lines in the 9 and 10 μm band were studied with a total sample gas pressure of 760 Torr. The temperature and laser frequency are supplied in each figure.

3. 100% O_2 results

In this last section of pressure broadened data the results obtained with oxygen as the buffer gas are presented, see Figures 74 through 81. Eight CO_2 laser lines in the 9 and 10 μm bands were studied with a total sample gas pressure of 760 Torr. The temperature and laser frequency are supplied in each figure.

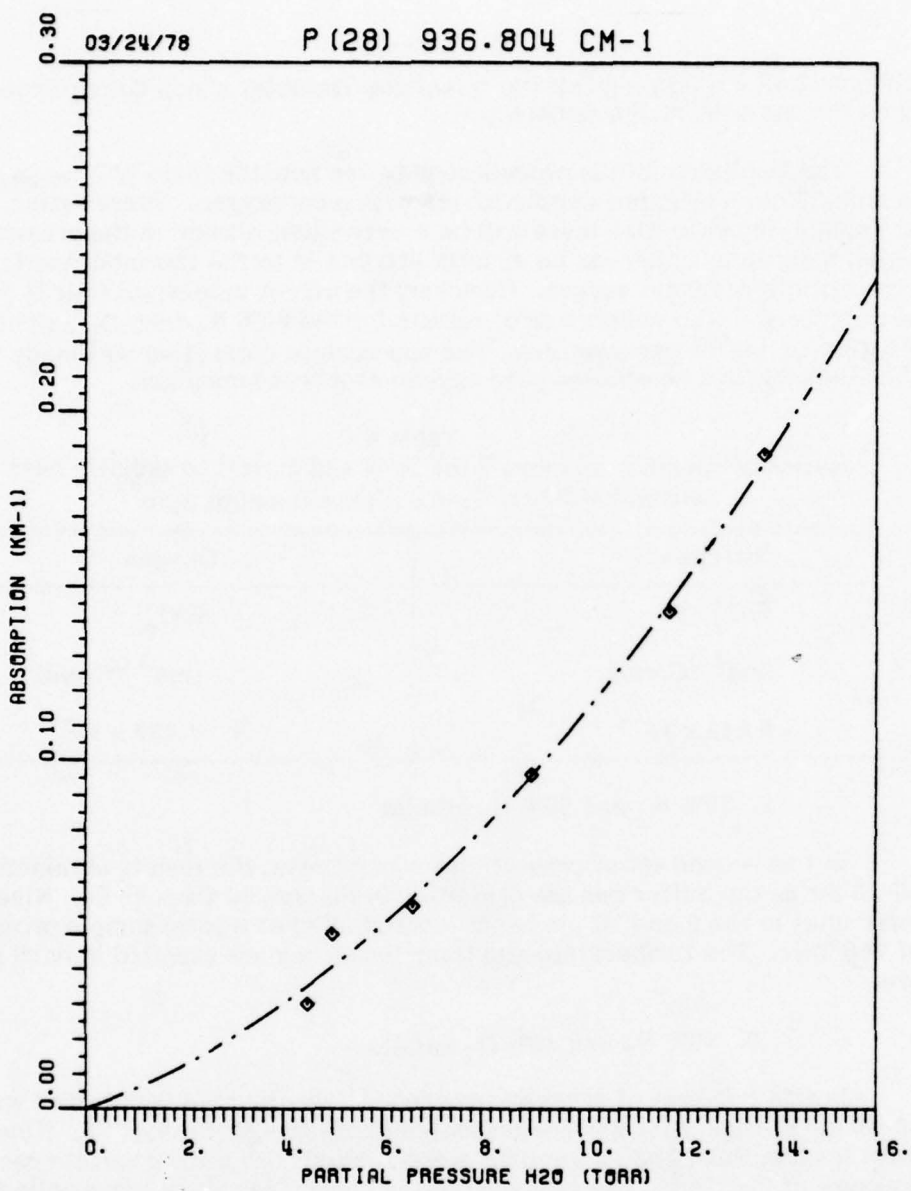


Figure 56. Measured H₂O in 80% N₂ and 20% O₂ absorption coefficient at a total pressure of 760 Torr for the P(28) CO₂ laser line at 936.804 cm⁻¹. Average spectrophone temperature was 24°C.

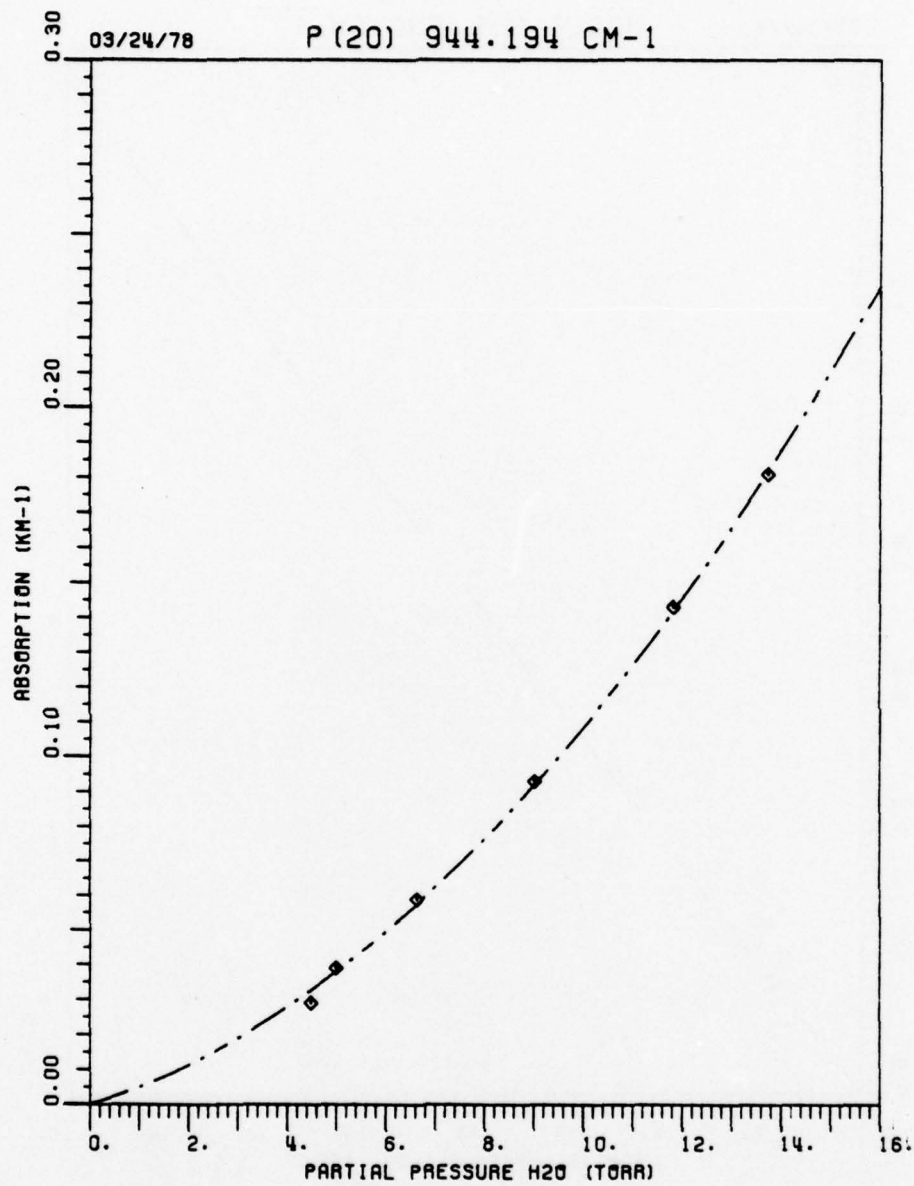


Figure 57. Measured H₂O in 80% N₂ and 20% O₂ absorption coefficient at a total pressure of 760 Torr for the P(20) CO₂ laser line at 944.194 cm⁻¹. Average spectrophone temperature was 24°C.

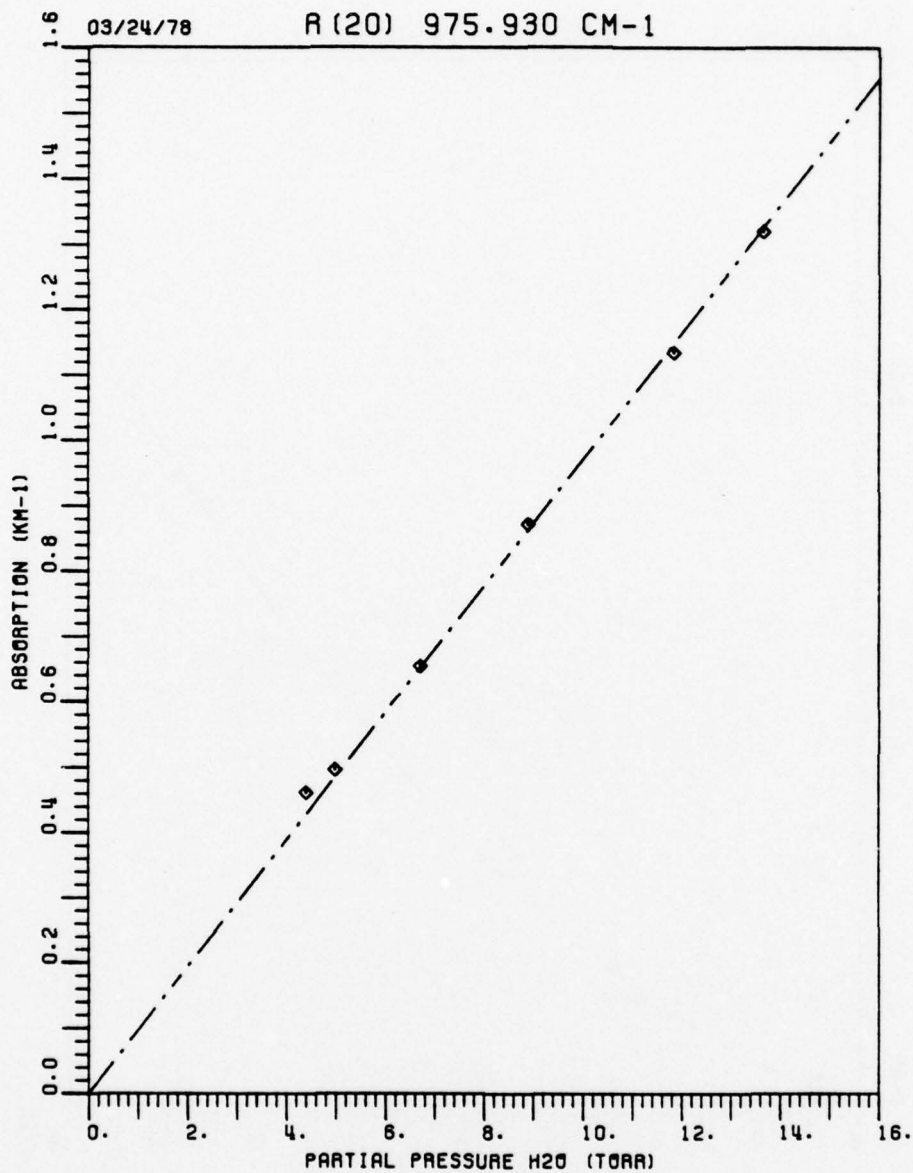


Figure 58. Measured H₂O in 80% N₂ and 20% O₂ absorption coefficient at a total pressure of 760 Torr for the R(20) CO₂ laser line at 975.930 cm⁻¹. Average spectrophone temperature was 24°C.

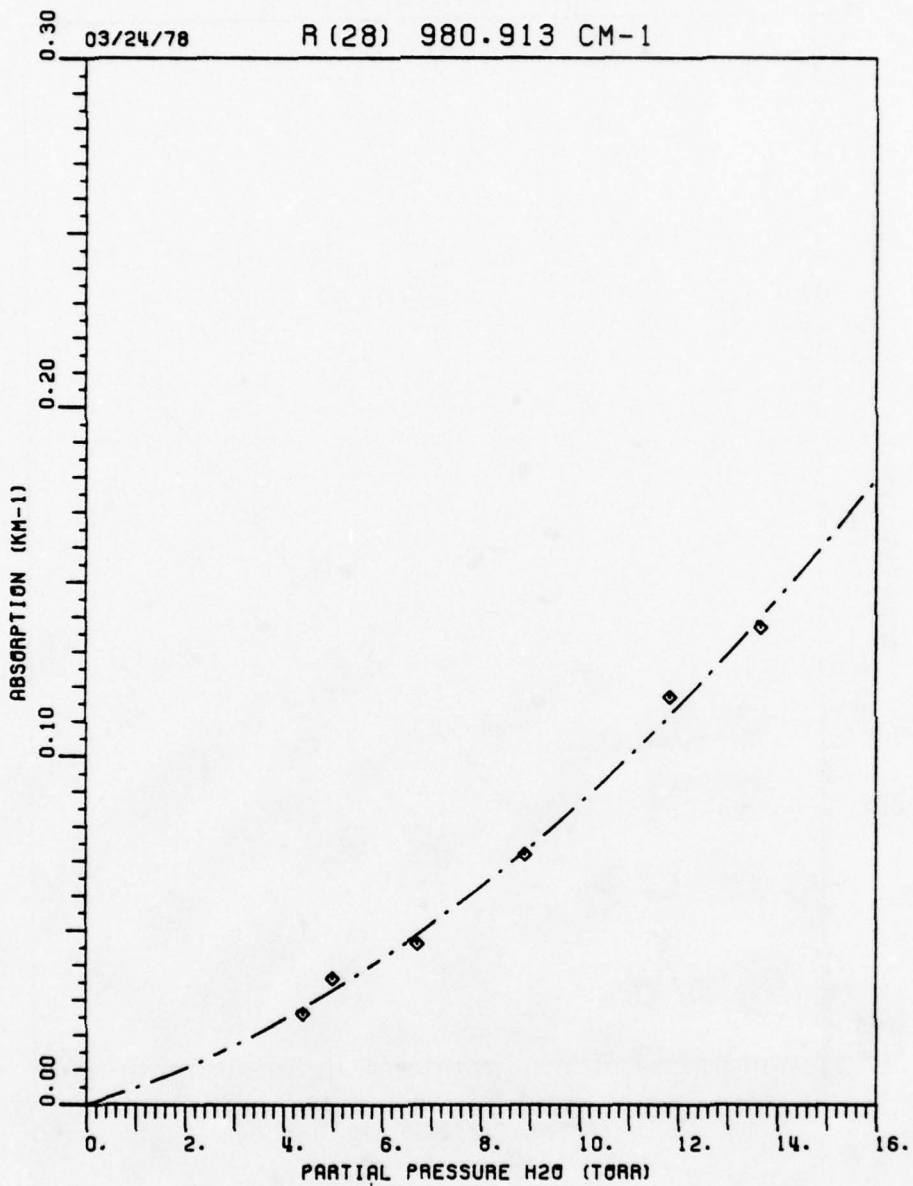


Figure 59. Measured H₂O in 80% N₂ and 20% O₂ absorption coefficient at a total pressure of 760 Torr for the R(28) CO₂ laser line at 980.913 cm⁻¹. Average spectrophone temperature was 24°C.

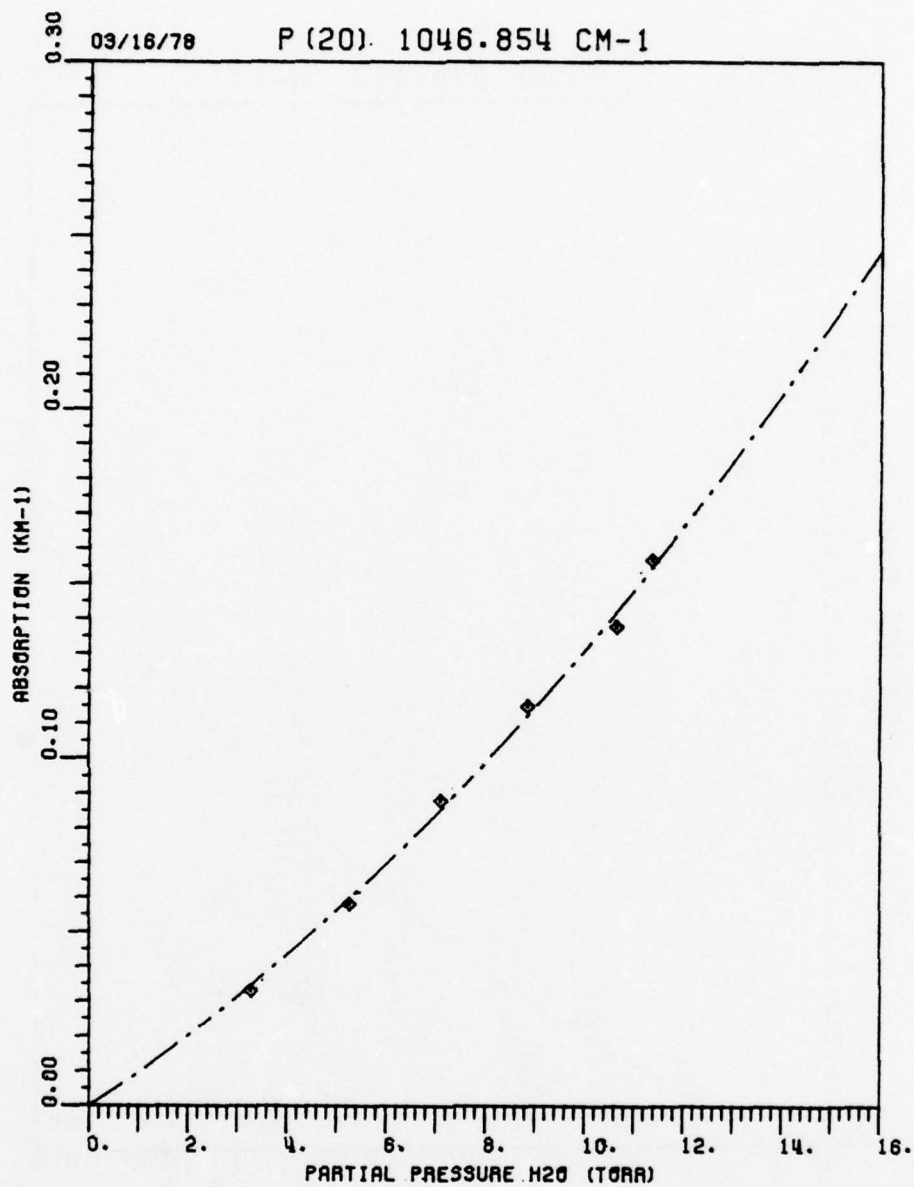


Figure 60. Measured H₂O in 80% N₂ and 20% O₂ absorption coefficient at a total pressure of 760 Torr for the P(20) CO₂ laser line at 1046.854 cm⁻¹. Average spectrophone temperature was 21°C.

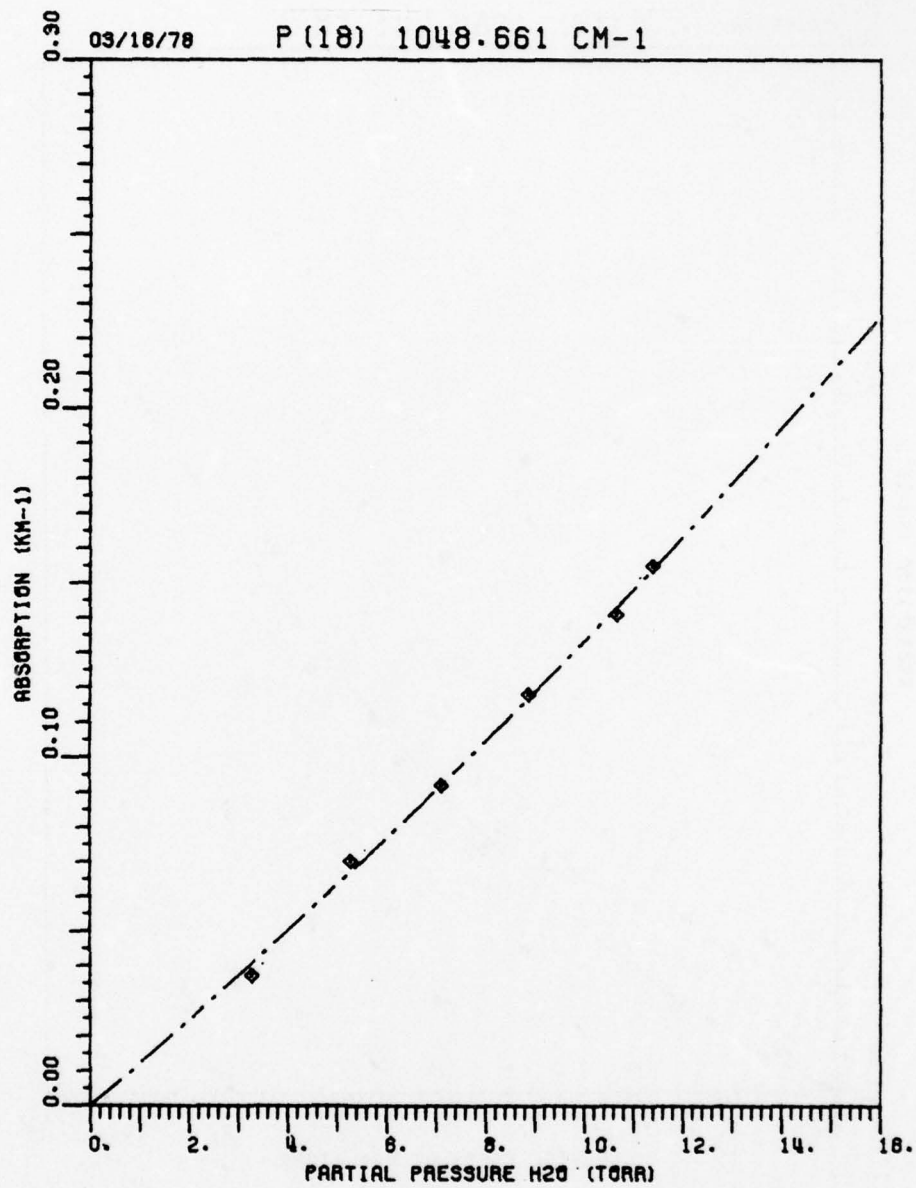


Figure 61. Measured H₂O in 80% N₂ and 20% O₂ absorption coefficient at a total pressure of 760 Torr for the P(18) CO₂ laser line at 1048.661 cm⁻¹. Average spectrophone temperature was 21°C.

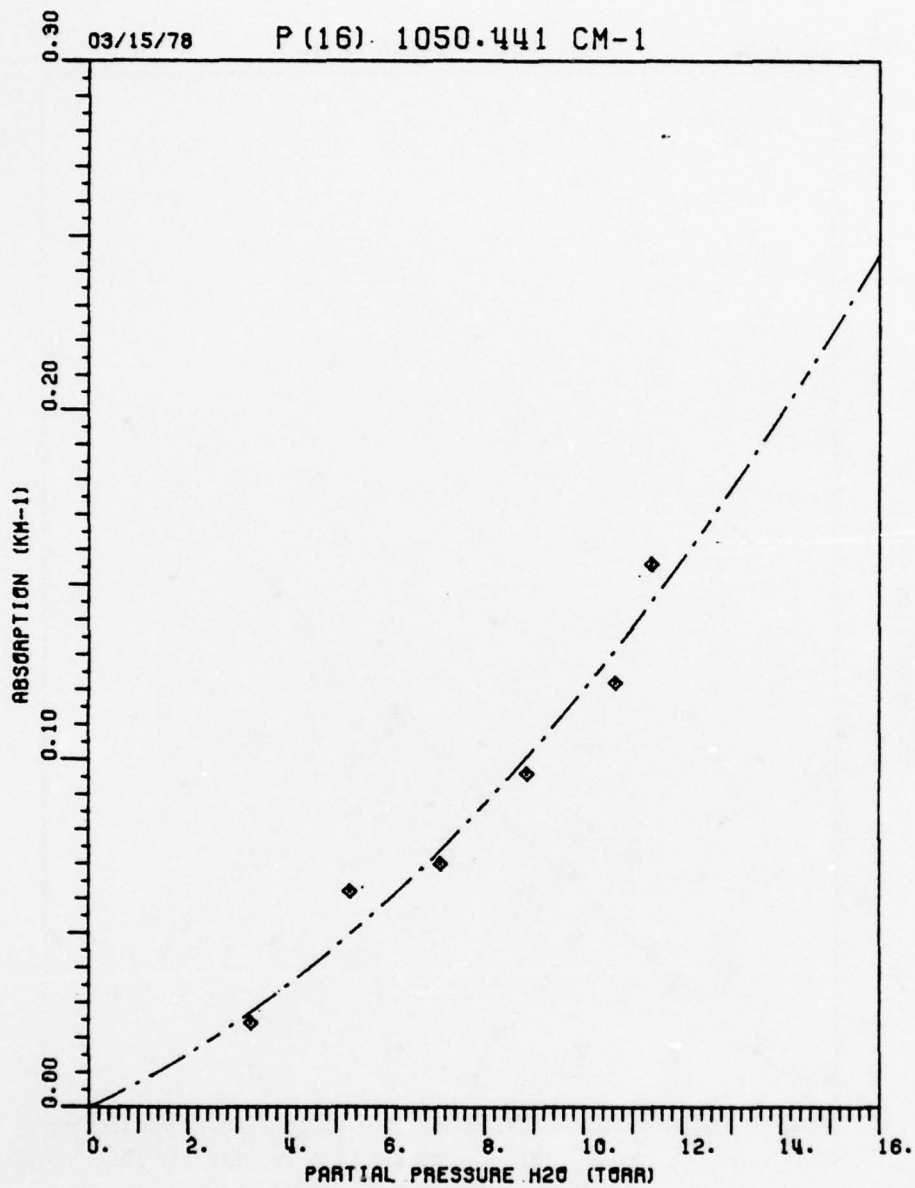


Figure 62. Measured H₂O in 80% N₂ and 20% O₂ absorption coefficient at a total pressure of 760 Torr for the P(16) CO₂ laser line at 1050.441 cm⁻¹. Average spectrophone temperature was 21°C.

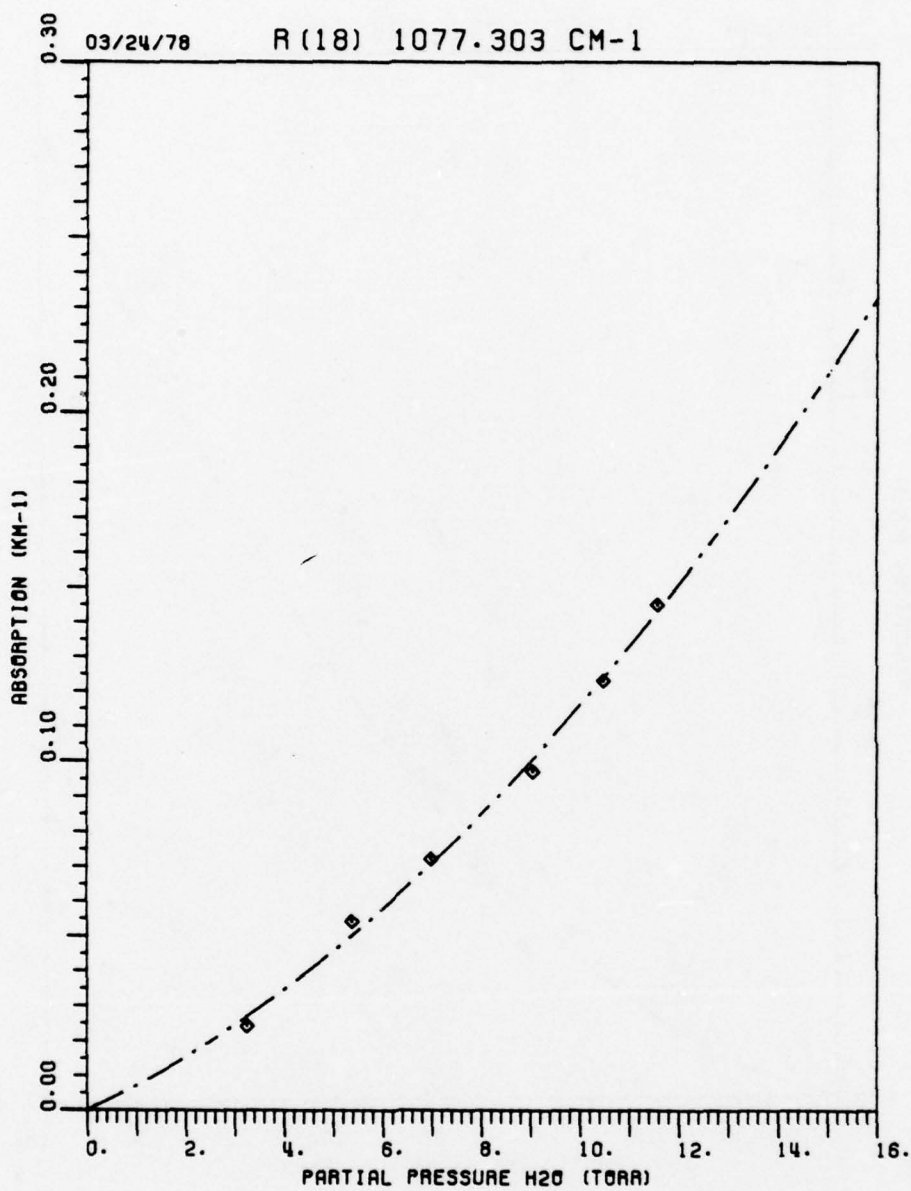


Figure 63. Measured H₂O in 80% N₂ and 20% O₂ absorption coefficient at a total pressure of 760 Torr for the R(18) CO₂ laser line at 1077.303 cm⁻¹. Average spectrophone temperature was 21°C.

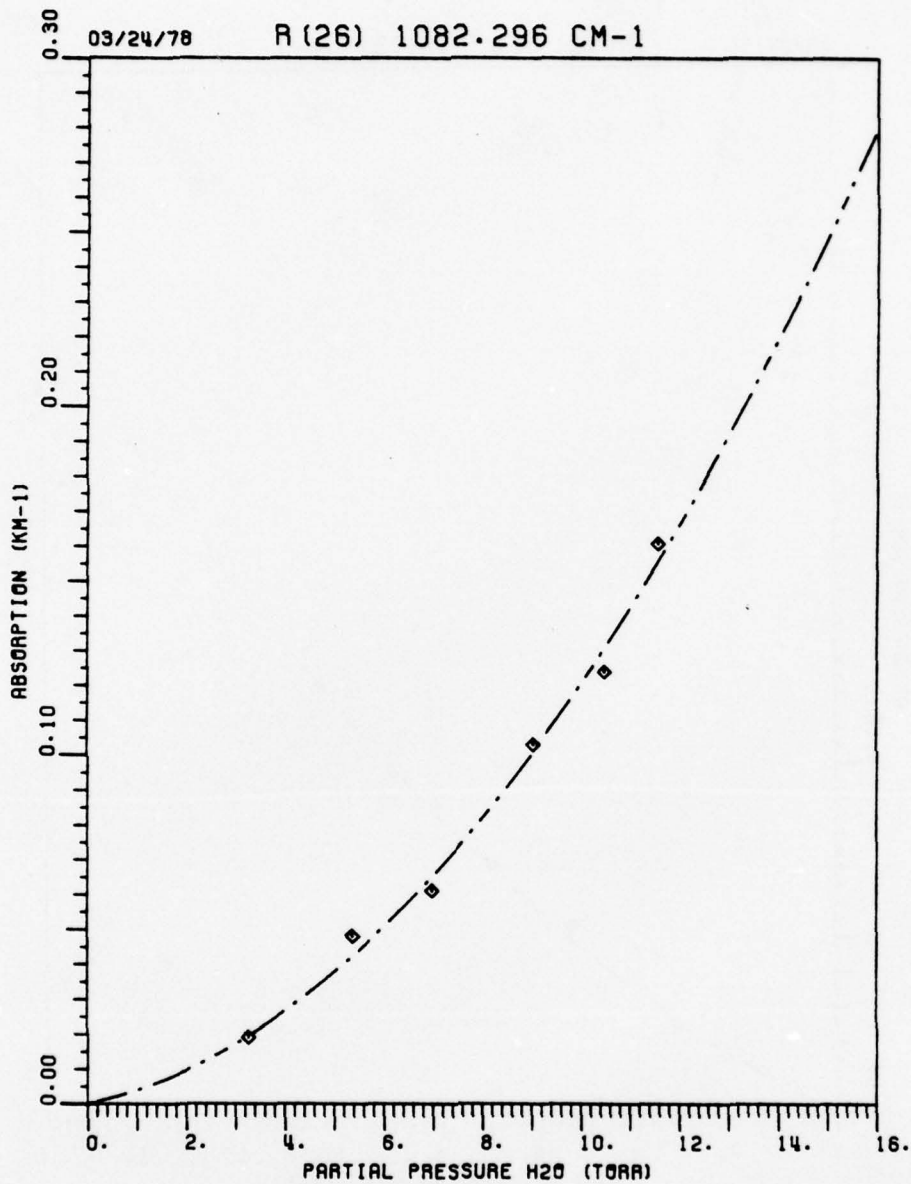


Figure 64. Measured H₂O in 80% N₂ and 20% O₂ absorption coefficient at a total pressure of 760 Torr for the R(26) CO₂ laser line at 1082.296 cm⁻¹. Average spectrophone temperature was 21°C.

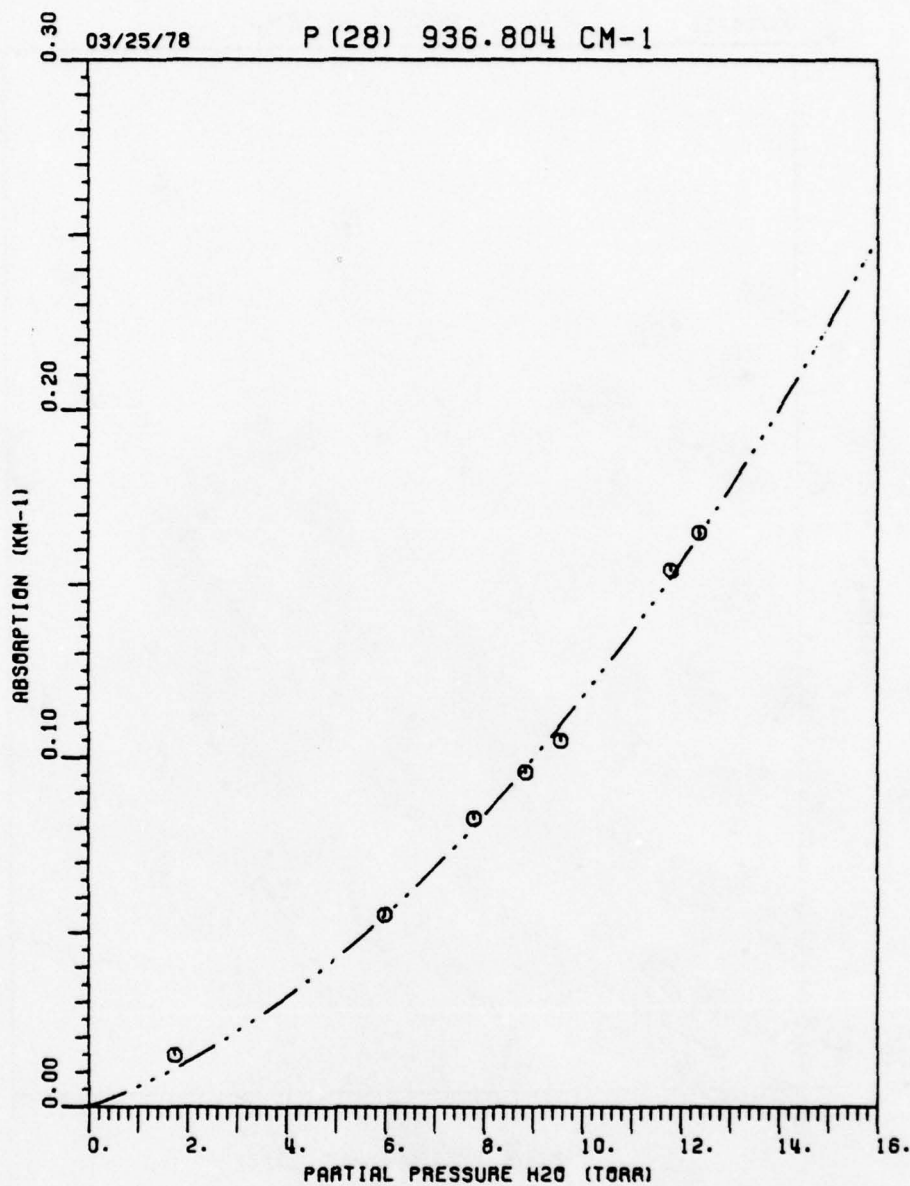


Figure 66. Measured H₂O in 60% N₂ and 40% O₂ absorption coefficient at a total pressure of 760 Torr for the P(28) CO₂ laser line at 936.804 cm⁻¹. Average spectrophone temperature was 23°C.

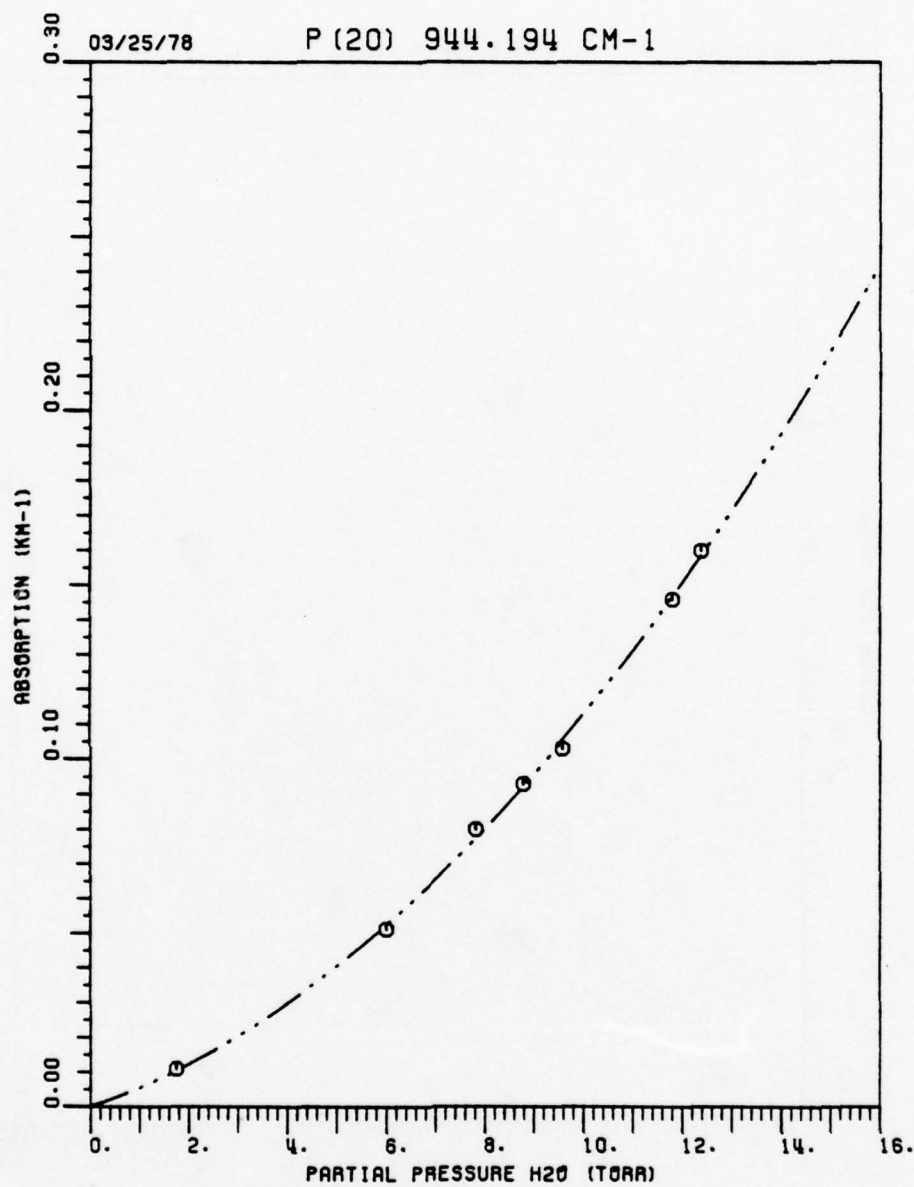


Figure 66. Measured H₂O in 60% N₂ and 40% O₂ absorption coefficient at a total pressure of 760 Torr for the P(20) CO₂ laser line at 944.194 cm⁻¹. Average spectrophone temperature was 23°C.

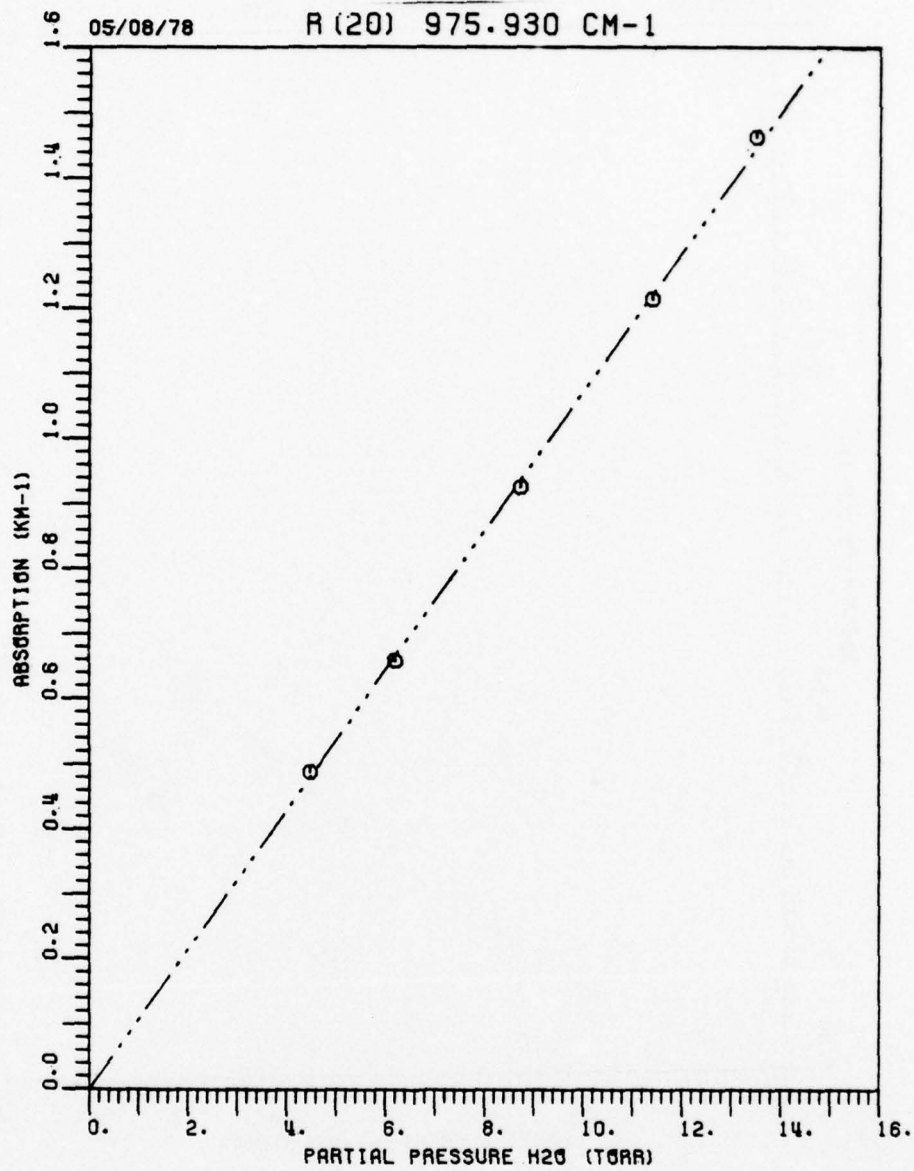


Figure 67. Measured H₂O in 60% N₂ and 40% O₂ absorption coefficient at a total pressure of 760 Torr for the R(20) CO₂ laser line at 975.930 cm⁻¹. Average spectrophone temperature was 23.6°C.

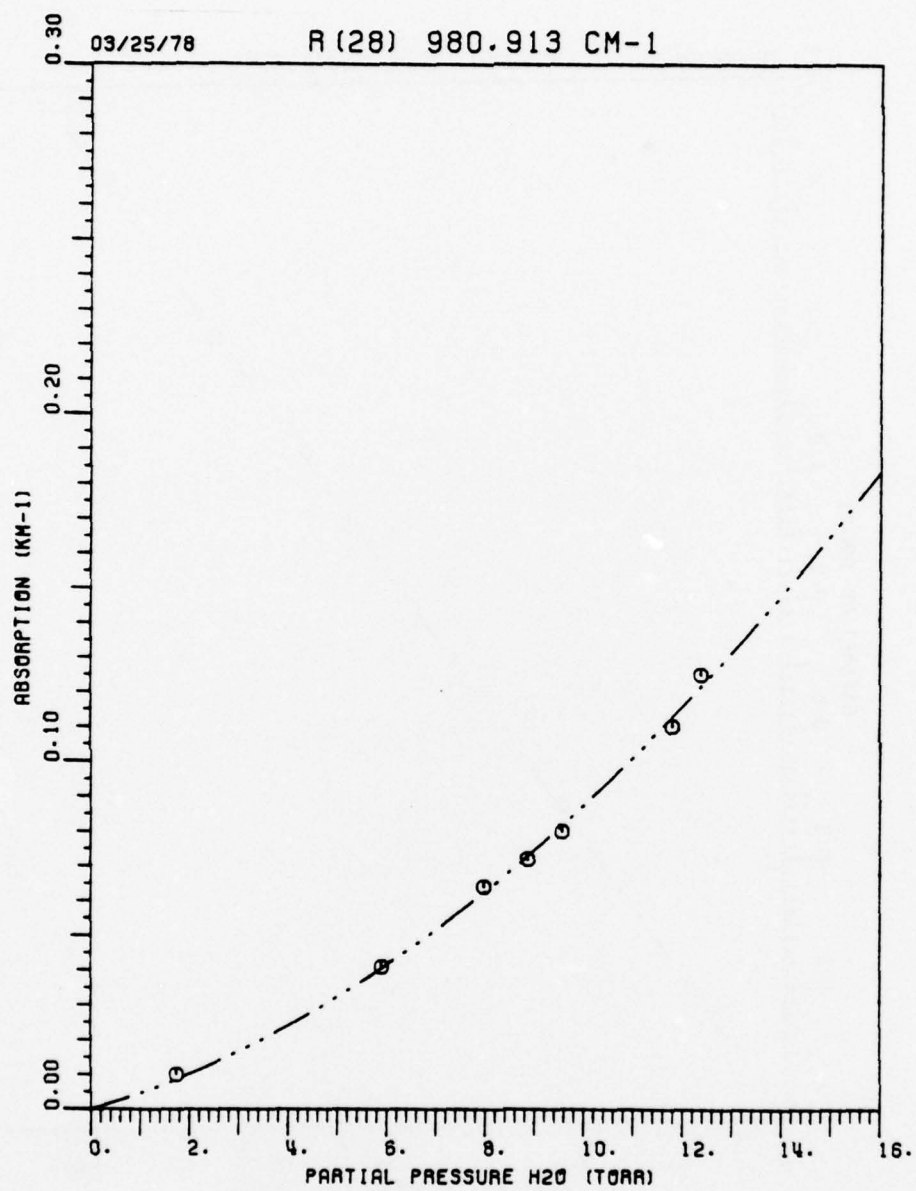


Figure 68. Measured H₂O in 60% N₂ and 40% O₂ absorption coefficient at a total pressure of 760 Torr for the R(28) CO₂ laser line at 980.913 cm⁻¹. Average spectrophone temperature was 23°C.

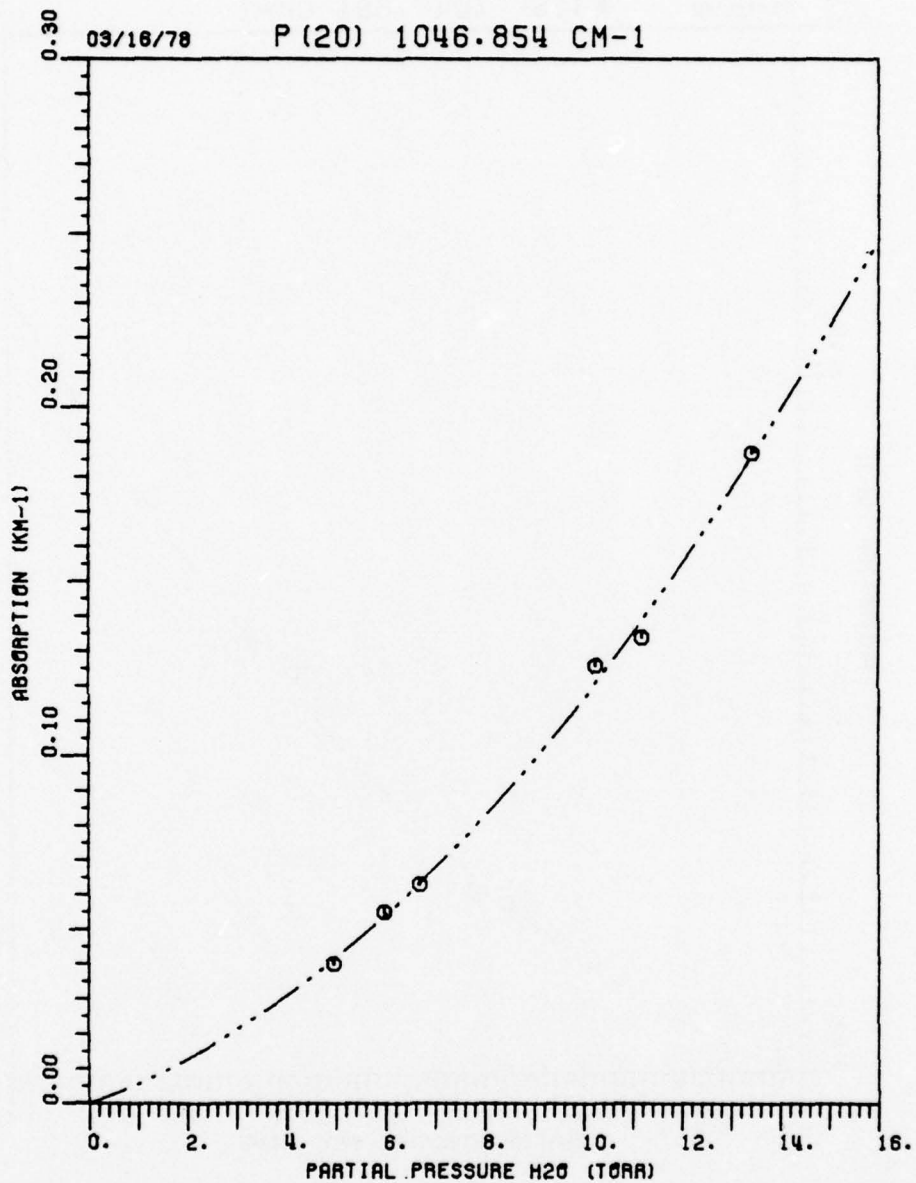


Figure 69. Measured H₂O in 60% N₂ and 40% O₂ absorption coefficient at a total pressure of 760 Torr for the P(20) CO₂ laser line at 1046.854 cm⁻¹. Average spectrophone temperature was 22°C.

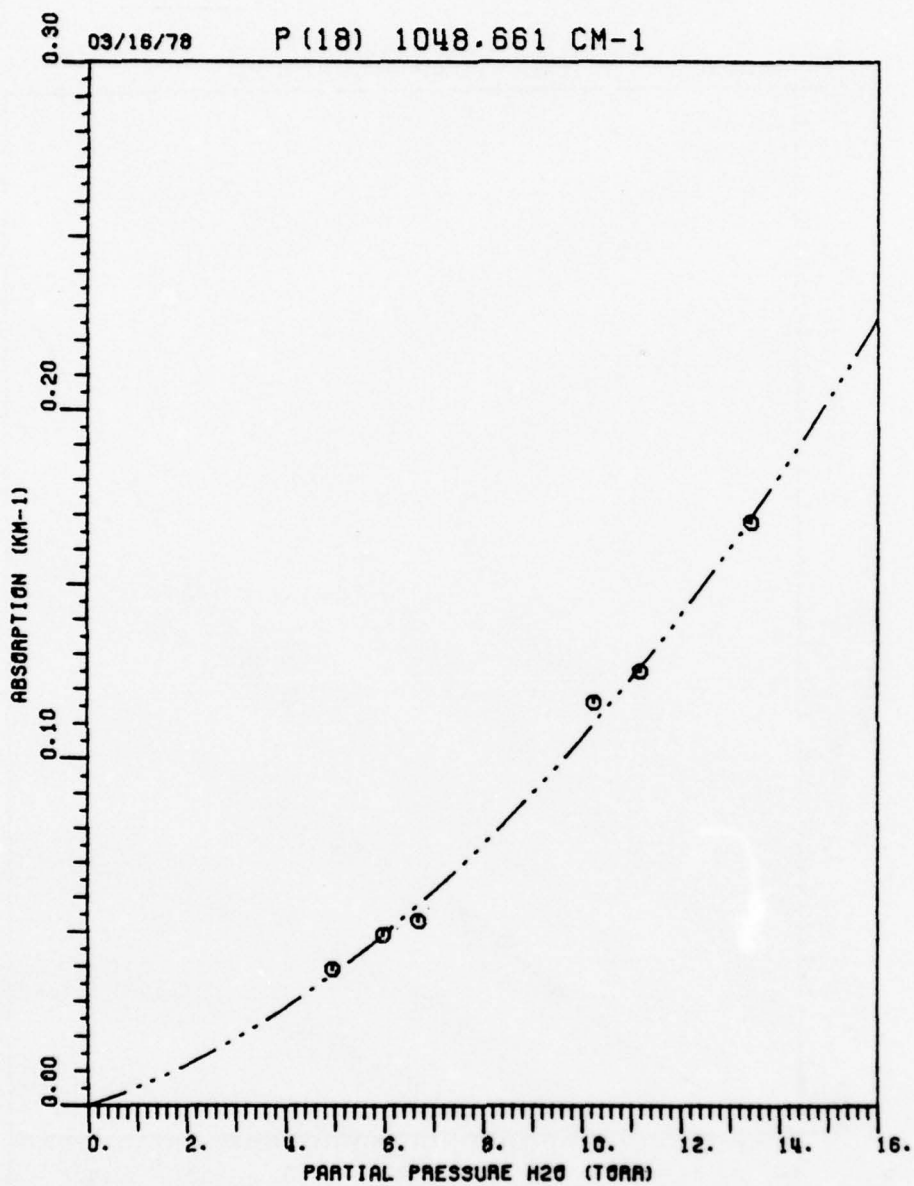


Figure 70. Measured H₂O in 60% N₂ and 40% O₂ absorption coefficient at a total pressure of 760 Torr for the P(18) CO₂ laser line at 1048.661 cm⁻¹. Average spectrophone temperature was 22°C.

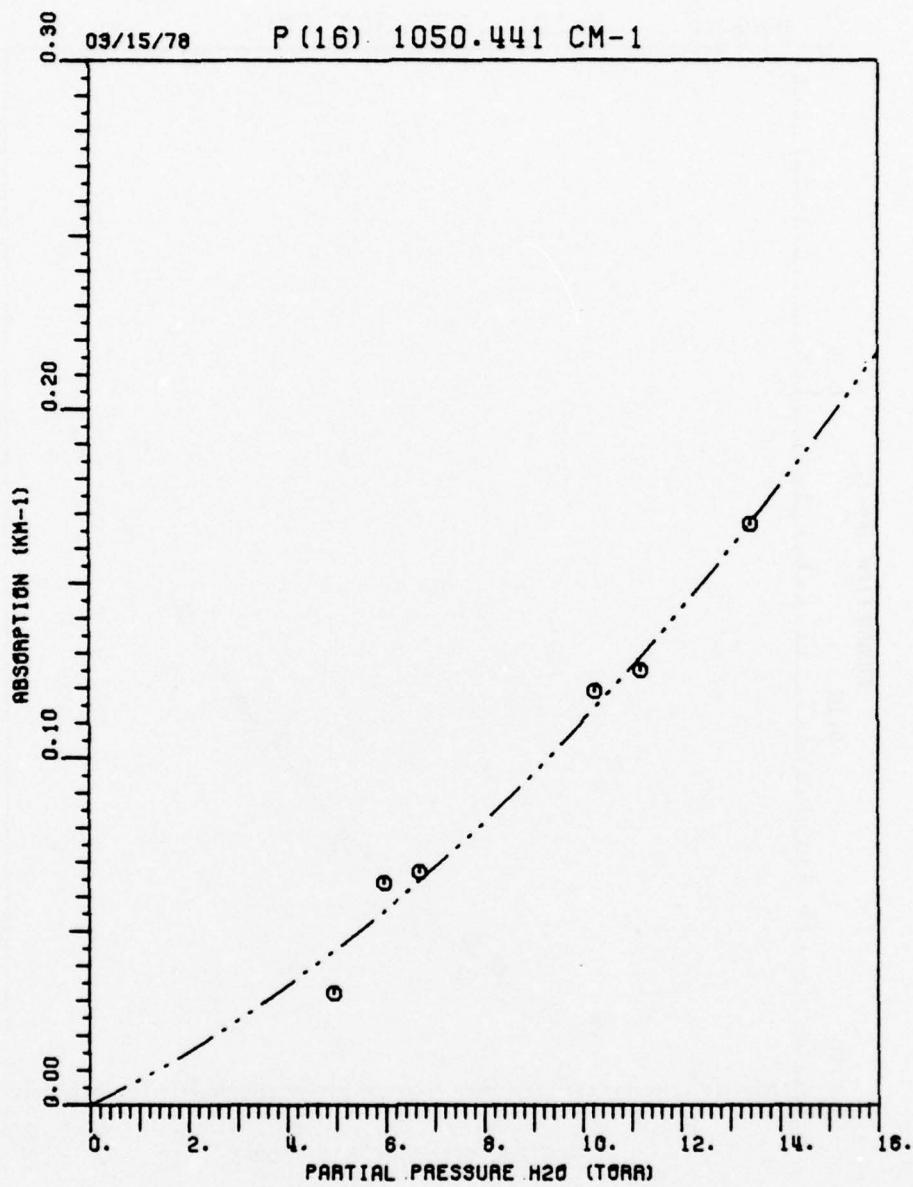


Figure 71. Measured H₂O in 60% N₂ and 40% O₂ absorption coefficient at a total pressure of 760 Torr for the P(16) CO₂ laser line at 1050.441 cm⁻¹. Average spectrophone temperature was 22°C.

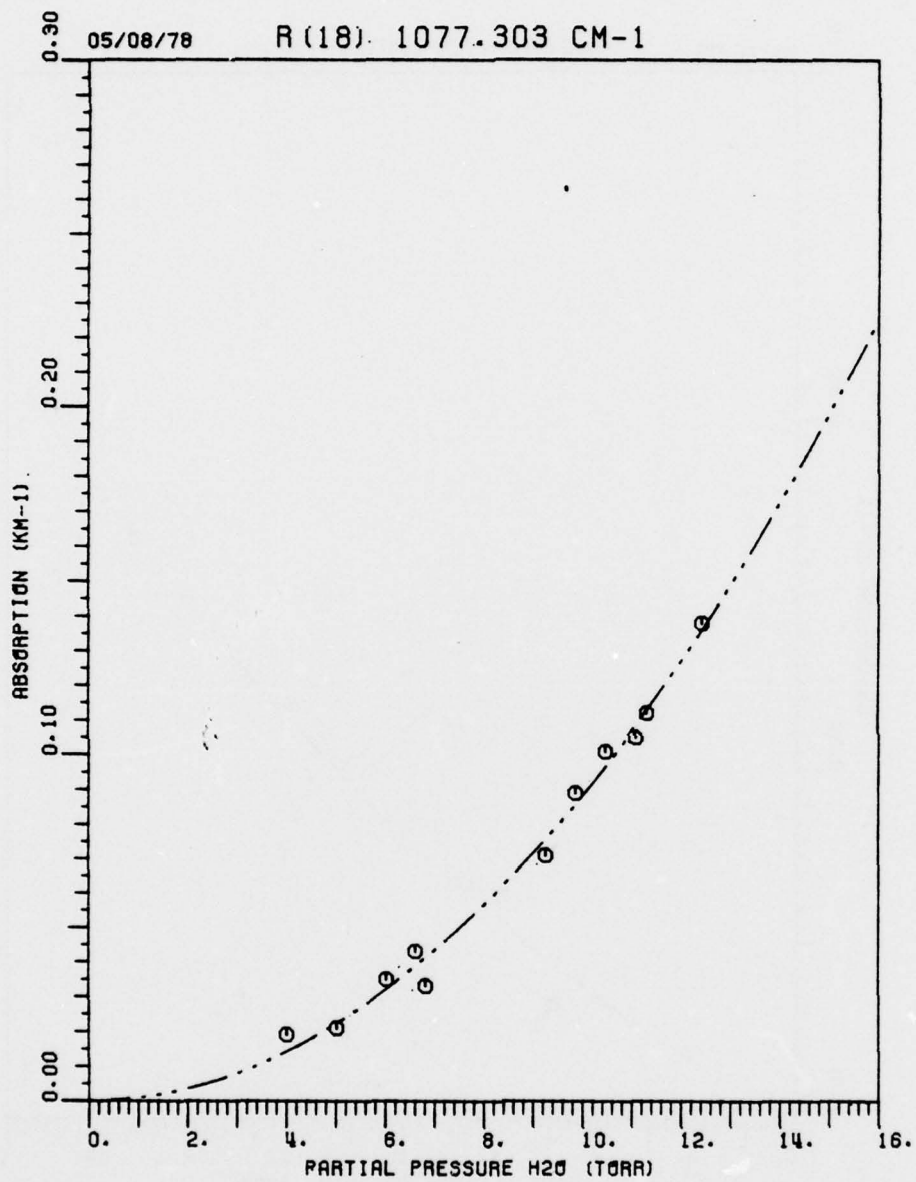


Figure 72. Measured H₂O in 60% N₂ and 40% O₂ absorption coefficient at a total pressure of 760 Torr for the R(18) CO₂ laser line at 1077.303 cm⁻¹. Average spectrophone temperature was 22.6°C.

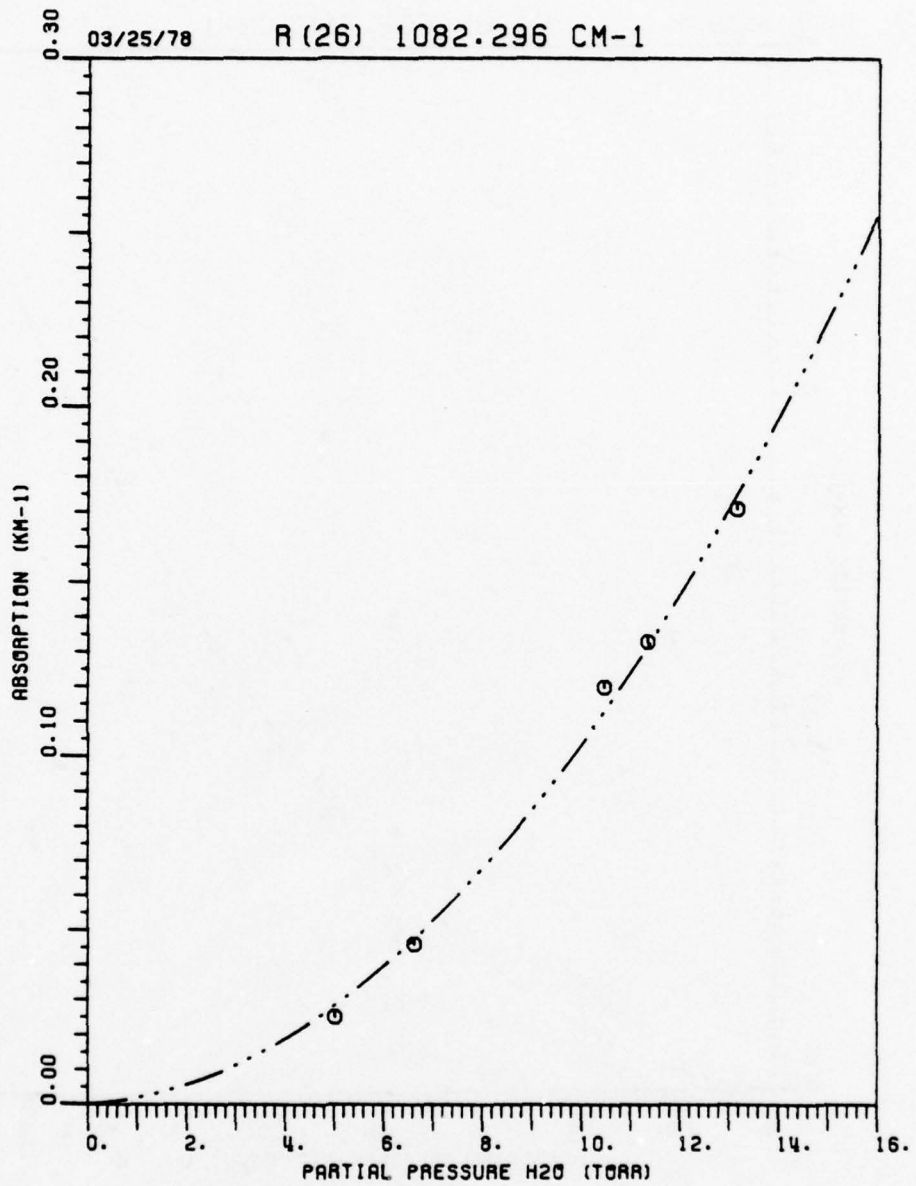


Figure 73. Measured H₂O in 60% N₂ and 40% O₂ absorption coefficient at a total pressure of 760 Torr for the R(26) CO₂ laser line at 1082.296 cm⁻¹. Average spectrophone temperature was 22°C.

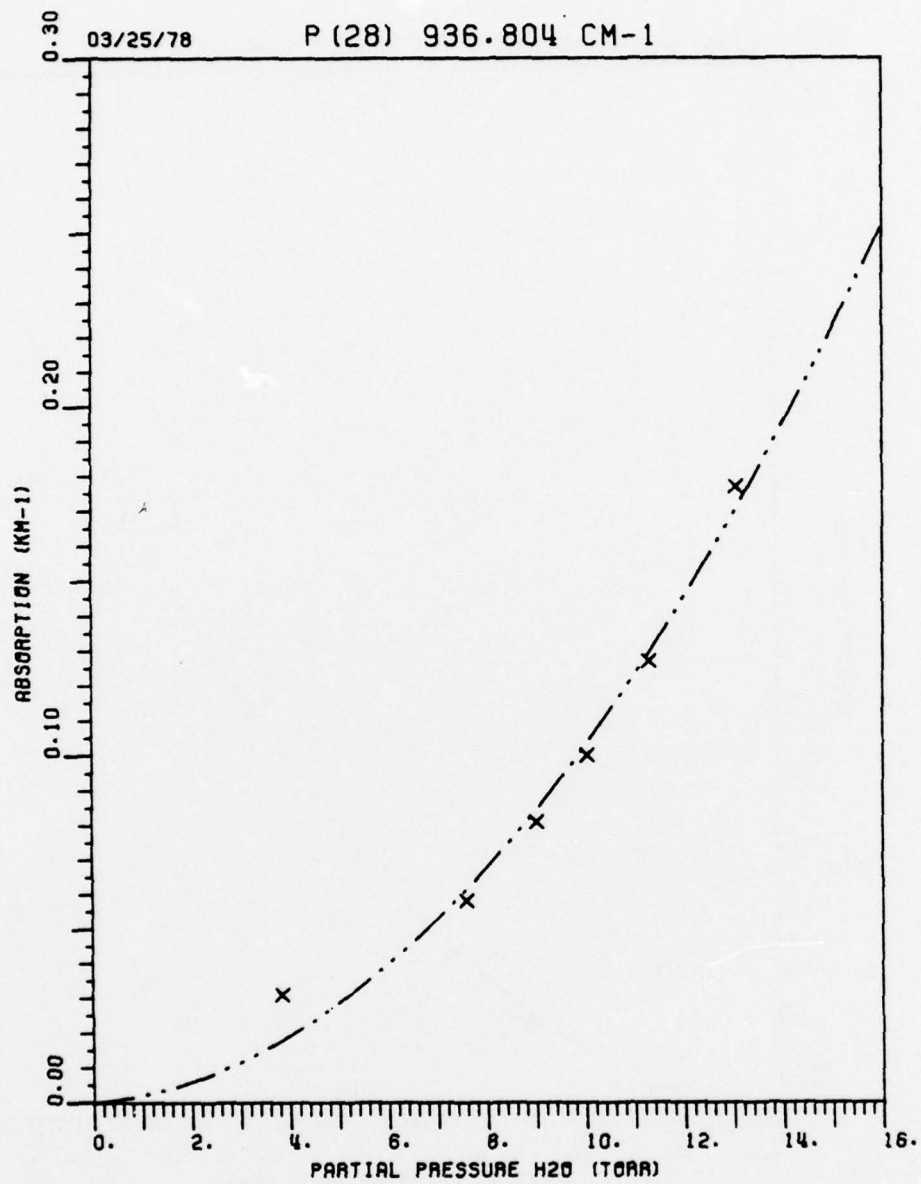


Figure 74. Measured H₂O in O₂ absorption coefficient at a total pressure of 760 Torr for the P(28) CO₂ laser line at 936.804 cm⁻¹. Average spectrophone temperature was 23°C.

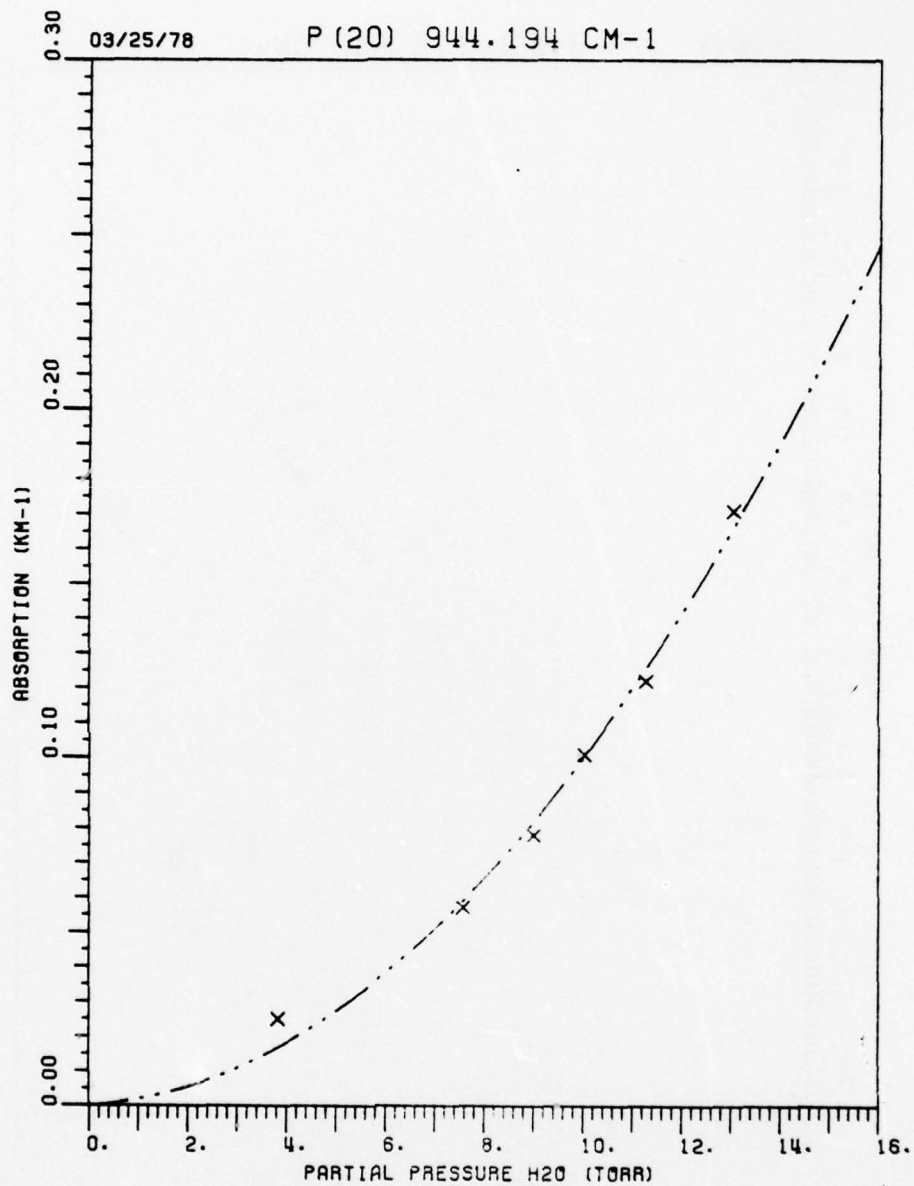


Figure 75. Measured H₂O in O₂ absorption coefficient at a total pressure of 760 Torr for the P(20) CO₂ laser line at 944.194 cm⁻¹. Average spectrophone temperature was 23°C.

03/25/78

R (20) 975.930 CM-1

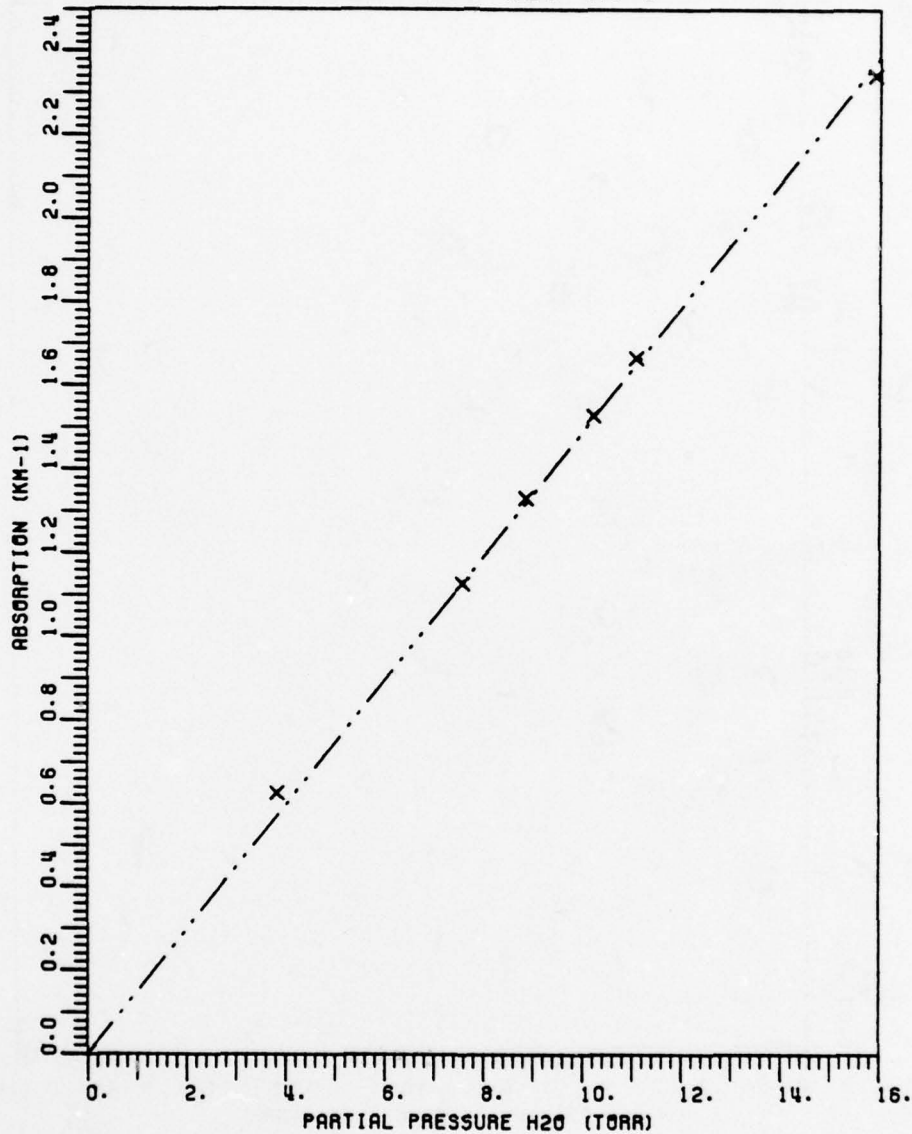


Figure 76. Measured H₂O in O₂ absorption coefficient at a total pressure of 760 Torr for the R(20) CO₂ laser line at 975.930 cm⁻¹. Average spectrophone temperature was 23°C.

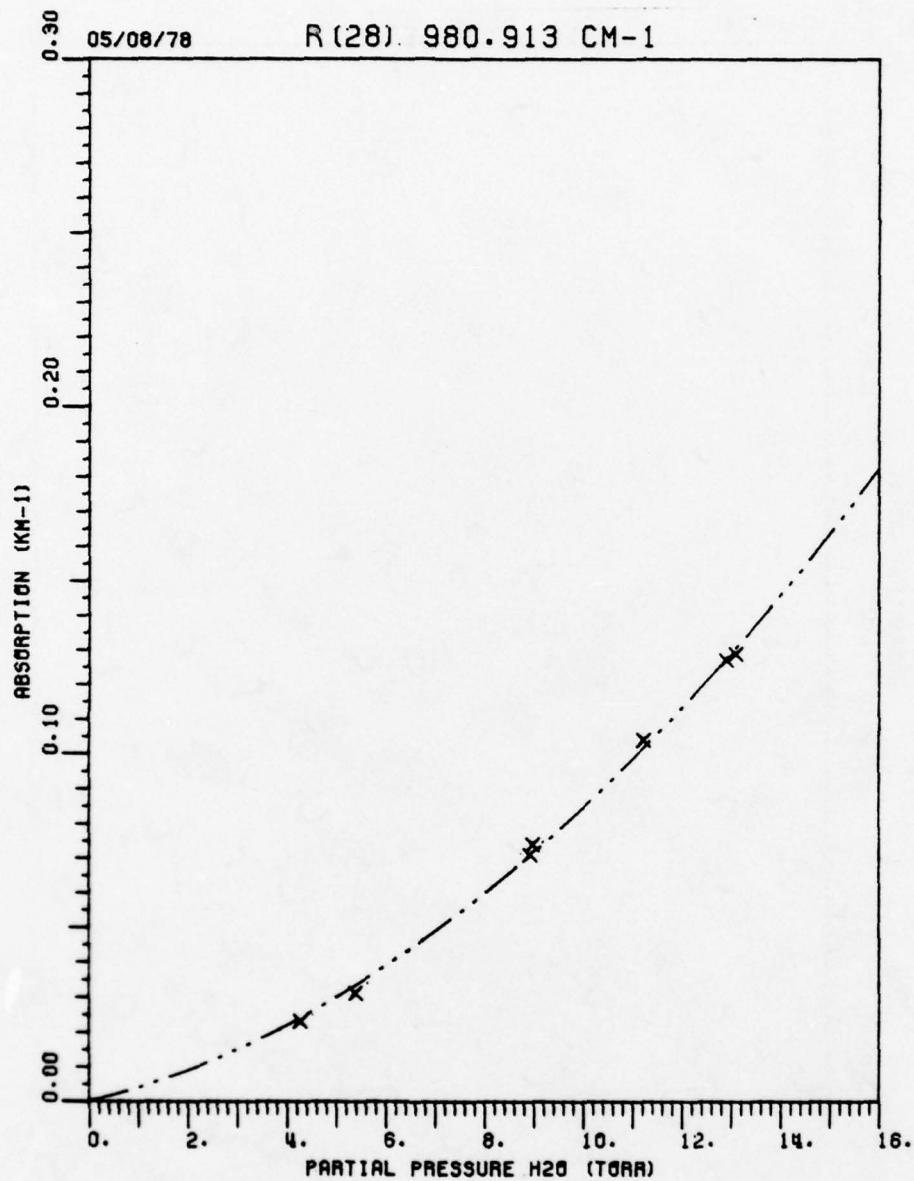


Figure 77. Measured H₂O in O₂ absorption coefficient at a total pressure of 760 Torr for the R(28) CO₂ laser line at 980.913 cm⁻¹. Average spectrophone temperature was 23.1°C.

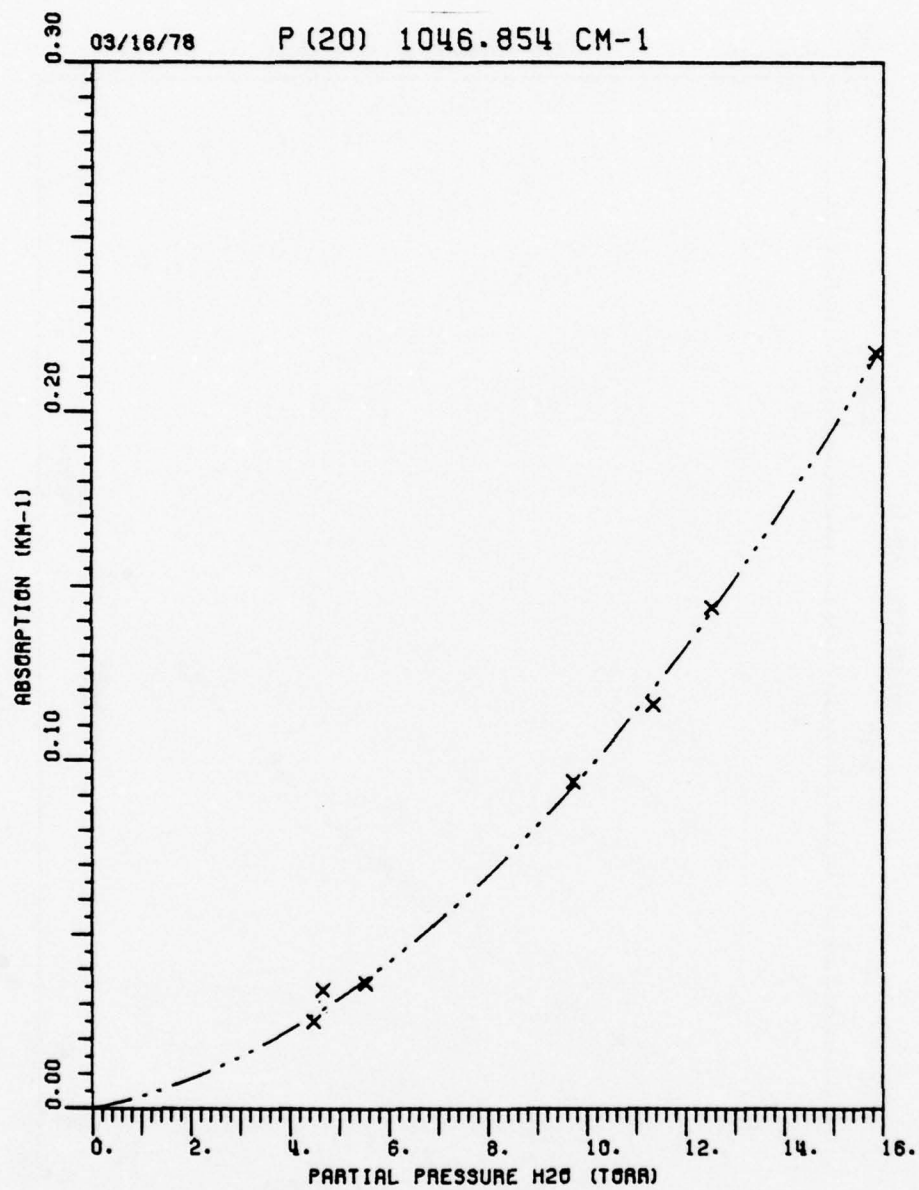


Figure 78. Measured H₂O in O₂ absorption coefficient at a total pressure of 760 Torr for the P(20) CO₂ laser line at 1046.854 cm⁻¹. Average spectrophone temperature was 22°C.

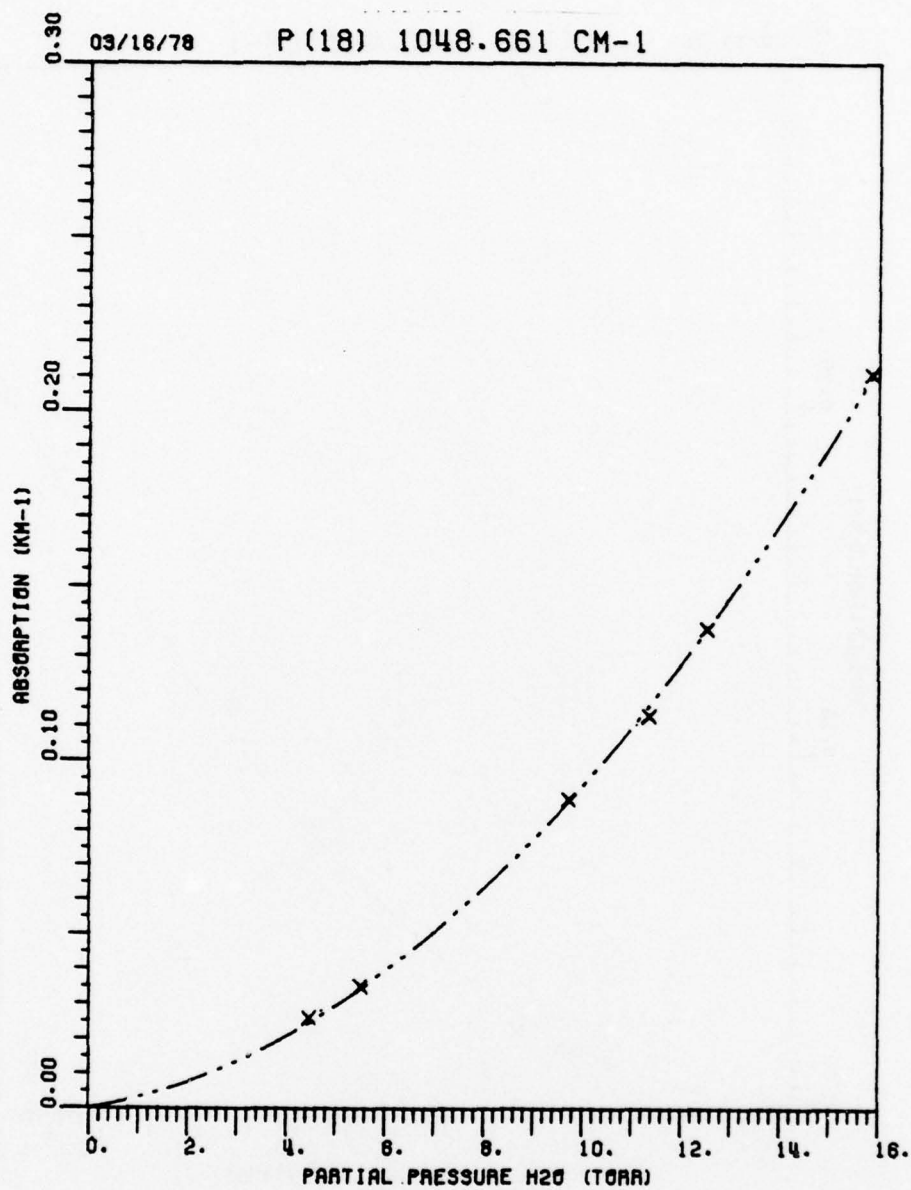


Figure 79. Measured H₂O in O₂ absorption coefficient at a total pressure of 760 Torr for the P(18) CO₂ laser line at 1048,661 cm⁻¹. Average spectrophone temperature was 22°C.

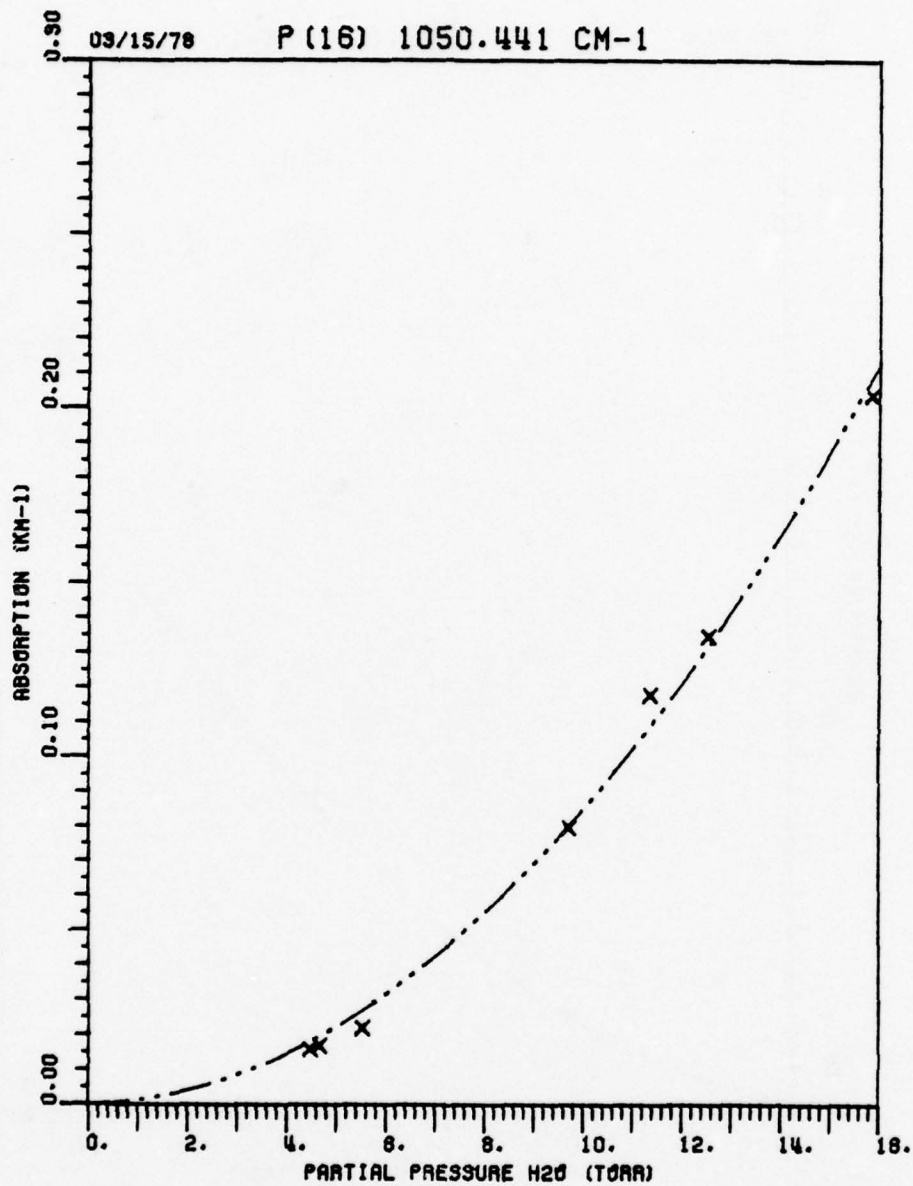


Figure 80. Measured H₂O in O₂ absorption coefficient at a total pressure of 760 Torr for the P(16) CO₂ laser line at 1050,441 cm⁻¹. Average spectrophone temperature was 22°C.

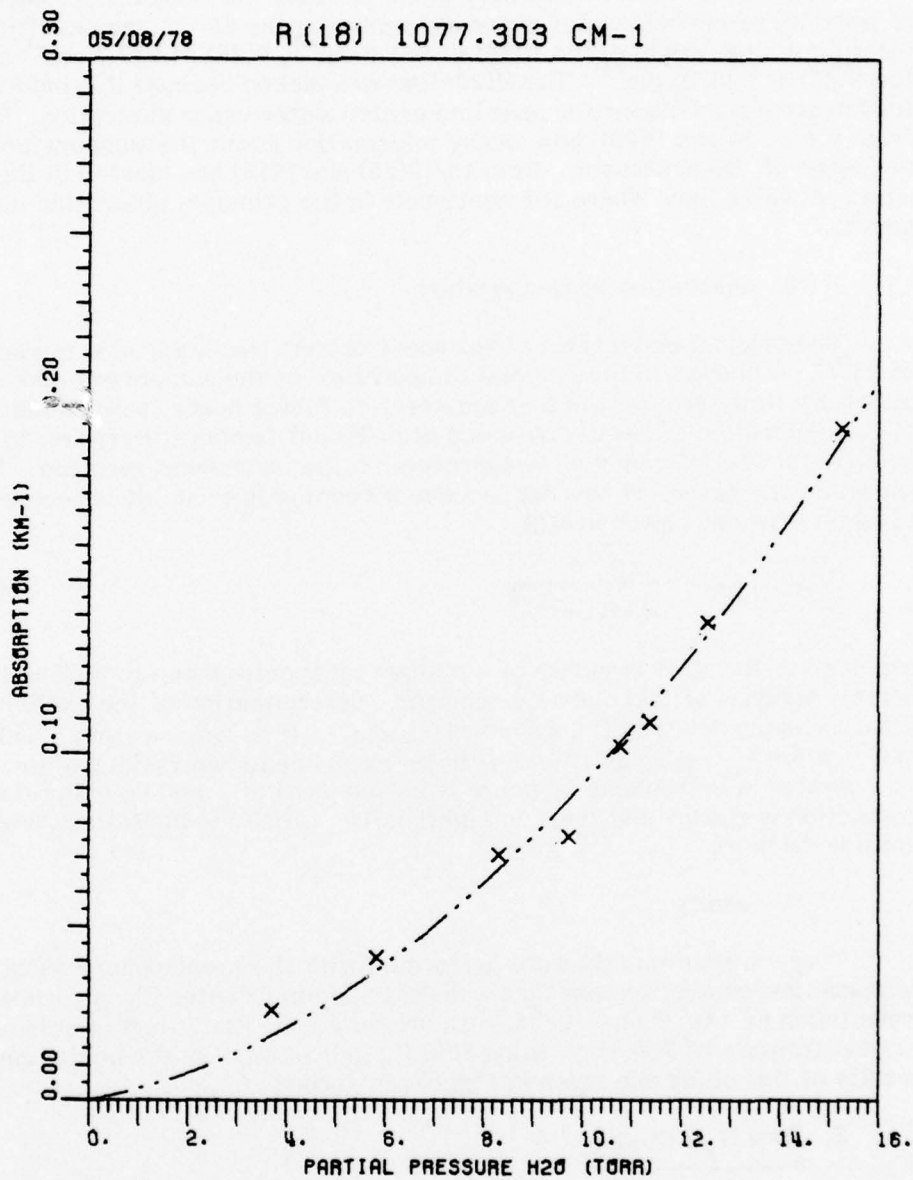


Figure 81. Measured H₂O in O₂ absorption coefficient at a total pressure of 760 Torr for the R(18) CO₂ laser line at 1077.303 cm⁻¹. Average spectrophone temperature was 22.6°C.

2. Temperature studies

Measurements were also performed to study the temperature dependence of pressure broadened water vapor absorption in the 10 μm region. Three laser lines were studied, the R(20) at 975.9 cm^{-1} , P(16) at 947.7 cm^{-1} and the P(20) at 944.19 cm^{-1} . The R(20) line was picked because it provides a temperature coefficient for near line center water vapor absorption. Results from the P(16) and P(20) data supply information about the temperature dependence of the continuum. Both the P(20) and P(16) are located in the far wings of water lines where the continuum is the principal absorption mechanism.

a. calibration vs temperature

The original calibration of the spectrophone was made at a temperature of 23°C . A change in the nominal temperature of the sample gas makes it necessary to determine whether a correction factor needs to be included in the calibration of results obtained at different temperatures; i.e., to compensate for the influence of temperature on the instrument response. To ascertain the nature of this dependence (assuming it exists) it is necessary to again consider equation (85)

$$(V_{\text{sig}}^F)_{\text{RMS}} = \frac{\sqrt{2} V_0}{\pi [1 + (\omega\tau)^2]^{1/2}} \quad (85)$$

which gives the RMS response of a cylindrical spectrophone to a Gaussian beam. Analysis of this question requires a determination of the explicit temperature dependence in the variables V_0 and τ . It so happens that τ is linear in T^{-1} while V_0 varies as $1/T$. For these experiments we also have that $(\omega\tau)^2 \gg 1$ so that spectrophone response is independent of T and no calibration correction is required at least to 1 part in 10^3 for the temperature range considered here.

b. results

These measurements were performed with the spectrophone using the temperature control system that was described in Chapter III. Measurements were taken at $\sim 16^\circ\text{C}$ and $\sim 28^\circ\text{C}$ with pressure broadened H_2O samples at a total pressure of 760 Torr, using 80% N_2 and 20% O_2 as the buffer gas. The results of this study are given in Figures 82 through 87.

3. Pure H_2O Studies

a. calibration vs pressure

For pure water vapor measurements the calibration coefficient of the spectrophone is dependent upon the particular water vapor pressure being considered. This situation is quite different from the pressure broadened studies in which the total pressure was held constant and the calibration could be considered independent of the H_2O partial pressure. In those experiments

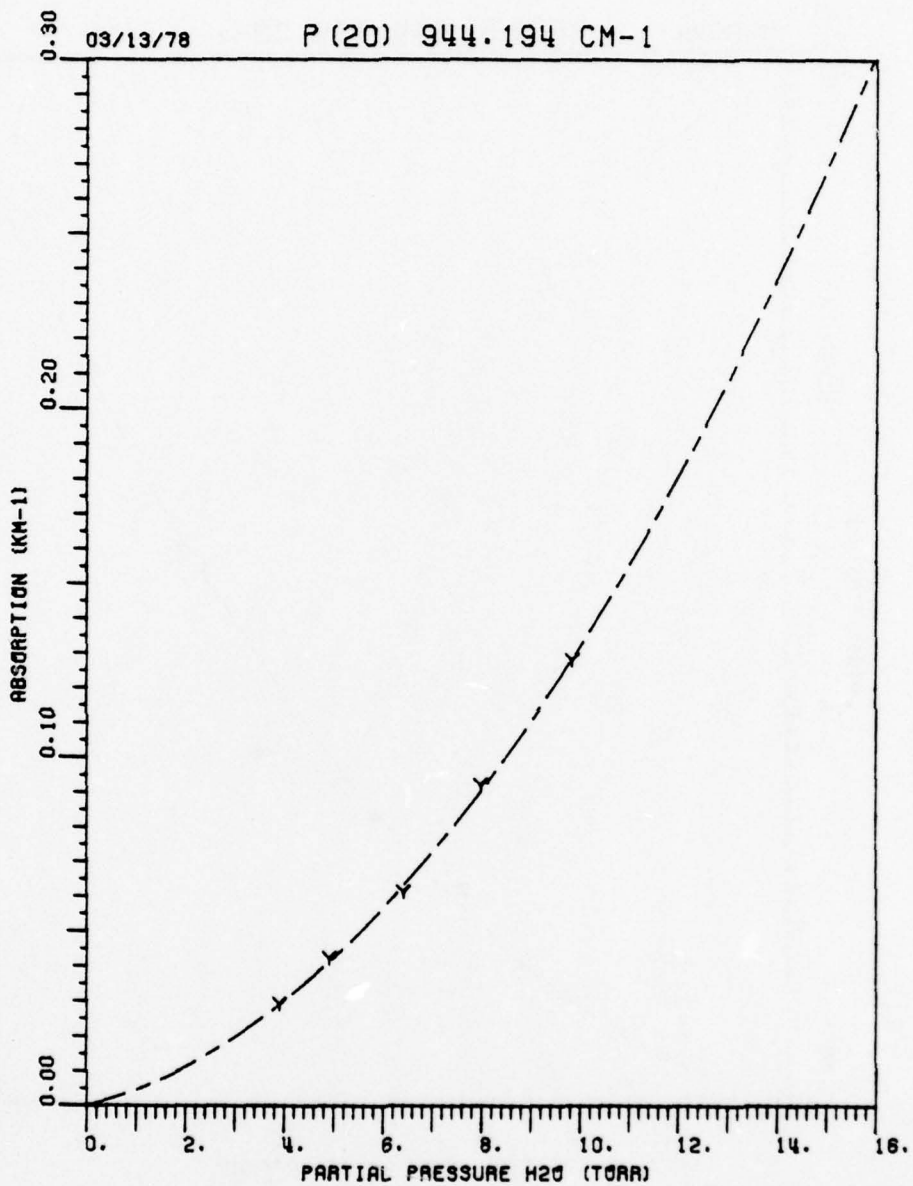


Figure 82. Measured H_2O in 80% N_2 and 20% O_2 absorption coefficient at a total pressure of 760 Torr for the P(20) CO_2 laser line at 944.194 cm^{-1} . Average spectrophone temperature was 15.9°C .

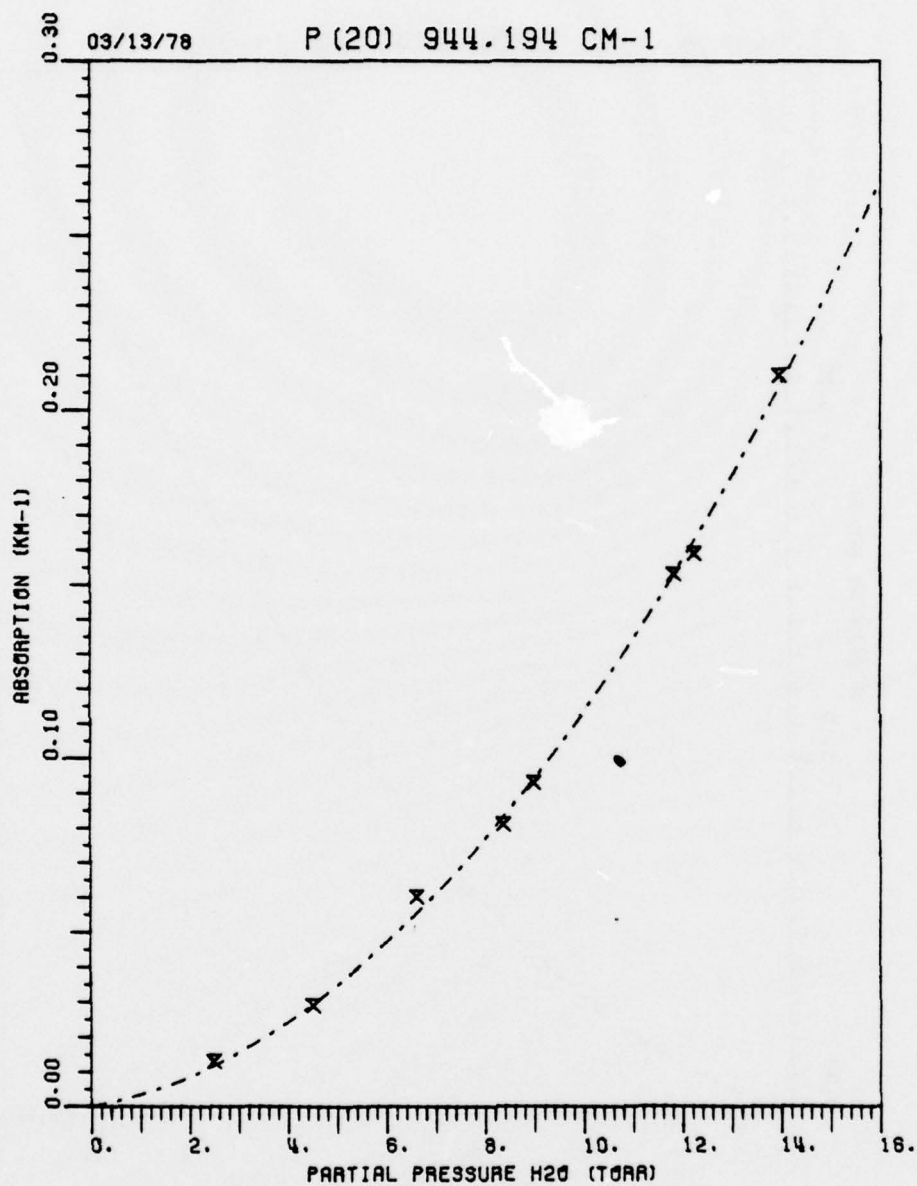


Figure 83. Measured H₂O in 80% N₂ and 20% O₂ absorption coefficient at a total pressure of 760 Torr for the P(20) CO₂ laser line at 944.194 cm⁻¹. Average spectrophone temperature was 27.6°C.

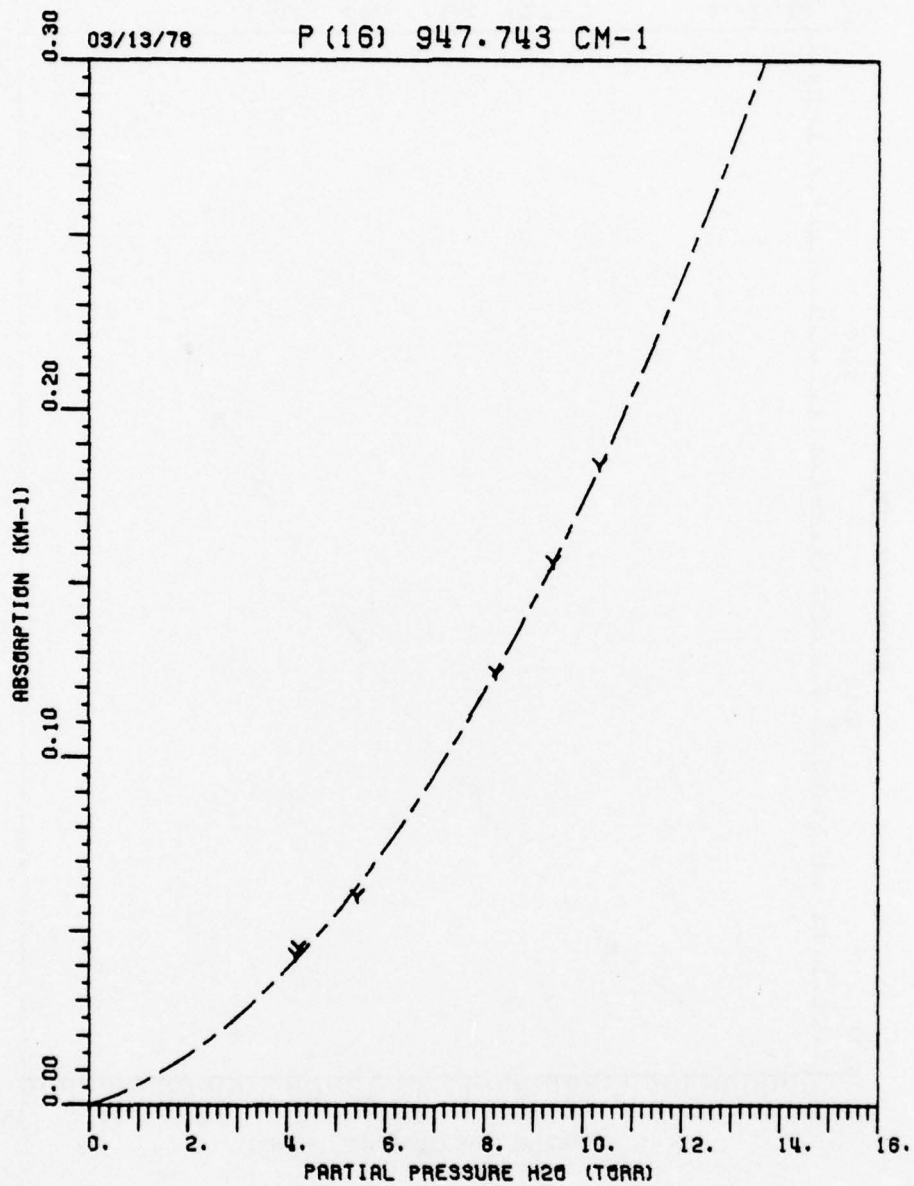


Figure 84. Measured H₂O in 80% N₂ and 20% O₂ absorption coefficient at a total pressure of 760 Torr for the P(16) CO₂ laser line at 947.743 cm⁻¹. Average spectrophone temperature was 16°C.

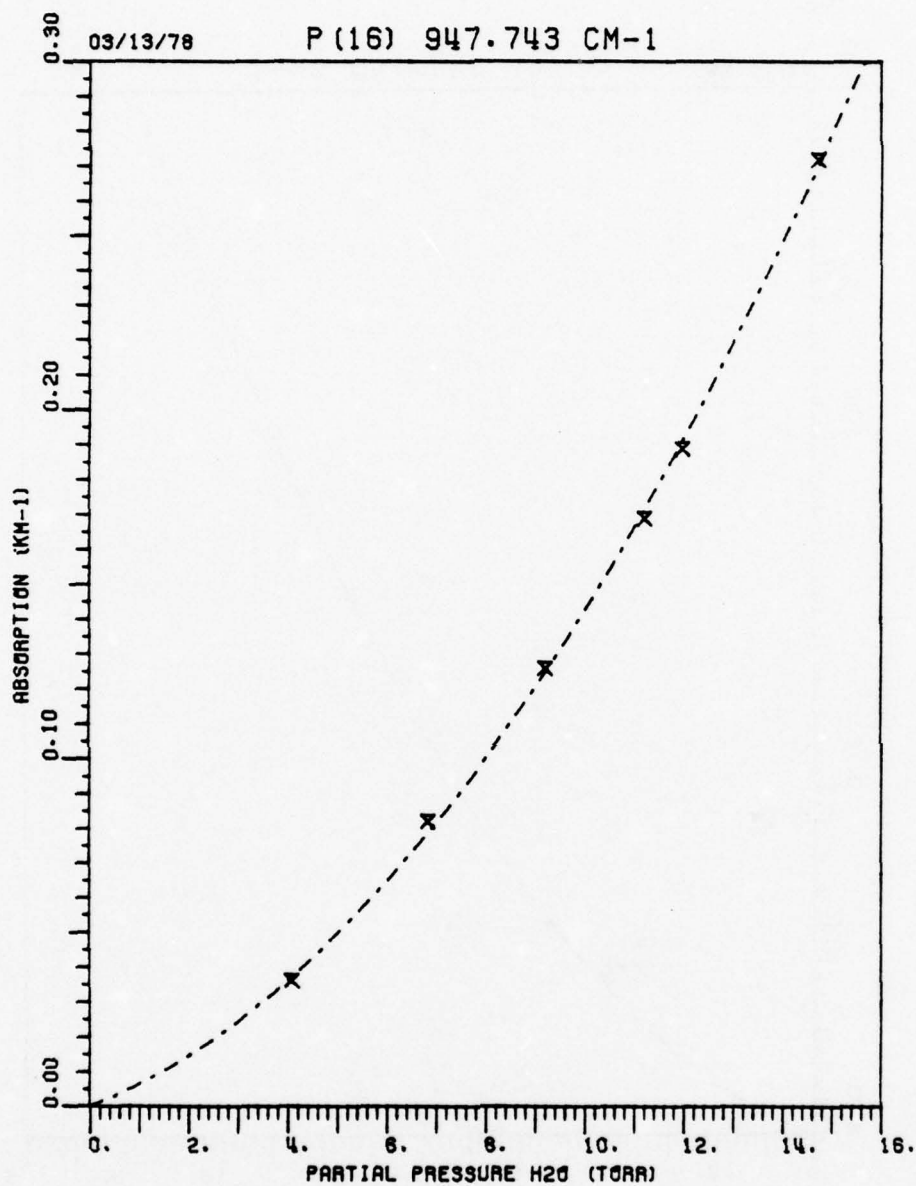


Figure 85. Measured H₂O in 80% N₂ and 20% O₂ absorption coefficient at a total pressure of 760 Torr for the P(16) CO₂ laser line at 947.743 cm⁻¹. Average spectrophone temperature was 27.6°C.

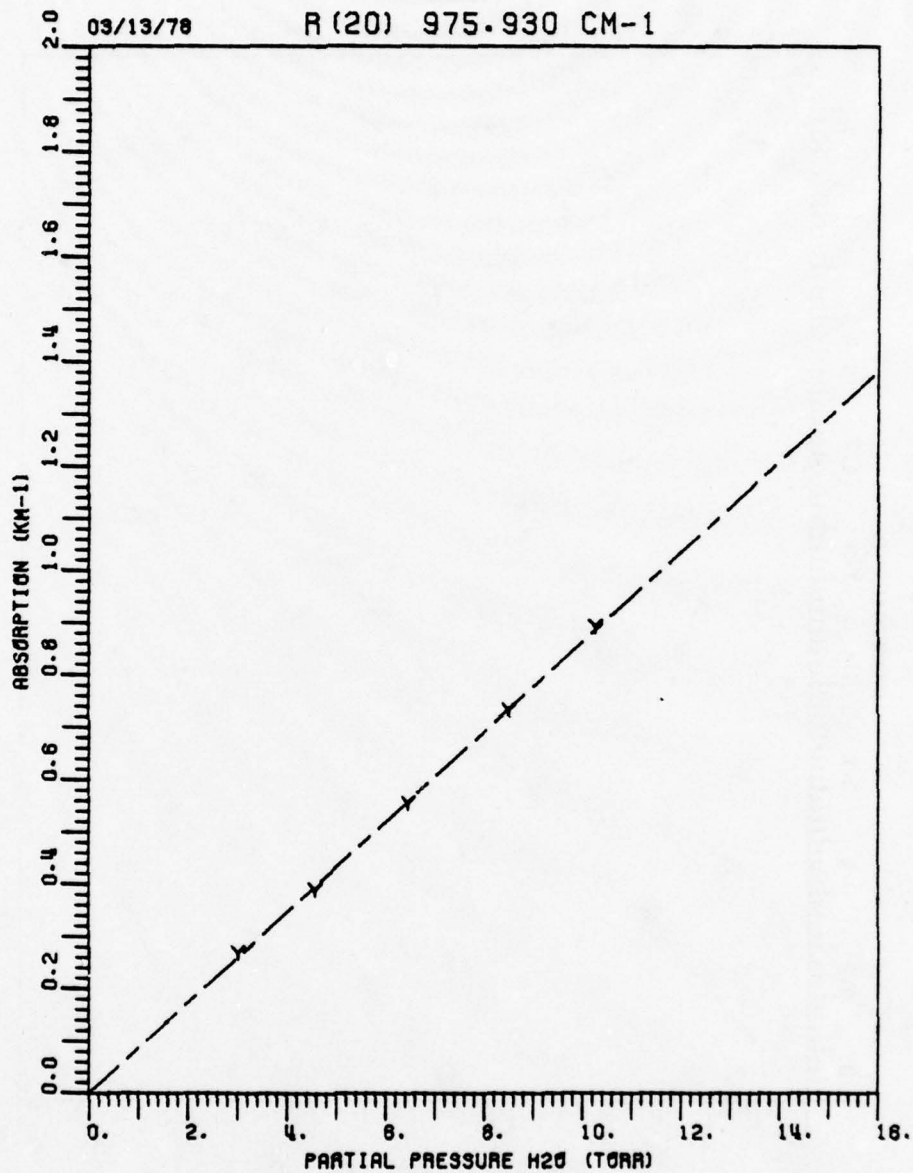


Figure 86. Measured H₂O in 80% N₂ and 20% O₂ absorption coefficient at a total pressure of 760 Torr for the R(20) CO₂ laser line at 975.930 cm⁻¹. Average spectrophone temperature was 15.6°C.

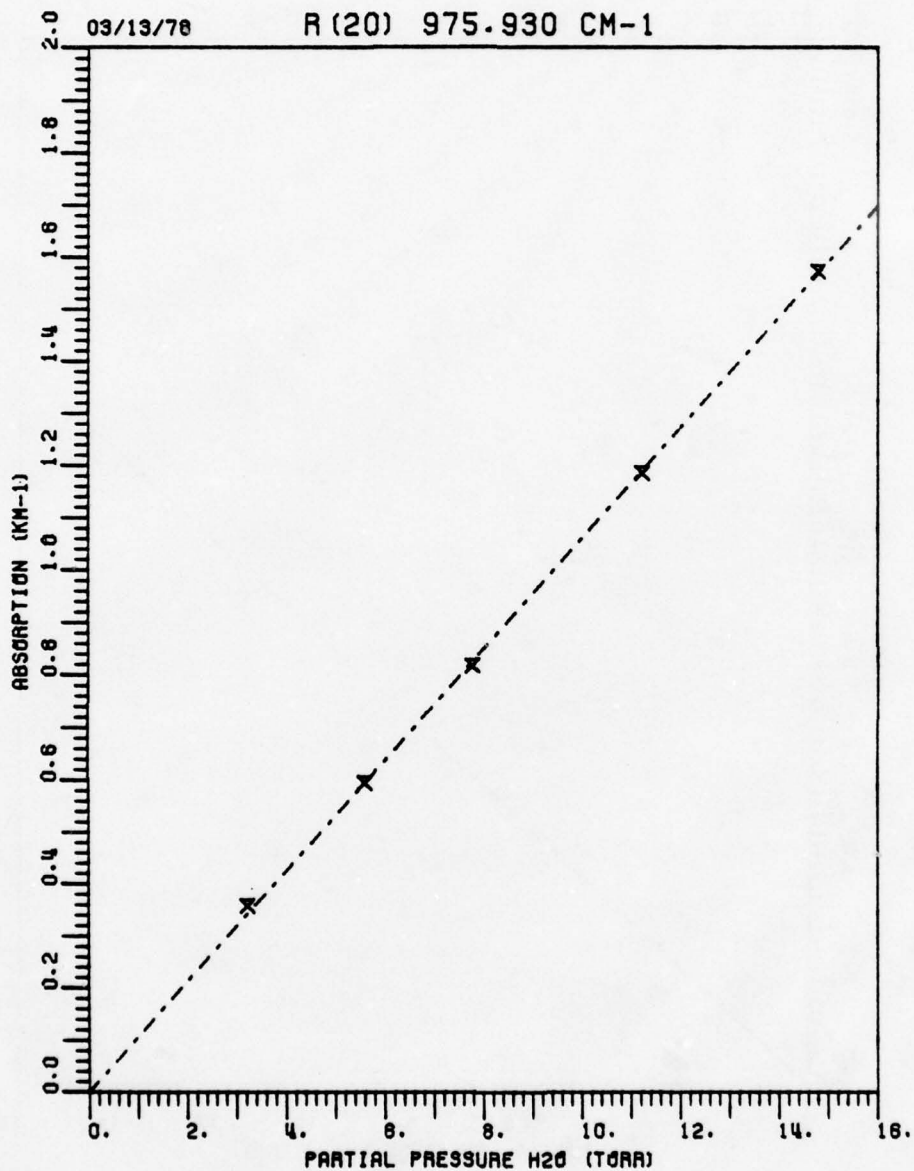


Figure 87. Measured H₂O in 80% N₂ and 20% O₂ absorption coefficient at a total pressure of 760 Torr for the R(20) CO₂ laser line at 975.930 cm⁻¹. Average spectrophone temperature was 27.6°C.

the thermodynamic properties of the sample gas are determined by the buffer gas and therefore, were essentially constant. The interpretation of the pure water vapor results becomes a much more complex problem because the magnitude and phase of the acoustic signal are dependent upon the total pressure; see the analysis of the spectrophone response, especially Equations (89) and (90).

To understand the nature of this pressure dependence, consider the following derivation of the calibration coefficient. First of all, we assume that the absorption coefficient of a pure water vapor sample at a pressure P_0 is known from White cell studies and is equal to α_0 . The calibration constant at the pressure P_0 is then given by

$$\theta(P_0) = \frac{\alpha_0}{(S/W)_0} \quad (96)$$

where $(S/W)_0$ is the normalized response of the spectrophone for a pure H_2O sample, also at the pressure P_0 . (It should be noted that a complete calibration of the spectrophone can easily be obtained by this technique, i.e., by performing a sequence of measurements at many different pressures P_0 . This, in fact, was the method used to calibrate the results given later in this section.) The absorption coefficient for a measurement at any other pressure P is found from the expression

$$\alpha(P) = \theta(P) (S/W), \quad (97)$$

where $\theta(P)$ is the calibration factor at the pressure P . Multiplying by $\theta(P_0)/\theta(P_0)$ we have

$$\alpha(P) = \frac{\theta(P)}{\theta(P_0)} \theta(P_0)(S/W). \quad (98)$$

Next we substitute from Equation (89) to obtain an expression for the ratio $\theta(P)/\theta(P_0)$ with the result that

$$\alpha(P) = \left[\frac{(P_0/P)^2 + (\omega\tau_0)^2}{1 + (\omega\tau_0)^2} \right]^{\frac{1}{2}} \theta(P_0)(S/W) \quad (99)$$

where τ_0 is the thermal relaxation time of the sample cell at the pressure P_0
and ω is the angular frequency of the mechanical chopper.

Therefore $\theta(P)$ can be written as

$$\theta(P) \equiv \frac{\alpha(P)}{(S/W)} = \left[\frac{(P_0/P)^2 + (\omega\tau_0)^2}{1 + (\omega\tau_0)^2} \right]^{\frac{1}{2}} \theta(P_0) \quad (100)$$

and for the parameters used in this study we have that

$$\theta(P) \sim \frac{P}{P_0} \theta(P_0) \quad (101)$$

This equation has been plotted in Figure 88. The solid curve represents the calibration function $\theta(P/P_0)$ as a function of the relative pressure (P/P_0) with the reference pressure P_0 taken as 8.87 Torr and $\theta(1)$ equal to 0.411. This reference pressure P_0 was arbitrarily chosen from those which were measured with the spectrophone. $\theta(1)$ was obtained by taking the ratio of White cell data, see Figure 122, and the normalized optoacoustic signal S/W for the pressure P_0 . The experimental data, given by the triangles, were obtained from spectrophone and White cell measurements of pure H_2O for the R(20) laser line at 975.9 cm^{-1} . This plot shows a general agreement between the pressure dependence indicated by the measured data and that given in Equation (101). However, to insure accurate results, the experimental data were used to calibrate the pure water vapor measurements given in this section.

b. results

This section contains the results of the spectrophone pure water vapor measurements which were calibrated using the technique just described. One laser line has been studied, the P(20) at 944.2 cm^{-1} , see Figure 89. In this figure the measured absorption coefficient, indicated by the asterisks, has been plotted vs the total pressure squared, i.e., p^2 in $(\text{Torr})^2$. The dashed line indicates a fit of those data to an equation of the form $k = Bp^2$, where k is the absorption coefficient and p is the pressure in Torr. The choice of this particular curve fit will be discussed in Chapter VI where the absolute accuracy of these data will also be considered.

B. White Cell Data and a Comparison with Spectrophone Results

In the remainder of this chapter the results of the White cell water vapor measurements are presented and compared (where possible) with the spectrophone data which has been given in the previous section. This comparison is made by plotting the two respective (spectrophone and White cell) sets of data on the same figure for all those laser lines in which an experiment was performed with both instruments. Laser frequencies which have only been treated in White cell experiments are easily distinguished in these figures as having only one set of data plotted.

With two exceptions, these transmittance measurements were performed with a path length of $\sim 1.5 \text{ km}$ and at room temperature. The appropriate laser frequency is denoted at the top of each plot and the average temperature of the sample gas is also listed in each figure. The first set of results are measurements of pressure broadened samples at a total pressure of 760 Torr. Three different buffer gases were employed in these measurements, nitrogen, 80% N_2 and 20% O_2 artificial air and 60% N_2 and 40% O_2 . The last set of results given in this chapter consists of data from pure water vapor studies.

09/20/78 H2O CALIBRATION AT R(20)

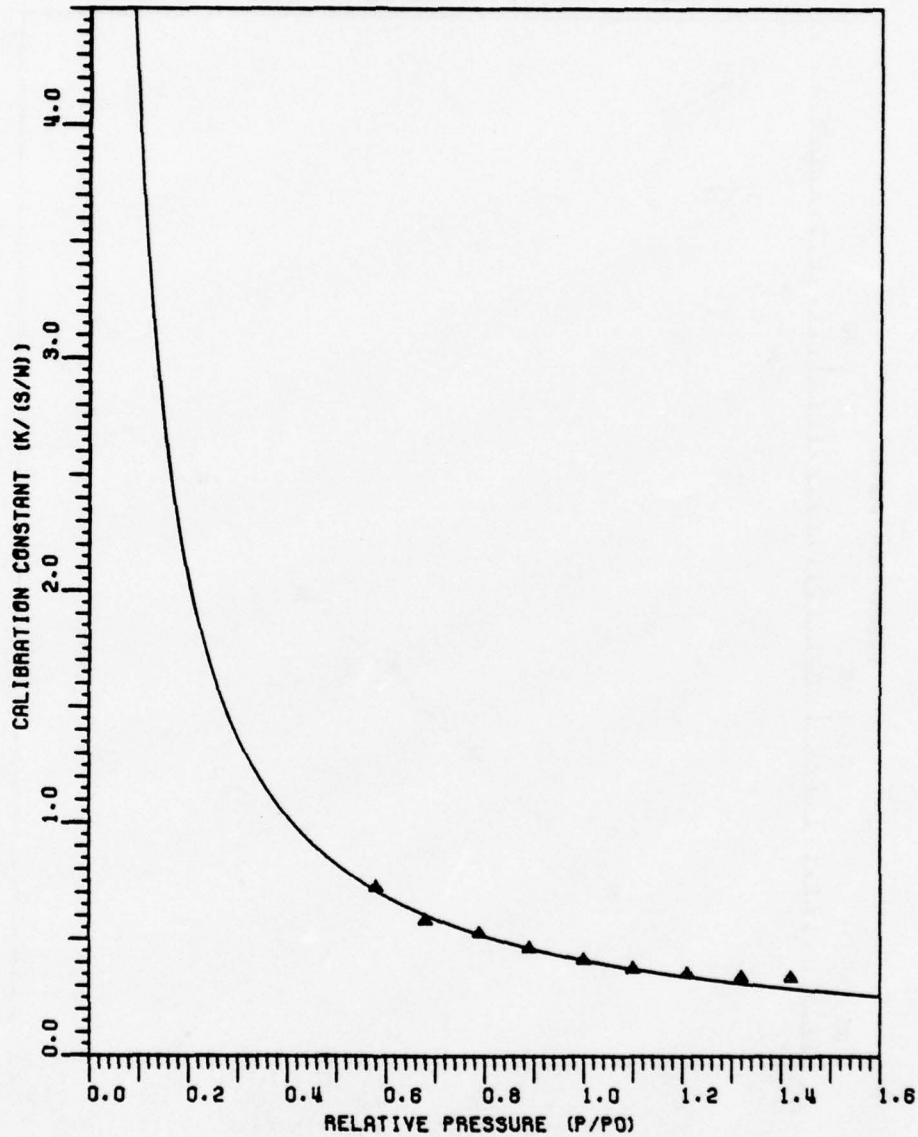


Figure 88. Plot of the calibration function vs relative pressure. The solid curve — gives $\theta(P/P_0)$ as a function of (P/P_0) using Equation (101) and $\theta(1) = 0.411$. The Δ 's are experimental data obtained for the R(20) laser line at 975.9 cm^{-1} .

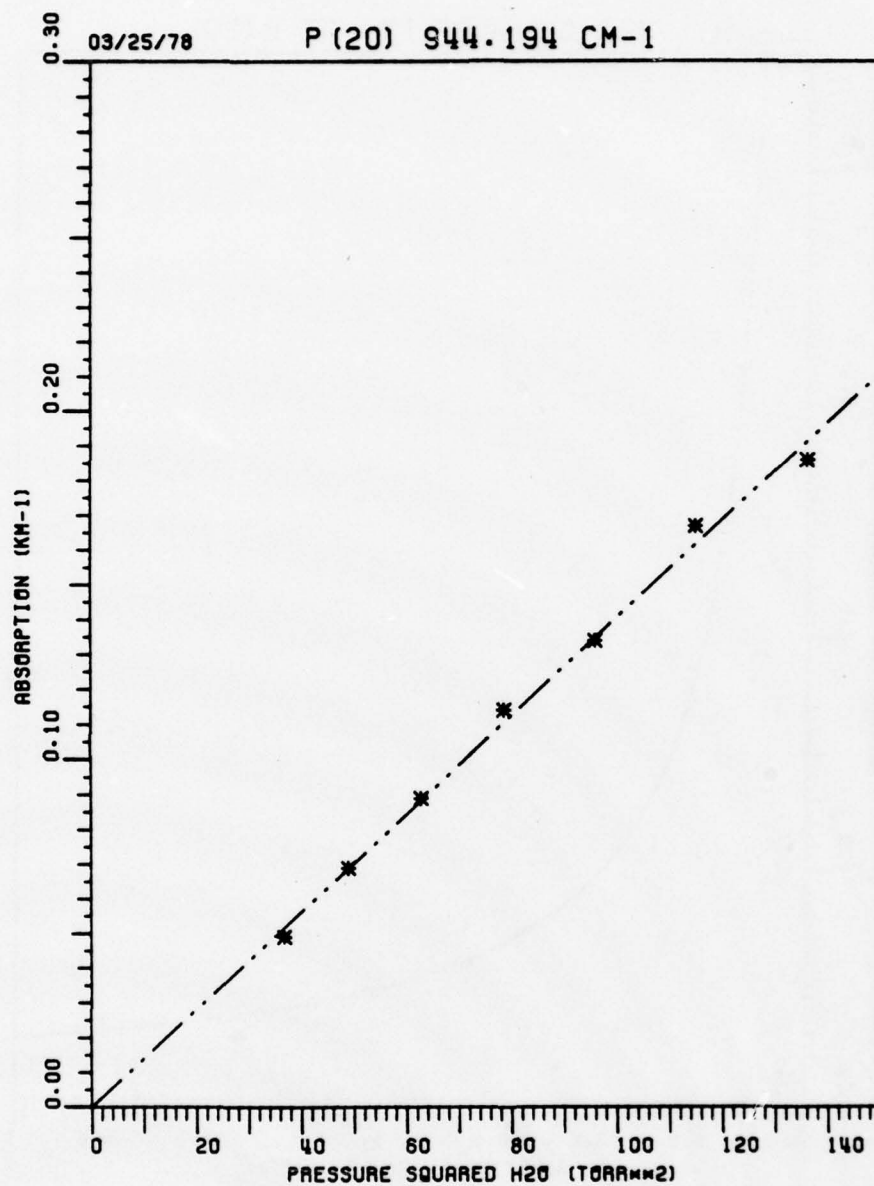


Figure 89. Measured water vapor absorption coefficient plotted as a function of the total pressure squared for the P(20) CO₂ laser line at 944.194 cm⁻¹. Average spectrophone temperature was 19°C.

1. Artificial air broadened samples

The 80% N₂ and 20% O₂ buffer gas for these measurements was obtained from commercially mixed cylinders of artificial air. The 60% N₂ and 40% O₂ gas was achieved by mixing nitrogen and oxygen in the designated ratio. In each experiment the background transmission was determined by filling the cell to one atm with a H₂O free sample of the appropriate broadening gas.

a. 100% N₂ results

Absorption in nitrogen broadened water vapor samples was studied (with the White cell) at 20 CO₂ laser lines in the 9.4 and 10.4 μm bands. The results of these measurements are given in Figures 90 through 109. On all of these figures the triangle indicates the measured data point, while the solid curve represents the best fit of those data to an equation of the form $k=Ap+Bp^2$, where k is the absorption coefficient in km^{-1} and p is the partial pressure of water in Torr. An exception is for the R(20) line at 975.93 cm^{-1} where the data has been fit to a linear equation, i.e., $k=Ap$. The choice of these particular curve fits will be discussed in Chapter VI.

A comparison with results of the previous sections has been made by plotting the spectrophone data, indicated by the diamonds on the corresponding figure with the White cell data. The curve fits for the optoacoustic results are indicated by the broken line. Discussion of the agreement between the results obtained with these two techniques is deferred until Chapter VI.

b. 80% N₂ and 20% O₂ results

Absorption in artificial air broadened water vapor samples was studied at five CO₂ laser lines in the 10.4 μm band. The results of these measurements are given in Figures 110 through 114. In all of these figures except R(20) the cross indicates the measured White cell data points, while the broken line represents the best fit of those data to an equation of the form $k=Ap+Bp^2$. For the R(20) line at 975.9 cm^{-1} the data has been fit to a linear equation, $k=Ap$.

Comparison with results of the previous section has been made by plotting the spectrophone data, indicated by the diamonds, on the same figure with the White cell data.

c. 60% N₂ and 40% O₂ results

Absorption in 60-40 air broadened water vapor samples was studied at five CO₂ laser lines in the 10.4 μm band. The results of these measurements are given in Figures 115 through 119. In all these figures except for R(20) the arrow heads indicate the measured White cell data points, while the dotted line represents the best fit of those data to an equation of the form $k=Ap+Bp^2$. For the R(20) line at 975.9 cm^{-1} the data has been fit to a linear equation, $k=Ap$.

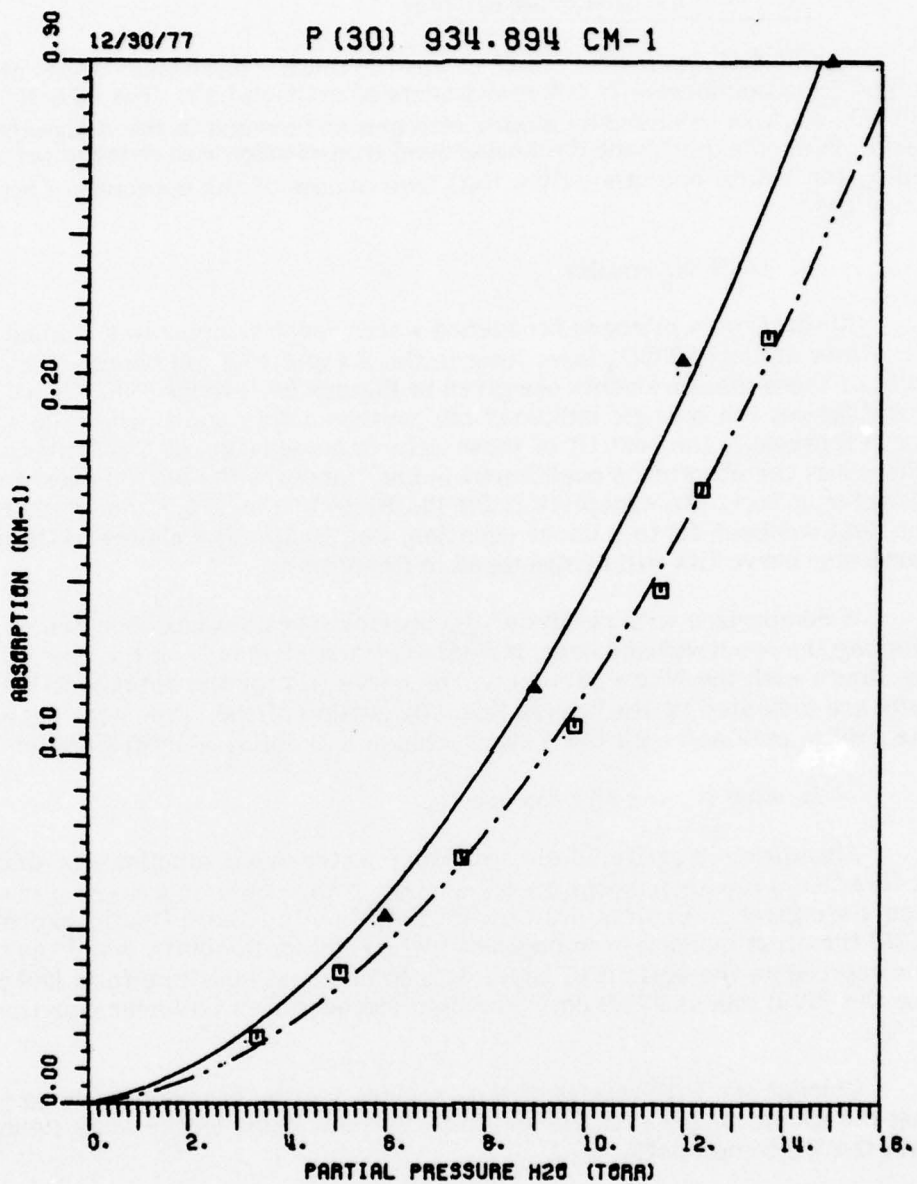


Figure 90. Measured H₂O in N₂ absorption coefficient at a total pressure of 760 Torr for the P(30) CO₂ laser line at 934.894 cm⁻¹. The White cell data, represented by the symbol Δ, was obtained at an average temperature of 22.5°C. The spectrophone data, represented by the symbol ◻, was obtained at an average temperature of 24.5°C.

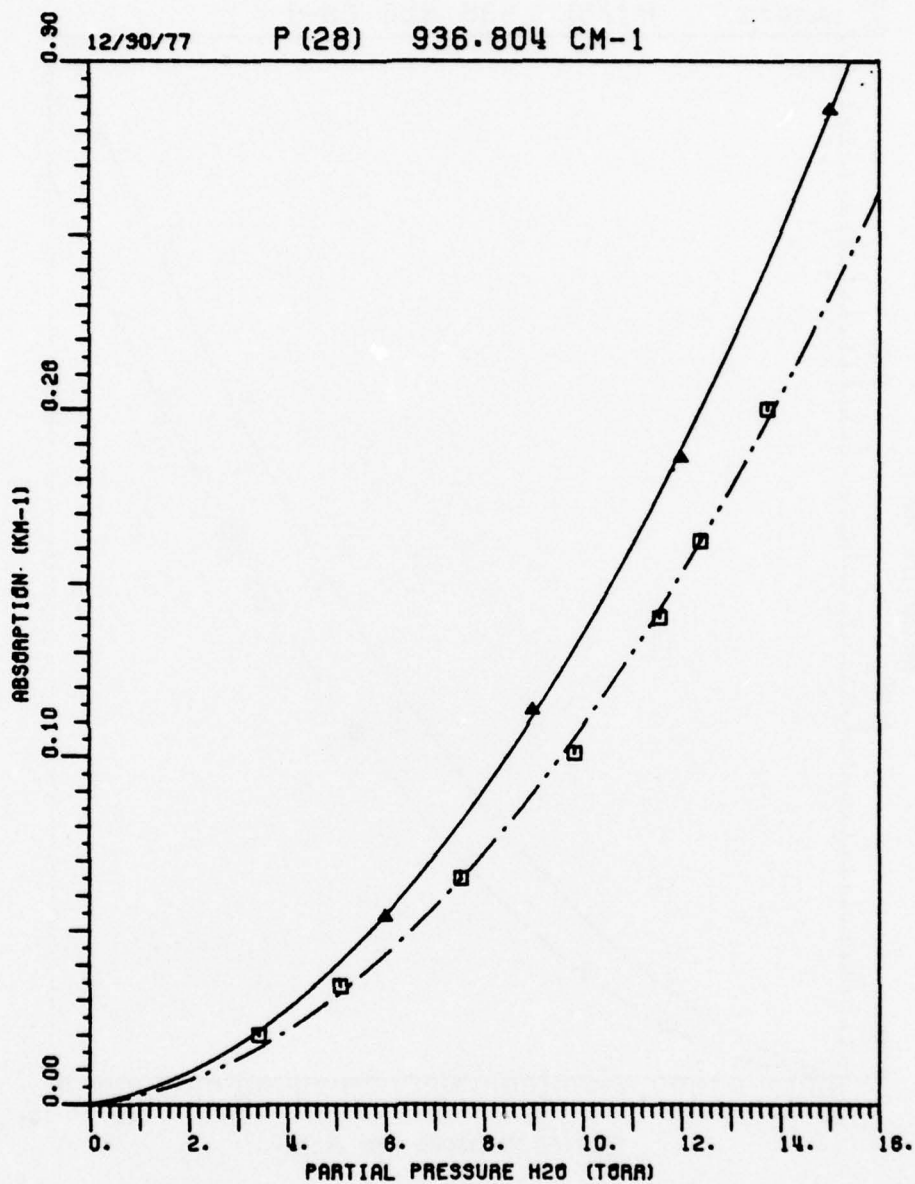


Figure 91. Measured H₂O in N₂ absorption coefficient at a total pressure of 760 Torr for the P(28) CO₂ laser line at 936.804 cm⁻¹. The White cell data, represented by the symbol Δ, was obtained at an average temperature of 22.5°C. The spectrophone data, represented by the symbol □, was obtained at an average temperature of 24.5°C.

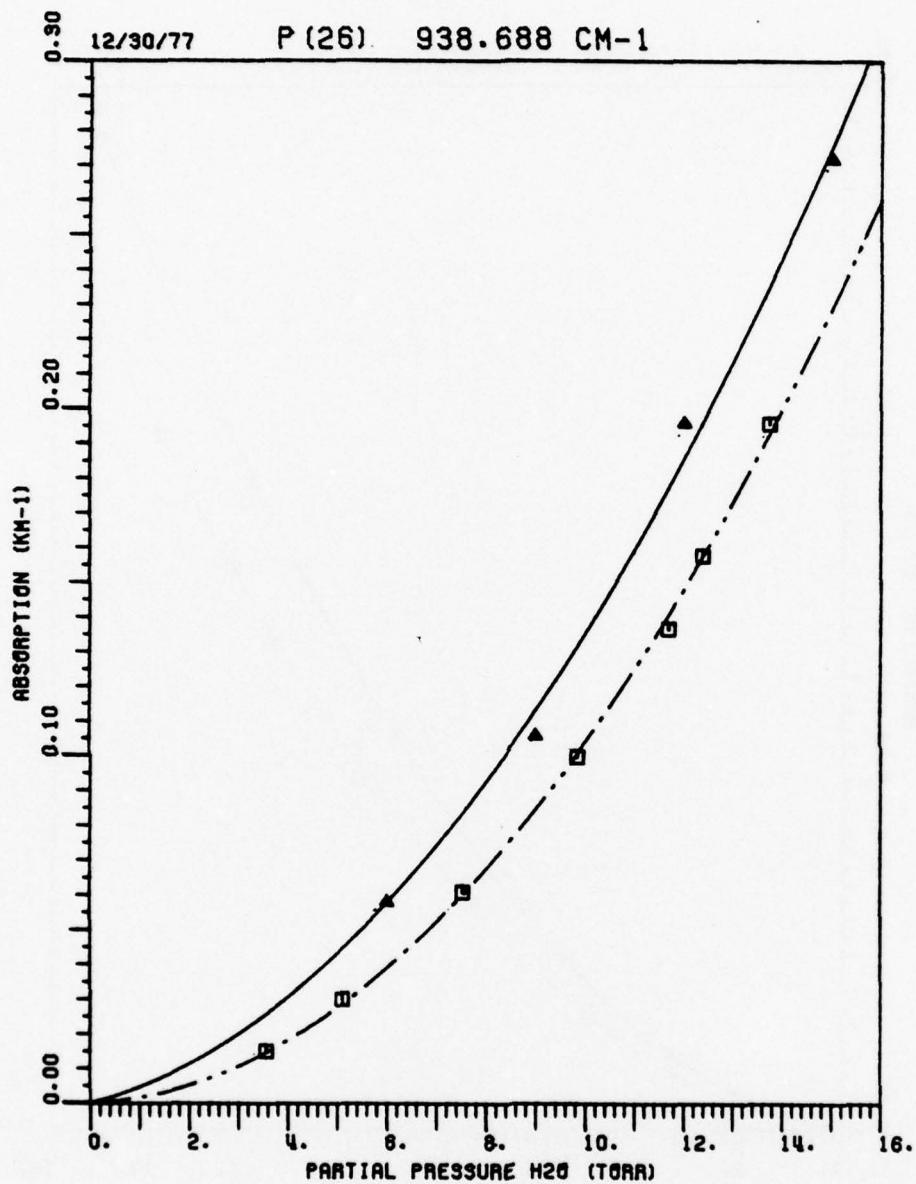


Figure 92. Measured H₂O in N₂ absorption coefficient at a total pressure of 760 Torr for the P(26) CO₂ laser line at 938.688 cm⁻¹. The White cell data, represented by the symbol Δ, was obtained at an average temperature of 22.5°C. The spectrophone data, represented by the symbol ◻, was obtained at an average temperature of 24.5°C.

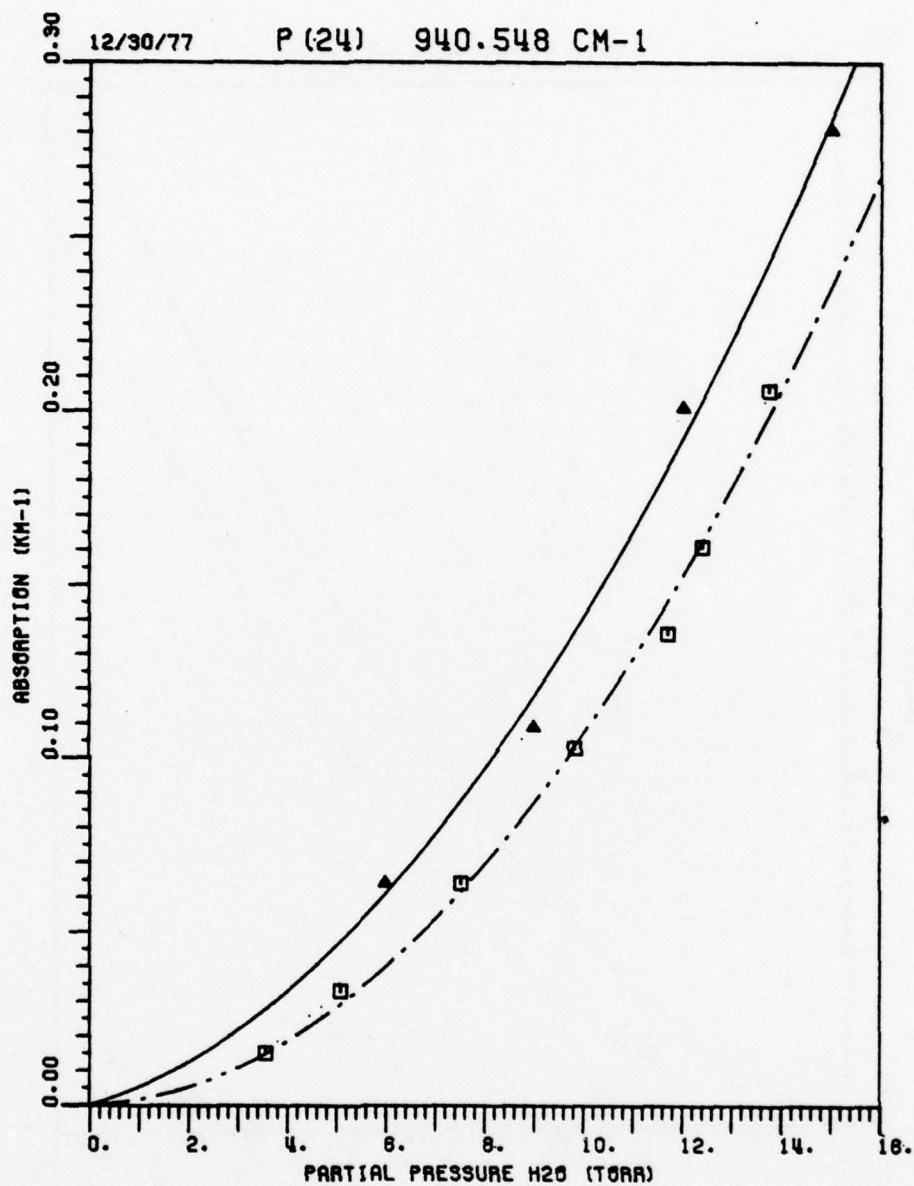


Figure 93. Measured H₂O in N₂ absorption coefficient at a total pressure of 760 Torr for the P(24) CO₂ laser line at 940.548 cm⁻¹. The White cell data, represented by the symbol Δ, was obtained at an average temperature of 22.5°C. The spectrophone data, represented by the symbol □, was obtained at an average temperature of 24.5°C.

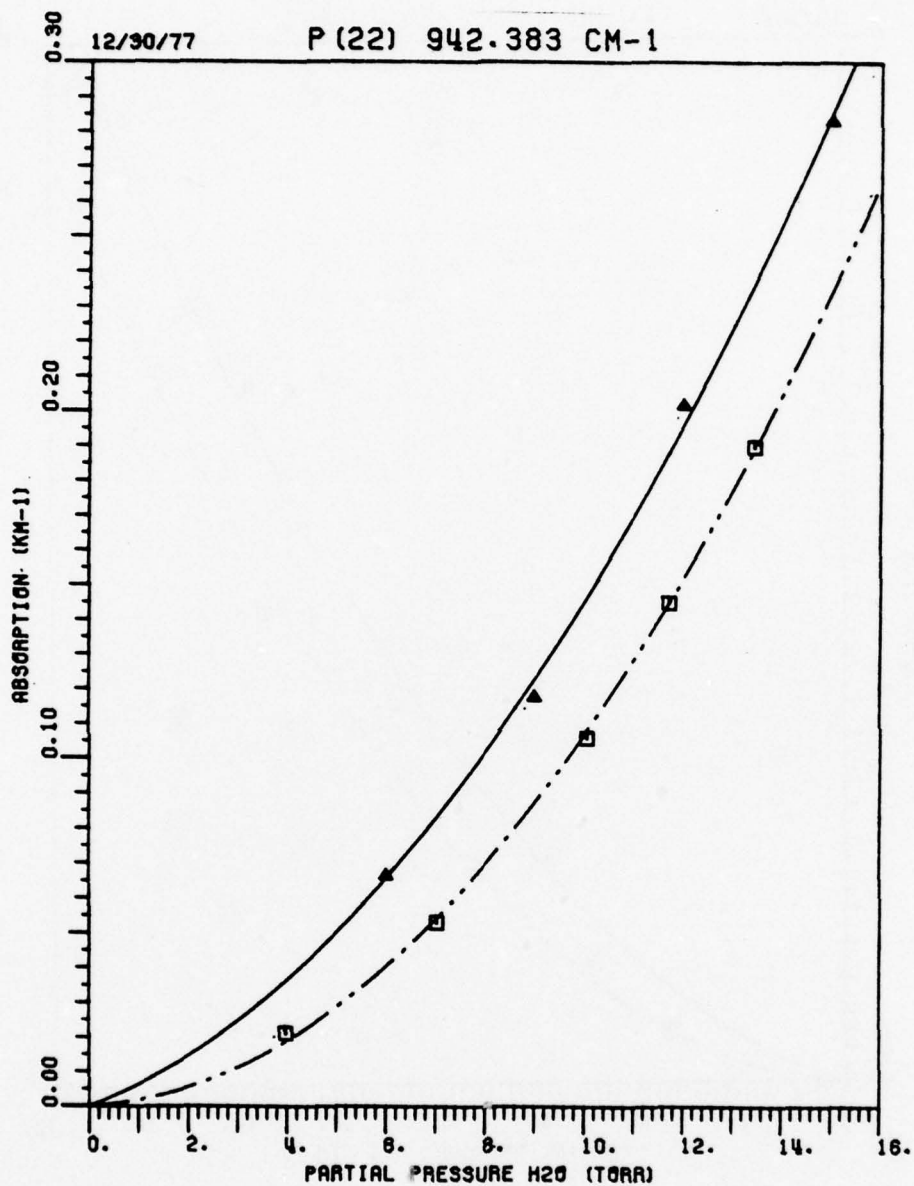


Figure 94. Measured H₂O in N₂ absorption coefficient at a total pressure of 760 Torr for the P(22) CO₂ laser line at 942.383 cm⁻¹. The White cell data, represented by the symbol Δ, was obtained at an average temperature of 22.5°C. The spectrophone data, represented by the symbol □, was obtained at an average temperature of 24.5°C.

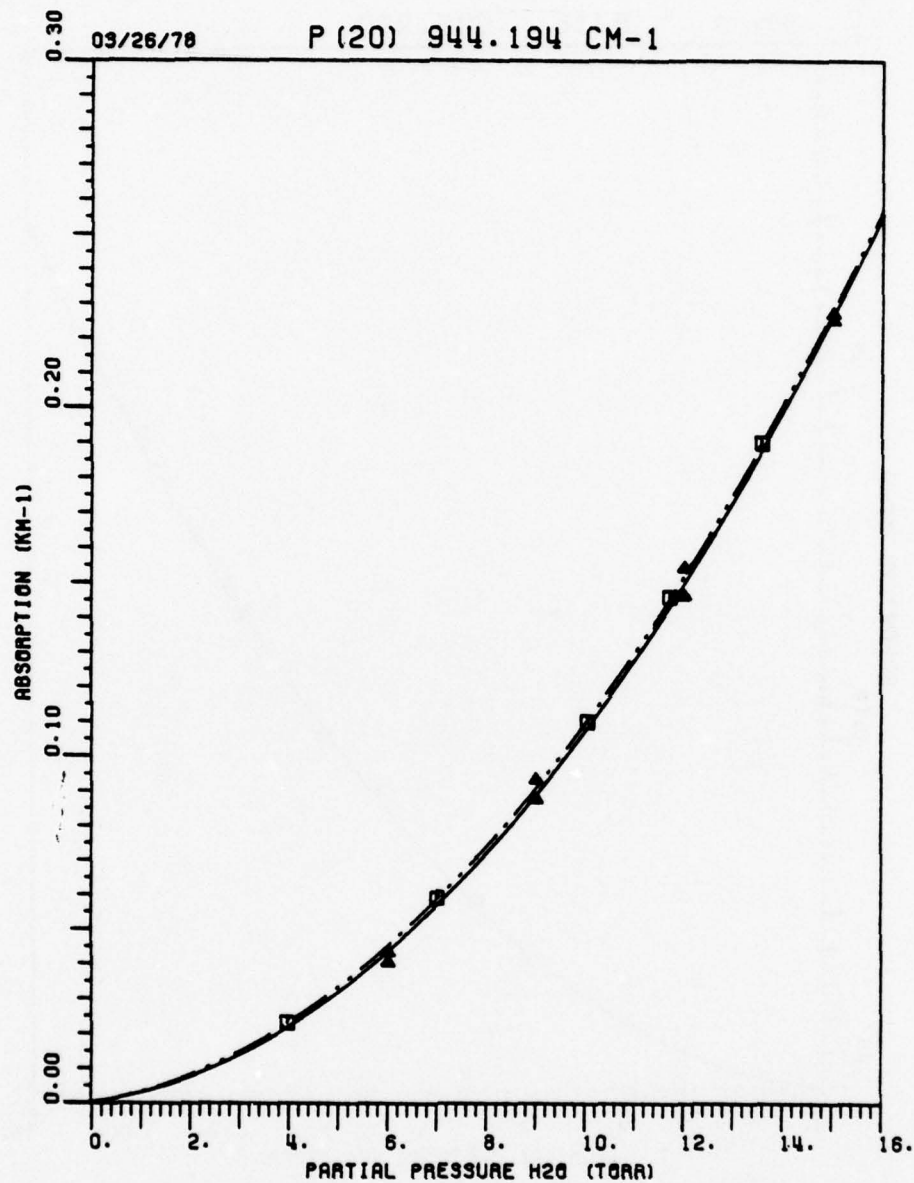


Figure 95. Measured H₂O in N₂ absorption coefficient at a total pressure of 760 Torr for the P(20) CO₂ laser line at 944.194 cm⁻¹. The White cell data, represented by the symbol Δ, was obtained at an average temperature of 22.5°C. The spectrophone data, represented by the symbol □, was obtained at an average temperature of 23.5°C.

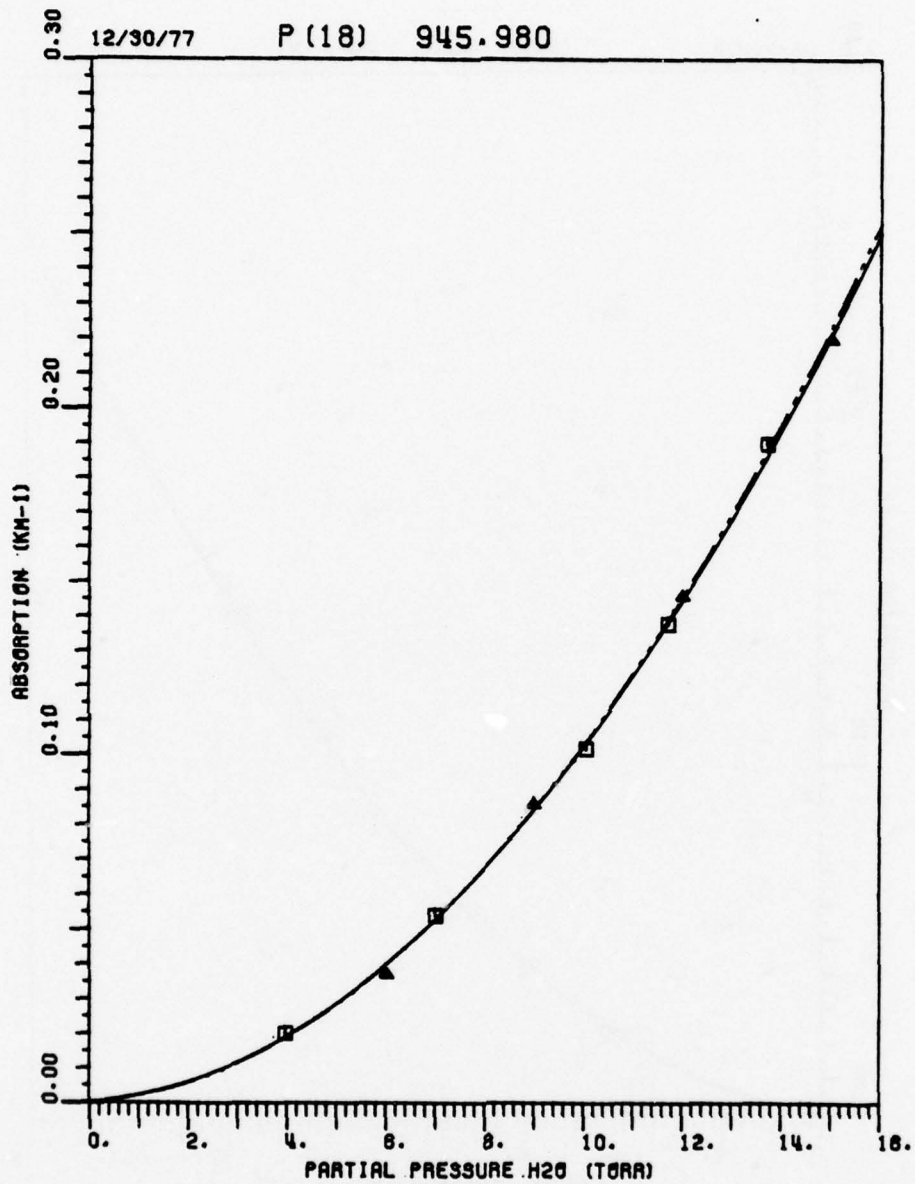


Figure 96. Measured H₂O in N₂ absorption coefficient at a total pressure of 760 Torr for the P(18) CO₂ laser line at 945.980 cm⁻¹. The White cell data, represented by the symbol Δ , was obtained at an average temperature of 22.5°C. The spectrophone data, represented by the symbol \square , was obtained at an average temperature of 24.5°C.

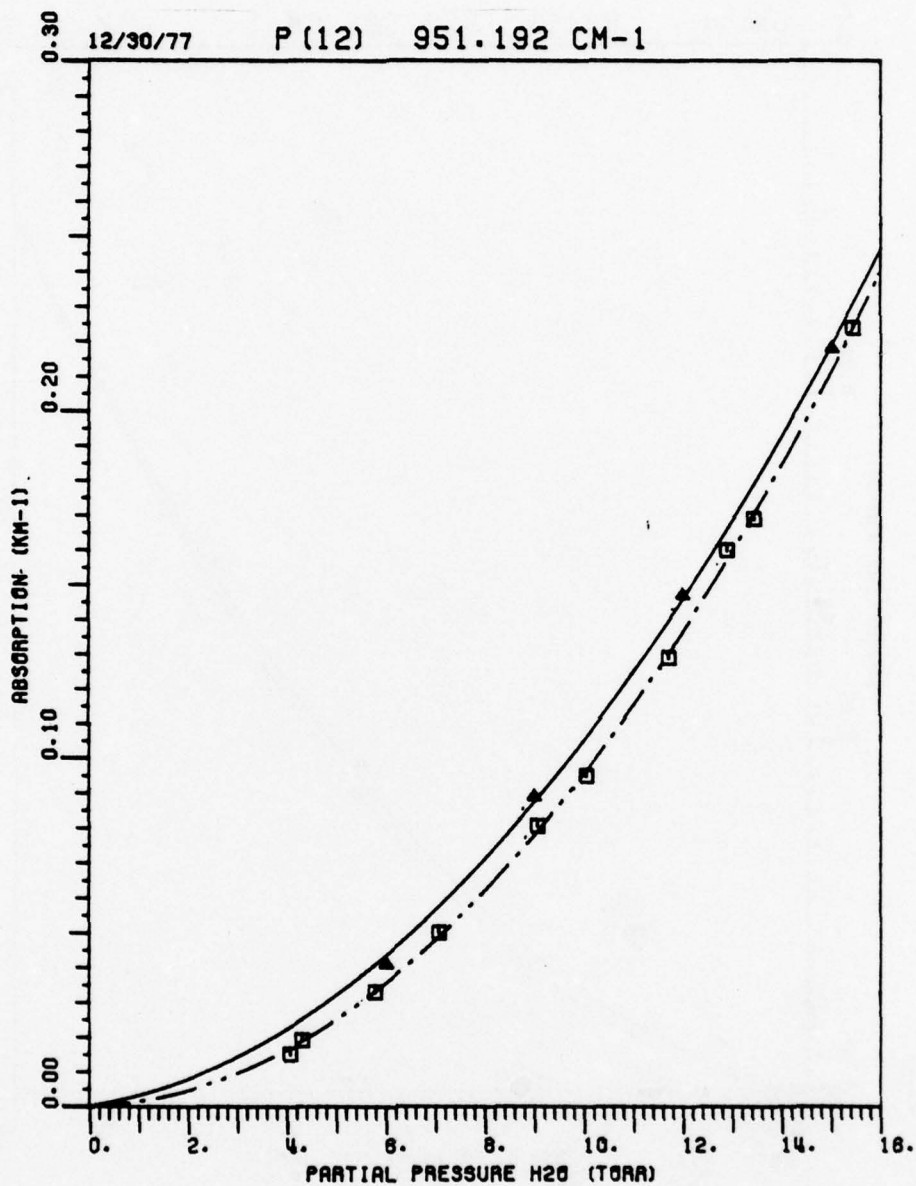


Figure 97. Measured H₂O in N₂ absorption coefficient at a total pressure of 760 Torr for the P(12) CO₂ laser line at 951.192 cm⁻¹. The White cell data, represented by the symbol Δ, was obtained at an average temperature of 22.5°C. The spectrophone data, represented by the symbol ◻, was obtained at an average temperature of 24.5°C.

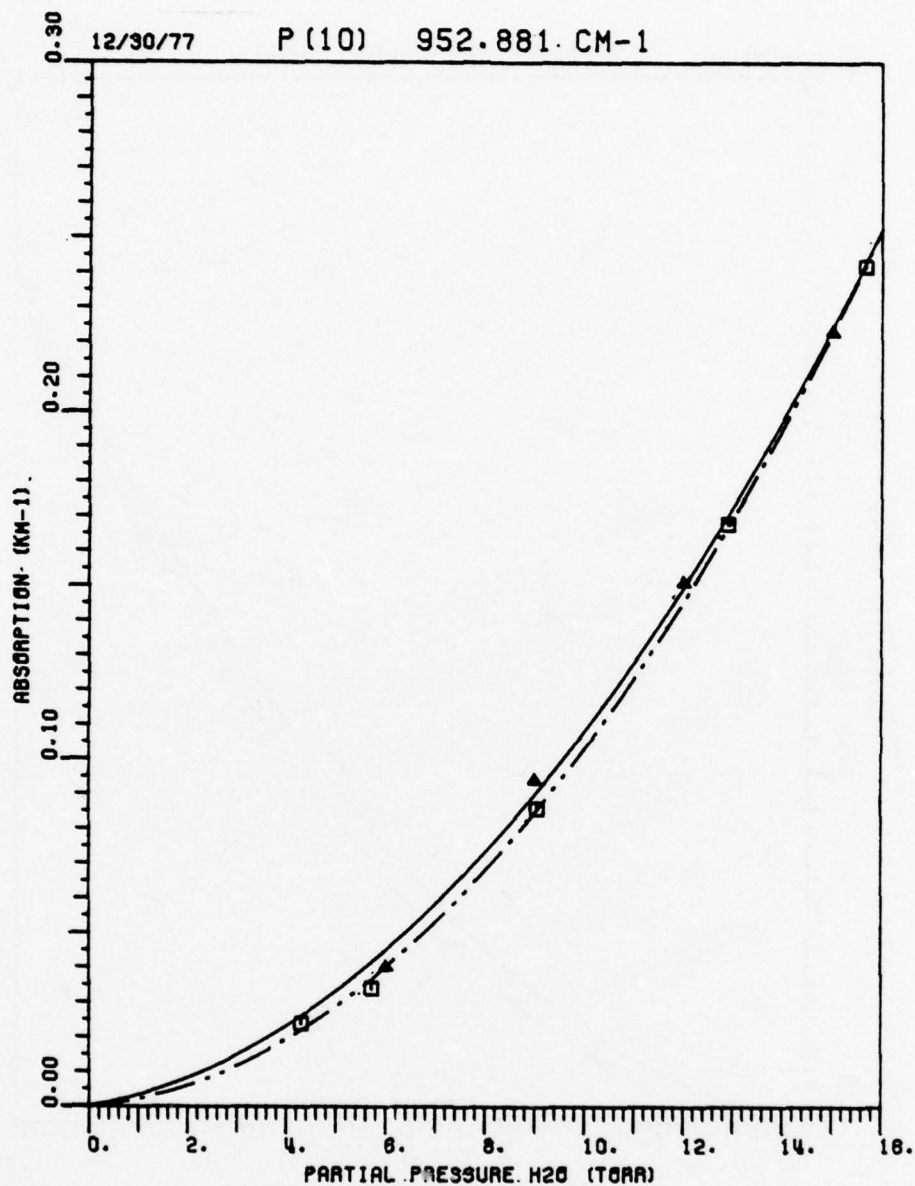


Figure 98. Measured H₂O in N₂ absorption coefficient at a total pressure of 760 Torr for the P(10) CO₂ laser line at 952.881 cm⁻¹. The White cell data, represented by the symbol Δ, was obtained at an average temperature of 22.5°C. The spectrophone data, represented by the symbol □, was obtained at an average temperature of 24.5°C.

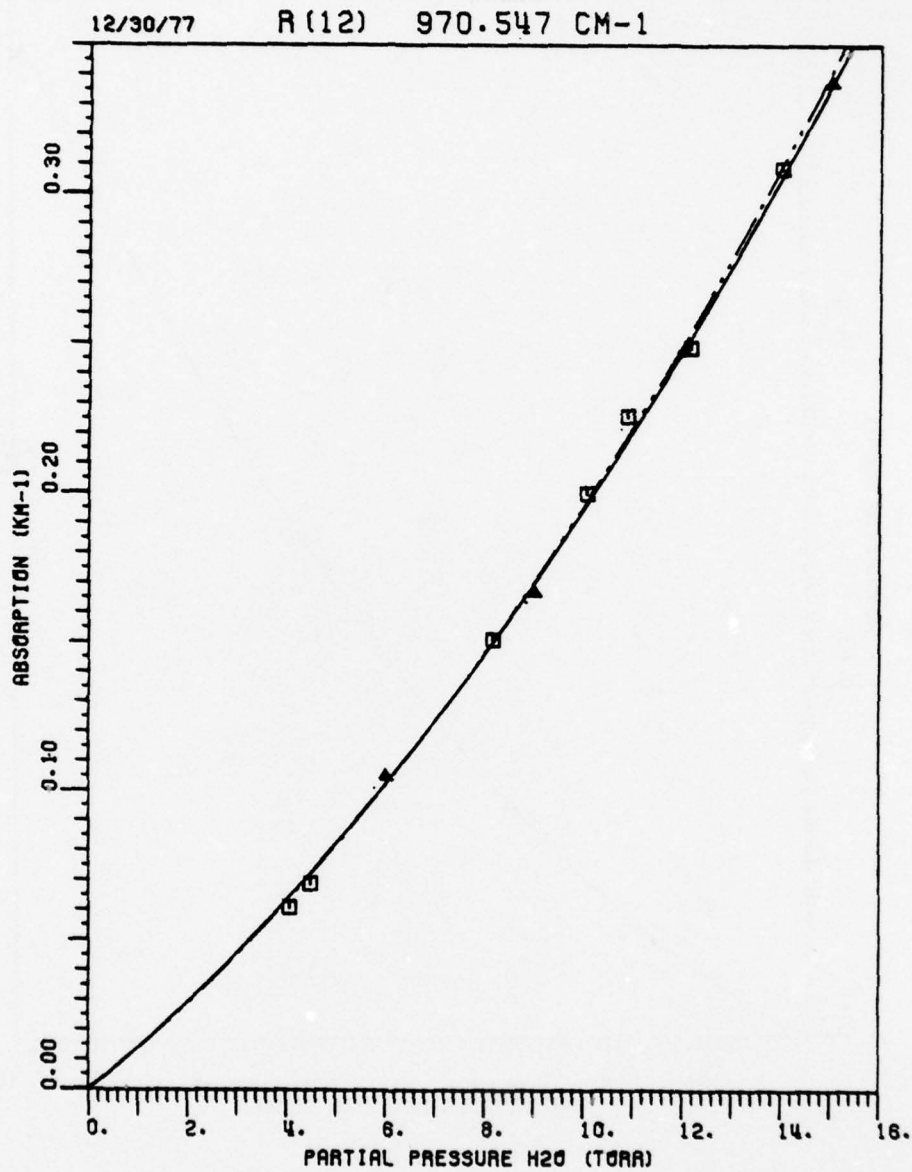


Figure 99. Measured H₂O in N₂ absorption coefficient at a total pressure of 760 Torr for the R(12) CO₂ laser line at 970.547 cm⁻¹. The White cell data, represented by the symbol △, was obtained at an average temperature of 22.5°C. The spectrophone data, represented by the symbol □, was obtained at an average temperature of 24.5°C.

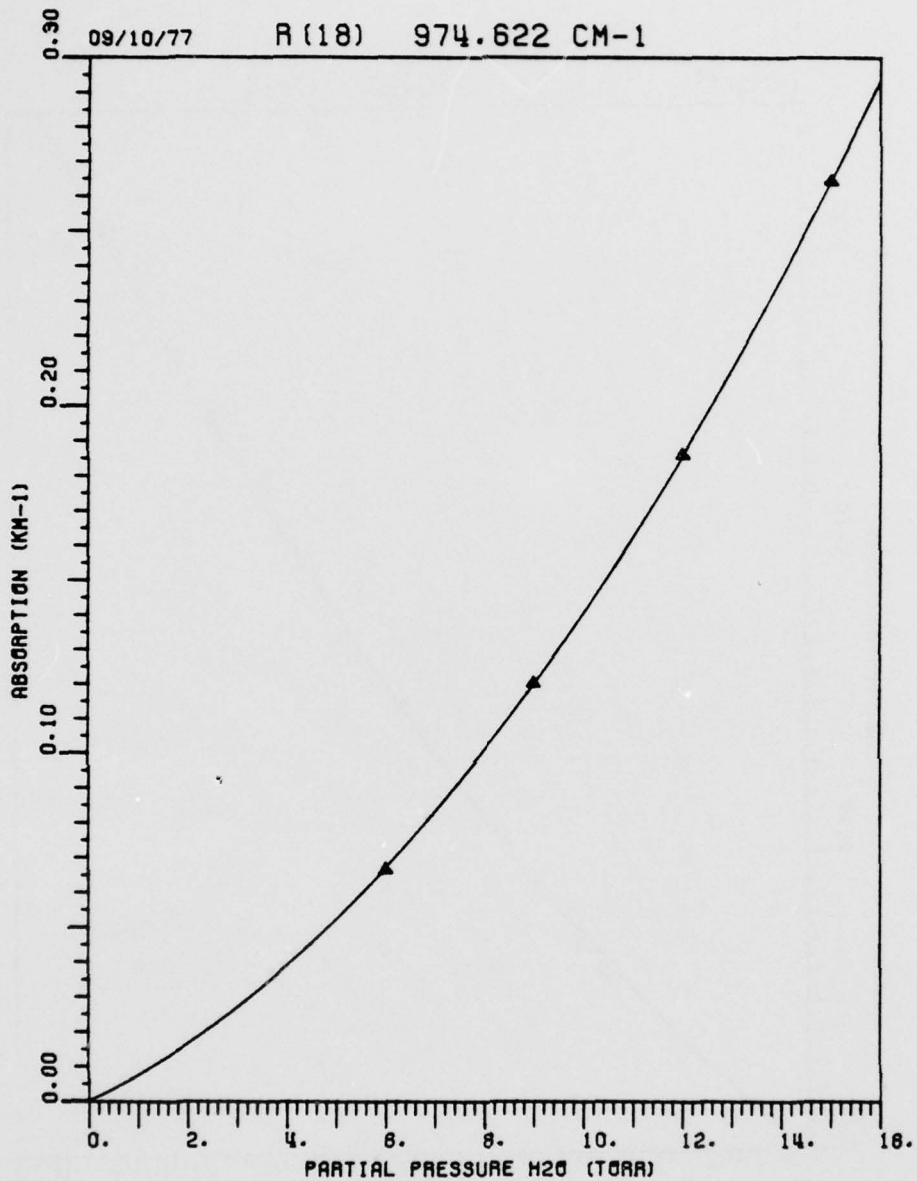


Figure 100. Measured H₂O in N₂ absorption coefficient at a total pressure of 760 Torr for the R(18) CO₂ laser line at 974.622 cm⁻¹. The White cell data, represented by the symbol Δ , was obtained at an average temperature of 22.5°C.

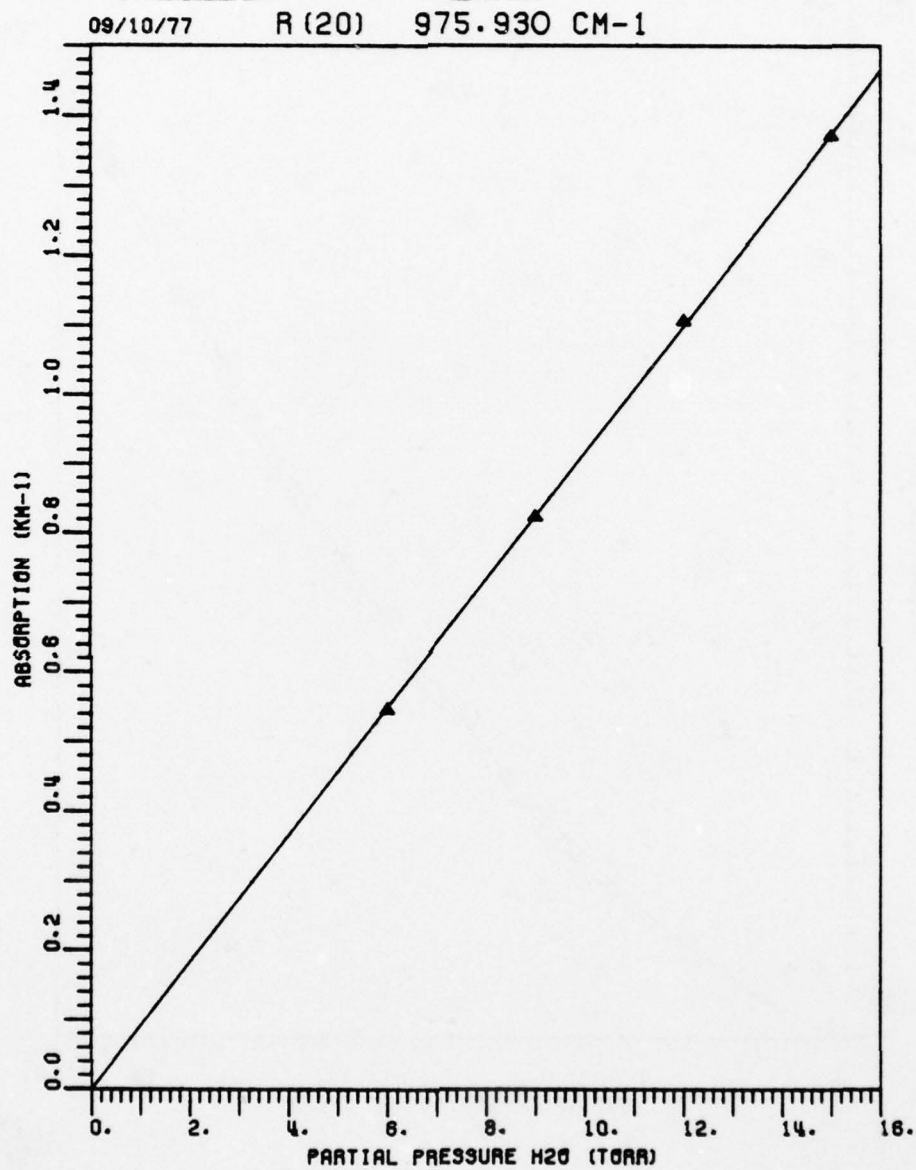


Figure 101. Measured H₂O in N₂ absorption coefficient at a total pressure of 760 Torr for the R(20) CO₂ laser line at 975.930 cm⁻¹. The White cell data, represented by the symbol Δ , was obtained at an average temperature of 22.5°C.

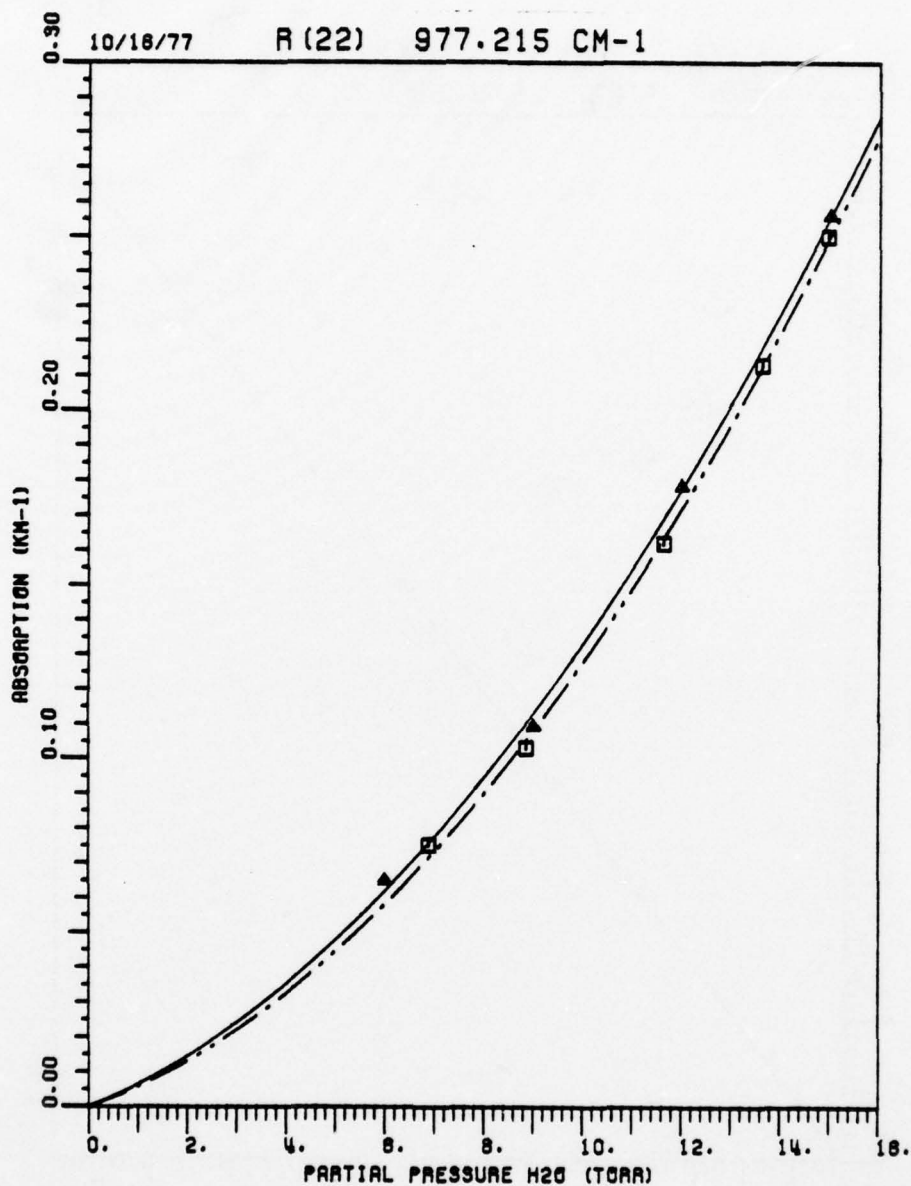


Figure 102. Measured H₂O in N₂ absorption coefficient at a total pressure of 760 Torr for the R(22) CO₂ laser line at 977.215 cm⁻¹. The White cell data, represented by the symbol Δ, was obtained at an average temperature of 22.5°C. The spectrophone data, represented by the symbol □, was obtained at an average temperature of 25.0°C.

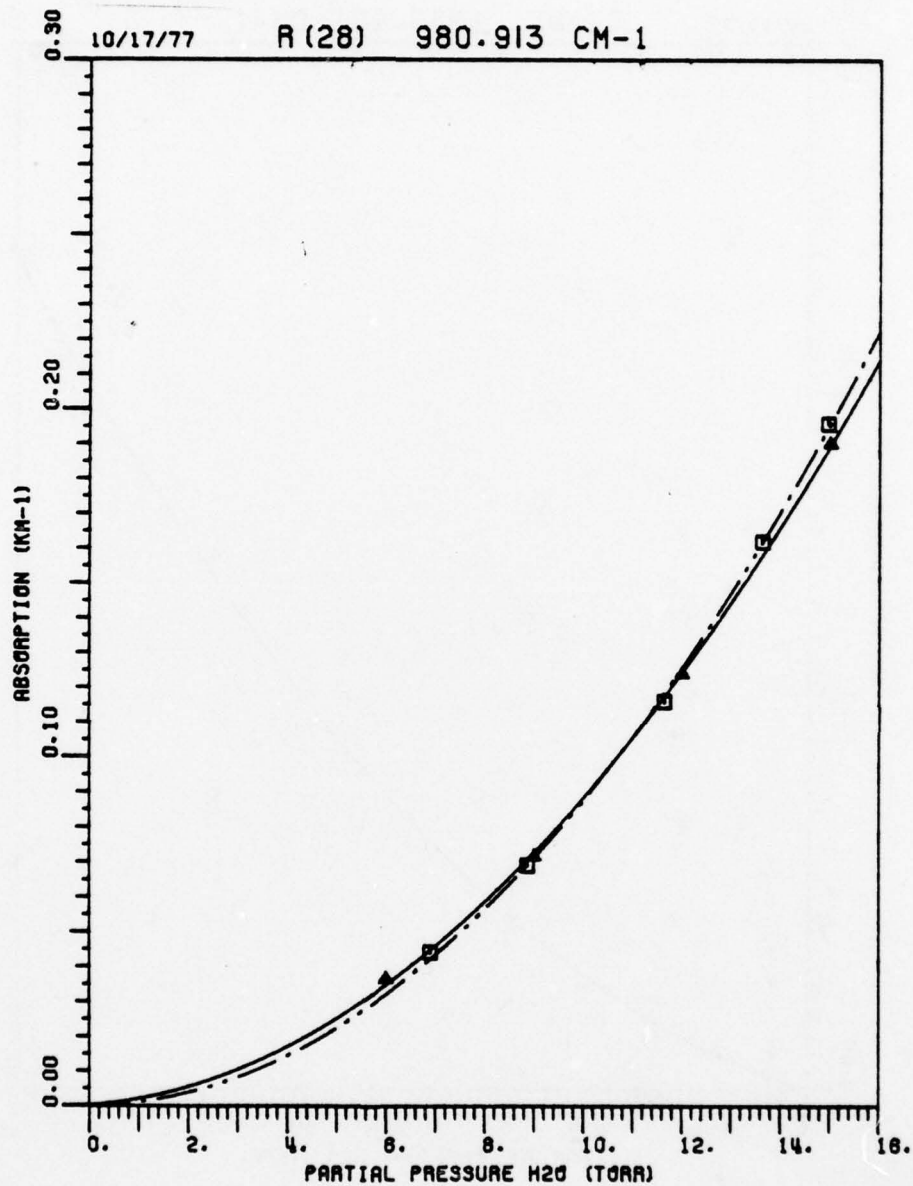


Figure 103. Measured H₂O in N₂ absorption coefficient at a total pressure of 760 Torr for the R(28) CO₂ laser line at 980.913 cm⁻¹. The White cell data, represented by the symbol Δ, was obtained at an average temperature of 22.5°C. The spectrophone data, represented by the symbol □, was obtained at an average temperature of 25°C.

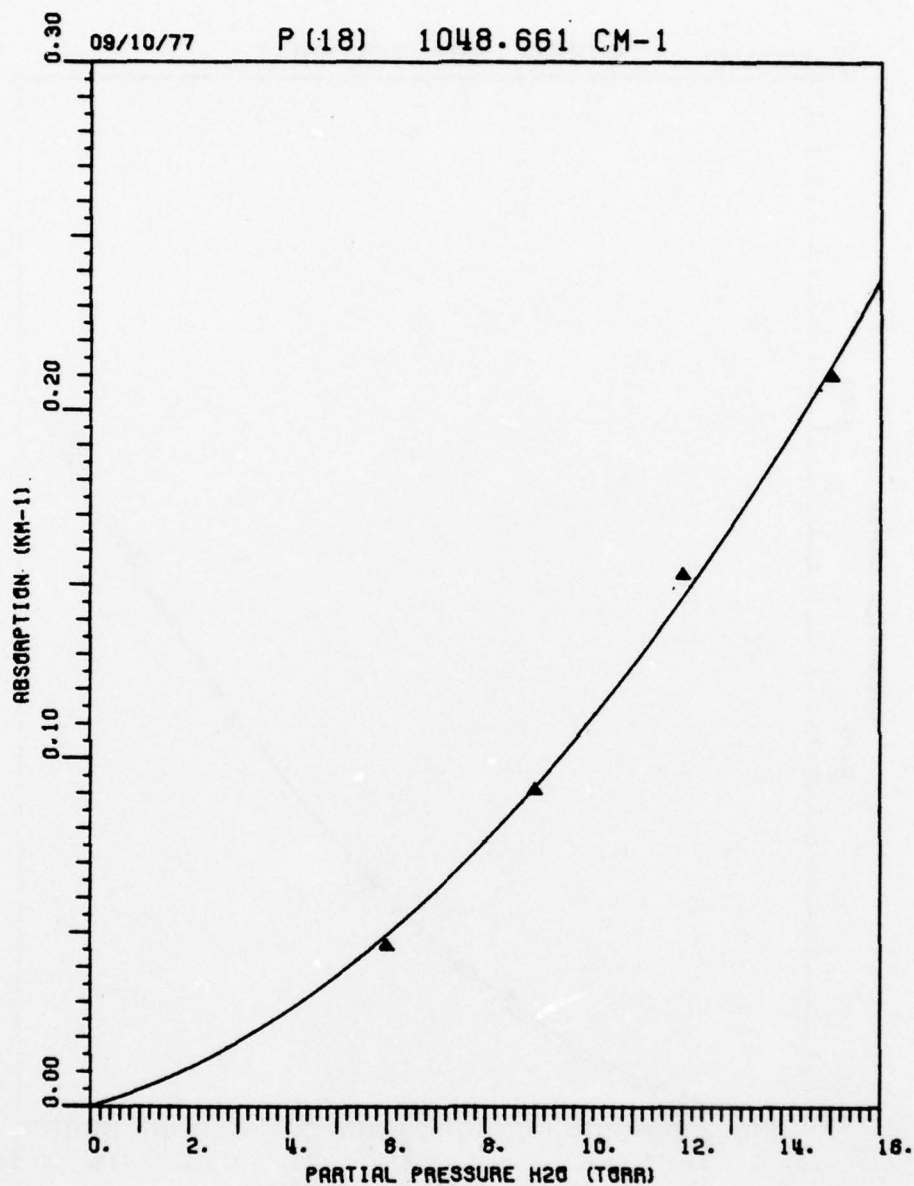


Figure 104. Measured H₂O in N₂ absorption coefficient at a total pressure of 760 Torr for the P(18) CO₂ laser line at 1048.661 cm⁻¹. The White cell data, represented by the symbol Δ, was obtained at an average temperature of 22.5°C.

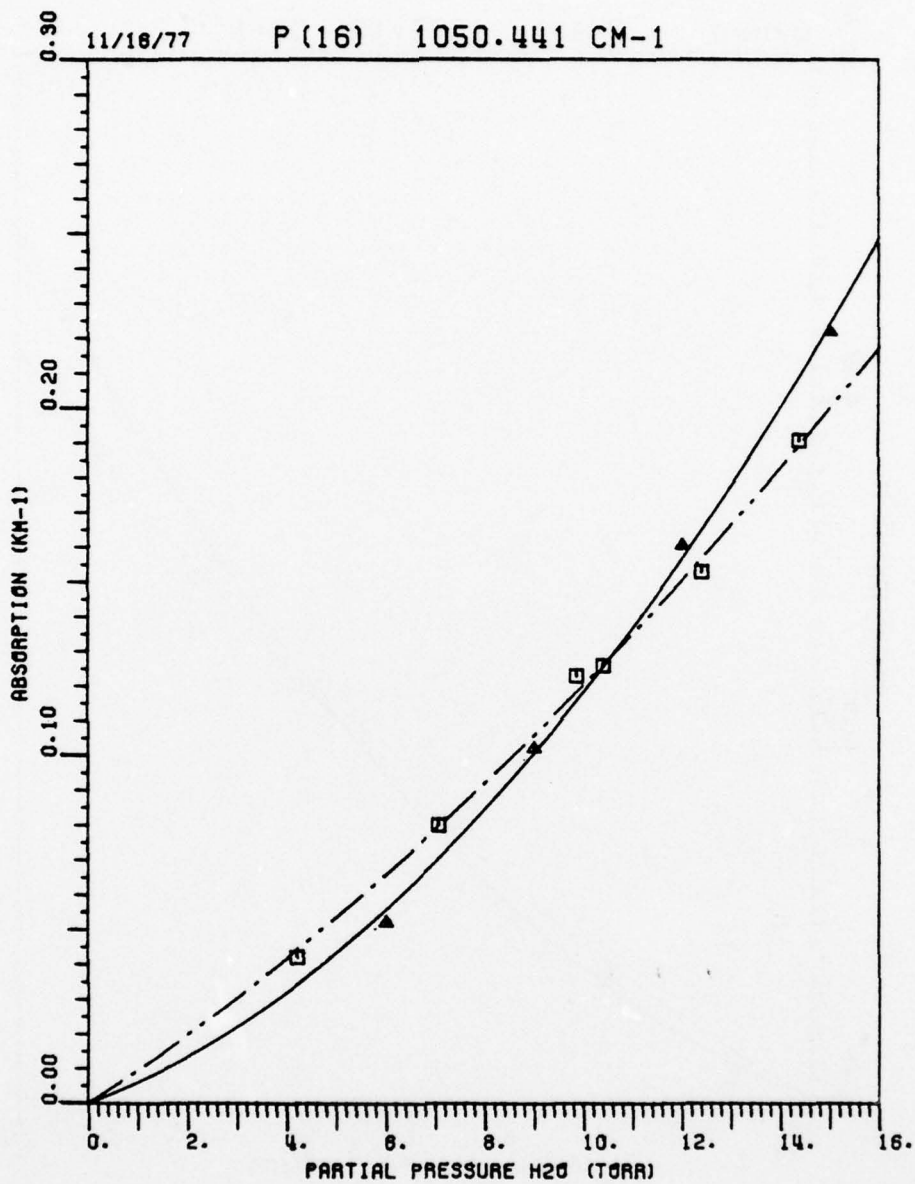


Figure 105. Measured H₂O in N₂ absorption coefficient at a total pressure of 760 Torr for the P(16) CO₂ laser line at 1050.441 cm⁻¹. The White cell data, represented by the symbol Δ, was obtained at an average temperature of 22.5°C. The spectrophone data, represented by the symbol □, was obtained at an average temperature of 23.5°C.

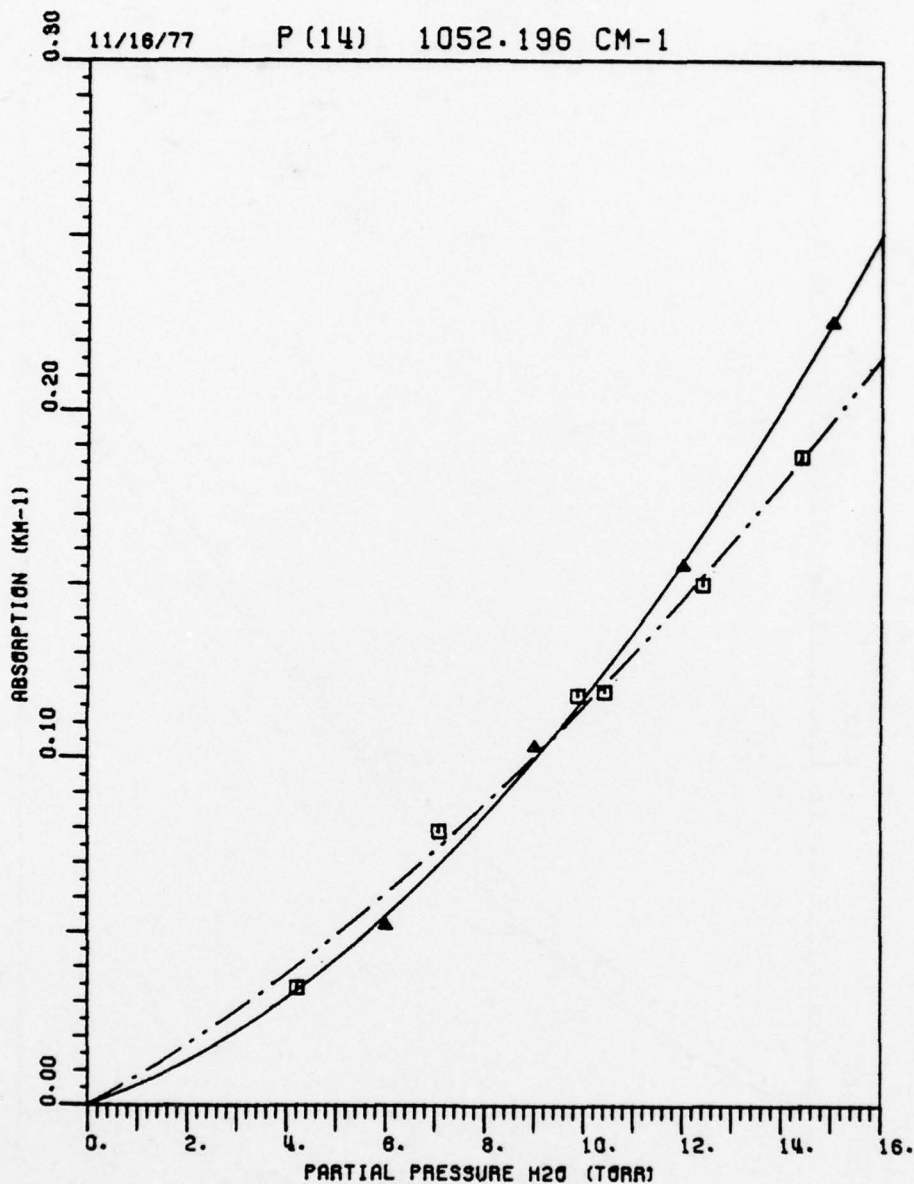


Figure 106. Measured H₂O in N₂ absorption coefficient at a total pressure of 760 Torr for the P(14) CO₂ laser line at 1052.196 cm⁻¹. The White cell data, represented by the symbol Δ, was obtained at an average temperature of 22.5°C. The spectrophone data, represented by the symbol □, was obtained at an average temperature of 23.5°C.

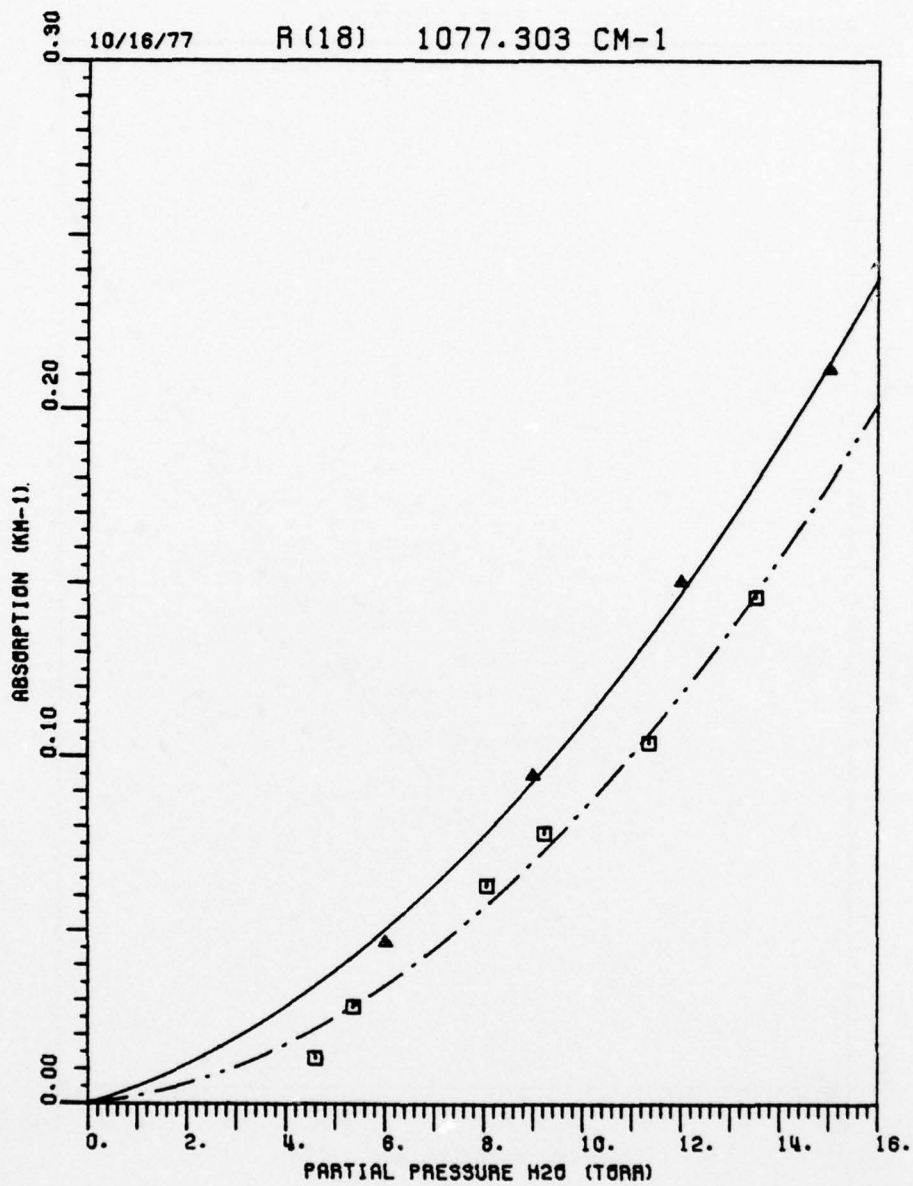


Figure 107. Measured H₂O in N₂ absorption coefficient at a total pressure of 760 Torr for the R(18) CO₂ laser line at 1077.303 cm⁻¹. The White cell data, represented by the symbol Δ , was obtained at an average temperature of 22.5°C. The spectrophone data, represented by the symbol \square , was obtained at an average temperature of 24.0°C.

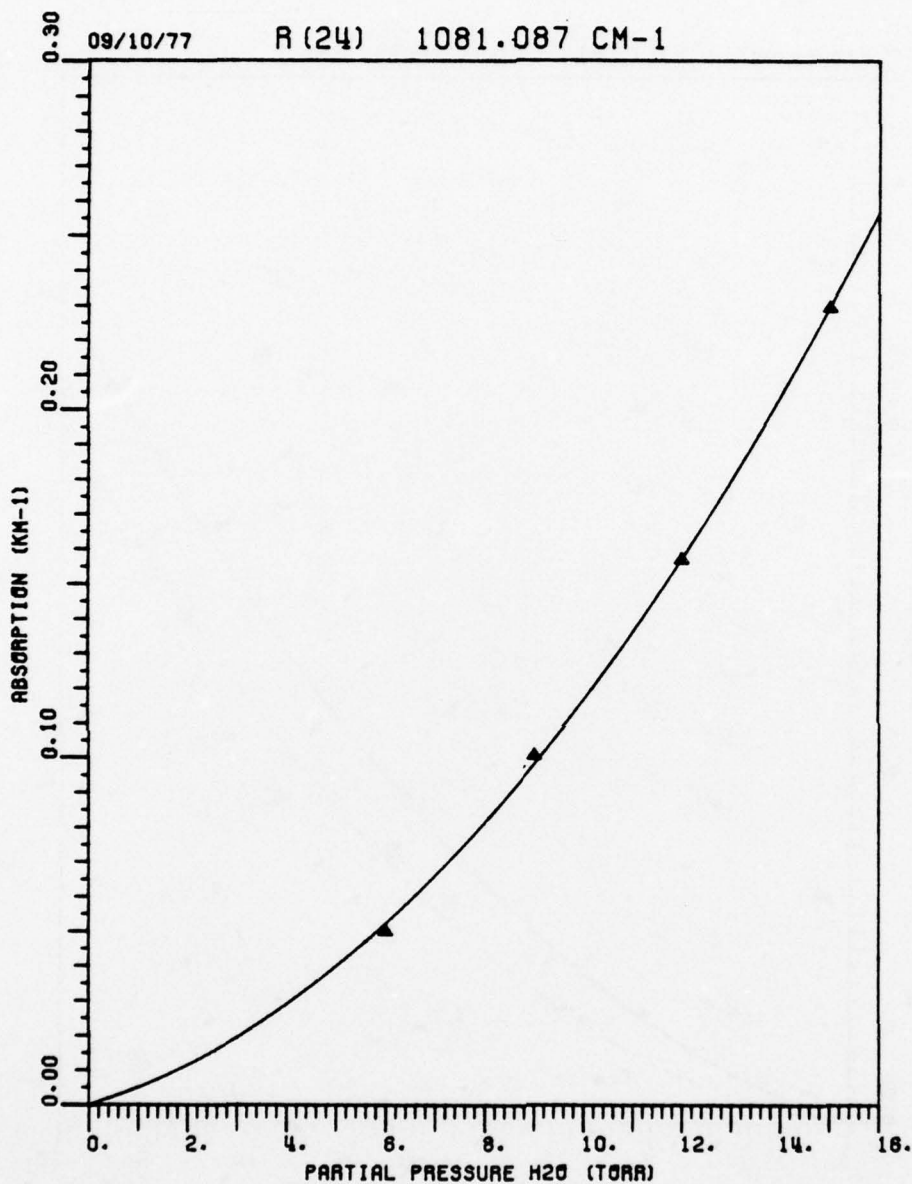


Figure 108. Measured H₂O in N₂ absorption coefficient at a total pressure of 760 Torr for the R(24) CO₂ laser line at 1081.087 cm⁻¹. The White cell data, represented by the symbol Δ , was obtained at an average temperature of 22.5°C.

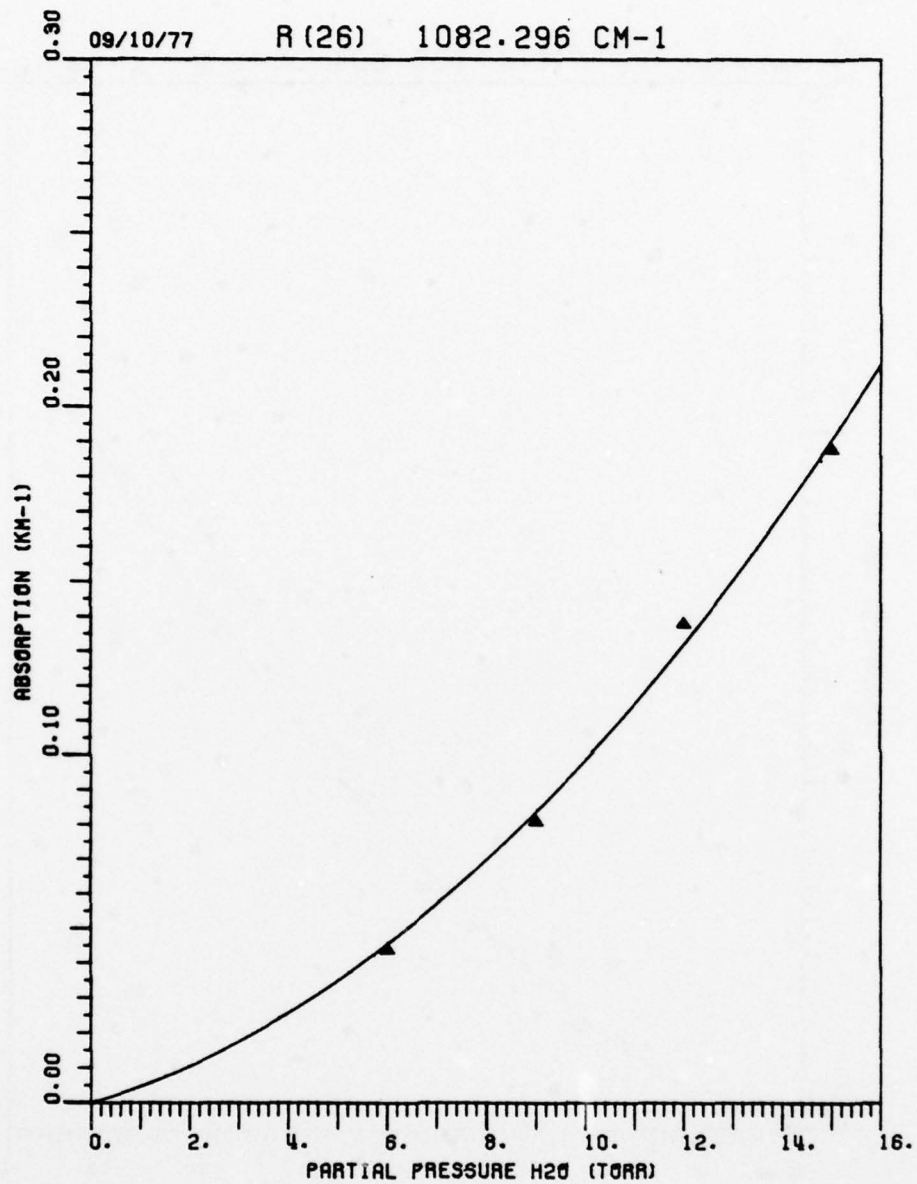


Figure 109. Measured H₂O in N₂ absorption coefficient at a total pressure of 760 Torr for the R(26) CO₂ laser line at 1082.296 cm⁻¹. The White cell data, represented by the symbol Δ , was obtained at an average temperature of 22.5°C.

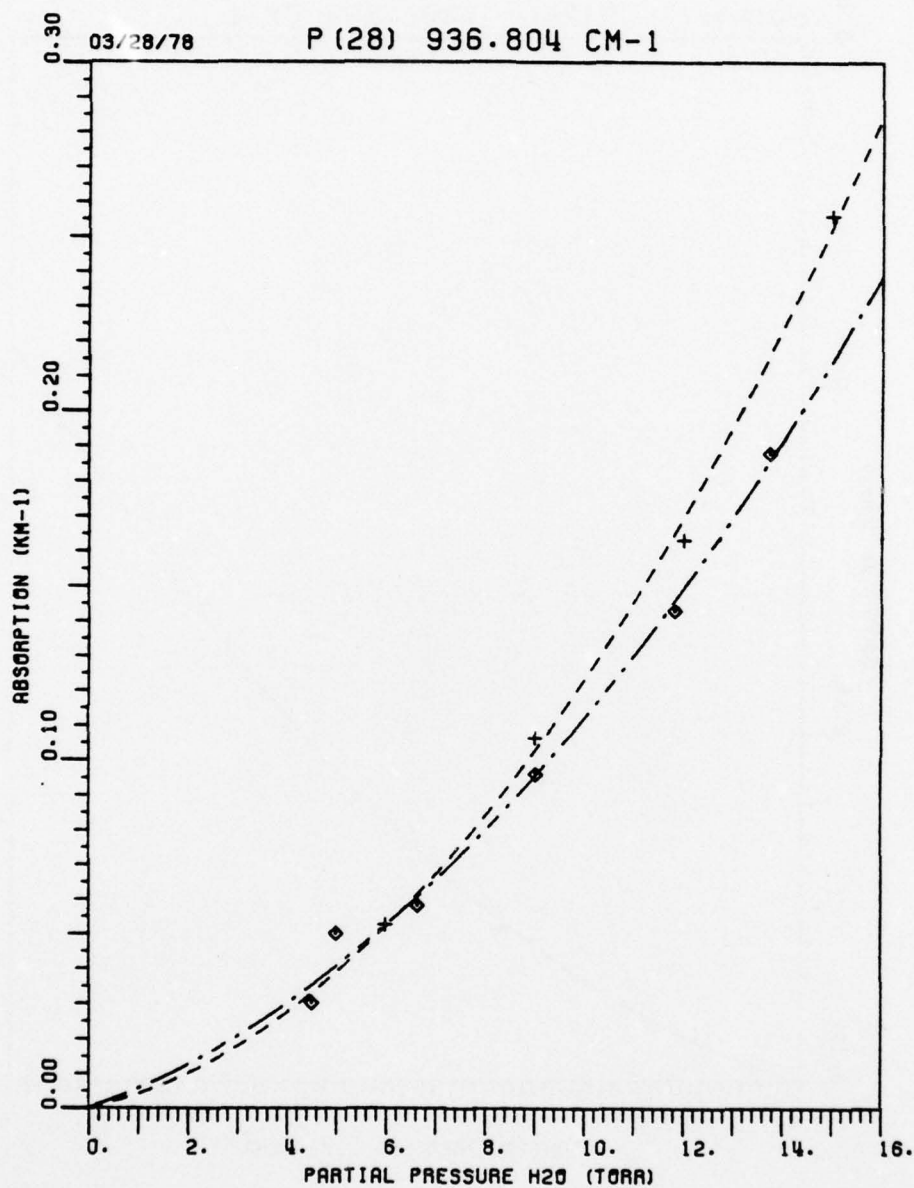


Figure 110. Measured H₂O in 80% N₂ and 20% O₂ absorption coefficient at a total pressure of 760 Torr for the P(28) CO₂ laser line at 936.804 cm⁻¹. The White cell data, represented by the symbol +, was obtained at an average temperature of 22°C. The spectrophone data, represented by the symbol ◇, was obtained at an average temperature of 24°C.

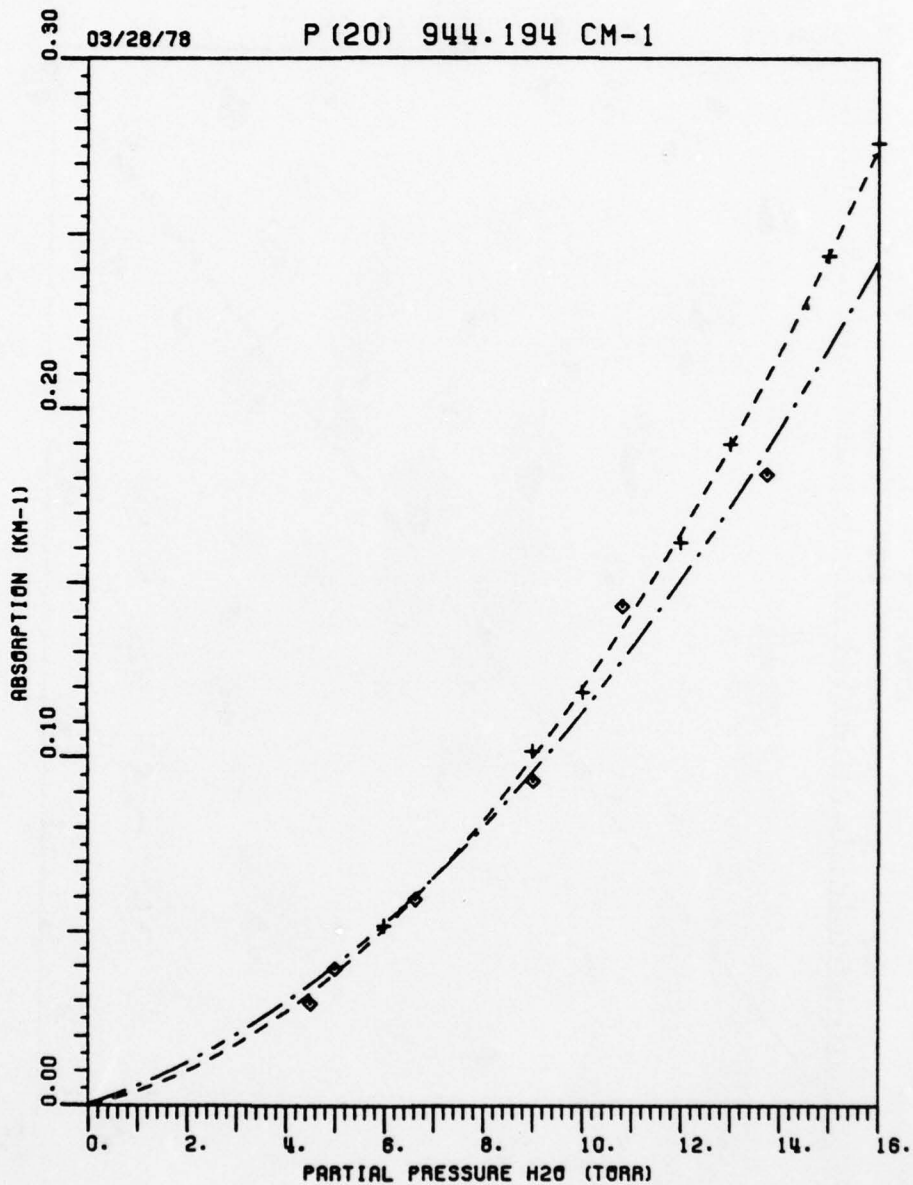


Figure 111. Measured H₂O in 80% N₂ and 20% O₂ absorption coefficient at a total pressure of 760 Torr for the P(20) CO₂ laser line at 944.194 cm⁻¹. The White cell data, represented by the symbol +, was obtained at an average temperature of 22°C. The spectrophone data, represented by the symbol ◇, was obtained at an average temperature of 24°C.

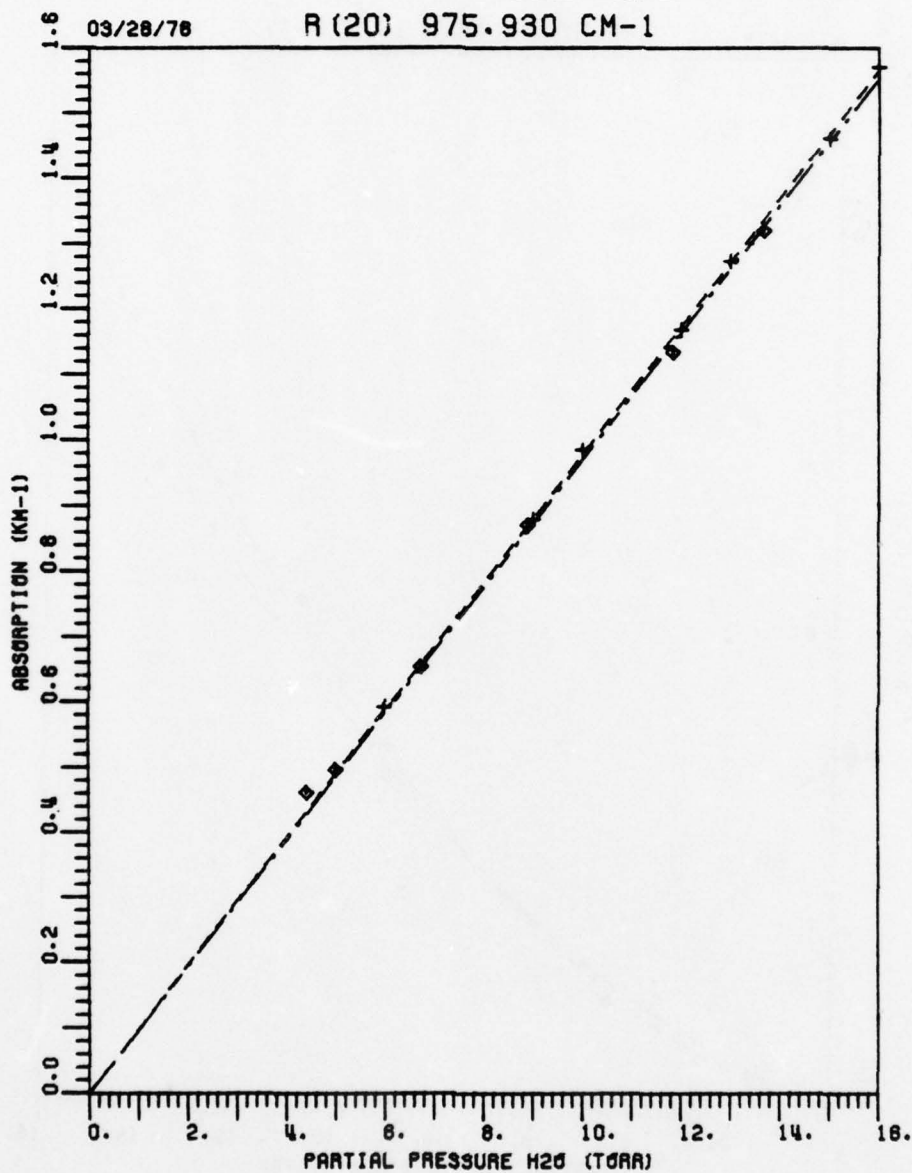


Figure 112. Measured H₂O in 80% N₂ and 20% O₂ absorption coefficient ⁻¹ at a total pressure of 760 Torr for the R(20) CO₂ laser line at 975.930 cm⁻¹. The White cell data, represented by the symbol +, was obtained at an average temperature of 22°C. The spectrophone data, represented by the symbol ◇, was obtained at an average temperature of 24°C.

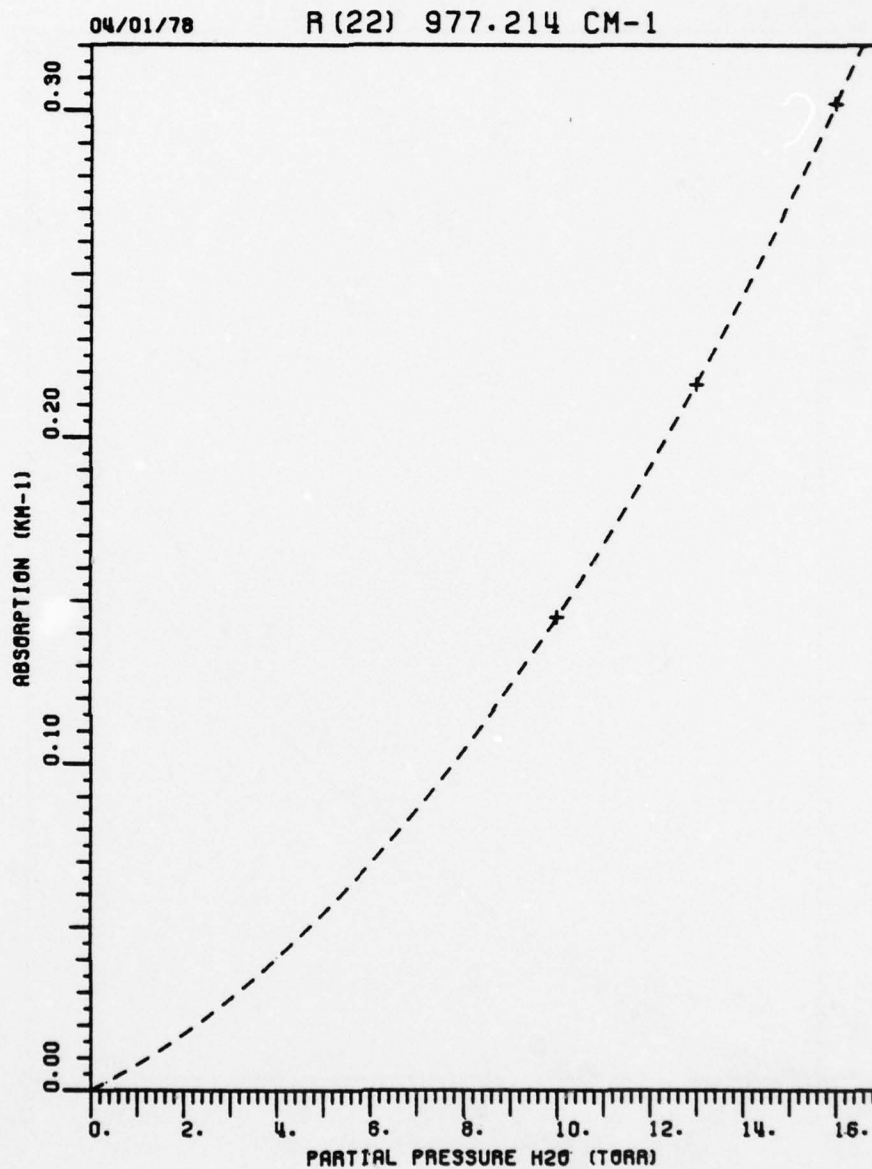


Figure 113. Measured H₂O in 80% N₂ and 20% O₂ absorption coefficient km^{-1} at a total pressure of 760 Torr for the R(22) CO₂ laser line at 977.214 cm^{-1} . The White cell data, represented by the symbol +, was obtained at an average temperature of 22°C .

AD-A058 631

OHIO STATE UNIV COLUMBUS ELECTROSCIENCE LAB

F/G 17/5

A STUDY OF WATER VAPOR ABSORPTION AT CO2 LASER FREQUENCIES USIN--ETC(U)

JUN 78 J C PETERSON

DAAG29-77-C-0010

UNCLASSIFIED

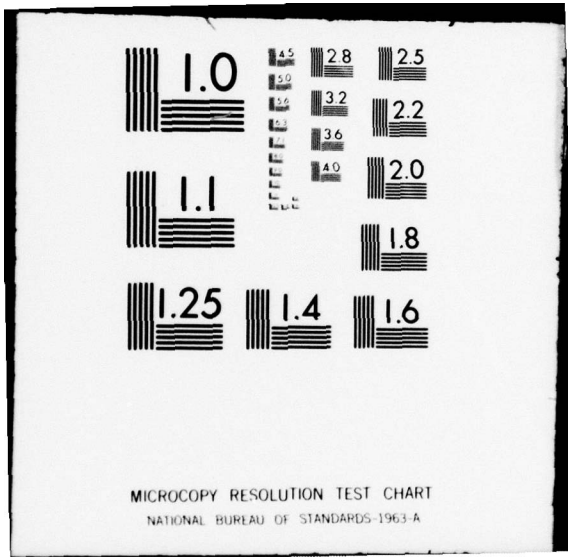
ESL-784701-2

ARO-14702.1-65

NL

3 OF 3
AD
A058631





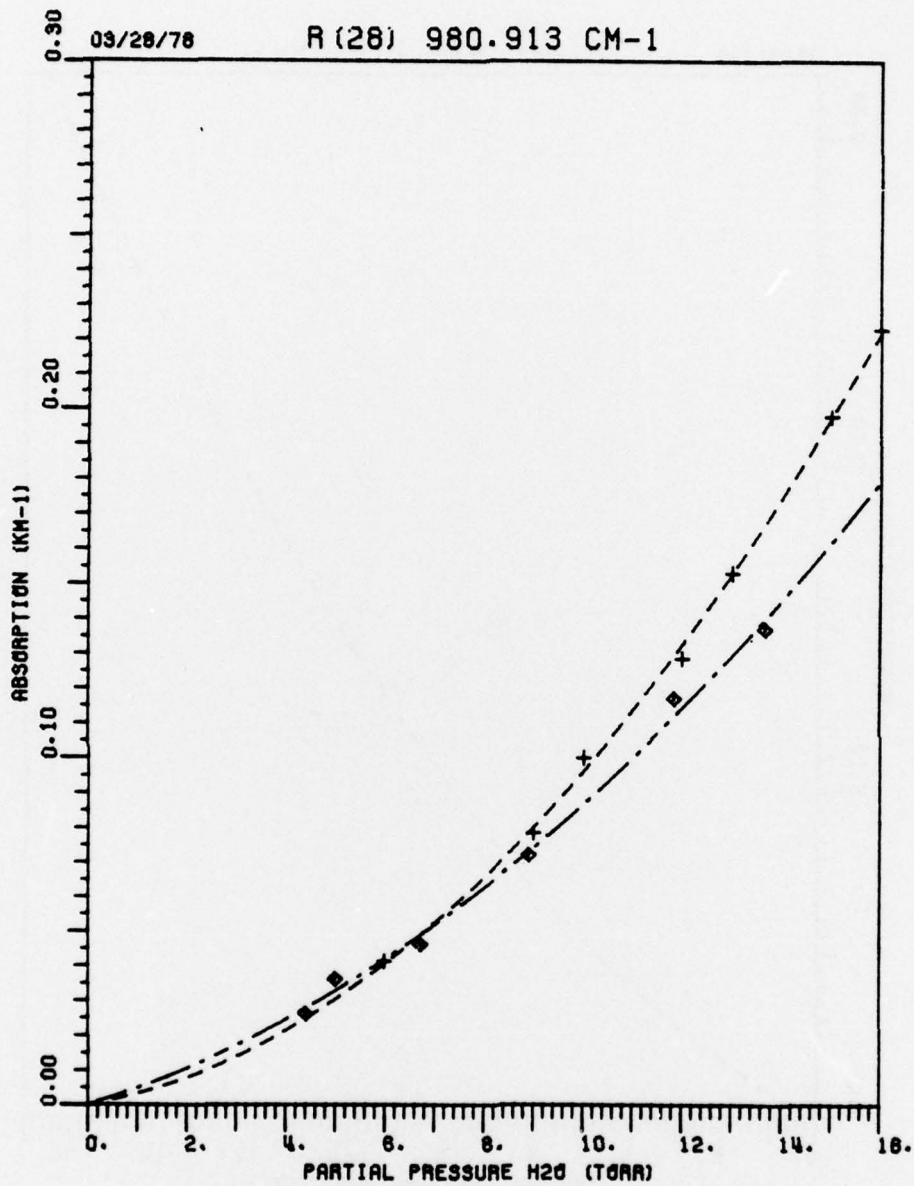


Figure 114. Measured H₂O in 80% N₂ and 20% O₂ absorption coefficient ⁻¹ at a total pressure of 760 Torr for the R(28) CO₂ laser line at 980.913 cm⁻¹. The White cell data, represented by the symbol +, was obtained at an average temperature of 22°C. The spectrophone data, represented by the symbol ◇, was obtained at an average temperature of 24°C.

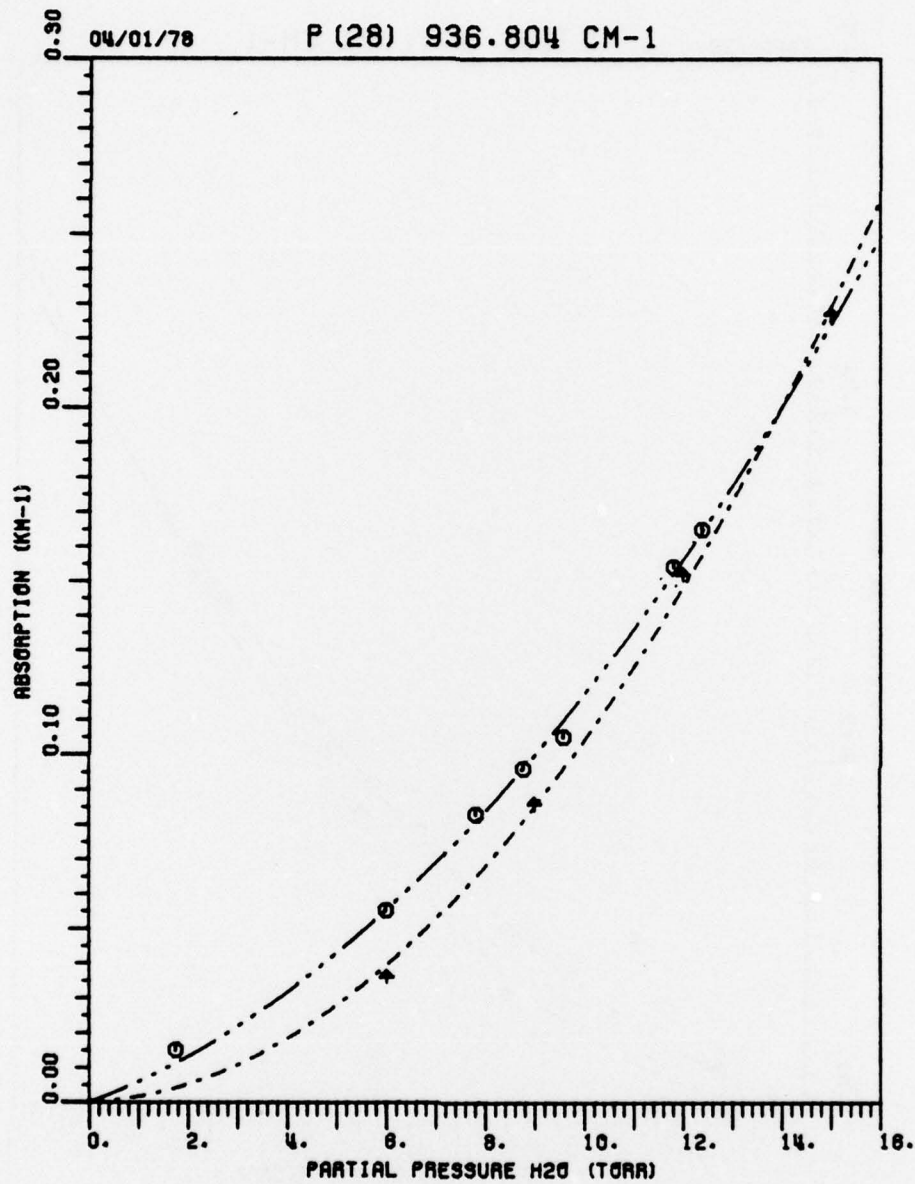


Figure 115. Measured H₂O in 60% N₂ and 40% O₂ absorption coefficient at a total pressure of 760 Torr for the P(28) CO₂ laser line at 936.804 cm⁻¹. The White cell data, represented by the symbol ▲ was obtained at an average temperature of 21.7°C. The spectrophone data, represented by the symbol ⊙ was obtained at an average temperature of 23°C.

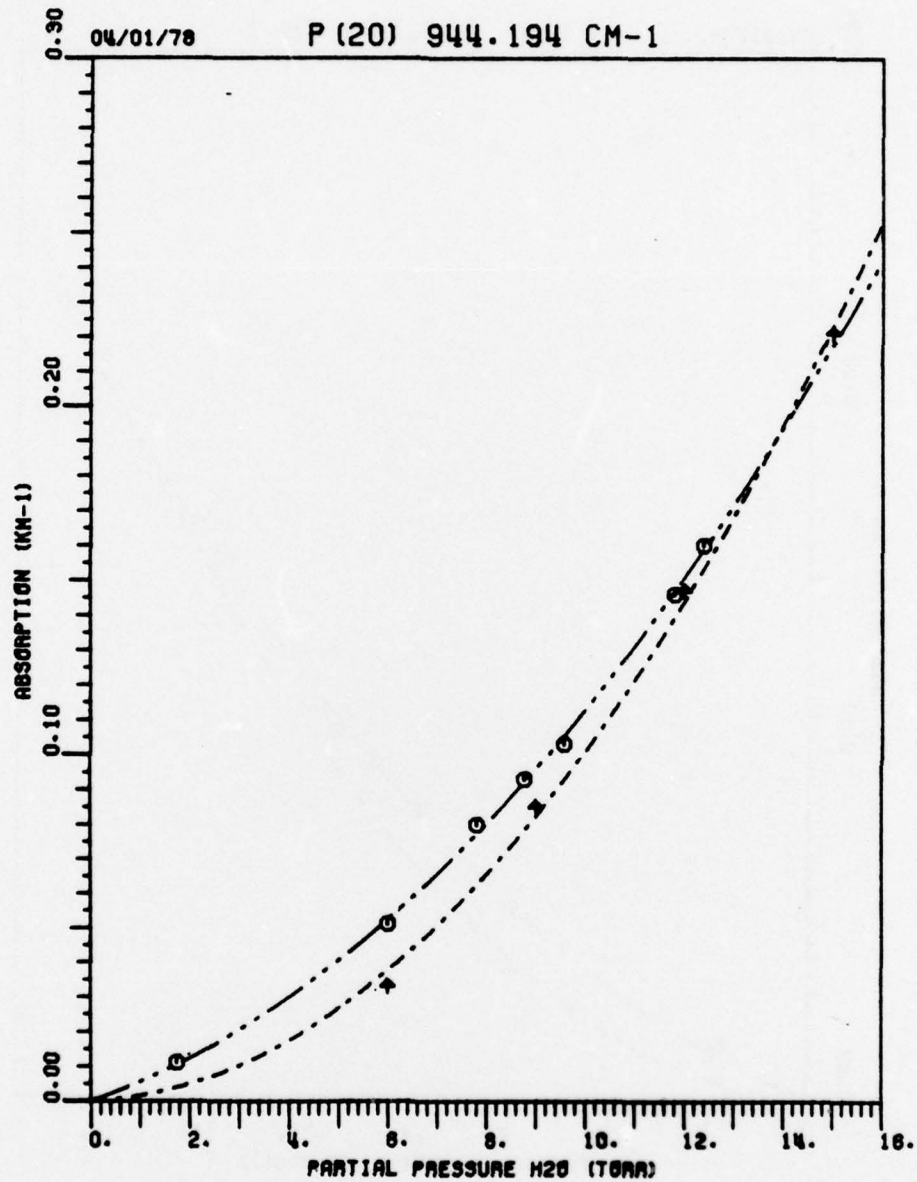


Figure 116. Measured H₂O in 60% N₂ and 40% O₂ absorption coefficient, at a total pressure of 760 Torr for the P(20) CO₂ laser line at 944.194 cm⁻¹. The White cell data, represented by the symbol + was obtained at an average temperature of 21.7°C. The spectrophone data, represented by the symbol O was obtained at an average temperature of 23°C.

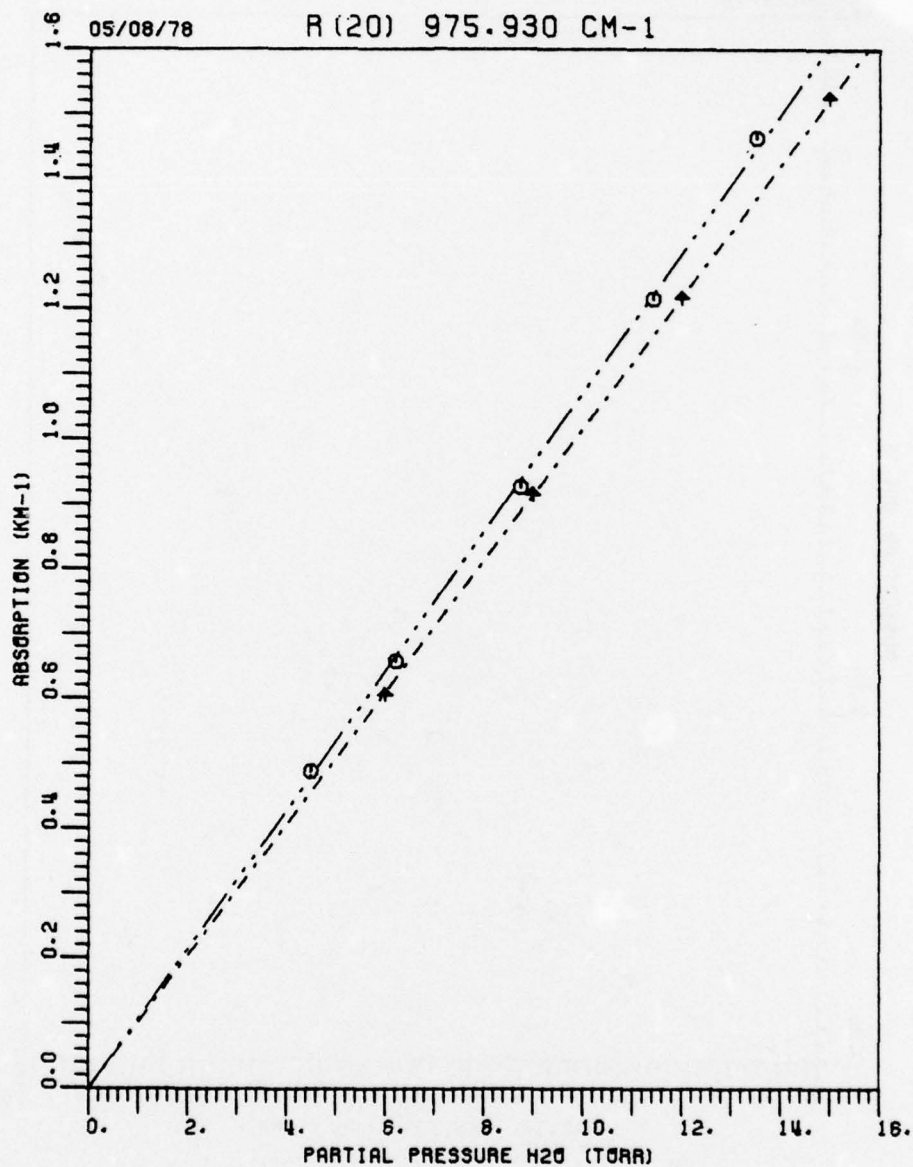


Figure 117. Measured H₂O in 60% N₂ and 40% O₂ absorption coefficient, at a total pressure of 760 Torr for the R(20) CO₂ laser line at 975.930 cm⁻¹. The White cell data, represented by the symbol † was obtained at an average temperature of 21.7°C. The spectrophone data, represented by the symbol ⊙ was obtained at an average temperature of 23.6°C.

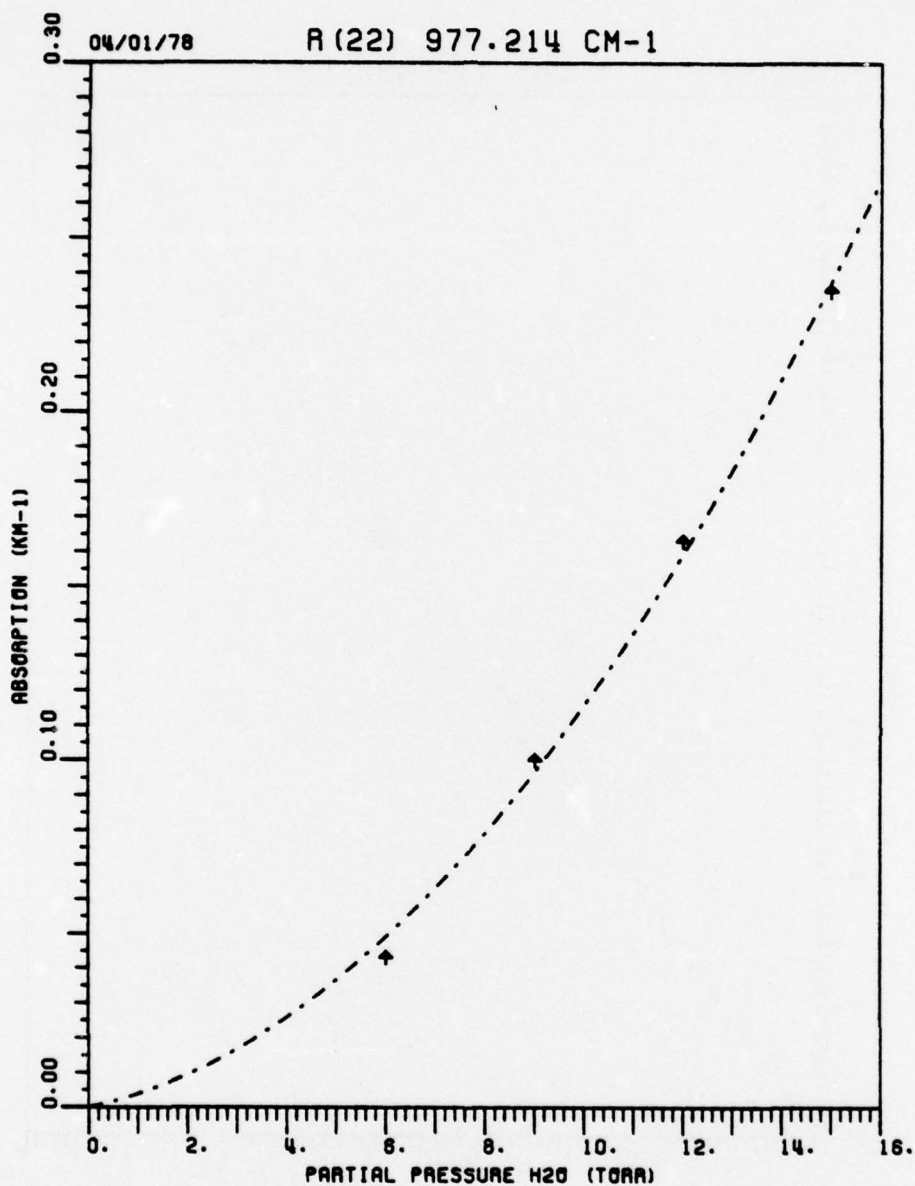


Figure 118. Measured H₂O in 60% N₂ and 40% O₂ absorption coefficient, at a total pressure of 760 Torr for the R(22) CO₂ laser line at 977.214 cm⁻¹. The White cell data, represented by the symbol ↑ was obtained at an average temperature of 21.7°.

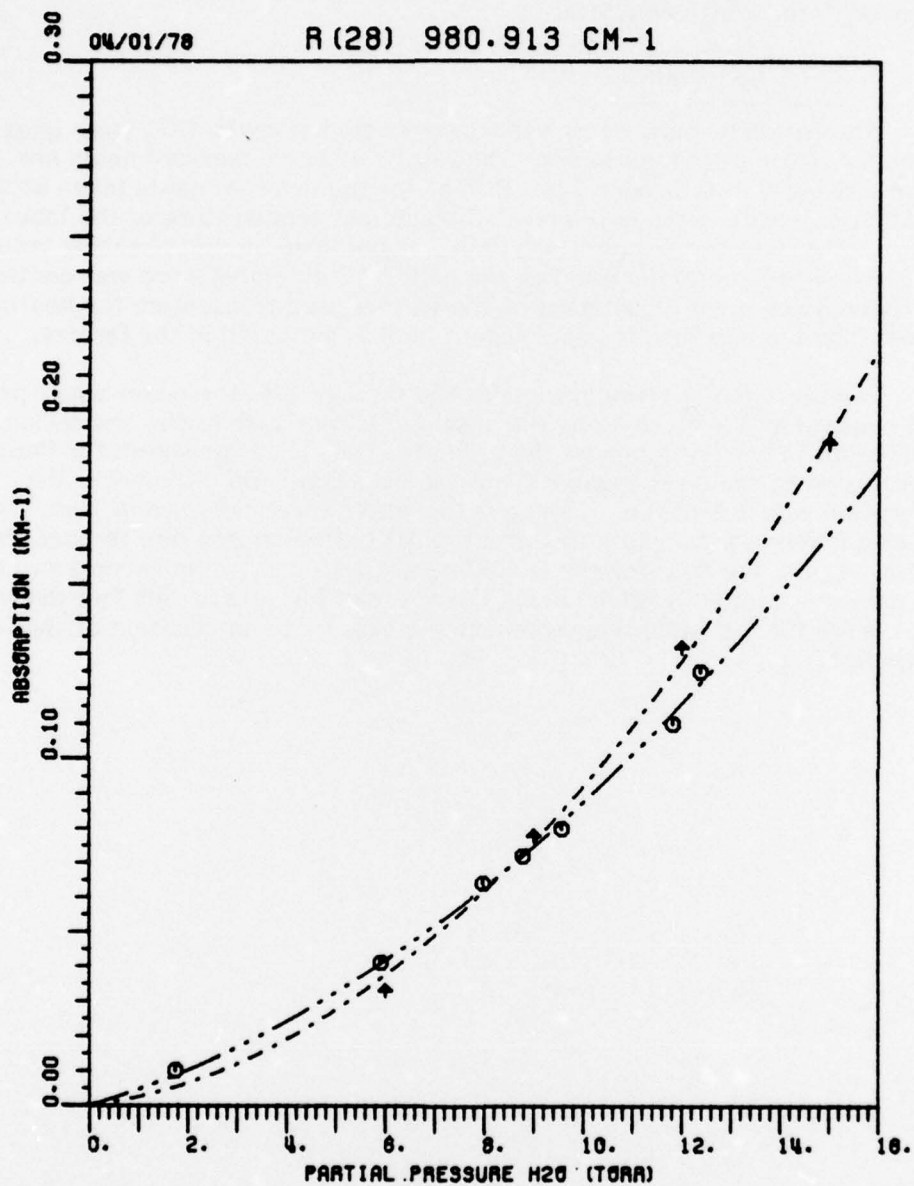


Figure 119. Measured H₂O in 60% N₂ and 40% O₂ absorption coefficient₁ at a total pressure of 760 Torr for the R(28) CO₂ laser line at 980.913 cm⁻¹. The White cell data, represented by the symbol ↑ was obtained at an average temperature of 21.7°C. The spectrophone data, represented by the symbol ⊙ was obtained at an average temperature of 23.0°C.

Comparison with the results of the previous section has been made by plotting the spectrophone data, indicated with the octagon on the same figure with the White cell data.

2. Pure H₂O studies

Absorption by pure water vapor was studied at seven CO₂ laser lines in the 9.4 μm and 10.4 μm bands. The results of these measurements are given in Figures 120 through 126. Except for the measurements taken at 28°C all of these results were obtained at the ambient temperature of the laboratory. The elevated temperature data was obtained by using heating tapes which were previously installed on the cell⁶⁴. The temperature was controlled by trial and error adjustment of the variacs used to energize the heating tapes. The temperature for each experiment is indicated in the figures.

For these plots, given in Figures 120 through 126, the water vapor pressure squared (p^2) is given along the abscissa in Torr², while the absorption coefficient in km^{-1} is given by the ordinate. The curve fits shown for these data represent the least squares fit to the equation $k=Bp^2$ where k is the absorption coefficient (km^{-1}) and p is the water vapor pressure in Torr. For the axis given in these plots this equation will be a straight line through the origin. Again, the data for the R(20) line at 975.9 cm^{-1} is an exception, i.e., the pressure, (not p^2) is given along the abscissa for data at this frequency. The curves for the R(20) line represent the best fit to an equation of the form $k=Ap+Bp^2$.

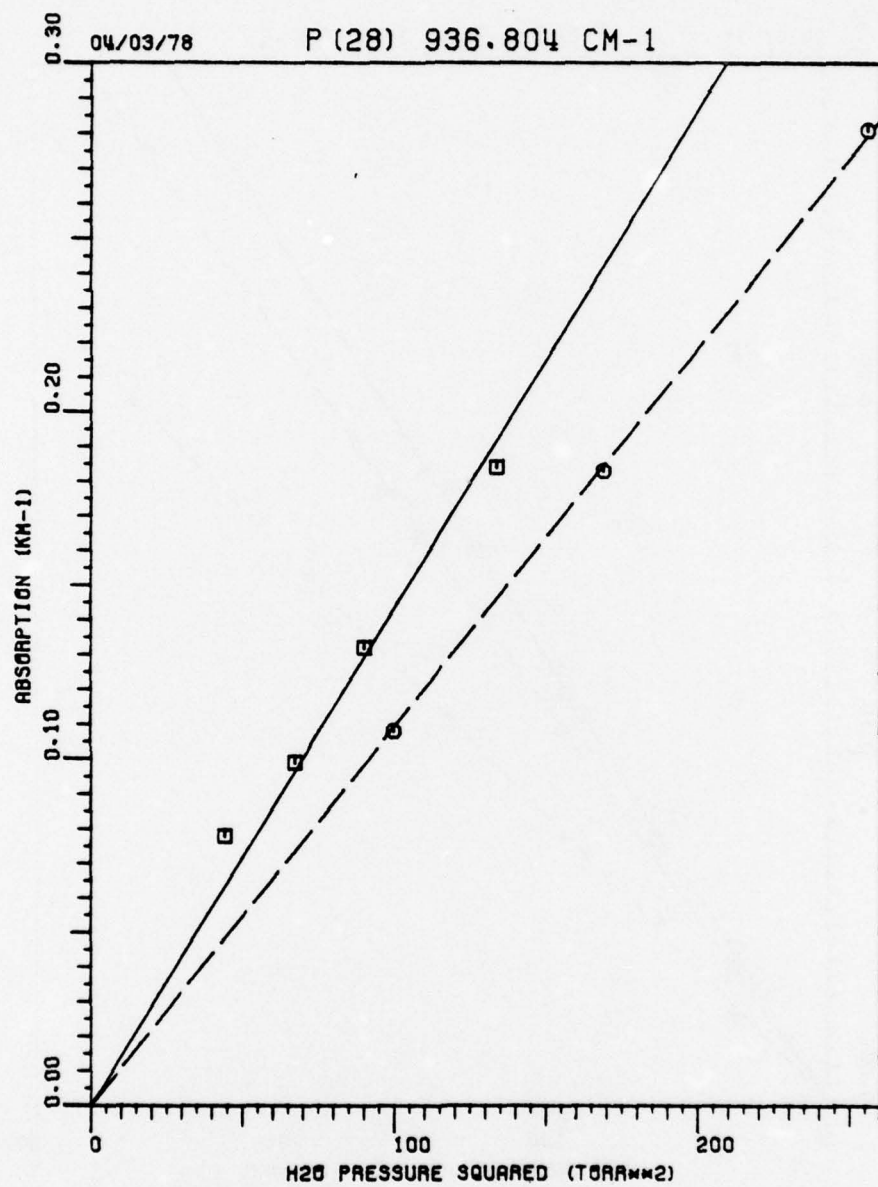


Figure 120. Measured pure water vapor absorption coefficient for the P(28) CO₂ laser line at 936.804 cm⁻¹. The White cell data, represented by the symbol □ was obtained at an average temperature of 18°C. The White cell data, represented by the symbol ○ was obtained at an average temperature of 21°C.

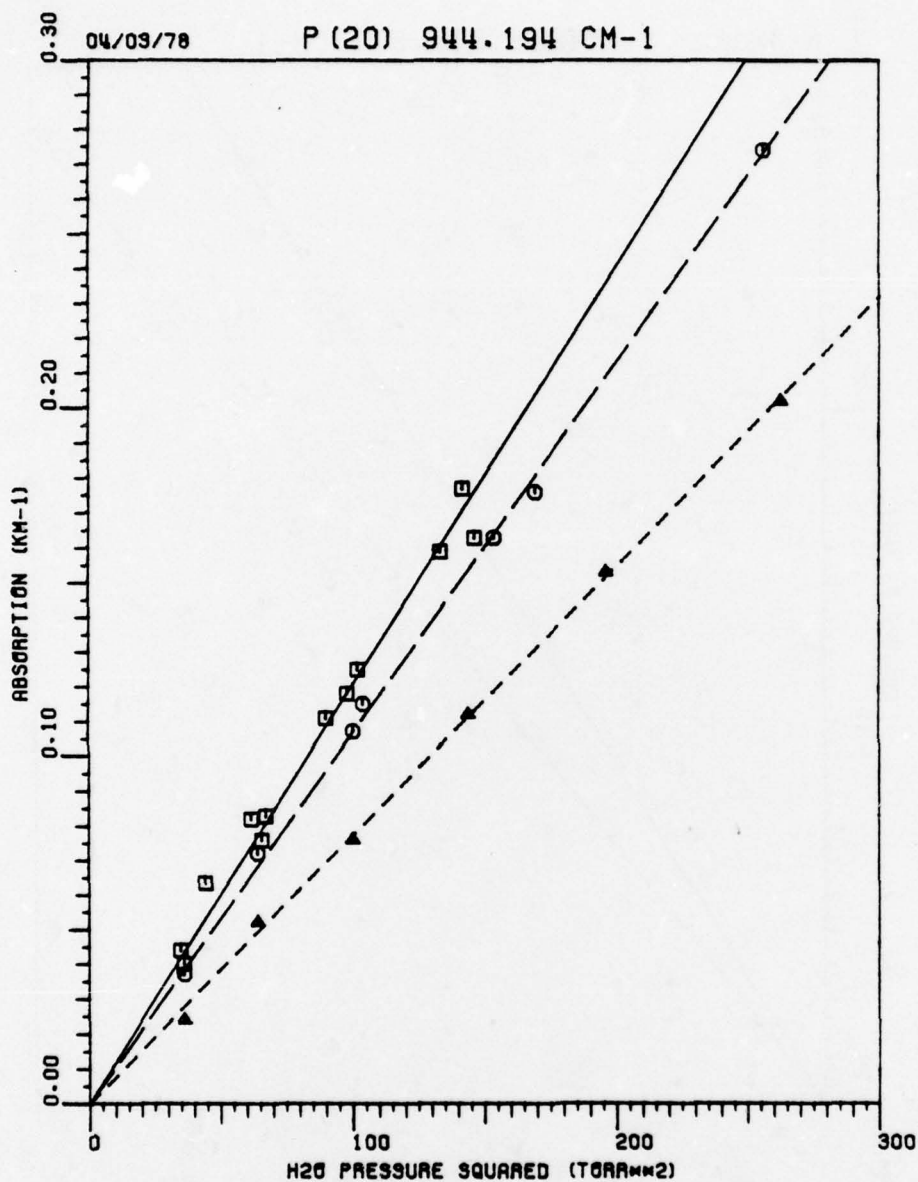


Figure 121. Measured pure water vapor absorption coefficient for the P(20) CO₂ laser line at 944.194 cm⁻¹. The White cell data, represented by the symbol □ was obtained at an average temperature of 18°C. The White cell data, represented by the symbol ○ was obtained at an average temperature of 21°C. The White cell data represented by the symbol △ was obtained an an average temperature of 28°C.

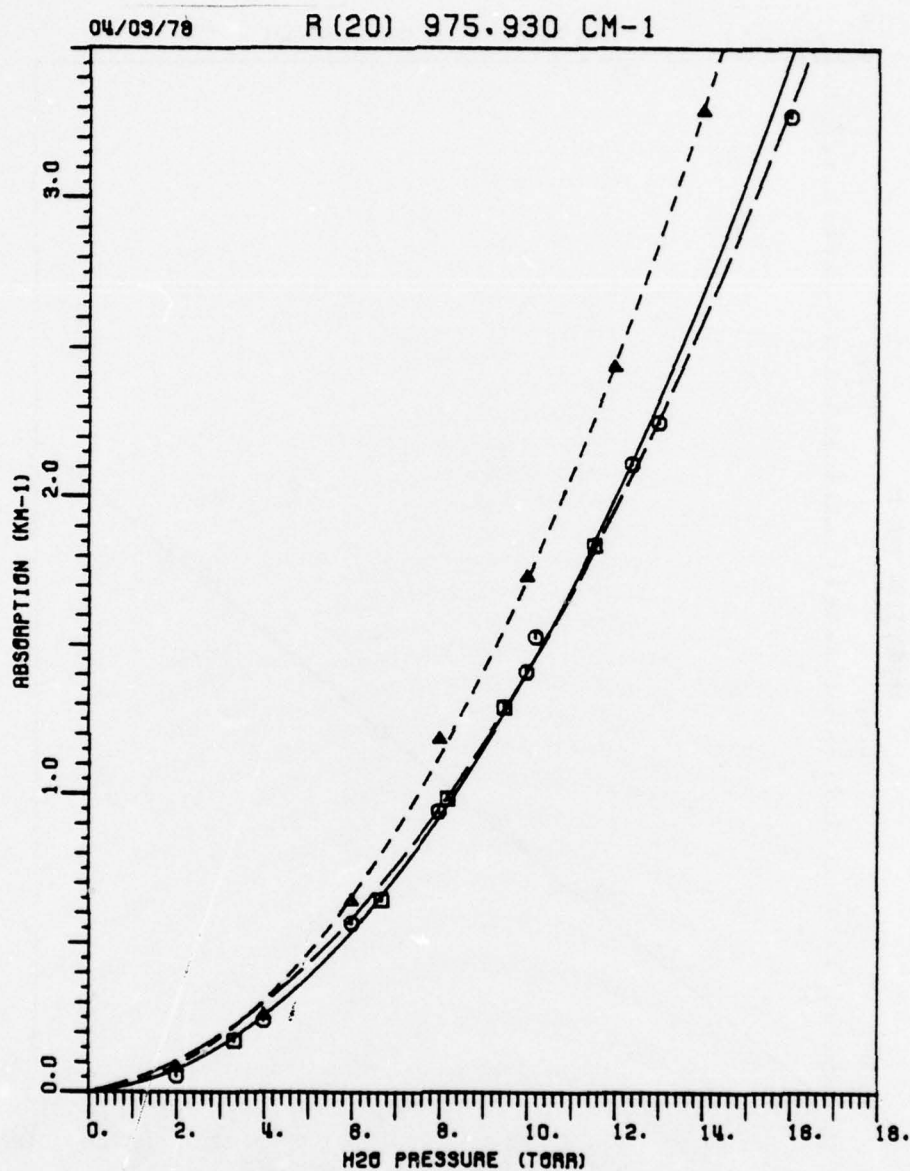


Figure 122. Measured pure water vapor absorption coefficient for the R(20) CO₂ laser line at 975.930 cm⁻¹. The White cell data, represented by the symbol □ was obtained at an average temperature of 18°C. The White cell data, represented by the symbol ○ was obtained at an average temperature of 21.5°C. The White cell data represented by the symbol △ was obtained at an average temperature of 28°C.

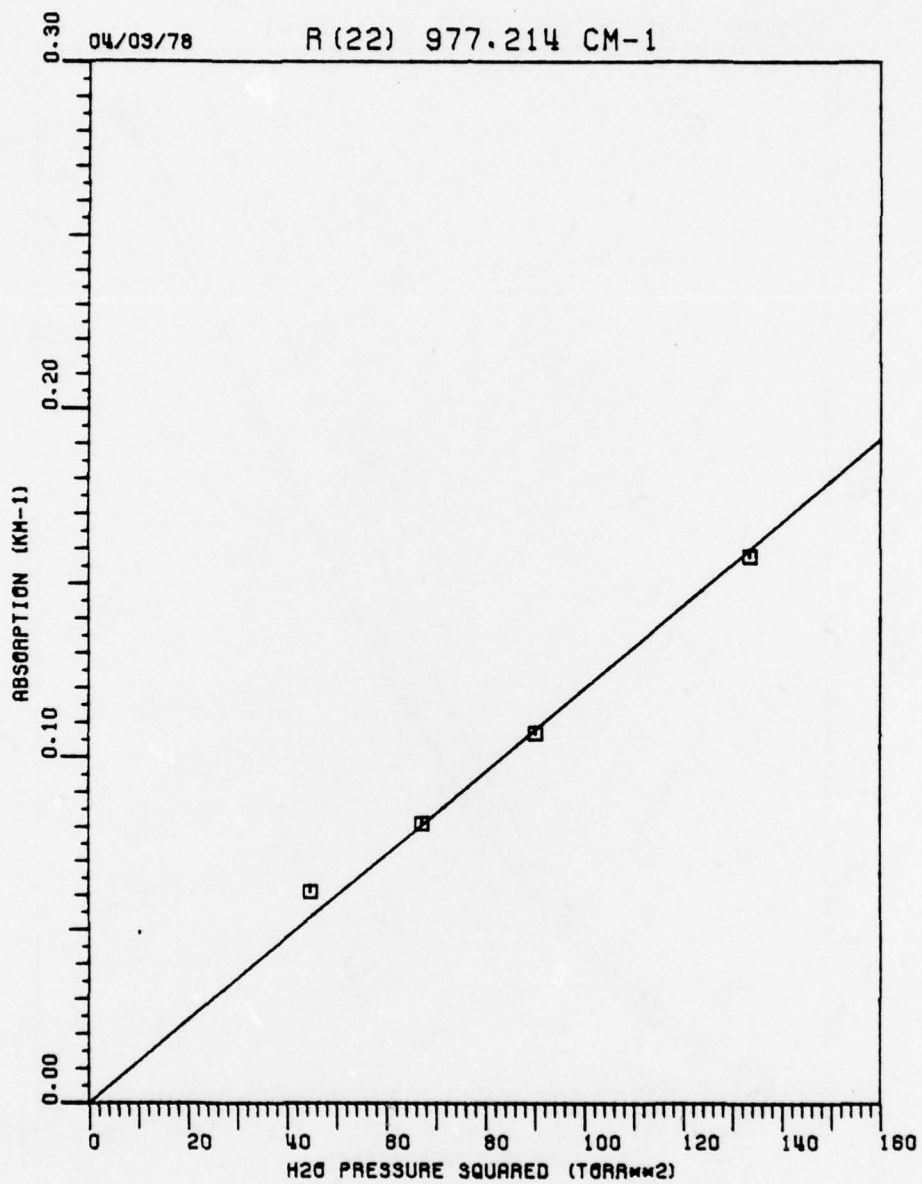


Figure 123. Measured pure water vapor absorption coefficient for the R(22) CO₂ laser line at 977.214 cm⁻¹. The White cell data, represented by the symbol □, was obtained at an average temperature of 18°C.

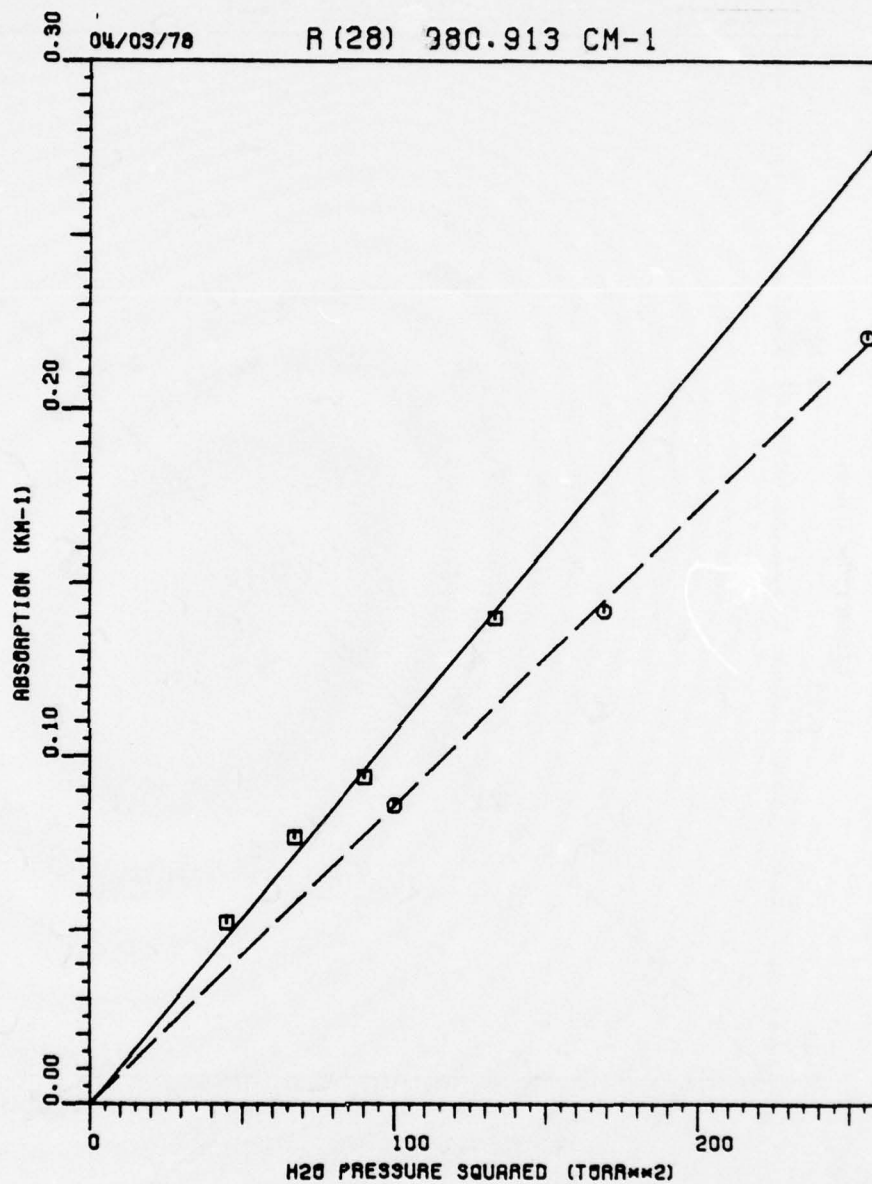


Figure 124. Measured pure water vapor absorption coefficient for the R(28) CO₂ laser line at 980.913 cm⁻¹. The White cell data, represented by the symbol □, was obtained at an average temperature of 18°C. The White cell data, represented by the symbol ○ was obtained at an average temperature of 21°C.

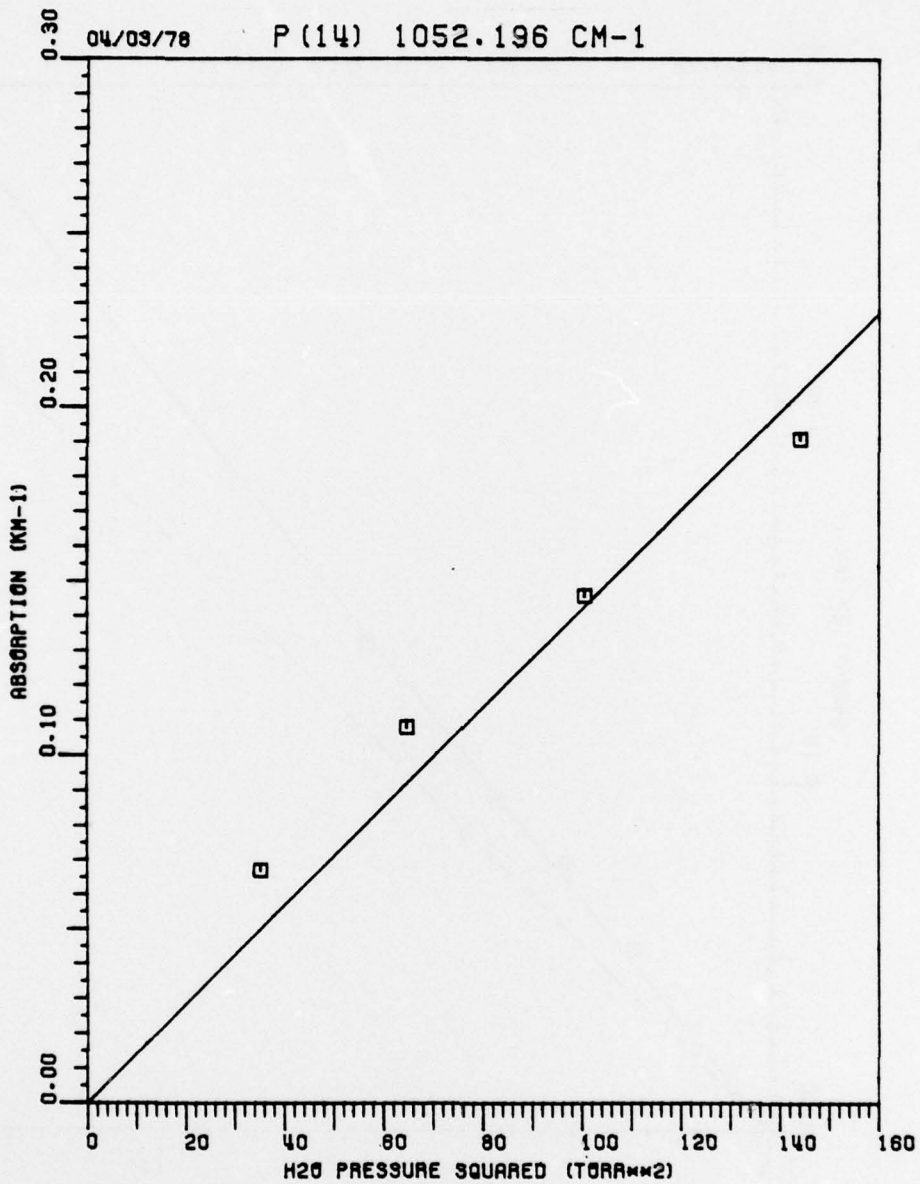


Figure 125. Measured pure water vapor absorption coefficient for the P(14) CO₂ laser line at 1052.196 cm⁻¹. The White cell data, represented by the symbol \square , was obtained at an average temperature of 18°C.

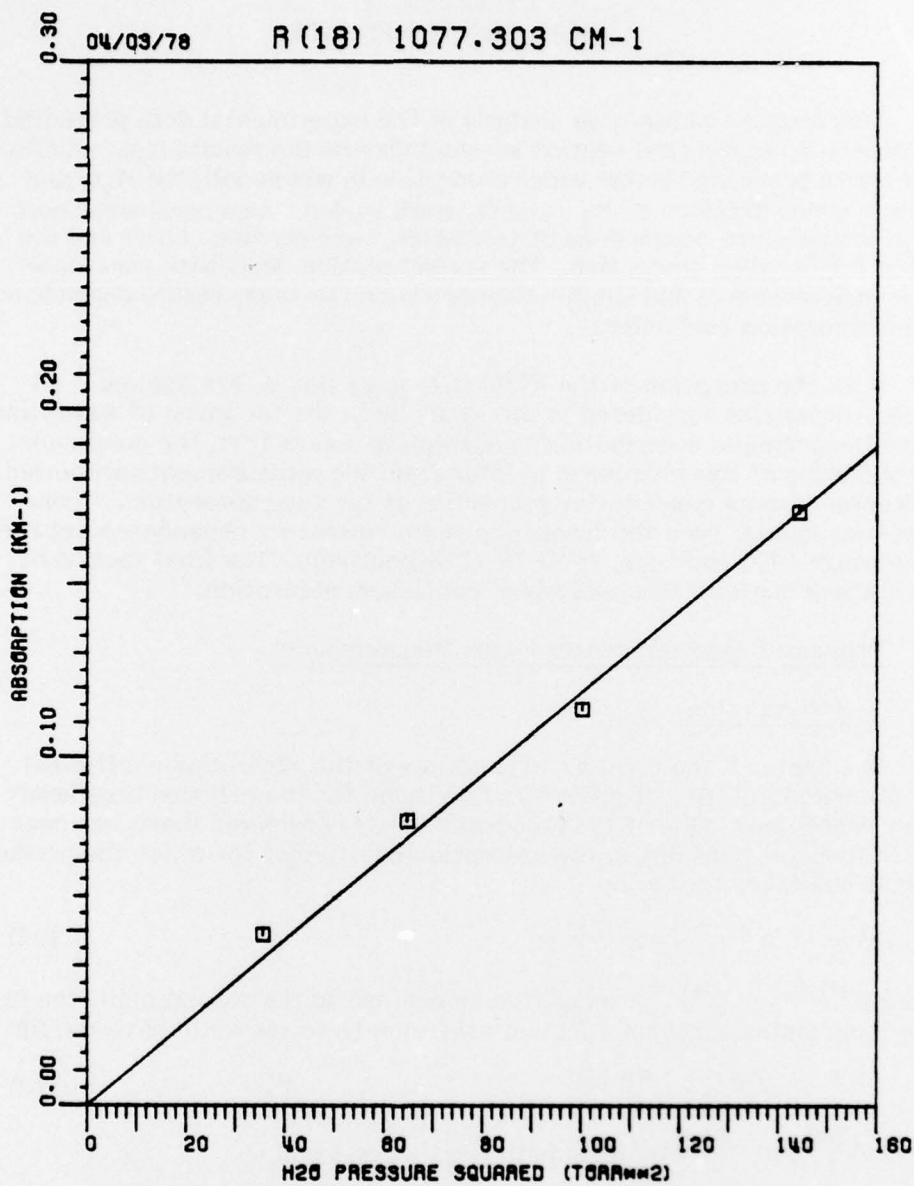


Figure 126. Measured pure water vapor absorption coefficient for the R(18) CO₂ laser line at 1077.303 cm⁻¹. The White cell data, represented by the symbol \square , was obtained at an average temperature of 18°C.

CHAPTER VI ANALYSIS OF RESULTS

This chapter contains an analysis of the experimental data presented in Chapter V. In the first section we shall discuss the results from studies of pressure broadened water vapor absorption in which both the H_2O and relative concentrations of N_2 and O_2 were varied. Also considered here is the temperature dependence of two cases, one near line center and the second for far wing absorption. The second section deals with pure water vapor measurements and similar discussions on the temperature dependence of the absorption coefficient.

With the exception of the R(20) CO_2 laser line at 975.930 cm^{-1} all of the frequencies considered in this study lie in the far wings of water lines where the principle contribution to absorption comes from the continuum. The objective of this chapter is to infer from the measurements presented in Chapter V some quantitative properties of far wing absorption. Those properties include both the frequency and temperature dependence between 930 through 1085 cm^{-1} and 16°C - 28°C respectively. The final section of this chapter contains this analysis of continuum absorption.

A. Pressure Broadened Water Vapor Measurements

1. Introduction

In Chapter II the pressure dependence of the absorption coefficient was discussed in terms of a Lorentz line shape for the collision broadened water vapor lines. One of the frequency limits considered there was near line center contributions to the absorption coefficient for which the pressure dependence takes the form

$$k^{NLC} = A^{NLC} p - B^{NLC} p^2 \quad (102)$$

where A^{NLC} and B^{NLC} are positive constants. In the second limit, the far wing contribution to the absorption coefficient was shown to have the form

$$k_i^{FW} = A_i^{FW} p + B_i^{FW} p^2 \quad (103)$$

where A_i^{FW} and B_i^{FW} are again both positive constants.

Pressure dependence of the absorption coefficient, $k(\nu)$, at frequencies which are not in proximity to an absorption line should (based on Equation (103)) take the form

$$k(\nu) = \sum_i [A_i^{FW} p + B_i^{FW} p^2] = Ap + Bp^2. \quad (104)$$

Table 5
 List of spectrophone and White cell curve fit coefficients for H₂O in N₂ measurements at a total pressure of 760 Torr. The data has been fit to an equation of the form $k=Ap+Bp^2$. Also given here are the sample temperature and figure numbers where these data are plotted.

ν	ID	Spectrophone				White Cell			
		A	B	T	Figs.	A	B	T	Figs.
934.894	P(30)	1.32E-3	1.04E-3	24.5	33,90	2.75E-3	1.19E-3	22.5	90
936.804	P(28)	1.63E-3	9.24E-4	24.5	34,91	2.44E-3	1.10E-3	22.5	91
938.688	P(26)	6.15E-4	9.79E-4	24.5	35,92	3.80E-3	9.73E-4	22.5	92
940.548	P(24)	6.11E-4	1.01E-3	24.5	36,93	4.34E-3	9.73E-4	22.5	93
942.383	P(22)	7.25E-4	9.93E-4	24.5	37,94	5.77E-3	8.64E-4	22.5	94
944.194	P(20)	2.39E-3	8.56E-4	23.5	38,95	1.96E-3	8.76E-4	22.5	95
945.980	P(18)	1.09E-3	9.21E-4	24.5	39,96	1.25E-3	9.00E-4	22.5	96
951.192	P(12)	4.67E-4	9.09E-4	24.5	40,97	2.35E-3	8.16E-4	22.5	97
952.881	P(10)	1.21E-3	9.11E-4	24.5	41,98	2.52E-3	8.30E-4	22.5	98
969.140	R(10)	3.09E-4	8.67E-4	24.5	42				
970.547	R(12)	1.32E-2	6.41E-4	24.5	43,99	1.34E-2	6.01E-4	22.5	99
971.930	R(14)	8.29E-3	1.16E-3	24.5	44				
973.288	R(16)	6.36E-3	7.90E-4	24.5	45				
974.622	R(18)					6.86E-3	7.19E-4	22.5	100
975.930	R(20)	9.16E-2		22.5	46	9.16E-2		22.5	101
977.214	R(22)	4.98E-3	7.80E-4	25.0	47,102	5.85E-3	7.46E-4	22.5	102
980.913	R(28)	1.84E-4	8.58E-4	25.0	48,103	1.24E-3	7.60E-4	22.5	103
1048.661	P(18)					4.22E-3	6.66E-4	22.5	104
1050.441	P(16)	9.38E-3	2.64E-4	23.5	49,105	5.54E-3	6.28E-4	22.5	105
1052.196	P(14)	7.92E-3	3.48E-4	23.5	50,106	5.12E-3	6.61E-4	22.5	106
1053.924	P(12)	7.25E-3	4.31E-4	23.5	51				
1073.278	R(12)	3.05E-3	8.52E-4	24.0	52				
1077.303	R(18)	1.51E-3	6.94E-4	24.0	53,107	4.43E-3	6.54E-4	22.5	107
1079.852	R(22)	1.27E-3	6.92E-4	24.0	54				
1081.087	R(24)	4.98E-4	7.66E-4	24.0	55	4.29E-3	7.35E-4	22.5	108
1082.296	R(26)					4.15E-3	5.71E-4	22.5	109

With the exception of data taken on the R(20) line at 975.93 cm^{-1} , the pressure broadened water vapor results at each laser frequency have been fit to a polynomial of the form given in Equation (104). At 975.93 cm^{-1} the absorption coefficient will have both a near line center and far wing contributions, so that

$$k(975.9 \text{ cm}^{-1}) = k^{NL,C} + \sum_i k_i^{FW} \quad (105)$$

2. Room temperature data

In Chapter V, results from spectrophone and White cell measurements of H_2O in N_2 , H_2O in 80-20 air, H_2O in 60-40 air and H_2O in O_2 absorption were plotted as a function of water vapor partial pressure.

a. curve fit coefficients

The curve fit coefficients for these four different sample gas mixtures are presented here in Tables 5 through 8 respectively. In these tables the positive coefficients A and B from Equation (104) are listed for each laser frequency studied together with the sample gas temperature and figure number(s) where the data has been plotted in Chapter V. The information contained in Tables 5 through 8 has been repeated in Tables 9 through 12 respectively using a different set of constants which facilitate comparison with the results of other researchers. Tables 9 through 12 give curve fits for these experimental data in terms of the constants $C_s^0(\nu)$ and γ , for which the absorption coefficient is expressed by⁶⁵

$$k(\nu) = C_s^0(\nu) w_{\text{H}_2\text{O}} [p_{\text{H}_2\text{O}} + \gamma(P - p_{\text{H}_2\text{O}})] \quad (106)$$

where $w_{\text{H}_2\text{O}}$ is the number density of water molecules,

$p_{\text{H}_2\text{O}}$ is the partial pressure of H_2O ,

γ is proportional to the ratio of the foreign and self-broadening coefficients

and $C_s^0(\nu)$ is a self broadening coefficient in $\text{molecules}^{-1} \text{atm}^{-1} \text{cm}^2$.

At 975.93 cm^{-1} (the R(20) laser line) $k(\nu)$ will have the form given by Equation (105). However, results of this and prior studies⁶⁶ indicate that to within experimental accuracy, the appropriate curve fit equation has the form

$$k(975.93 \text{ cm}^{-1}) = Ap = C_s^0 p w_{\text{H}_2\text{O}} \quad (107)$$

Table 6
 List of spectrophone and White cell curve fit coefficients for H₂O in 80% N₂ and 20% O₂ absorption measurements at a total pressure of 760 Torr. The data has been fit to an equation of the form $k=Ap+Bp^2$. Also given here are the sample gas temperature and figure number(s) where these data are plotted.

ν	ID	Spectrophone				White Cell			
		A	B	T	Figs	A	B	T	Figs.
936.804	P(28)	5.04E-3	6.18E-4	24	56,110	3.18E-3	9.14E-4	22	100
944.194	P(20)	4.80E-3	6.47E-4	24	57,111	3.26E-3	8.70E-4	22	111
975.930	R(20)	9.71E-2		24	58,112	9.79E-2		22	112
977.214	R(22)					7.12E-3	7.35E-4	22	113
980.913	R(28)	4.42E-3	4.25E-4	24	59,114	2.47E-3	7.14E-4	22	114
1046.854	P(20)	9.31E-3	3.81E-4	21	60				
1048.661	P(18)	1.20E-2	1.38E-4	21	61				
1050.441	P(16)	6.51E-3	5.50E-4	21	62				
1077.303	R(18)	6.68E-3	4.93E-4	21	63				
1082.296	R(26)	3.03E-3	9.05E-4	21	64				

Table 7
 List of spectrophone and White cell curve fit coefficients for H₂O in 60% N₂ and 40% O₂ absorption measurements at a total pressure 760 Torr. The data has been fit to an equation of the form $k=Ap+Bp^2$. Also given here are the sample gas temperature and the figure number(s) where these data are plotted.

ν	ID	Spectrophone				White Cell			
		A	B	T	Figs	A	B	T	Figs.
936.804	P(28)	5.27E-3	6.46E-4	23	65,115	7.33E-4	9.69E-4	21.7	115
944.194	P(20)	4.88E-3	6.42E-4	23	66,116	5.46E-4	9.55E-4	21.7	116
975.930	R(20)	1.07E-1		23.6	67,117	1.02E-1		21.7	117
977.214	R(22)					3.03E-3	8.54E-4	21.7	118
980.913	R(28)	4.17E-3	4.57E-4	23	68,119	1.80E-3	7.39E-4	21.7	119
1046.854	P(20)	5.11E-3	6.52E-4	22	69				
1048.661	P(18)	4.64E-3	5.94E-4	22	70				
1050.441	P(16)	6.85E-3	4.18E-4	22	71				
1077.303	R(18)	7.12E-5	8.76E-4	22.6	72				
1082.296	R(26)	9.43E-4	9.42E-4	22	73				

Table 8
 List of spectrophone curve fit coefficients for H₂O in O₂ absorption measurements at a total pressure of 760 Torr. The data has been fit to an equation of the form $k=Ap+Bp^2$. Also given here are the sample gas temperature and the figure number(s) where these data are plotted.

		Spectrophone			
ν	ID	A	B	T	Figs.
936.804	P(28)	1.20E-3	9.12E-4	23	74
944.194	P(20)	8.72E-4	9.12E-4	23	75
975.930	R(20)	1.49E-1		23	76
980.913	R(28)	3.54E-3	4.92E-4	23.1	77
1046.854	P(20)	3.01E-3	6.69E-4	22	78
1048.661	P(18)	2.46E-3	6.81E-4	22	79
1050.441	P(16)	4.64E-4	8.03E-4	22	80
1077.303	R(18)	2.63E-3	6.46E-4	22.6	81

Table 9
 List of spectrophone and White cell curve fit coefficients for H₂O in N₂ measurements at a total pressure of 760 Torr. The data has been fit to an equation of the form $k(\nu) = C_S^O(\nu) w_{H_2O} [\gamma(P - P_{H_2O})]$. Also given here are the sample gas temperature and figure number(s) where these data are plotted.

ν	ID	Spectrophone				White Cell			
		$C_S^O \times 10^{22}$	γ	T	Figs.	$C_S^O \times 10^{22}$	γ	T	Figs.
934.894	P(30)	2.44	1.67E-3	24.5	33,90	2.78	3.03E-3	22.5	90
936.804	P(28)	2.17	2.32E-3	24.5	34,91	2.57	2.91E-3	22.5	91
938.688	P(26)	2.29	8.26E-4	24.5	35,92	2.27	5.11E-3	22.5	92
940.548	P(24)	2.37	7.95E-4	24.5	36,93	2.28	5.83E-3	22.5	93
942.383	P(22)	2.33	9.60E-4	24.5	37,94	2.03	8.71E-3	22.5	94
944.194	P(20)	2.00	3.66E-3	23.5	38,95	2.04	2.94E-3	22.5	95
945.980	P(18)	2.16	1.55E-3	24.5	39,96	2.10	1.82E-3	22.5	96
947.743	P(16)								
951.192	P(12)	2.13	6.76E-4	24.5	40,97	1.90	3.78E-3	22.5	97
952.881	P(10)	2.14	1.74E-3	24.5	41,98	1.94	3.98E-3	22.5	98
969.140	R(10)	2.03	4.69E-4	24.5	42				
970.547	R(12)	1.54	2.64E-2	24.5	43,99	1.44	2.85E-2	22.5	99
971.930	R(14)	2.74	9.32E-3	24.5	44				
973.288	R(16)	1.87	1.05E-2	24.5	45				
974.622	R(18)					1.69	1.24E-2	22.5	100
975.930	R(20)	0.280	1.00	22.5	46	.280	1.00		101
977.214	R(22)	1.84	8.33E-3	25.0	47,102	1.75	1.02E-2	22.5	102
980.913	R(28)	2.01	2.82E-4	25	48,103	1.77	2.14E-3	22.5	103
1048.661	P(18)					1.56	8.27E-3	22.5	104
1050.441	P(16)	0.645	4.47E-2	23.5	49,105	1.48	1.15E-2	22.5	105
1052.196	P(14)	0.836	2.91E-2	23.5	50,106	1.55	1.01E-2	22.5	106
1053.924	P(12)	1.03	2.17E-4	23.5	51				
1073.278	R(12)	2.00	4.69E-3	24.0	52				
1077.303	R(18)	1.63	2.85E-3	24.0	53,107	1.53	8.83E-3	22.5	107
1079.852	R(22)	1.62	2.41E-3	24.0	54				
1081.087	R(24)	1.79	8.55E-4	24.0	55	1.72	7.62E-3	22.5	108
1082.296	R(26)					1.34	9.47E-3	22.5	109

Table 10
 List of spectrophone and White cell curve fit coefficients for H₂O
 in 80% N₂ and 20% O₂ absorption measurements at a total
 pressure of 760 Torr. The data has been fit to an equation
 of the form $k(\nu) = C_S^O(\nu) w_{H_2O} [P_{H_2O} + \gamma(P - P_{H_2O})]$. Also
 given here are the sample gas temperature and figure
 number(s) where the data are plotted.

ν	ID	Spectrophone				White Cell			
		$C_S^O \times 10^{22}$	γ	T	Figs.	$C_S^O \times 10^{22}$	γ	T	Figs.
936.804	P(28)	1.46	1.06E-2	24	56,110	2.13	4.56E-3	22	110
944.194	P(20)	1.53	9.67E-3	24	57,111	2.03	4.91E-3	22	111
975.930	R(20)	.299	1.00	24	58,112	.299	1.00	22	112
977.214	R(22)					1.73	1.26E-2	22	113
980.913	R(28)	1.01	1.35E-2	24	59,114	1.67	4.53E-3	22	114
1046.854	P(20)	.910	3.12E-2	21	60				
1048.661	P(18)	.356	1.03E-1	21	61				
1050.441	P(16)	1.29	1.53E-2	21	62				
1077.303	R(18)	1.16	1.75E-2	21	63				
1082.296	R(26)	2.10	4.39E-3	21	64				

Table 11
 List of spectrophone and White cell curve fit coefficients for H₂O in
 60% N₂ and 40% O₂ absorption measurements at a total pressure
 of 760 Torr. The data has been fit to an equation of the form
 $k(\nu) = C_S^O(\nu) w_{H_2O} [P_{H_2O} + \gamma(P - P_{H_2O})]$. Also given here are the
 sample gas temperature and the figure number(s)
 where these data are plotted.

ν	ID	Spectrophone				White Cell			
		$C_S^O \times 10^{22}$	γ	T	Figs.	$C_S^O \times 10^{22}$	γ	T	Figs.
936.804	P(28)	1.52	1.06E-2	23	65,115	2.25	9.94E-4	21.7	115
944.194	P(20)	1.51	9.90E-3	23	66,116	2.22	7.52E-4	21.7	116
975.930	R(20)	.329	1.00	23.6	67,117	.312	1.00	21.7	117
977.214	R(22)					1.99	4.65E-3	21.7	118
980.913	R(28)	1.08	1.19E-2	23	68,119	1.72	3.19E-3	21.7	119
1046.854	P(20)	1.53	1.02E-2	22	69				
1048.661	P(18)	1.39	1.02E-2	22	70				
1050.441	P(16)	.991	2.11E-2	22	71				
1077.303	R(18)	2.04	1.07E-4	22.6	72				
1082.296	R(26)	2.19	1.32E-3	22	73				

Table 12
 List of spectrophone curve fit coefficients for H₂O in O₂ absorption measurements at a total pressure of 760 Torr. The data has been fit to an equation of the form $k(\nu) = C_s^O(\nu) w_{H_2O} [P_{H_2O} + \gamma(P - P_{H_2O})]$.
 Also given here the the sample gas temperatures and the figure numbers where these data are plotted.

Spectrophone					
ν	ID	$C_s^O \times 10^{22}$	γ	T	Figs.
936.804	P(28)	2.13	1.73E-3	23	74
944.194	P(20)	2.13	1.26E-3	23	75
975.930	R(20)	.457	1.00	23	76
980.913	R(28)	1.16	9.38E-3	23.1	77
1046.854	P(20)	1.56	5.89E-3	22	78
1048.661	P(18)	1.59	4.73E-3	22	79
1050.441	P(16)	1.87	7.60E-4	22	80
1077.303	R(18)	1.51	5.33E-3	22.6	81

This is the equation to which data at the R(20) laser line have been fit in Tables 5 through 12. Consideration of Equations (102) and (103) shows that in order for k to be linear with water vapor partial pressure it is necessary that

$$-B^{NLC} + \sum B_i^{FW} = 0, \quad (108)$$

or using the equations (37) and (43) this implies

$$\frac{R-1}{p_a^0 760} \left[1 - 3 \left(\frac{\nu - \nu_0}{\alpha_L^0} \right)^2 \left(\frac{p_a^0 (R-1) + 760}{760} \right)^2 \right] \left[\frac{p_a^0 (R-1) + 760}{760} \right] \frac{S^0}{\pi \alpha_L^0} \quad (109)$$

$$\approx \frac{(R-1)}{(R-1)p_a^0 + 760p_a^0} \sum_i \left(\frac{\alpha_{L_i}^0}{\nu - \nu_{0i}} \right)^2 \frac{S_i^0}{\pi \alpha_{L_i}^0}$$

where the term on the left hand side represents B^{NLC} and the terms on the right hand side give $\sum B_i^{FW}$. The separation between the R(20) CO₂ laser line at 975.93 cm⁻¹ and the adjacent water line can be found by solving Equation (108) for $(\nu - \nu_0)$, i.e.,

$$|\nu - \nu_0| = \alpha_L^0 \left\{ 1 - \left(\frac{760}{p_e^0} \right)^2 \frac{\sum_i \left(\frac{\alpha_{L_i}^0}{\nu - \nu_{0i}} \right)^2 \frac{S_i^0}{\alpha_{L_i}^0}}{s^0 / \alpha_L^0} \right\}^{\frac{1}{2}} \frac{760}{\sqrt{3} P_e^0} \quad (110)$$

The series in the numerator can be evaluated using the AFCRL line compilation with the result that $|\nu - \nu_0|$ should be on the order of .495 α_L , where α_L is approximately 0.0405 cm⁻¹.⁶⁷ According to this same reference $|\nu - \nu_0|$ is 0.082, but this separation results in a calculated absorption coefficient which is much smaller than that observed experimentally. Based on this simple calculation we estimate that the separation is actually 0.02 cm⁻¹.

b. comparison of results

In this section two comparisons will be noted, the first is between the spectrophone and White cell data taken in this study. The second is between the results of this study and those of previous workers.

1. this study

Figures 90 through 109 in Chapter V display a comparison between the White cell and spectrophone measurements of water vapor in nitrogen absorption. With the exception of the P(22) through P(30) lines in the 10.4 μ m band and the R(18) line at 1077.3 cm⁻¹ the agreement is quite good. The

inconsistencies at the P(22) through P(30) lines can possibly be associated with the fact that these five lines were all measured on the same day. This implies that an error associated with measuring the background transmission of the cell would appear at all five laser lines. It should also be noted here that the data recorded at these five lines were taken at a reduced path length of only 1 km while all other White cell results were obtained at 1.5 km. In light of the discussion given in Chapter III on the susceptibility of transmittance measurements to errors in highly transmitting samples this author tends to support the spectrophone data.

A direct comparison of all the results at a single water vapor partial pressure, 14.3 Torr is given in Figure 127 where absorption in km^{-1} is plotted vs wavenumber in cm^{-1} . In this figure the White cell data is indicated by the triangles and the spectrophone results by the squares. A close examination of Figure 127 shows that (if the rapid local variation around 970 cm^{-1} are ignored) water vapor absorption decreases slowly with increasing wavenumber. More will be said concerning frequency dependence when the continuum is discussed in the final section of this chapter.

The results obtained with the nitrogen-oxygen buffer gas mixtures are compared in Figures 110 through 119 of Chapter V. These results indicate reasonable agreement between the two techniques. In particular the data at 975.93 cm^{-1} demonstrates that the spectrophone calibration is accurate to better than 1%. The results of absorption measurements with 80-20 air, given in Figures 110 through 114, indicate that a slightly lower absorption is being measured with the spectrophone than by the White cell. With the 60-40 buffer gas mixture this pattern is reversed, see Figures 115 through 119, and the spectrophone measurements indicate a slightly higher absorption than the White cell data.

A plot of all the 80-20 artificial air results is given in Figure 128 where absorption has been plotted vs wavenumber. This plot provides an overall comparison of these results at a water vapor partial pressure of 14.3 Torr and again shows that H_2O absorption is a slowly varying function of frequency. In Figure 128 the spectrophone data are given by the diamonds, while the White cell data are indicated with the crosses. The spectrophone data were taken at $\sim 24^\circ\text{C}$, while the White cell measurements were made at $\sim 22^\circ\text{C}$; this temperature difference accounts for some of the discrepancy observed in Figure 128.

2. previous studies

The most extensive set of data with which to form a comparison comes from the work of Shumate, et al. at the Jet Propulsion Laboratory, JPL⁶⁸. They have used a resonant spectrophone to measure H_2O in air absorption at 49 CO_2 laser lines. To formulate a comparison, we have fit their data, listed at three water vapor partial pressures (5, 10 and 15 Torr) to Equation (104) for each laser frequency. Using the A and B coefficient obtained from

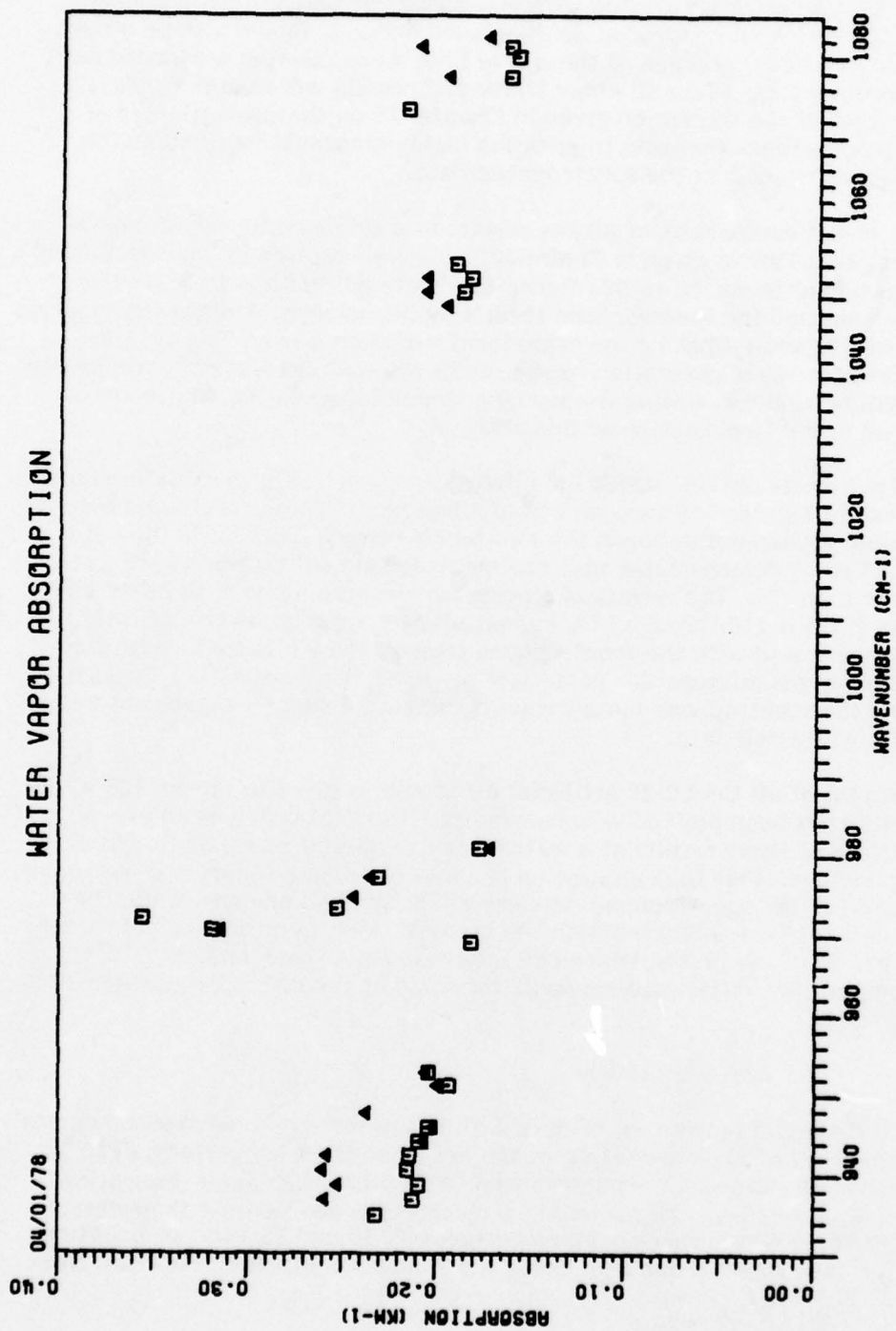


Figure 127. Measured H₂O in N₂ absorption as a function of the CO₂ laser line wavenumber. The water vapor partial pressure is 14.3 Torr and the total pressure is 760 Torr. Average temperature is 23.4°C.

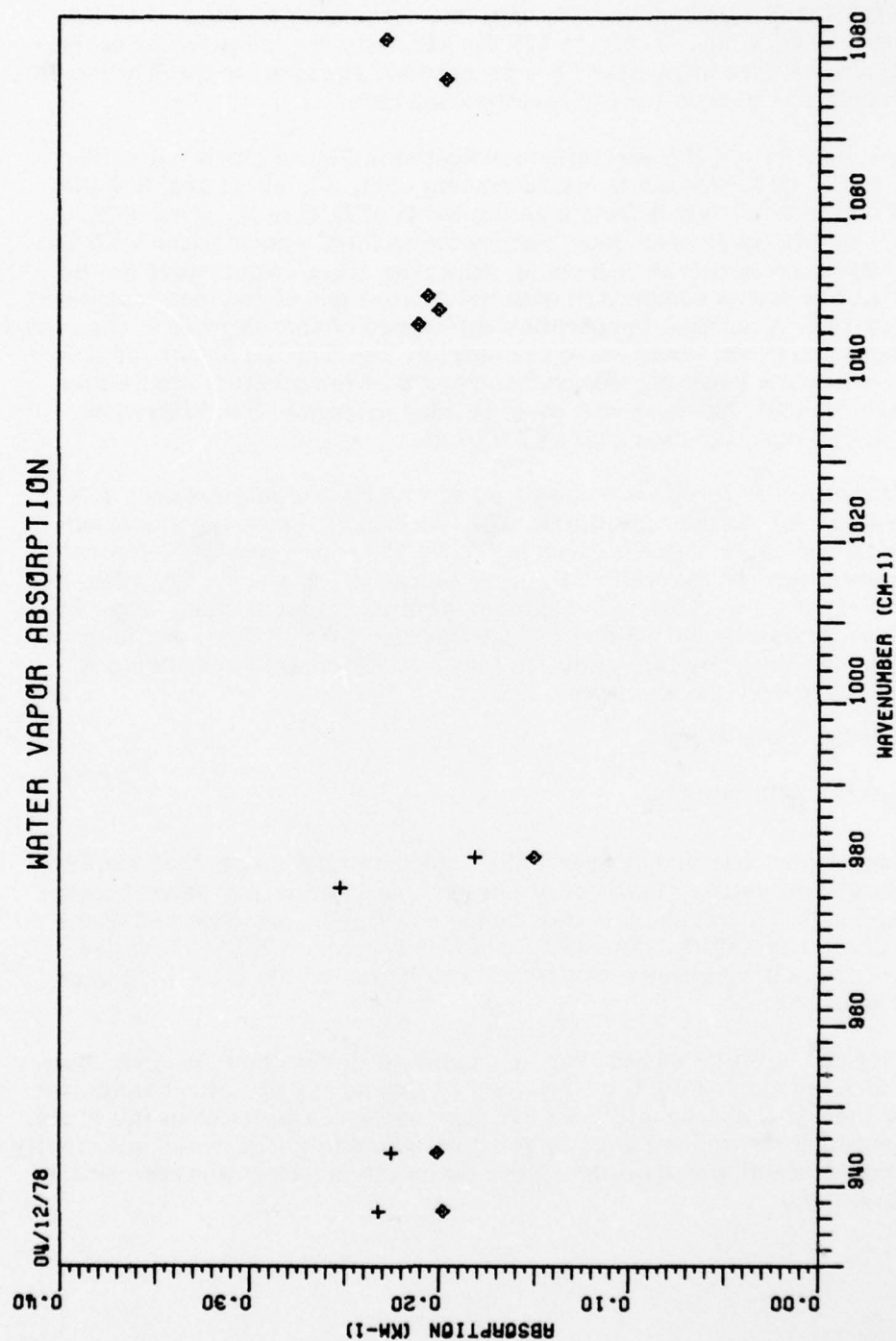


Figure 128. Measured H₂O in 80-20 air absorption in km⁻¹ as a function of wavenumber for a water vapor partial pressure of 14.3 Torr. The spectrophone data indicated by the symbol ◇; the White cell data is given by the symbol +.

these curve fits, the absorption at a partial pressure of 14.3 was calculated. Figure 129 shows a plot of the JPL data vs wavenumber together with the results from this study. In Figure 129 the JPL data are indicated by crosses while the results from this study are denoted by triangles for the White cell experiments and squares for the spectrophone data.

To some extent the comparison indicated in Figure 129 is not valid since the JPL data represents measurements of H_2O in air at $300^\circ K$ while the data from this study is from measurements of H_2O in N_2 at $\sim 296^\circ K$. In this regard it would seem most reasonable to form a comparison with the H_2O in 80-20 air results of this study. However, those results have not been included since such a comparison does not remove any of the inconsistencies in Figure 129. A nominal temperature difference of four degrees in the sample gas is significant and would cause the measurements at the higher temperature to indicate a lower absorption (see results of temperature studies) but it is doubtful that this argument could be used to explain the differences observed in Figure 129 near the $9.4 \mu m$ band.

In Figure 129 results are compared at a single partial pressure; it is also desirable to consider absorption as a function of water vapor concentration. A typical example is given in Figure 130 where results of the two studies are given for the R(22) CO_2 laser line at 977.214 cm^{-1} . The JPL data (denoted by the crosses) indicate an absorption that is much larger at low partial pressures and smaller at high (greater than 16 Torr) partial pressures than predicted by this study. In terms of the curve fit constants A and B of Equation (104) we have

$$\begin{aligned} A^{JPL} &> A^{\text{this study}} \\ B^{JPL} &< B^{\text{this study}} \end{aligned} \quad (111)$$

This condition is observed at nearly all frequencies and means that the JPL data has less curvature. In terms of physical parameters, the second condition implies that a smaller self-broadening coefficient was observed in the JPL data than this study. An example of this is given in Table 13, where values of the self broadening coefficient are listed for the P(20) CO_2 laser line at 944.194 cm^{-1} .

McCoy⁶⁹ also measured H_2O in air absorption for the P(20) CO_2 laser line at 944.194 cm^{-1} using the White cell at this laboratory. His results (denote by the wyes) appear in Figure 131 together with results from this study. The agreement shown here is quite good; unfortunately McCoy did not specify the temperature at which his data were taken which makes this comparison a little obscure.

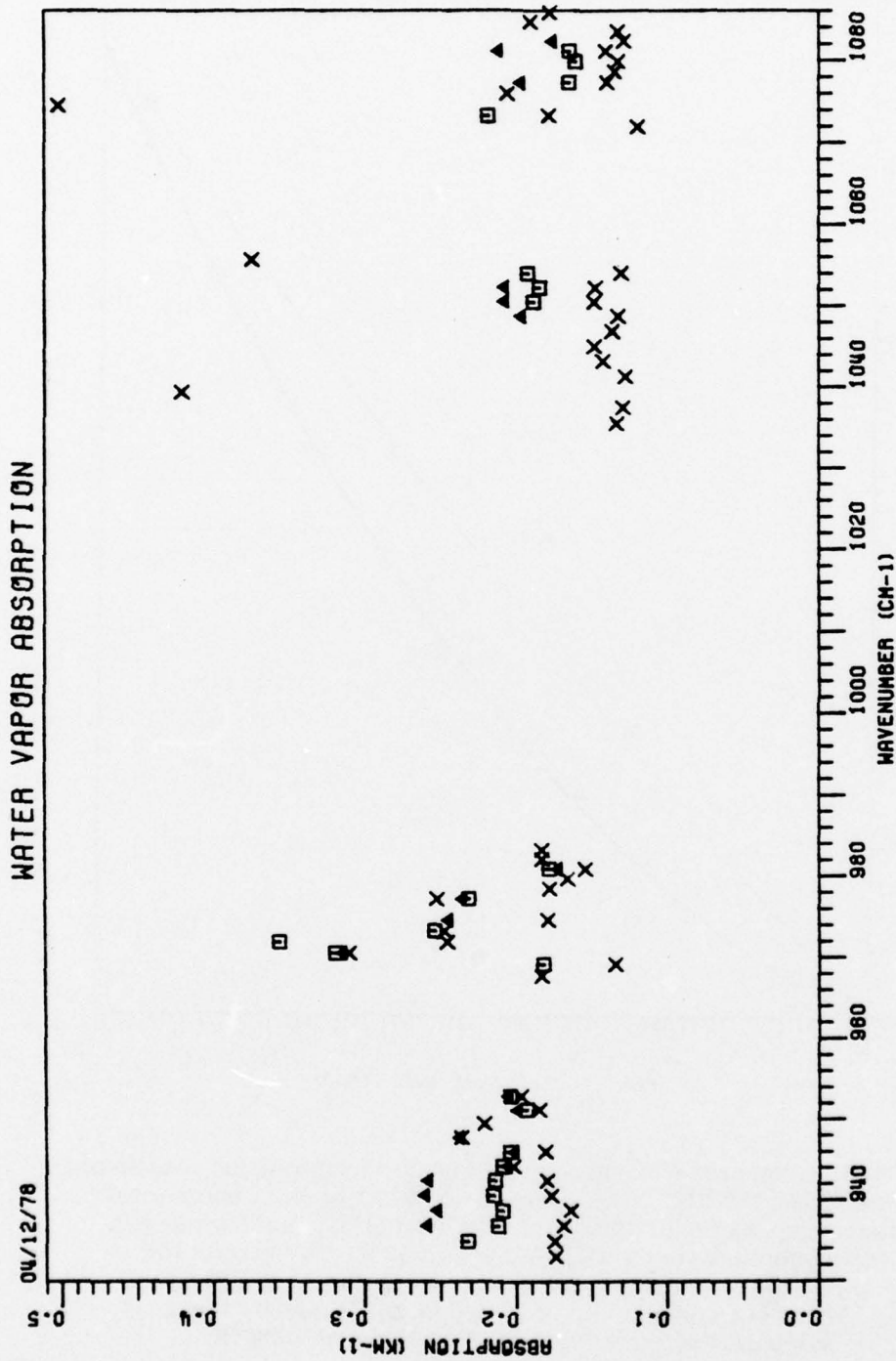


Figure 129. Measured absorption (in km^{-1}) of CO_2 laser radiation as a function of frequency (in cm^{-1}) for a water vapor partial pressure of 14.3 Torr. JPL data are indicated by the symbol X, while the results from this study are given by \square for spectrophone data and Δ for White cell results.

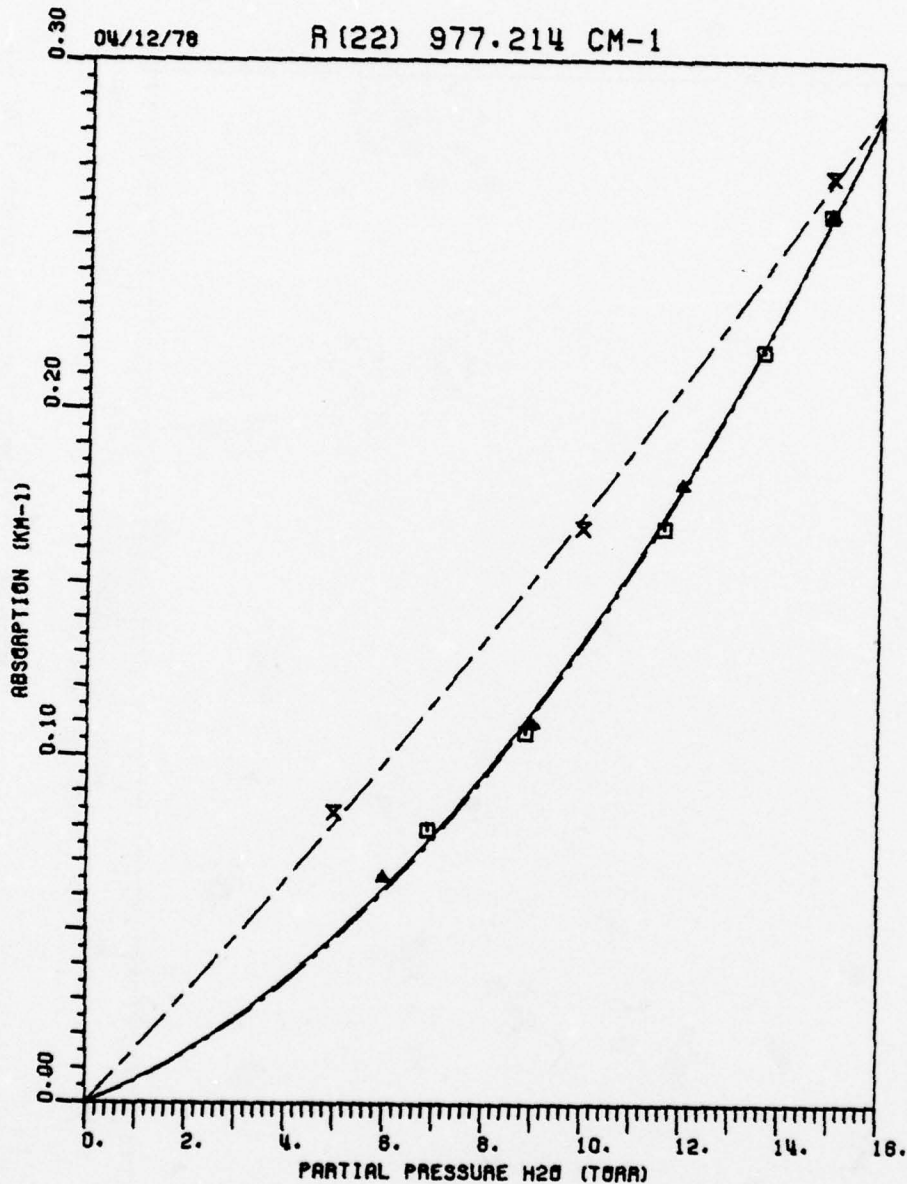


Figure 130. Comparison of measured water vapor absorption coefficient (in km^{-1}) for the R(22) CO_2 laser line at 977.214 cm^{-1} and a total sample gas pressure of 760 Torr. The symbol X indicates the JPL experimental data for H_2O in air at 300°K . The results for H_2O in N_2 from this study are given by the symbol \square for the spectrophone data recorded at 298°K and by the symbol Δ for the White cell data taken at $\sim 296^\circ\text{K}$.

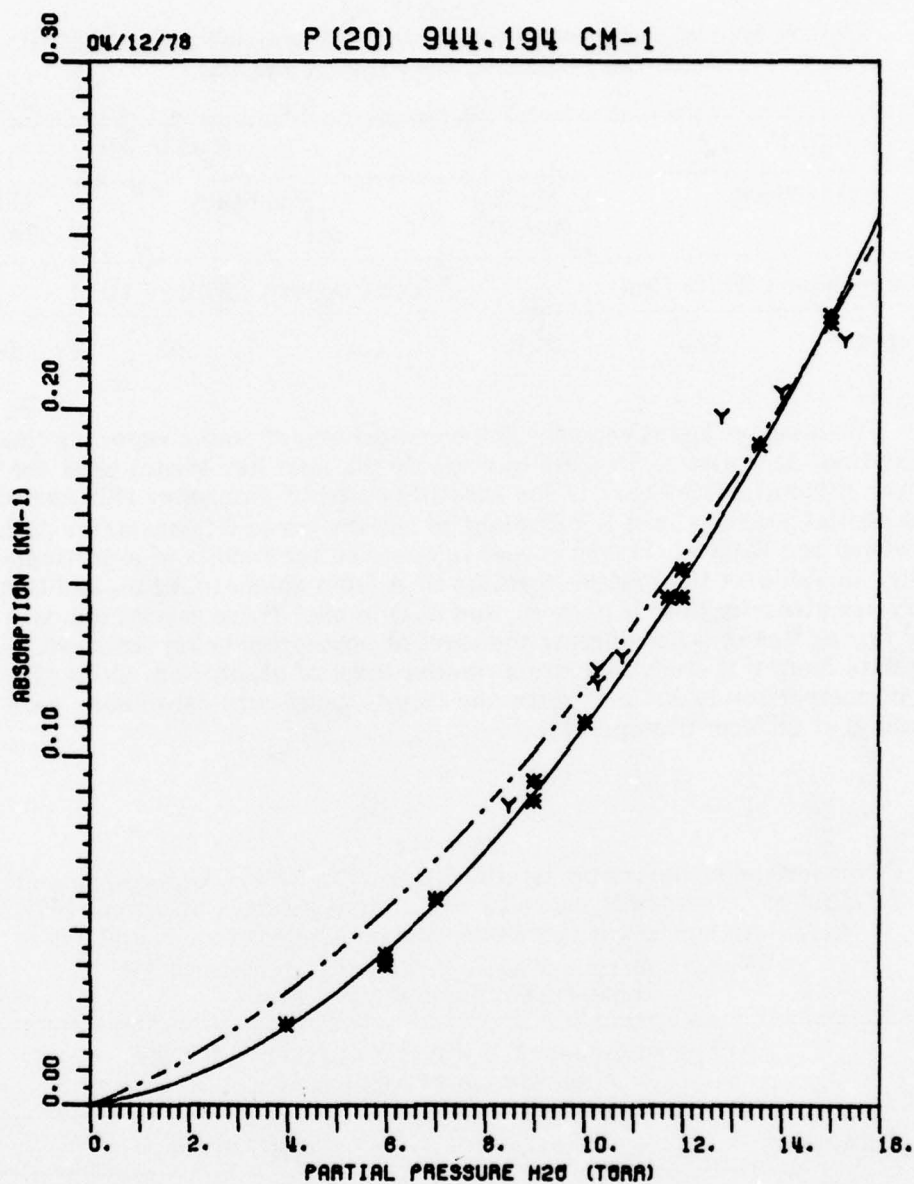


Figure 131. Measured absorption in km^{-1} as a function of water vapor partial pressure in Torr for the P(20) CO_2 laser line at 944.194 cm^{-1} . The symbol Y indicates the results obtained by McCoy for a H_2O in air sample at a total pressure of 700 Torr. Data from spectrophone and White cell measurements of H_2O in N_2 at a total pressure of 760 Torr are given by the symbol * for this study. The broken curve — — — indicates the least square fit of McCoy's data to Equation (129) while the solid curve gives the best fit to the data from this study.

Table 13
Comparison of measured values of the self broadening coefficient
for the P(20) CO₂ laser line at 944.194.

H ₂ O in N ₂			H ₂ O in Air		
This Study		McCoy Ref. 69	This Study		JPL Ref. 68
Spectrophone	White Cell		Spectrophone	White Cell	
272	339	193	102	203	88

The analysis just given provides a comparison of water vapor continuum absorption. It is also of interest to consider the near line center behavior for the R(20) at 975.93 cm⁻¹. The absorption at this frequency is linear with H₂O partial pressure so it is sufficient to list the curve fit parameter A (i.e., the slope) see Equation (107) in order to describe the results of a particular study. In Table 14 the measured values of A from Shumate, et al. and this study are given for both H₂O in N₂ and H₂O in air. These results indicate only fair agreement, considering the level of absorption being observed. The data from this study indicate a smaller level of absorption, although direct comparison is difficult since the results being considered here were obtained at different temperatures.

Table 14
Comparison of measured values of A for the R(20) CO₂ laser line at
975.93 cm⁻¹. A is the curve fit coefficient given in Equation (107),
i.e., k=Ap where k is the absorption coefficient (km⁻¹) and p is
the H₂O partial pressure (Torr). Total pressure for
these measurements was 1 atm.

Measured Values of A where k=Ap (km ⁻¹) for the R(20) Line at 975.93 cm ⁻¹ .					
H ₂ O in N ₂		H ₂ O in Air			
JPL, 300°K	This Study 296°K	JPL 300°K	301°K	This Study 297°K	289°K
0.99	0.92	1.10	1.06	0.97	0.86

c. effects of oxygen

In Chapter V results are also given from experiments in which the nitrogen and oxygen content of the broadening gas was varied. Table 15 provides a list of figures where the spectrophone and White cell data can be found for the laser lines used to study this effect. Since neither N_2 nor O_2 are infrared active, their influence on the absorption process arises from the collision broadening of the water vapor absorption lines.

Table 15
List of figures where the indicated pressure broadened water vapor absorption data may be found. The * indicates that this figure will show a comparison of spectrophone and White cell data.

ν	ID	H ₂ O in N ₂ Figure No.	H ₂ O in 80-20 Air Figure No.	H ₂ O in 60-40 Air Figure No.	H ₂ O in O ₂ Figure No.
936.804	P(28)	34,91*	56,110*	65,115*	74
944.194	P(20)	38,95*	57,111*	66,116*	75
975.930	R(20)	46,101	58,112*	67,117*	76
977.215	R(22)	47,102*	113	118	
980.913	R(28)	48,103*	59,114*	68,119*	77
1046.854	P(20)		60	69	78
1048.661	P(18)	104	61	70	79
1050.441	P(16)	105	62	71	80
1077.303	R(18)	107	63	72	81
1082.296	R(26)	109	64	73	

The explicit dependence of the line profile on the relative oxygen concentration can be found by substituting the equation for halfwidth, Equation (15), into the equation for the Lorentz line shape, Equation (13), with the result that

$$g_L(\nu - \nu_0) = \frac{1}{\alpha_L} \frac{p_e(x)/p_e(x^0)}{\left[\frac{p_e(x)}{p_e(x^0)} \right]^2 + \left(\frac{\nu - \nu_0}{\alpha_L} \right)^2} \quad (112)$$

where x is the fraction of oxygen in the buffer gas, i.e.,
 $p_e(x) = p_a [B - (Fx + 1 - x)] + 760 [Fx + 1 - x]$,
 $p_e(x^0)$ is an arbitrary reference effective pressure,
 α_L is the Lorentz half width at $p_e = p_e(x^0)$,
 p_a is the absorber partial pressure,
 B is the selfbroadening coefficient,
 and F is the foreign broadening coefficient.

Several workers have established that oxygen is a less effective broadening molecule than nitrogen^{70,71,68} so that F must be less than one.

The influence of oxygen on the absorption coefficient will enter directly through the parameter x , i.e., $x=0$ corresponds to no oxygen present while $x=1$ is the case of a buffer gas consisting of 100% O_2 . The contribution of a single absorption line to $k(\nu)$ is given by

$$k(\nu; x) = \frac{s}{\pi \alpha_L} \frac{1 - ax}{(1 - ax)^2 + \left(\frac{\nu - \nu_0}{\alpha_L} \right)^2} \quad (113)$$

in which the constant a is defined as

$$a = (1 - F) \left[\frac{760 - p_a}{p_e(0)} \right] \quad (114)$$

and $p_e(x^0) \equiv p_e(0)$. Now, if $ax \ll 1$ $\} (1 - ax)^2 \sim 1$ Equation (113) can be approximated by

$$k(\nu; x) \sim \frac{s}{\pi \alpha_L} \frac{1 - ax}{1 + \left(\frac{\nu - \nu_0}{\alpha_L} \right)^2} \quad (115)$$

which simply says that $k(\nu; x)$ will slowly decrease as x increases, i.e., as oxygen is added.

In general ax does not satisfy the strict inequality $ax \ll 1$ so that a more complete analysis of Equation (113) is required. Further inspection of this equation shows that it has exactly the same form as the real (i.e., reactive) part of the atomic susceptibility function, provided we identify $(1 - ax)$ as the independent variable. In Figure 132 a plot of equation (113) is shown with k as the dependent variable and $(1 - ax)$ as the independent variable. It should be noted that negative values of $(1 - ax)$ have no physical significance and that $0 < (1 - ax) \leq 1$. Also as oxygen is added the parameter x ($0 < x < 1$) will increase so that the independent variable $(1 - ax)$ must decrease in value, i.e., as the oxygen concentration increases we must trace the curve in Figure 132 back toward the origin.

In the far wing approximation $(\nu - \nu_0 / \alpha_L) \gg 1$, so that the maximum in Equation (113) will occur, see Figure 132, for $(1 - ax)$ greater than 1 which is outside the range of physically meaningful values. For this case, the absorption coefficient does not obtain a maximum but will show a monotonic decrease as the oxygen concentration increases, i.e., as $(1 - ax)$ decreases. This behavior is essentially consistent with that observed in the experimental data shown in Figures 133 through 137 where plots of spectrophone measurements with varying relative concentrations of nitrogen and oxygen are given. These data show a trend of decreasing absorption with increasing oxygen. Comments concerning the White cell data will follow shortly.

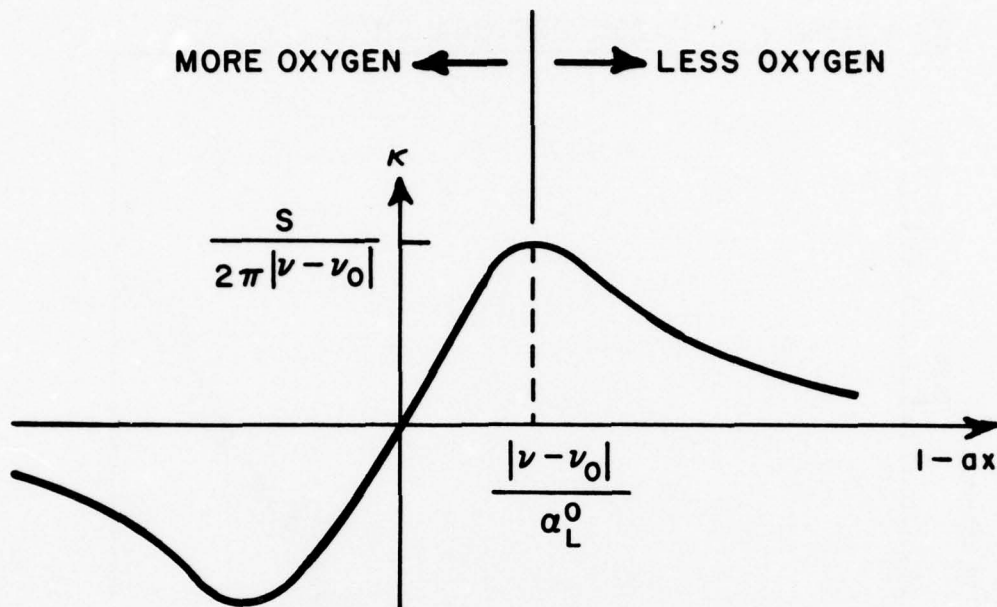


Figure 132. Plot of Equation (113) as a function of the variable $(1-ax)$. Where x gives the fraction of oxygen in the buffer gas.

For a near line center contribution to the absorption coefficient

$$0 \leq \frac{|\nu-\nu_0|}{\alpha'_L} \leq 1, \text{ so that the maximum, } S/(2\pi|\nu-\nu_0|) \text{ can actually occur.}$$

Note that this requires the laser line reside within the half width of the absorption line. Further examination of this case shows that two situations are possible:

1. $1 \geq \frac{|\nu-\nu_0|}{\alpha'_L}$
2. $1 > \frac{|\nu-\nu_0|}{\alpha'_L}$

In the first case k will also show a steady (monotonic) decrease as the oxygen concentration increases. For the second case k will increase as oxygen is added until $1-ax = |\nu-\nu_0|/\alpha'_L$ after which a decrease in absorption follows,

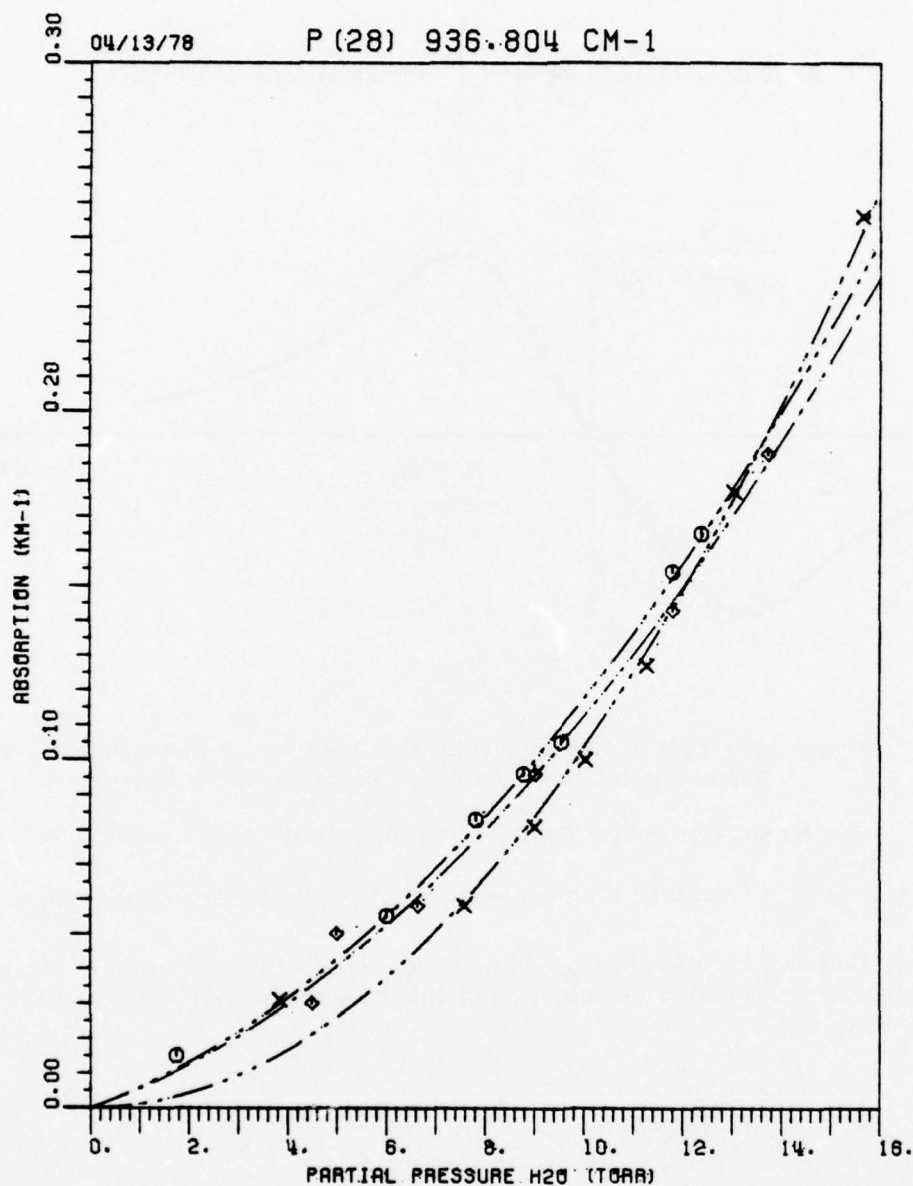


Figure 133. Measured water vapor absorption coefficient at a total pressure of 760 Torr, for the P(28) CO₂ laser line at 936.804 cm⁻¹. The symbol ♦ indicates spectrophone results for H₂O in 80-20 air at a temperature of 24°C. The symbol ○ indicates spectrophone results for H₂O in 60-40 air at a temperature of 23°C. The symbol X indicates spectrophone results for H₂O in O₂ at a temperature of 23°C.

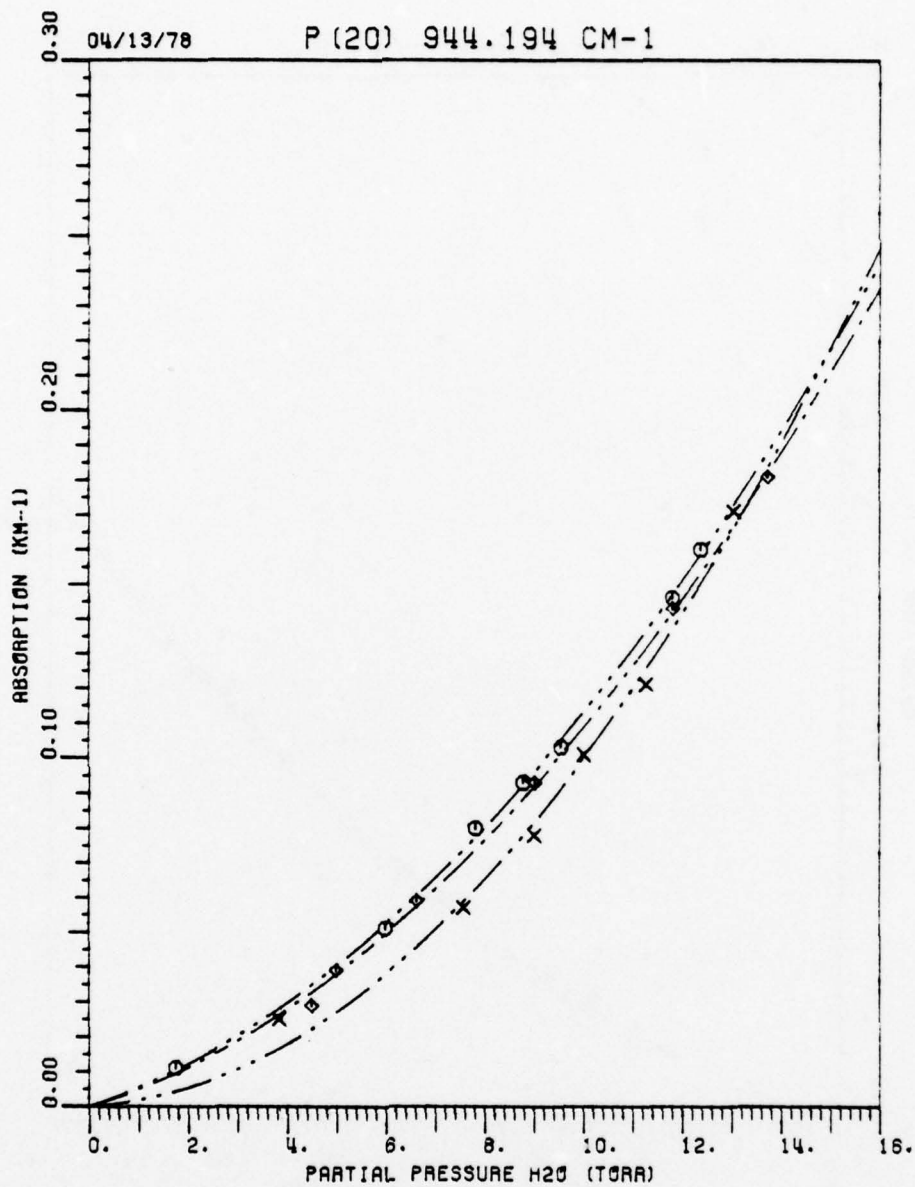


Figure 134. Measured water vapor absorption coefficient at a total pressure of 760 Torr, for the P(20) CO₂ laser line at 944.194 cm⁻¹. The symbol ◊ indicates spectrophone results for H₂O in 80-20 air at a temperature of 24°C. The symbol ⊙ indicates spectrophone results for H₂O in 60-40 air at a temperature of 23°C. The symbol X indicates spectrophone results for H₂O in O₂ at a temperature of 23°C.

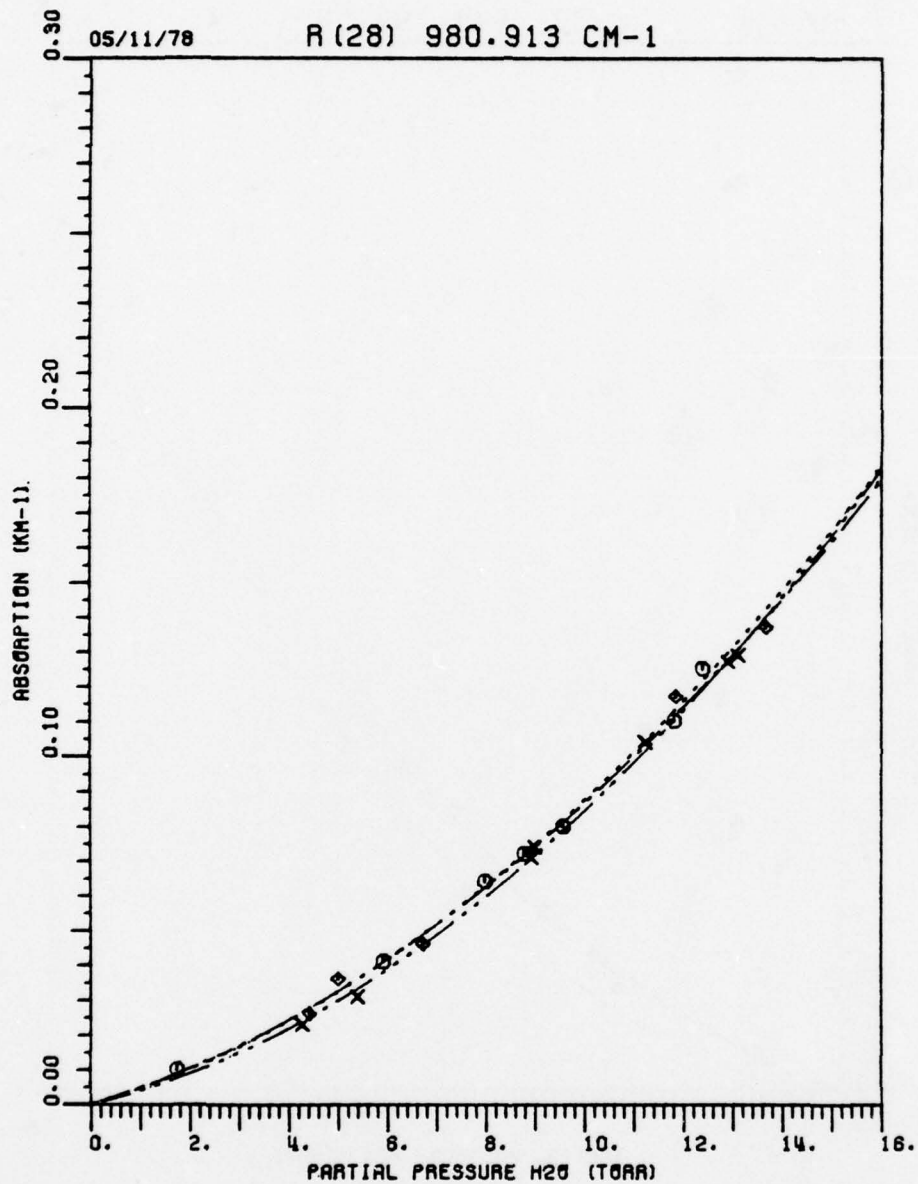


Figure 135. Measured water vapor absorption coefficient at a total pressure of 760 Torr, for the R(28) CO₂ laser line at 980.913 cm⁻¹. The symbol ◇ indicates spectrophone results for H₂O in 80-20 air at a temperature of 24°C. The symbol ○ indicates spectrophone results for H₂O in 60-40 air at a temperature of 23°C. The symbol X indicates spectrophone results for H₂O in O₂ at a temperature of 23°C.

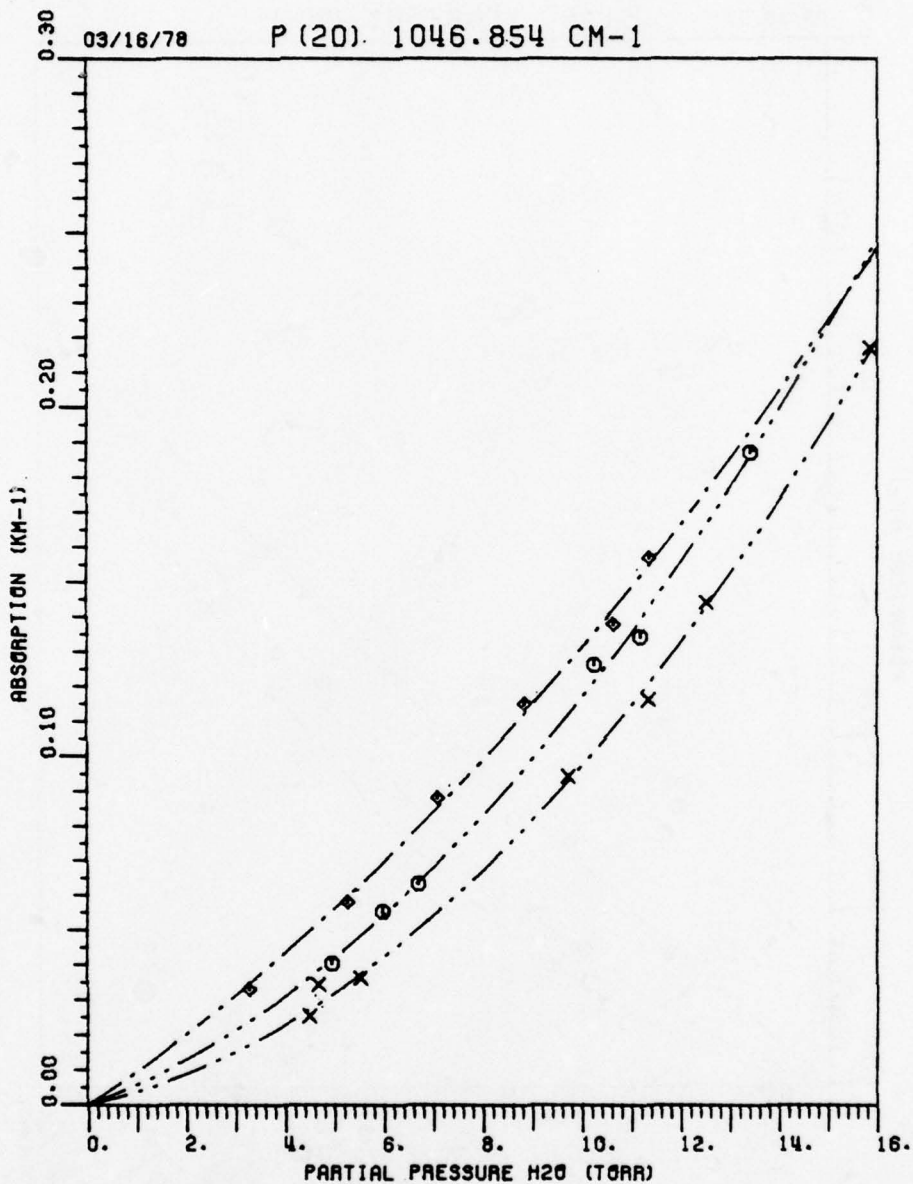


Figure 136. Measured water vapor absorption coefficient at a total pressure of 760 Torr, for the P(20) CO₂ laser line at 1046.854 cm⁻¹. The symbol ♦ indicates spectrophone results for H₂O in 80-20 air at a temperature of 24°C. The symbol ○ indicates spectrophone results for H₂O in 60-40 air at a temperature of 23°C. The symbol X indicates spectrophone results for H₂O in O₂ at a temperature of 23°C.

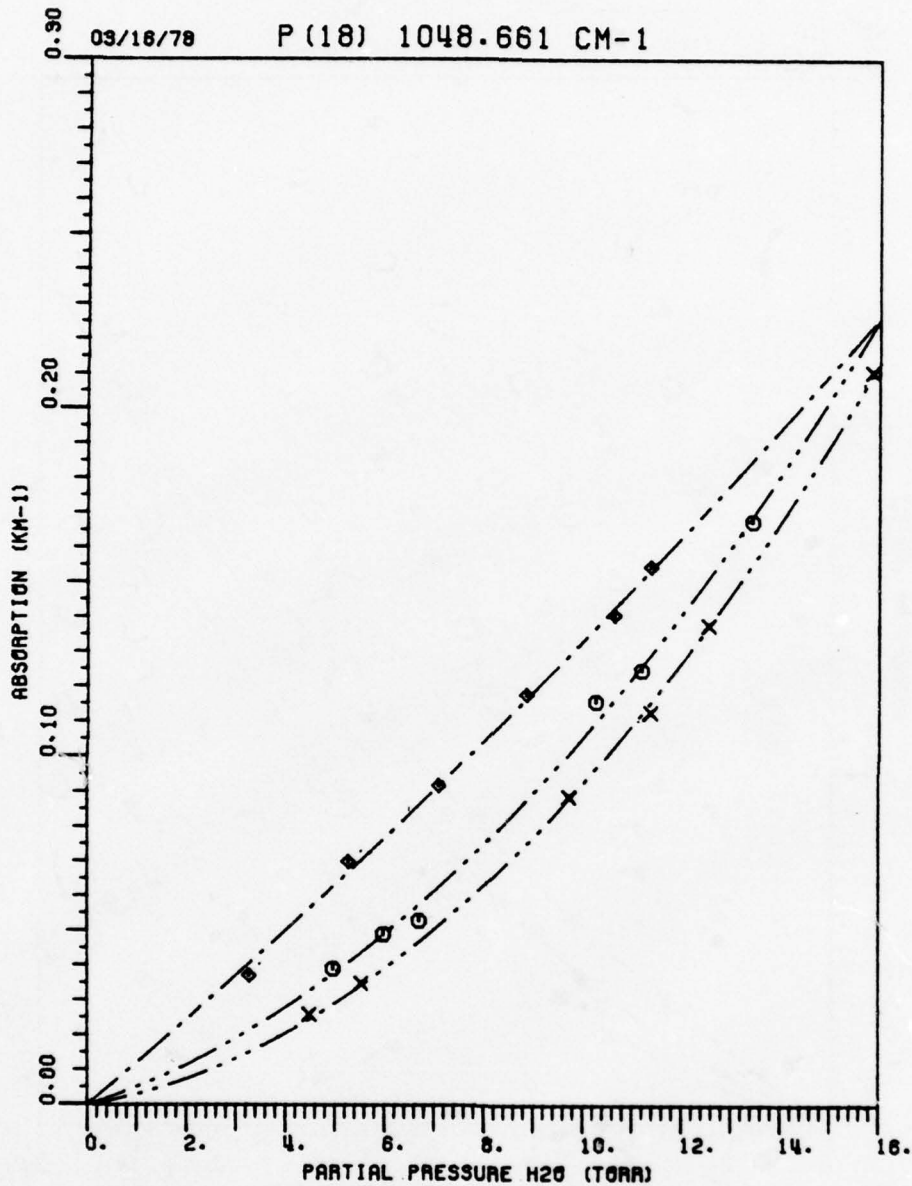


Figure 137. Measured water vapor absorption coefficient at a total pressure of 760 Torr, for the P(18) CO₂ laser line 1048.661 cm⁻¹. The symbol ◇ indicates spectrophone results for H₂O in 80-20 air at a temperature of 24°C. The symbol ○ indicates spectrophone results for H₂O in 60-40 air at a temperature of 23°C. The symbol X indicates spectrophone results for H₂O in O₂ at a temperature of 23°C.

see Figure 132. It should be noted here that k will increase as O_2 is added only if $|v - v_0| / \alpha_L < 1$. Since this behavior is observed for the R(20) CO_2 laser line at 975.93 cm^{-1} , i.e., k increased as the relative oxygen concentration was raised, the laser line must be located within the half width of the H_2O absorption line. This observation further substantiates the results calculated with Equation (110). In Figure 138 the measured absorption coefficient at the R(20) laser line is plotted vs water vapor partial pressure, for four different buffer gas mixtures, pure N_2 , 80-20 air, 60-40 air, and pure O_2 .

In Figures 139 through 143 comparison plots of the White cell measurements with three different buffer gas concentrations are given. An interesting aspect of these results is the anomalous increase of absorption with the 80-20 air mixture at the P(20), R(22) and R(28) laser lines. We have attempted to analyze this behavior in terms of the theory just presented using a modified line shape such as that given by Equation (19). The result is that the maximum shown in Figure 132 will occur at frequencies outside the Lorentz half width for a suitably modified line shape, i.e., by varying the parameter a in Equation (19). Using this model it can be argued⁷² that the increase observed with the 80-20 air mixture represents the absorption coefficient passing through a maximum as the effective pressure P_e decreases, i.e., oxygen is added. However, this explanation only provides a qualitative description that does not accurately model the behavior observed in Figures 140, 142 and 143. This discrepancy can possibly be explained by the fact that

1. The major contribution to absorption at these (P(20), R(22) and R(28)) laser lines comes from the continuum, i.e., the far wings (if we reject the water dimer and cluster theories).
2. The increase observed here falls within the possible limits of experimental error.

M. E. Thomas⁷³ has performed an experiment in which the water vapor partial pressure was held constant and the effective pressure varied by changing the total sample gas pressure, i.e., adding nitrogen. Preliminary results of his experiment indicate that the anomalous increases being considered here were not produced by a change in the effective pressure of the gas mixture.

3. Temperature Studies

The temperature dependence of pressure broadened water vapor absorption at three CO_2 laser lines was studied with the spectrophone.

a. curve fit coefficients

The curve fit parameters for these lines are listed in Tables 16 and 17 together with the corresponding temperature of the sample gas. Also given are figures in which the data is plotted. The A and B coefficients of Equations (104) and (107) are listed in Table 16, while the constants $C_s^{O(v)}$ and γ of Equation (106) are given in Table 17.

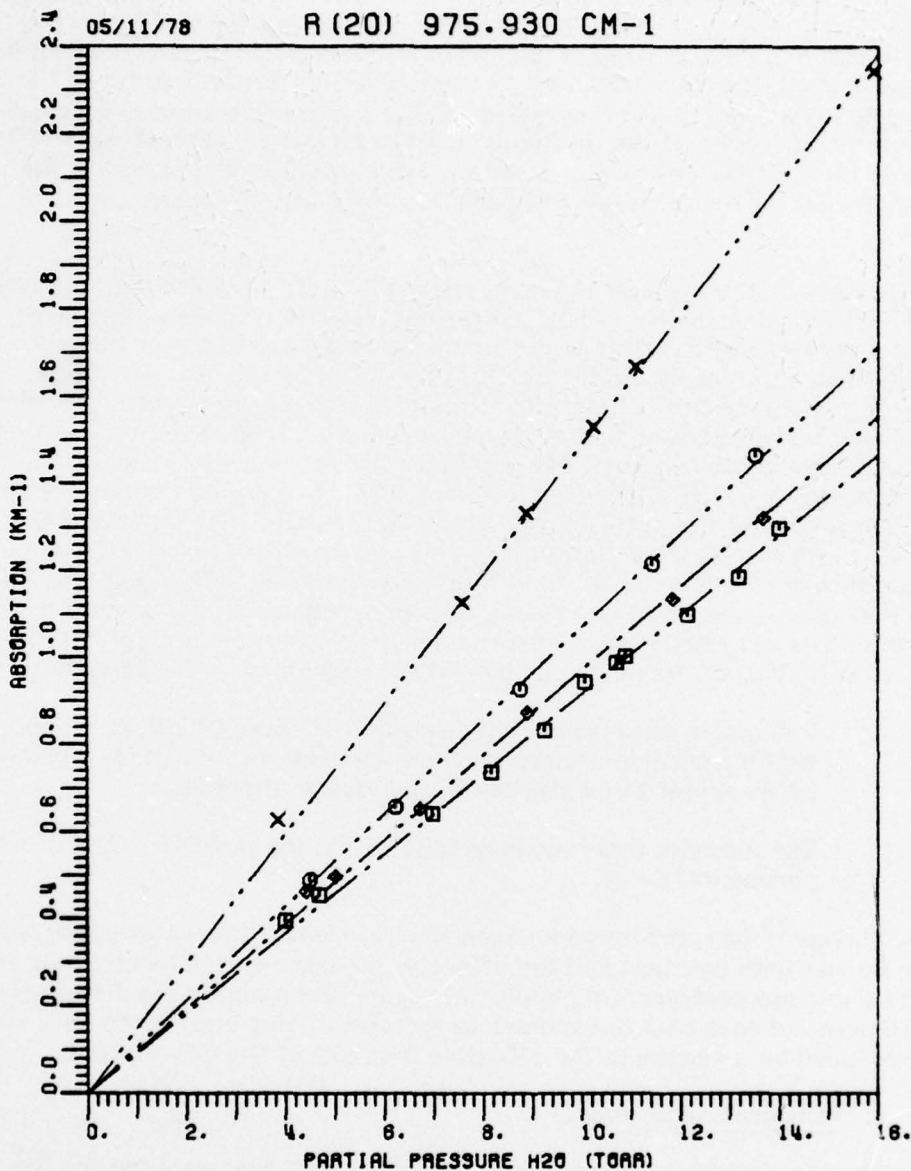


Figure 138. Measured water vapor absorption coefficient at a total pressure of 760 Torr, for the R(20) CO₂ laser line at 975.930 cm⁻¹. The symbol \diamond indicates spectrophone results for H₂O in 80-20 air at a temperature of 24°C. The symbol \square indicates spectrophone results for H₂O in N₂ at a temperature of 22.5°C. The symbol \times indicates spectrophone results for H₂O in O₂ at a temperature of 23°C. The symbol \circ indicates spectrophone results for H₂O in 60-40 air at a temperature of 23.6°C.

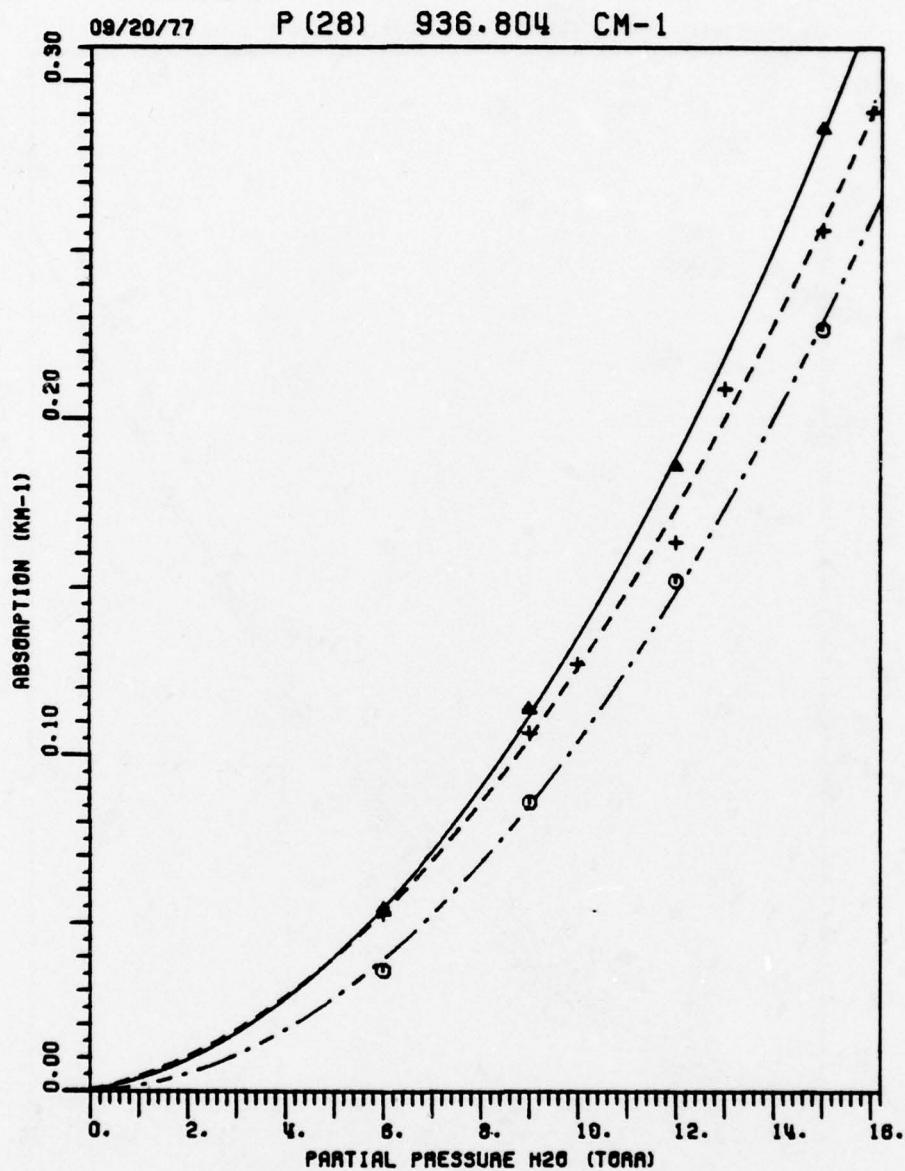


Figure 139. Measured water vapor absorption coefficient at a total pressure of 760 Torr, for the P(28) CO₂ laser line at 936.804 cm⁻¹. The symbol Δ indicates White cell results for H₂O in N₂ at a temperature of 22.5°C. The symbol + indicates White cell results for H₂O in 80-20 air at a temperature of 22°C. The symbol \square indicates White cell results for H₂O in 60-40 air at a temperature of 22°C.

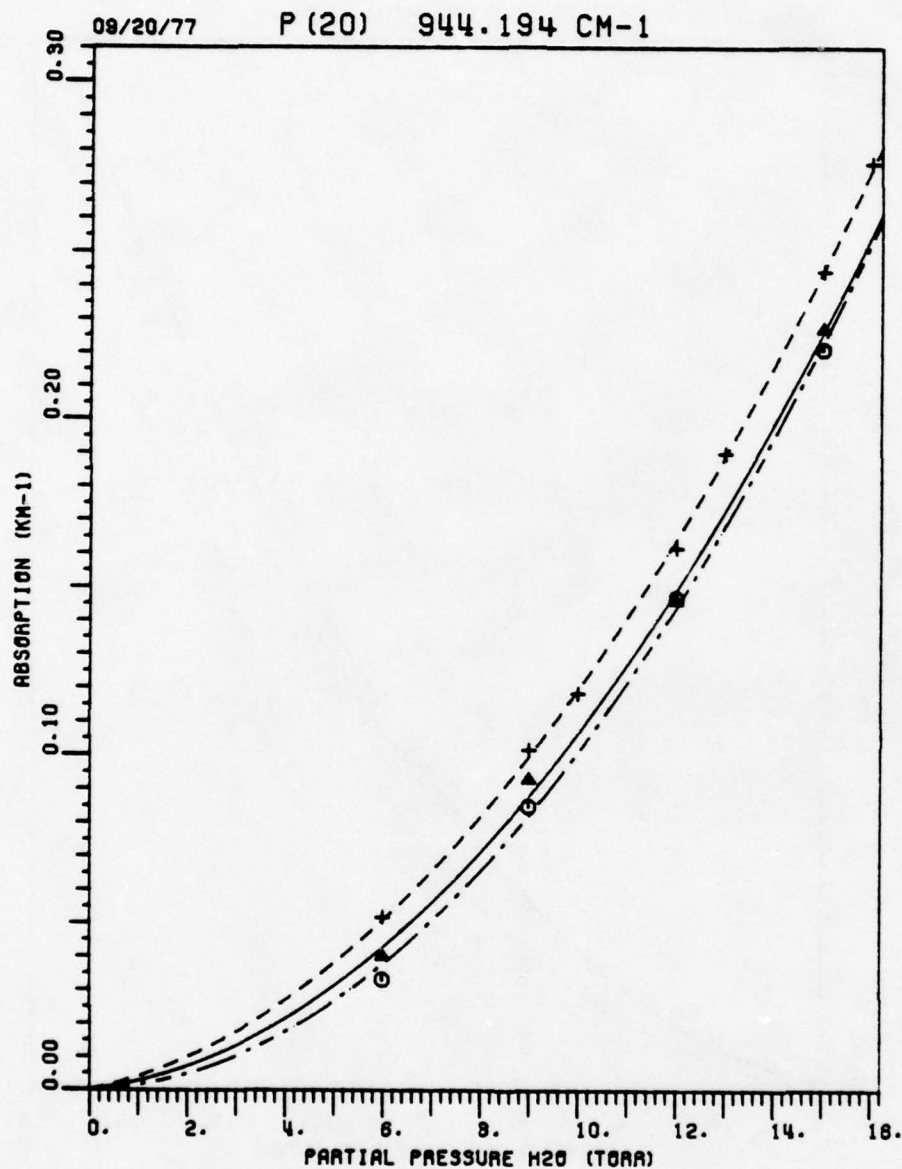


Figure 140. Measured water vapor absorption coefficient at a total pressure of 760 Torr, for the P(20) CO₂ laser line at 944.194 cm⁻¹. The symbol Δ indicates White cell results for H₂O in N₂ at a temperature of 22.5°C. The symbol + indicates White cell results for H₂O in 80-20 air at a temperature of 22°C. The symbol \ominus indicates White cell results for H₂O in 60-40 air at a temperature of 22°C.

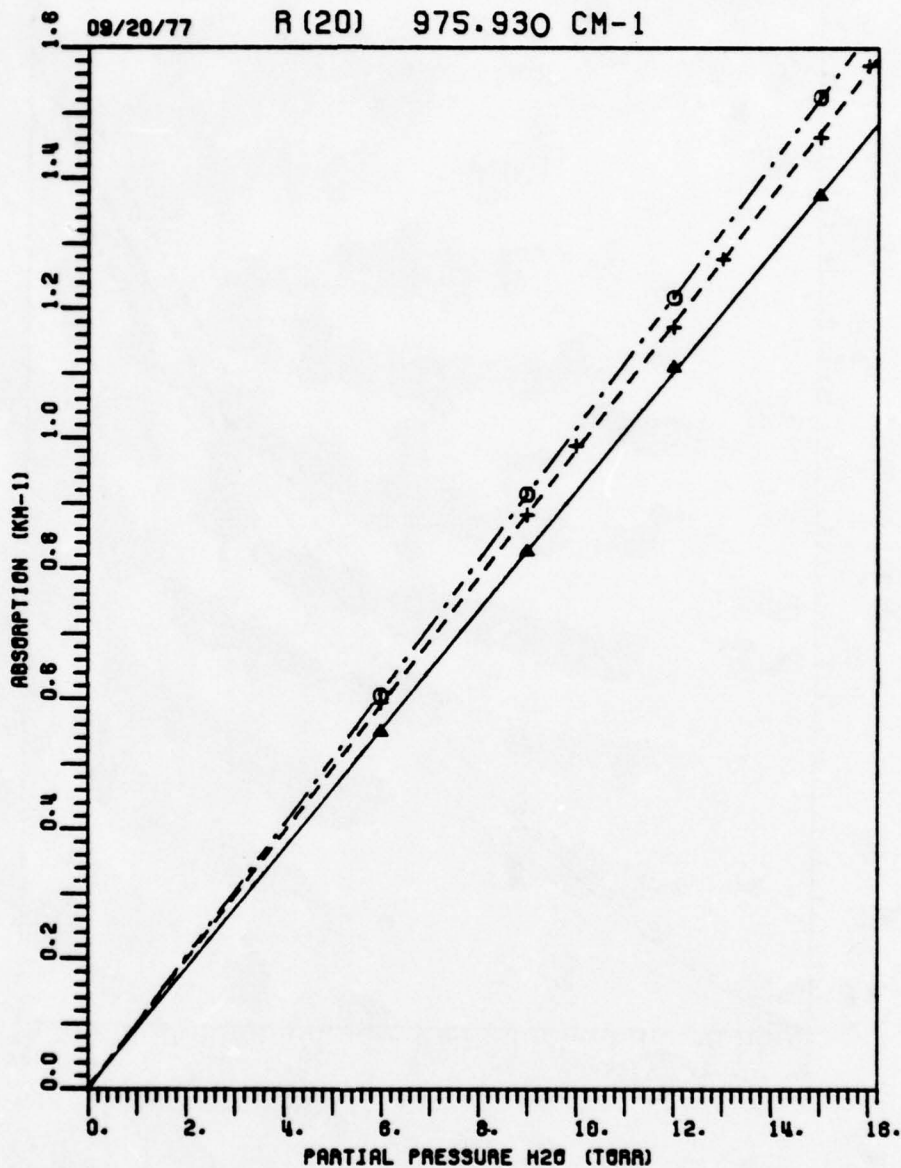


Figure 141. Measured water vapor absorption coefficient at a total pressure of 760 Torr, for the R(20) CO₂ laser line at 975.930 cm⁻¹. The symbol Δ indicates White cell results for H₂O in N₂ at a temperature of 22.5°C. The symbol + indicates White cell results for H₂O in 80-20 air at a temperature of 22°C. The symbol \circ indicates White cell results for H₂O in 60-40 air at a temperature of 22°C.

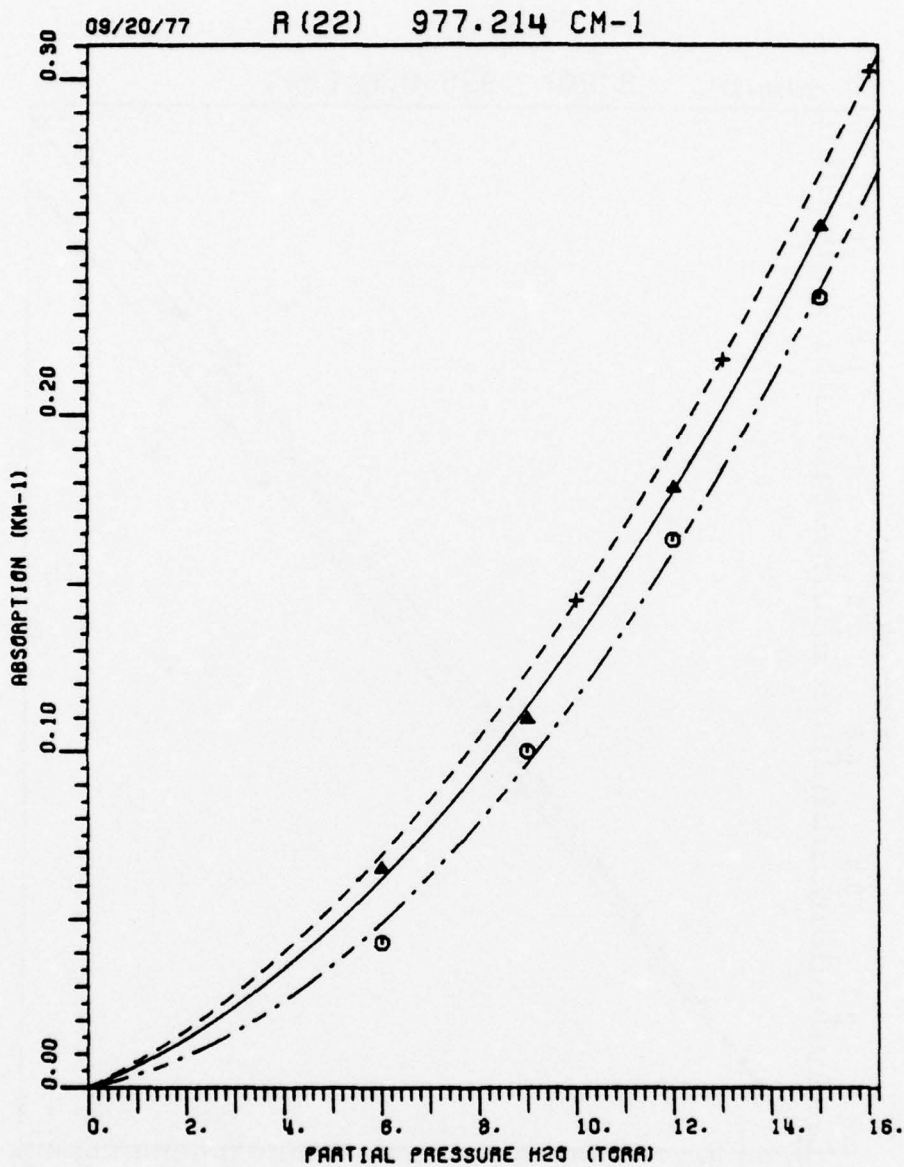


Figure 142. Measured water vapor absorption coefficient at a total pressure of 760 Torr, for the R(22) CO₂ laser line at 977.214 cm⁻¹. The symbol Δ indicates White cell results for H₂O in N₂ at a temperature of 22.5°C. The symbol + indicates White cell results for H₂O in 80-20 air at a temperature of 22°C. The symbol ○ indicates White cell results for H₂O in 60-40 air at a temperature of 22°C.

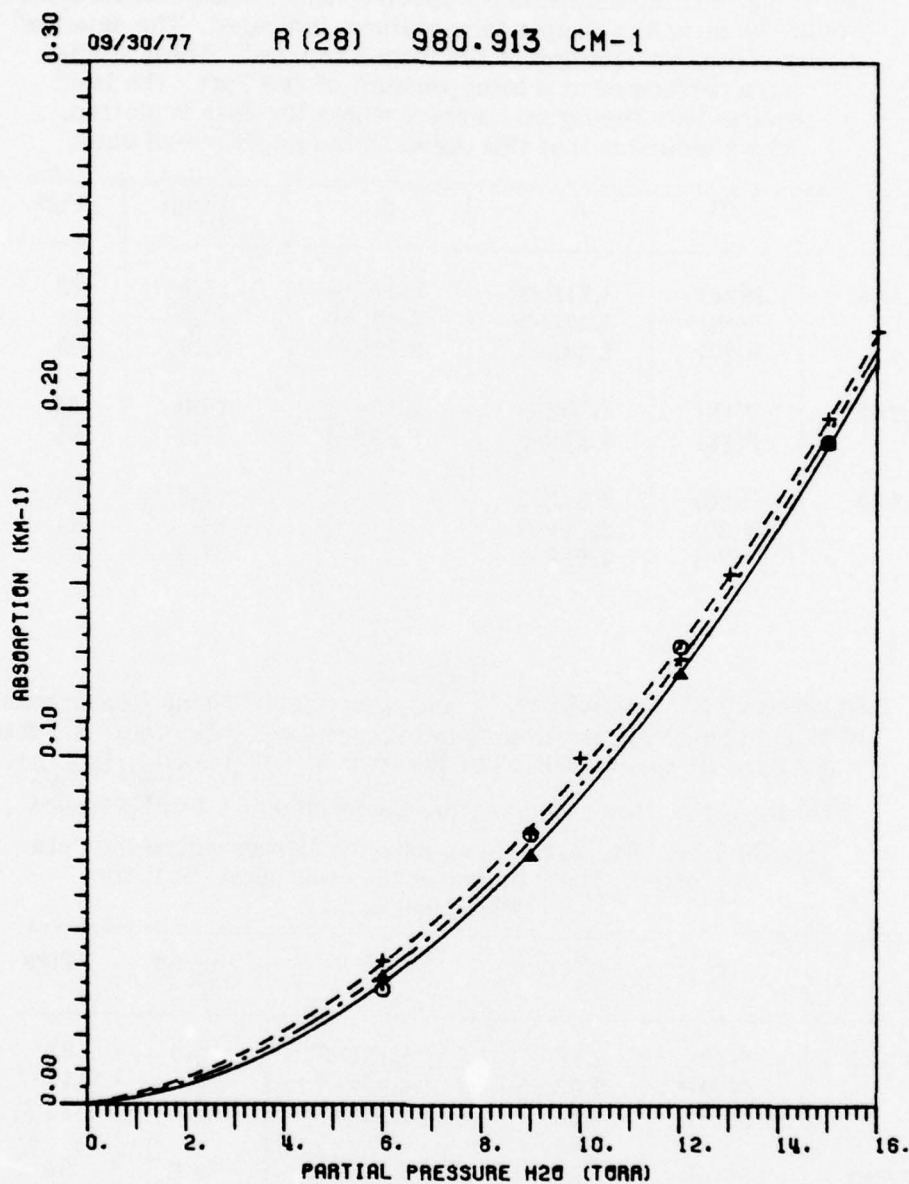


Figure 143. Measured water vapor absorption coefficient at a total pressure of 760 Torr, for the R(28) CO₂ laser line at 980.913 cm⁻¹. The symbol Δ indicates White cell results for H₂O in N₂ at a temperature of 22.5°C. The symbol + indicates White cell results for H₂O in 80-20 air at a temperature of 22°C. The symbol \odot indicates White cell results for H₂O in 60-40 air at a temperature of 22°C.

Table 16

List of curve fit coefficients for spectrophone measurements of H_2O in 80-20 air at the sample temperatures indicated. The data has been fit to an equation of the form $k=Ap+Bp^2$. These studies were performed at a total pressure of 760 Torr. The last column lists the figure numbers where the data is plotted. The * indicates that this curve fit is for White cell data.

$\nu_{cm^{-1}}$	ID	A	B	Temp °C	Figs.
944.194	P(20)	3.71E-3	9.47E-4	15.9	82
	P(20)*	3.26E-3	8.70E-4	22.0	111
	P(20)	2.58E-3	8.77E-4	27.6	83
947.742	P(16)	4.73E-3	1.26E-3	16.0	84
	P(16)	5.57E-3	8.69E-4	27.6	85
975.930	R(20)	8.64E-2		15.6	86
	R(20)	9.71E-2		24	58
	R(20)	1.06E-1		27.6	87

Table 17

List of curve fit coefficients, C_s^0 and γ for spectrophone measurements of H_2O in 80-20 air at the sample temperatures indicated. The data has been fit to an equation of the form $k(\nu)=C_s^0(\nu)w_{H_2O}[p_{H_2O}^+ \gamma(p-p_{H_2O})]$. These studies were performed at a total pressure of 760 Torr. The last column lists the figures where the data is plotted. The * indicates that this curve fit is for White cell data.

$\nu_{cm^{-1}}$	ID	$C_s^0 \times 10^{22}$	γ	Temp °C	Figs
944.194	P(20)	2.16	5.13E-3	15.9	82
	P(20)*	2.03	4.91E-3	22	111
	P(20)	2.08	3.86E-3	27.6	83
947.742	P(16)	2.88	4.92E-3	16.0	84
	P(16)	2.07	8.36E-3	27.6	85
975.930	R(20)	0.258	1.0	15.6	86
	R(20)	0.299	1.0	24.0	58
	R(20)	0.330	1.0	27.6	87

b. temperature coefficient

1. near line center

Two cases will again be considered, the first is that of near line center absorption for the R(20) CO₂ laser line at 975.93 cm⁻¹. Inspection of Figure 2 shows that for a typical water vapor line in the 10 μm region k will show a very significant increase with a rising temperature. In Figure 144 the measured absorption coefficient is plotted against water vapor partial pressure for three temperatures, 15.6°C, 24°C and 27.6°C. These experimental results demonstrate a significant increase in the absorption coefficient as the temperature was raised from 15.6°C to 27.6°C. A quantitative comparison between the experimental results and the theoretical predictions of Equation(37) is given in Figure 145 where the percentage change in k has been plotted vs temperature. The solid curve is a plot of Equation (38) using a lower state energy level, E₀ of 1557.838 cm⁻¹ for the water line and a reference temperature of T⁰ = 300°K. Considering the simplicity of the model being used here, i.e., the far wing contributions are ignored, these results indicate good agreement.

2. far wings

In this development we shall assume that the temperature dependence of water vapor continuum absorption at the 10 μm P(16) and P(20) laser lines can be attributed to the far wing properties of H₂O absorption lines. The results of H₂O in 80-20 air measurements at 16°C and 27.6°C for these two laser lines are given in Figures 146 and 147, respectively. These data indicate a significant decrease in absorption as the temperature is raised from 16°C to 27°C. A consideration of Equation (41) shows that the relative change in the absorption coefficient, i.e., Δk/k, should be independent of the absorber partial pressure or

$$\frac{\Delta k}{k} (p_a) = \text{constant.} \quad (116)$$

However, a close examination of the data presented in Figures 146 and 147 shows that the percentage change in the absorption coefficient per degree Kelvin is not a constant over the entire range of water vapor partial pressures. In particular the curves for the absorption data at the P(16) laser line cross near a H₂O partial pressure of 2 Torr, see Figure 147. Since the condition given by Equation (116) is not observed, an interpretation of these results will require either a modification of the basic theory presented in Chapter II or a tacit acknowledgment of experimental error. We shall choose the latter.

If one employs the dimer theory of continuum absorption it is possible to explain this behavior in terms of the (H₂O)₂ contribution to the temperature dependence. Since the concentration of dimers is expected to vary as the square of water vapor partial pressure their contribution (to the temperature dependence) would also be a function of p_a. A second alternative is to acknowledge the presence of an experimental error on the order of 0.002 cm⁻¹ in these measurements. The results at the P(20) laser line indicate

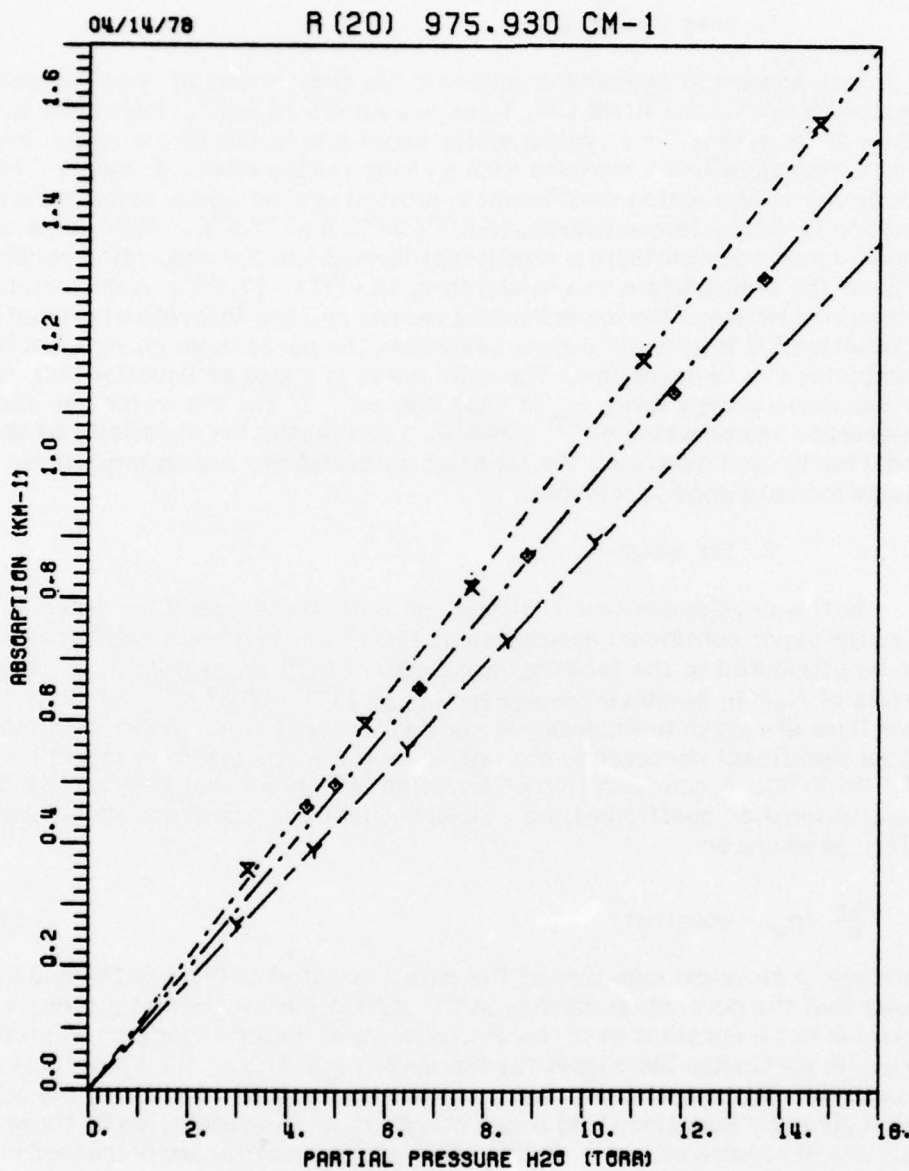


Figure 144. Measured absorption coefficient of H₂O in 80-20 air for the R(20) CO₂ laser line at 975.930 cm⁻¹ with sample gas temperature as a parameter. The spectrophone results at 15.6°C are indicated by the symbol Y. The spectrophone results at 24°C are indicated by the symbol ◇. The spectrophone results at 27.6°C are indicated by the symbol X. The total sample gas pressure is 760 Torr.

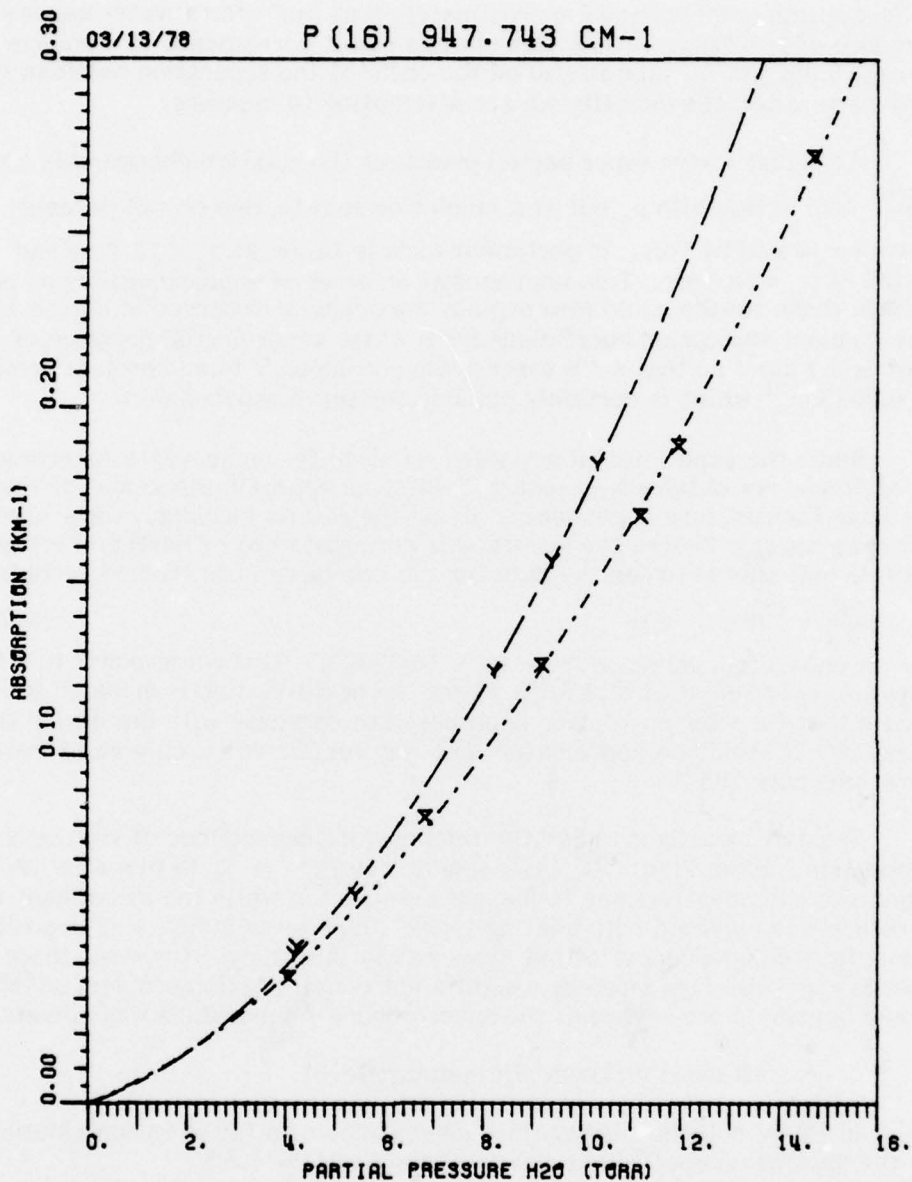


Figure 147. Measured absorption coefficient of H₂O in 80-20 air for the P(16) CO₂ laser line at 947.743 cm⁻¹ with sample gas temperature as a parameter. The spectrophone results at 16.0°C are indicated by the symbol Y. The spectrophone results at 27.6°C are indicated by the symbol X. The total sample gas pressure is 760 Torr.

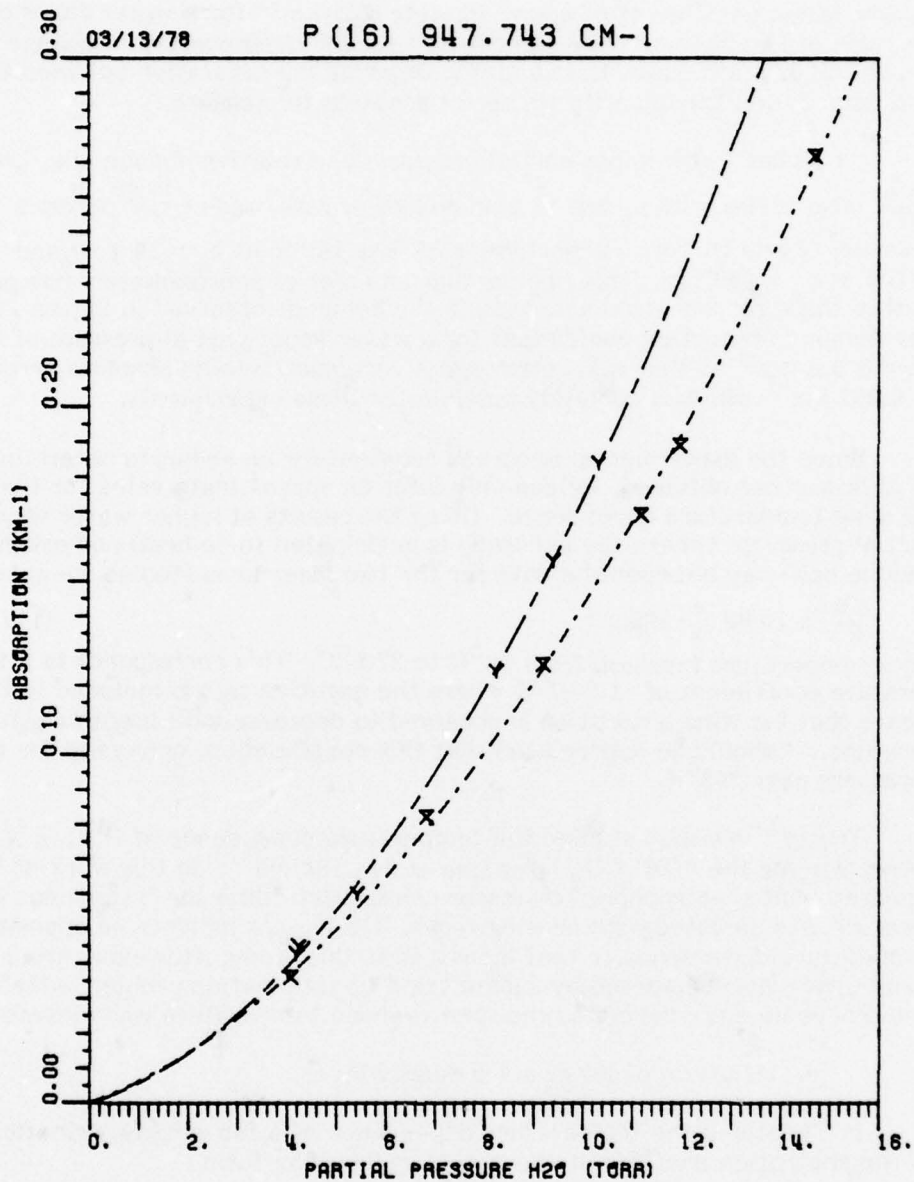


Figure 147. Measured absorption coefficient of H₂O in 80-20 air for the P(16) CO₂ laser line at 947.743 cm⁻¹ with sample gas temperature as a parameter. The spectrophone results at 16.0°C are indicated by the symbol Y. The spectrophone results at 27.6°C are indicated by the symbol X. The total sample gas pressure is 760 Torr.

an absorption coefficient of approximately 0.01 km^{-1} for a water vapor partial pressure of two Torr. A 20% error in this result corresponds to a change of only 0.002 km^{-1} which is also on the order of the separation between the two curves, i.e., the quantity we are attempting to measure.

At higher water vapor partial pressures the relative change in k , i.e., $\frac{\Delta k/k}{\Delta T}$ also varies with p_a but at a much slower rate, one or two percent between 10 and 14 Torr. In particular $\Delta k/k$ is 14.9% at $p_a = 10$ Torr and 13.3% at $p_a = 14$ Torr. This implies that an error of approximately one percent in these results could also explain the behavior observed in Figure 146. The nominal absorption coefficient for a water vapor partial pressure of 14 Torr is 0.2 km^{-1} so that a 1% error again corresponds to an absolute error of 0.002 km^{-1} which is certainly possible for these experiments.

Since the experimental accuracy required for an accurate determination of $\Delta k/k$ was not obtained, we can only infer an approximate value for the far wing temperature dependence. Using the results at higher water vapor partial pressures (where the accuracy is anticipated to be best) and estimating a value half-way between the data for the two laser lines studied we obtain

$$\frac{\Delta k}{k} \times 100\% \sim -20\% \quad (117)$$

for a temperature increase from 16°C to 27.6°C . This corresponds to a temperature coefficient of $-1.7\%/^\circ\text{K}$ where the negative sign is included to indicate that far wing absorption is observed to decrease with increasing temperature. It should be appreciated that this coefficient is only valid for temperatures near 295°K .

Trusty⁷⁴ has also studied the temperature dependence of H_2O in N_2 absorption for the P(20) CO_2 laser line at 944.194 cm^{-1} . In this work he used a nonresonant spectrophone⁴ to measure absorption while the instrument temperature was elevated with heating tapes. His results indicate an opposite temperature dependence to that measured in this study. However, those results were also hampered by a significant contamination problem which would become more severe as the spectrophone temperature was elevated.

c. influence of lower state energy level

In Chapter II the temperature dependence of a far wing contribution to the absorption coefficient was shown to have the form

$$k_i = \left(\frac{T^0}{T}\right)^3 \exp\left[\frac{E_{l_i}}{kT^0} - \frac{T-T^0}{T}\right] \left(\frac{\alpha_{L_i}^0}{\nu - \nu_{o_i}}\right)^2 \frac{S_i^{o'}}{\pi \alpha_{L_i}^0} \quad (118)$$

It was also demonstrated that both magnitude and sign of the temperature coefficient, i.e., $\Delta k_i/k_i$, are determined by the magnitude of E_{l_i} , the lower state energy level of the absorption line, see Figure 3. This can be explicitly shown by taking the differential of Equation (118) and solving for the relative change in the absorption coefficient per degree Kelvin, which is given by

$$\frac{\Delta k_i/k_i}{\Delta T} = \frac{1}{T} \left[\frac{E_{\ell_i}}{kT} - 3 \right] + \frac{o(\Delta T^2)}{T} \quad (119)$$

If we consider a nominal temperature, $T \sim 300^\circ\text{K}$ Equation (119) becomes

$$\frac{\Delta k_i/k_i}{\Delta T} (T=300) \times 100\% \sim 1.7 \times 10^{-3} [\nu_i - 600] \quad (120)$$

where ν_i is the lower state energy level in cm^{-1} } E_{ℓ_i} equals $h\nu_i$. This equation clearly shows that

$$\frac{\Delta k_i/k_i}{\Delta T} \begin{cases} < 0 & \nu_i < 600 \text{ cm}^{-1} \\ > 0 & \nu_i > 600 \text{ cm}^{-1} \end{cases} \quad (121)$$

for a temperature of 300°K .

The above argument was given in terms of the contribution from a single absorption line, but a logical extension of these results shows that

$$\frac{\Delta k/k}{\Delta T} \times 100\% \geq -1\% \quad (122)$$

which simply says that the model described by Equation (117) predicts a minimum temperature coefficient of -1%. This result obviously conflicts with the experimental data which indicates a temperature coefficient on the order of -1.7%. Since the inequality given in Equation (122) was obtained for $E_{\ell_i} \sim 0$, the equality can never hold and it becomes clear that the far wing formulation given in Chapter II will not model the water vapor temperature dependence which is observed in Figures (146) and (147).

In Equation (119) the term -3 comes from the differential of $(T^0/T)^3$ which is responsible for reducing the absorption coefficient as the temperature increases. It is interesting to consider the power of (T^0/T) required to produce a temperature coefficient of -1.7%. If we assume a nominal lower state energy of $\nu \sim 300 \text{ cm}^{-1}$ and use the equation

$$\frac{\Delta k/k}{\Delta T} \times 100\% \sim 1.7 \times 10^{-3} [\nu - 200 n] \quad (123)$$

where n would be the power of (T^0/T) appearing in Equation (118), it is easy to show that n must be ~ 6.5 for $\frac{\Delta k/k}{\Delta T} \times 100\%$ to be -1.7. There is no theoretical basis for such a modification (known to this author) but this result does indicate a measure of the inconsistency between experimental data and the simple theory described in Chapter II.

B. Pure Water Vapor Measurements

1. Introduction

In Chapter II the pressure dependence of the absorption coefficient was developed for the case of a pressure broadened water vapor sample gas. If we extend those arguments to the case of a pure water vapor sample and continue to assume a Lorentz line shape, the far wing approximation for the absorption coefficient is given by

$$k^{FW} \approx p_a^2 \sum_i \left(\frac{T^0}{T} \right)^3 \frac{S_i^0}{\pi \alpha_{L_i}^0} \left[\frac{\alpha_{L_i}^0}{\nu - \nu_{0i}} \right]^2 \frac{e^{-\frac{E_{\ell_i}}{kT^0}} \frac{T-T^0}{T}}{p_e^0 p_a^0}. \quad (124)$$

This equation shows that the far wing contributions to the absorption coefficient will be a linear function of the absorber pressure squared.

An analysis for the pressure dependence of the absorption coefficient at the 10 μm R(20) CO_2 laser line can also be carried out using the development given in Chapter II with the result that

$$k = Xp^2 + Y + Zp^{-2} \quad (125)$$

where X, Y and Z are constants. This expression demonstrates one of the problems encountered in using the Lorentz line shape for pure H_2O studies. The near line center contribution to the absorption coefficient introduces the p^{-2} term which causes k to become infinite as the pressure approaches zero. A precise analysis using the Voigt line shape would prevent such a (non-physical) singularity.

2. Ambient and elevated temperature data

a. curve fit coefficients

Except for the data taken at the 10 μm R(20) laser line, all of the pure water vapor measurements have been fit to an equation of the form

$$k = B' p^2 \quad (126)$$

where B' is a positive constant. The results of these curve fits for each laser frequency studied are listed in Table 18, together with the corresponding temperature of the sample gas. Also presented in this table are the figure number(s) where the plotted data may be found, and the self broadening coefficient, $C_{S(y)}^0$ given by Equation (106). The data for the R(20) laser line at 975.930 cm^{-1} have been fit to the arbitrary empirical formula

Table 18
 Curve fit coefficients for pure water vapor absorption measurements at the temperature indicated in column five. The data has been fit to an equation of the form $k=B'p^2$, where p^2 is the (water vapor) pressure squared in Torr.² Also given here is the coefficient C_s^O from the equation $K(\nu)=C_s^O(\nu)w_{H_2O}p_{H_2O}$, where w_{H_2O} is the number density of water molecules, see Equation (106). The * indicates that this measurement was performed in the spectrophone, all other results were obtained from White cell experiments.

ν cm ⁻¹	Pure H ₂ O Curve Fit Coefficients				
	ID	B'	$C_s^O \times 10^{22}$ (cm ² atm ⁻¹ molecules ⁻¹)	Temp °C	Figs.
936.804	P(28)	1.43E-3	3.27	18	120
	P(28)	1.09E-3	2.52	21	120
944.194	P(20)*	1.41E-3	3.24	19	89
	P(20)	1.20E-3	2.75	18	121
	P(20)	1.07E-3	2.48	21.5	121
	P(20)	7.73E-4	1.83	28	121
977.214	R(22)	1.20E-3	2.75	18	123
980.913	R(28)	1.07 E-3	2.45	18	124
	R(28)	8.57 E-4	1.98	21	124
1052.196	P(14)	1.42E-3	3.25	18	125
1077.303	R(18)	1.19E-3	2.72	18	126

$$k = A' p + B' p^2 \quad (127)$$

for the plots given in Figure 122. These data have also been fit to the Equation (125). Table 19 lists both the A', B' ; and X, Y, Z sets of coefficients for this special case.

Table 19
Curve fit coefficients for pure water vapor absorption measurements at 975.930 cm^{-1} . The data has been fit to an equation of the form $k=A'p+B'p^2$ as well as an equation of the form $k=Xp^2+Y+Zp^{-2}$. Also listed here is the average temperature at which the data was recorded. The results were obtained by White cell measurements.

ν cm^{-1}	Pure H ₂ O Curve Fit Coefficients at 975.930 cm^{-1}							Figs.
	ID	A'	B'	X	Y	Z	Temp °C	
975.930	R(20)	1.36E-2	1.59E-2	1.66E-2	5.94E-2	-2.20E-1	28	92
	R(20)	3.05E-2	1.10E-2	1.34E-2	1.63E-1	-7.16E-1	21.5	92
	R(20)	1.32E-2	1.27E-2	1.32E-2	8.96E-2	-7.29E-1	18	92

b. comparison of spectrophone and White cell data

The curve fit coefficients for the spectrophone and White cell data at the P(20) laser line indicate (see Table 18) that rather poor agreement exists between the two techniques for this pure water vapor measurement. (The author feels that a systematic error is being observed in the spectrophone results since the absorption measured is significantly greater than expected.) However, it is encouraging to note that the spectrophone data shows the proper linear behavior with p^2 , see Figure 89, although the results given here do not have (what is believed to be) the correct magnitude.

A possible source for this discrepancy is an inaccuracy of the White cell calibration data at the $10 \mu\text{m}$ R(20) laser line, see Figure 122. The pure water vapor White cell results for this laser line show an apparent inconsistency between the measurements at 18°C and 21.5°C . A comparison with the results taken at 28°C indicates that a reasonable temperature dependence is not observed for the data taken at 18°C and/or 21.5°C . This is quite significant since the 18°C data was used to calibrate the spectrophone measurements for the P(20) laser line at 944.194 cm^{-1} . The possibility of contamination in the H₂O sample is always present, but for now it is more reasonable to suspect that a calibration error has produced the discrepancy in the pure water vapor data at the P(20) line.

c. temperature dependence

The temperature dependence of k^{FW} for a pure water vapor sample is given in Equation (124) and is the same as that predicted for the pressure broadened data. This similarity follows from the derivation of Equation (124) which is based upon the development given for the pressure broadened case found in Chapter II. As was previously noted, this model does not give the proper temperature dependence for collision broadened water vapor absorption, so it should not be surprising if it does not properly describe pure H_2O absorption. In this analysis, the temperature coefficient, θ will also be defined as the percentage change in k , the absorption coefficient, per degree Kelvin, or in terms of the curve fit parameter B'

$$\bar{\theta}(T) = \frac{\Delta k/k}{\Delta T} \times 100\% \sim \frac{(B'_1 - B'_2)/\bar{B}}{\Delta T} \times 100\% \quad (128)$$

where B'_1 is the constant coefficient appearing in Equation (126) for the data taken at a temperature T_1 ,

B'_2 is the constant coefficient appearing in Equation (126) for the data taken as the temperature T_2 ,

\bar{B} is the average of B'_1 and B'_2 , i.e., $(B'_1 + B'_2)/2$,

ΔT is the temperature differential, $T_1 - T_2$

and \bar{T} is the nominal temperature, i.e., $(T_1 + T_2)/2$.

Equation (128) has been evaluated for each laser line at which pure water vapor measurements were conducted at more than one temperature. The results of these calculations are shown in Table 20. In each case the observed temperature coefficient is less than negative one, which again indicates that the simple Lorentz line shape model will not describe the temperature dependence of the water vapor continuum, see Equation (122). These results also indicate a significantly larger temperature dependence than was found in the pressure broadened H_2O studies.

Arefov and Dianov-Klokov⁷⁵ have also measured pure H_2O absorption as a function of temperature for laser frequencies near $10.6 \mu m$. Their results are plotted together with the results of this study in Figure 148. The data from this study come from the White cell measurements at the P(20) laser line. This comparison indicates a reasonably good agreement between the two studies and confirms a substantial negative temperature coefficient for continuum absorption.

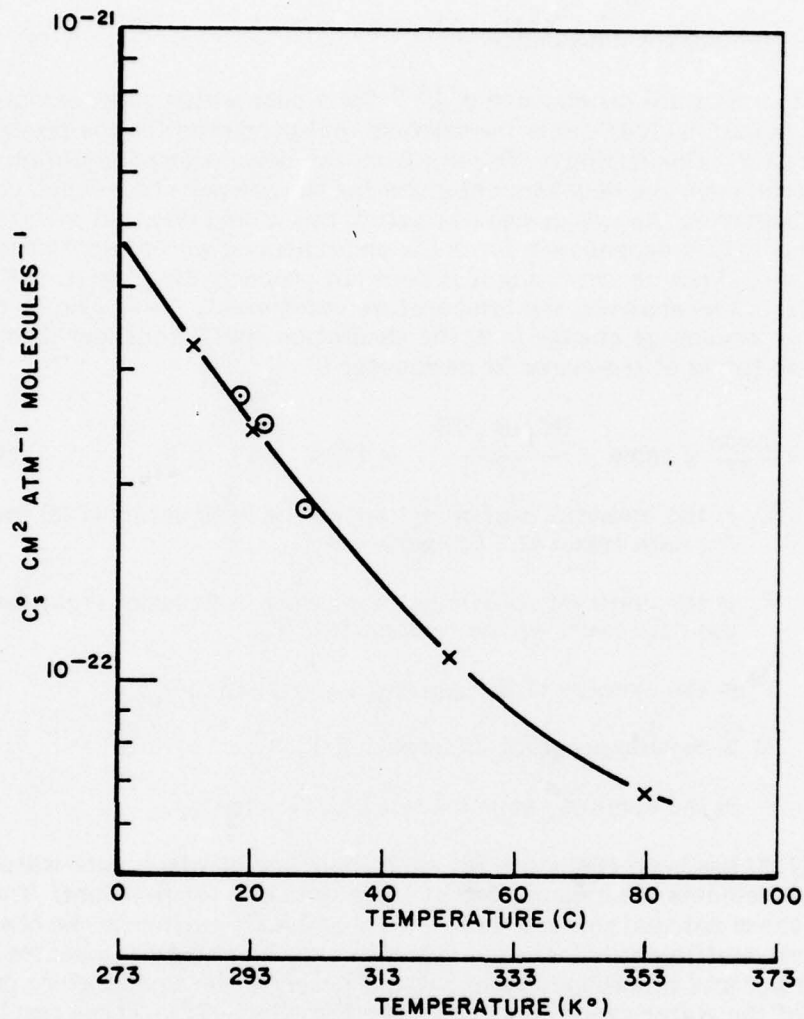


Figure 148. Measured values of the self broadening coefficient, C_s (v) as a function of temperature near $10.6 \mu\text{m}$ for pure water vapor samples. The symbol \odot indicates the data from this study obtained at the $10.6 \mu\text{m}$ P(20) in White cell measurements. The symbol X gives the result of Arefev and Dianov-Klokov (Reference 75).

Table 20
List of measured temperature coefficient, θ as defined in Equation (128), for the pure water vapor absorption measurements.

ν cm ⁻¹	Pure H ₂ O Temperature Coefficients					
	ID	B' ₁	B' ₂	T °K	θ %	\bar{T} °C
936.804	P(28)	1.09E-3	1.43E-3	3	-9.0	19.5
944.194	P(20)	1.07E-3	1.20E-3	3.5	-3.27	19.75
	P(20)	7.73E-4	1.07E-3	6.5	-4.96	24.75
980.913	R(28)	8.57E-4	1.07E-3	3	-7.37	19.5

c. the continuum

In this section the results of the spectrophone and White cell studies of H₂O in N₂ absorption will be used to model the frequency dependence of the continuum. It will be assumed that this phenomenon can be described in terms of the far wing contributions of the rotational water vapor band near 200 cm⁻¹ and the vibration-rotation ν_2 band near 2000 cm⁻¹. With this approach the continuum absorption, k_c is given by a sum of far wing absorption from these two bands, i.e.,

$$k_c = k_R^{FW} + k_{\nu_2}^{FW} \quad (129)$$

where k_R^{FW} is the sum of the rotational band contributions near 10 μm

and $k_{\nu_2}^{FW}$ is the sum of the ν_2 band contributions near 10 μm .

We shall also assume that a Lorentz line shape is applicable for both bands so that

$$k_c \sim \sum_i \frac{S_i^R \alpha_i^R}{\pi} \frac{1}{(\nu - \nu_{oi}^R)^2} + \sum_j \frac{S_j^{\nu_2}}{\pi} \frac{1}{(\nu - \nu_{oj}^{\nu_2})^2} \quad (130)$$

where S_i^R is the rotational band line strength of the i th absorption line,

$S_j^{\nu_2}$ is the ν_2 band line strength of the j th absorption line,

α_i^R is the rotational band half-width of the i th absorption line,

α_j^2 is the ν_2 band half-width of the jth absorption line,
 ν_{oi}^R is the rotational band line center of the ith absorption line,
 and ν_{oj}^2 is the ν_2 band line center of the jth absorption line.

Now using the conditions that

$$\frac{\nu_{oi}^R}{\nu} < 1 \quad (131)$$

and

$$\frac{\nu}{\nu_{oj}^2} < 1 \quad (132)$$

in the expansion of

$$k_c \sim \sum_i \frac{S_i^R \alpha_i^R}{\pi \nu^2} \frac{1}{\left[1 - \left(\frac{\nu_{oi}^R}{\nu}\right)\right]^2} + \sum_j \frac{S_j^2 \alpha_j^2}{\pi (\nu_{oj}^2)^2} \frac{1}{\left[1 - \left(\frac{\nu}{\nu_{oj}^2}\right)\right]^2} \quad (133)$$

we obtain

$$k_c \sim \sum_i \frac{S_i^R \alpha_i^R}{\pi \nu^2} \left[1 + 2 \left(\frac{\nu_{oi}^R}{\nu}\right) + \dots\right] + \sum_j \frac{S_j^2 \alpha_j^2}{\pi (\nu_{oj}^2)^2} \left[1 + 2 \left(\frac{\nu}{\nu_{oj}^2}\right) + \dots\right] \quad (134)$$

To obtain a simple model for the continuum we shall drop all terms in the expansion except for the constant in which case Equation (134) becomes

$$k_c \sim A^R \nu^{-2} + A^{\nu_2} \quad (135)$$

to first order, where

A^R is a positive constant giving the contribution of the rotational band,

and A^{ν_2} is a positive constant giving the contribution of the ν_2 band.

In Figure 149 the results from the spectrophone study of H_2O in N_2 absorption are plotted vs wavenumber for a water vapor partial pressure of 14.3 Torr. The solid curve in this figure represents the least square fit of these data to Equation (135). Similarly in Figure 150 the results from the White cell measurements are shown together with the least square fit of those data to Equation (135).

□ 14.3 TORR H2O IN N2. SPEC - 24 DEG C

□ $\gamma = 1.63150 \times 10^5 \times \lambda_{\text{cm}}^{-2} + 4.51692 \times 10^{-6}$

H2O IN N2 ABSORPTION

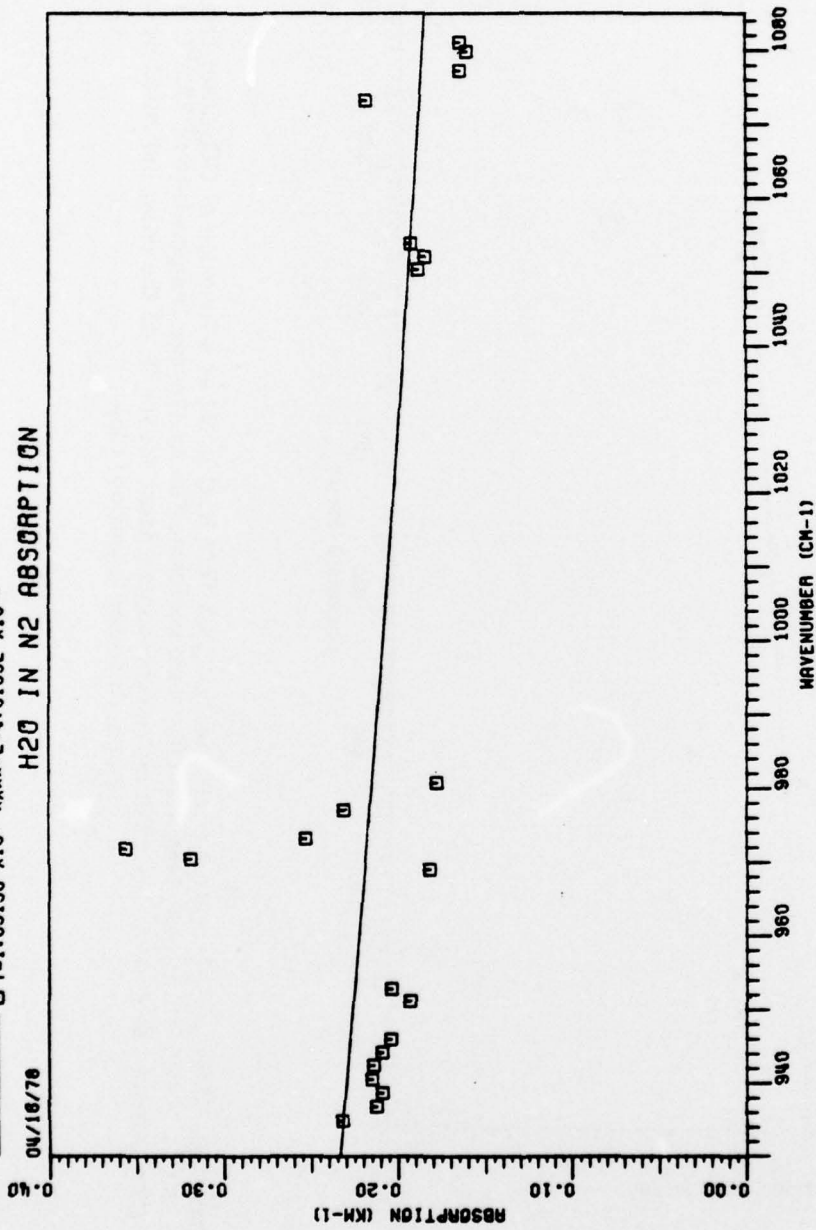


Figure 149. Measured absorption coefficient of 14.3 Torr H₂O in N₂ as a function of CO₂ laser frequency in cm⁻¹. These spectrophone measurements were performed at an average temperature of 24°C and a total pressure of 1 atm. The solid curve represents a least square fit of the data, indicated by the symbol □, to the Equation (135).

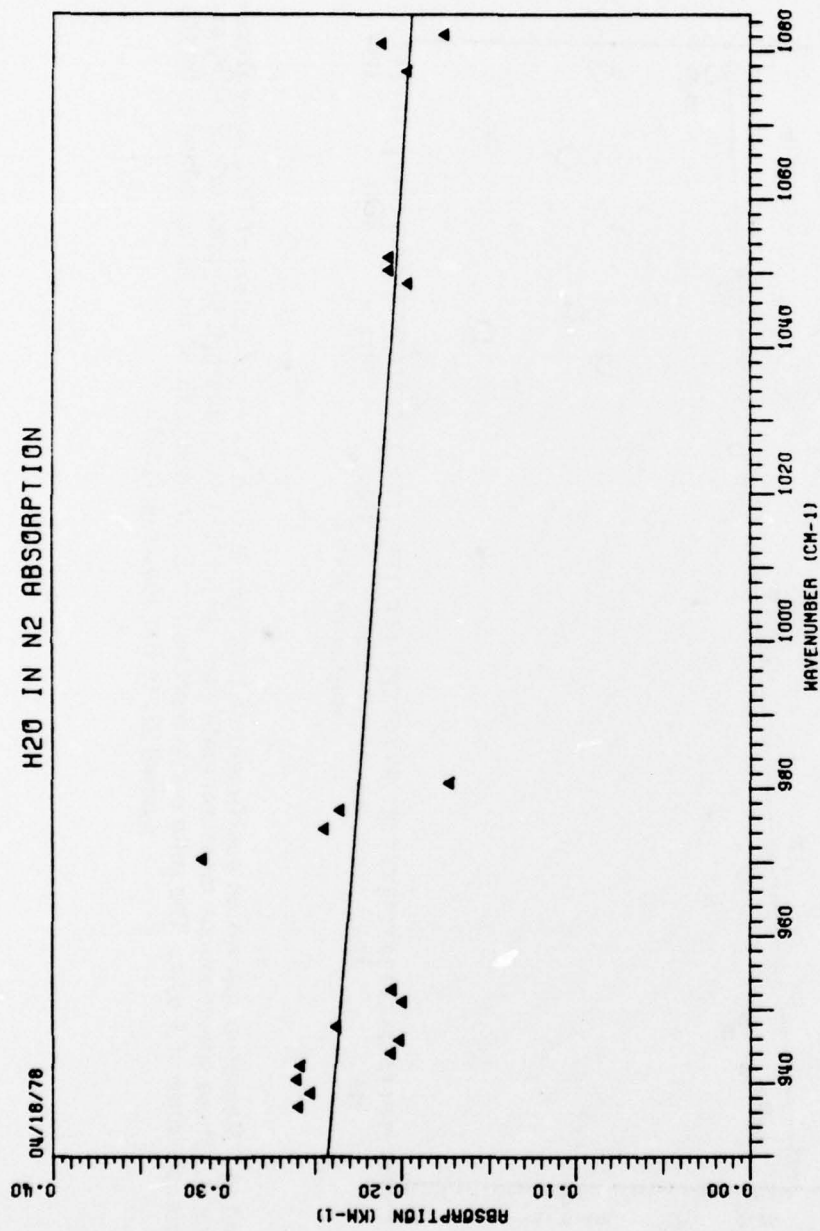


Figure 150. Measured absorption coefficient of 14.3 Torr H₂O in N₂ as a function of CO₂ laser frequency in cm⁻¹. These White cell measurements were performed at an average temperature of 22.5°C and a total pressure of 1 atm. The solid curve represents a least square fit of the data, indicated by the symbol Δ , to the Equation (135).

The continuum absorption which we are attempting to model is presumed to be a slowly varying function of frequency so it is reasonable to speculate that the rapid fluctuation observed in Figures 149 and 150, near 980 cm^{-1} indicate the effects of local absorption lines. Hence, the rapid variations do not represent the phenomenon which we are attempting to model with Equation (135). To obtain a more consistent and therefore accurate representation of the far wing contributions of the rotational and ν_2 band the experimental data was re-analyzed after such local contributions were accounted for⁶⁷, i.e., the local H_2O absorption was subtracted from the raw data. In Figures 151 and 152 the "corrected" spectrophone and White cell data, respectively have been plotted as a function of wavenumber, the solid curves represent the least square fits to Equation (135). In Table 21 the coefficients for this equation are tabulated for both the "corrected" and original data of both the spectrophone and White cell studies. These coefficients provide a model for the continuum absorption near 9 and $10\ \mu\text{m}$ at temperatures near 295°K and for a water vapor partial pressure of 14.3 Torr.

The temperature dependence of the continuum under these same conditions was previously analyzed from the spectrophone temperature studies of H_2O in N_2 absorption at the $10\ \mu\text{m}$ P(16) and P(20) laser line. Those results indicated a temperature coefficient of -1.7% for the conditions we have just defined. Knowledge of this temperature dependence plus the coefficients listed in Table 21 provides a quantitative, if semi-empirical model for the water vapor continuum near $10\ \mu\text{m}$.

Table 21

List of the coefficients, A^R and A^{ν_2} which appear in Equation (135) of the text, i.e., $k_c \sim A^R \nu^{-2} + A^{\nu_2} \nu^2$ which represents the frequency dependence of the far wing contributions to absorption near 9 and $10\ \mu\text{m}$. These coefficients were obtained from a least square fit of spectrophone and White cell data for 14.3 Torr H_2O in N_2 at a total pressure of 1 atm.

	A^R		A^{ν_2}	
	Original	"Corrected"	Original	"Corrected"
Spectrophone 24°C	1.63E 5	1.88E 5	4.52E-2	2.10E-3
White Cell 22.5°C	1.60E 5	1.50E 5	5.84E-2	5.29E-2

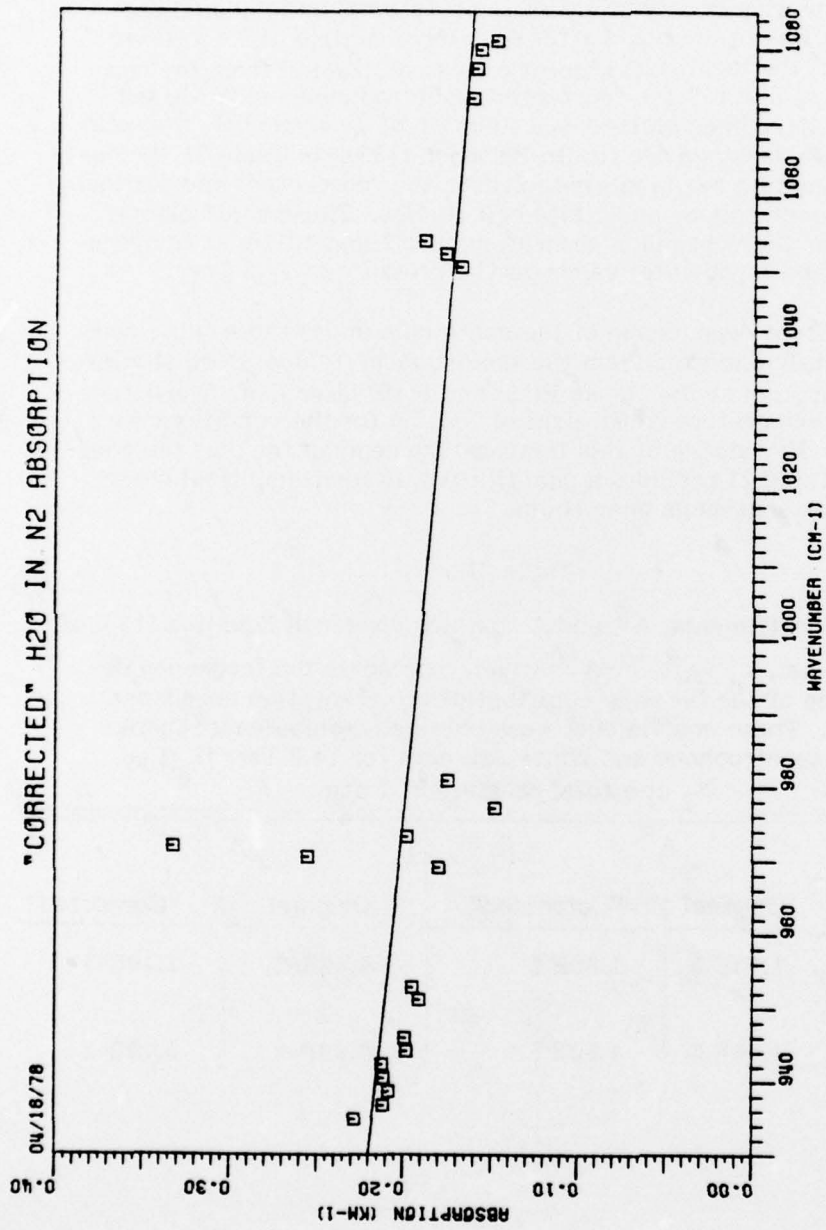


Figure 151. Plot of "corrected" spectrophone absorption coefficient results (as defined in the text) vs. CO₂ laser frequency in cm⁻¹ for 14.3 Torr of H₂O in N₂ at a total pressure of 760 Torr and a nominal temperature of 24°C. The solid curve gives the least square fit of the "corrected" data, indicated by the symbol □, to the Equation (135).

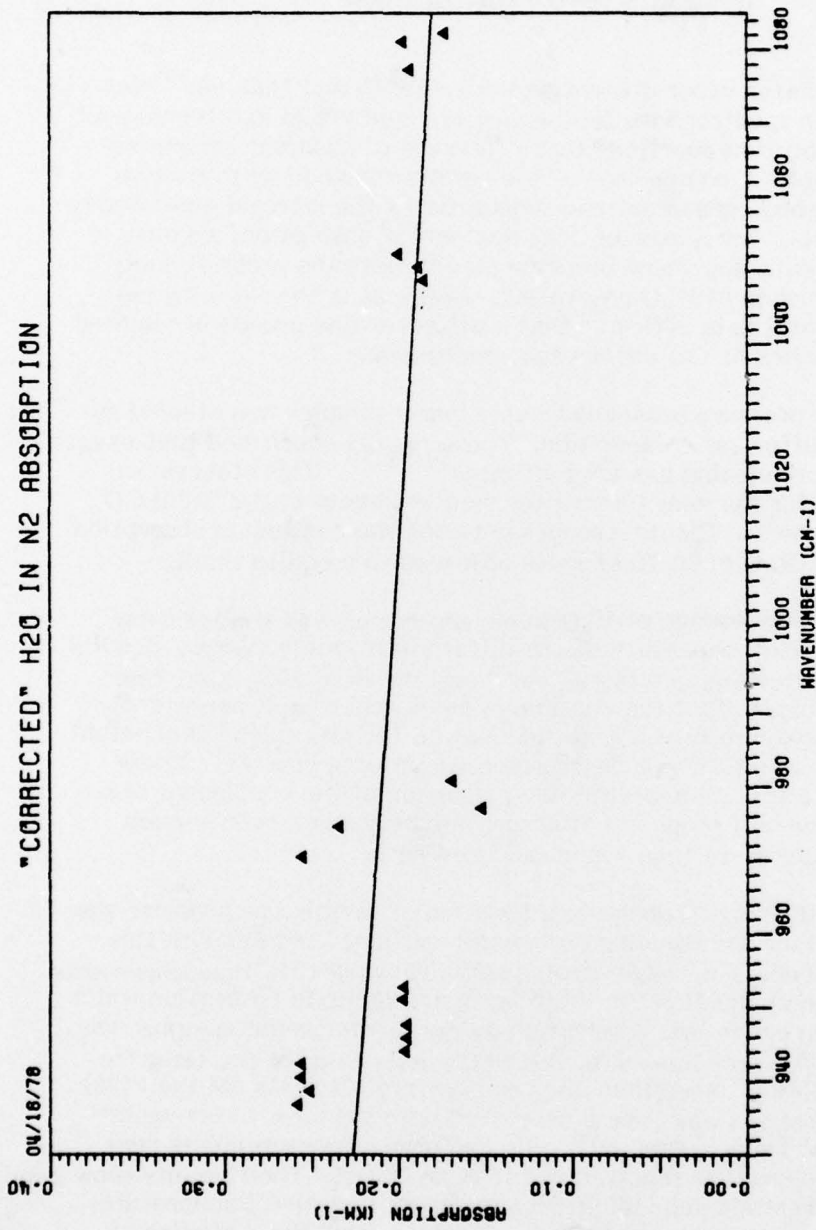


Figure 152 Plot of "corrected" White cell absorption coefficient results (as defined in the text) vs. CO₂ laser frequency in cm⁻¹ for 14.3 Torr of H₂O in N₂ at a total pressure of 760 Torr and a nominal temperature of 22.5°C. The solid curve gives the least square fit of the "corrected" data, indicated by the symbol Δ, to the Equation (135).

CHAPTER VII SUMMARY AND CONCLUSIONS

In this study water vapor absorption between 930 and 1085 cm^{-1} was examined using both spectrophone (optoacoustic) and White cell techniques to measure the absorption coefficient as a function of absorber concentration and temperature. A comparison of the results obtained by these two methods indicates good agreement and substantiates the internal consistency of the measurements. For a case of near line center absorption, we have shown that the Lorentz line shape properly models both the pressure and temperature dependence of H_2O absorption. However in the far wing regions the experimental data affirm⁷⁶ that a different line profile is required to model the properties of the water vapor continuum.

Absorption in pressure broadened water vapor samples was studied as a function of the buffer gas composition. These results confirmed that oxygen is a less effective broadening gas than nitrogen^{77,78,79}. This observation was most apparent for the near line center measurements at the R(20) CO_2 laser line, 975.930 cm^{-1} . The differences between the continuum absorption of (H_2O in N_2) and (H_2O in 80-20 air) was observed to be quite small.

Temperature dependence of H_2O in air absorption was studied using the temperature control capability of the differential spectrophone. Results for the P(20) CO_2 laser line at 944.194 cm^{-1} and the P(16) CO_2 laser line at 947.742 cm^{-1} indicate that the continuum has a negative temperature coefficient of approximately -1.7% at 295°K , i.e., the absorption coefficient decreases at a rate of $\sim 1.7\%$ per degree increase in temperature. These results also indicate that an accurate determination of the continuum temperature dependence will require that absorption be studied over a much wider range in temperature than was considered here.

Response of the spectrophone as a function of sample gas pressure was analyzed and a method for studying pure water vapor absorption with this instrument introduced. The results from preliminary pure H_2O measurements in the spectrophone at the $10.6\text{ }\mu\text{m}$ P(20) laser line indicate absorption which is $\sim 15\%$ higher than expected. Absorption by pure water vapor samples was studied at seven CO_2 laser lines with the White cell. Four of the laser frequencies were studied at more than one temperature. Results for the P(20) CO_2 laser line at 944.194 cm^{-1} were compared with the pure water vapor study of Arefev and Dianov-Klokov⁸⁰, who performed measurements near $10.6\text{ }\mu\text{m}$ over a temperature range from 281°K to 350°K . Their results show good agreement with this study and indicate a significant negative temperature coefficient for the continuum absorption. The data from these studies of

pure water vapor absorption would suggest a temperature coefficient between -3 and -9% at 300°K, which is at least twice that observed in the pressure broadened measurements.

The purpose of this study was to obtain accurate water vapor absorption measurements at CO₂ laser frequencies and from these results infer properties of the water vapor continuum near 9 and 10 μm. The data from this study indicate that as a function of frequency, continuum absorption can be modeled with the equation

$$k_c \sim 1.72 \times 10^5 \nu^{-2} + 2.47 \times 10^{-2} \quad (136)$$

where ν is the frequency in wavenumbers (cm⁻¹). The constants in this equation were determined from spectrophone and White cell absorption measurements of 14.3 Torr H₂O in N₂ at a total pressure of 1 atm. near 295°K. The temperature dependence under these same conditions was determined to be

$$\frac{\Delta k/k}{\Delta T} \times 100 \sim -1.7\% \quad (137)$$

in which $\Delta k/k$ is the relative change in absorption produced by a temperature variation, ΔT .

REFERENCES

1. R. A. McClatchey, W. S. Benedict, S. A. Clough, D. E. Burch, R. F. Calfee, K. Fox, L. S. Rothman, and J. S. Garing, "AFCRL Atmospheric Absorption Line Parameters Compilation," Air Force Cambridge Research Laboratory Technical Report AFCRL-TR-73-0096, January 1973.
2. R. E. Roberts, J. E. A. Selby and L. M. Biberman, *Applied Optics*, Vol. 15, No. 9, page 2085, September (1976).
3. S. P. Langley, "The Solar and Lunar Spectrum," *Memoirs National Academy of Science IV*, (1888), page 159.
4. W. M. Elsasser, Heat Transfer by Infrared Radiation in the Atmosphere, Harvard Meteorological Studies No. 6, Harvard University Press, (1942).
5. H. W. Yates and J. H. Taylor, "Infrared Transmission of the Atmosphere," *NRL Report 5453* (June 1960) (AD 240-88).
6. A. Adel, "Atmospheric Absorption of Infrared Solar Radiation at the Lowell Observatory I," *The Astrophysical Journal*, Vol. 89, No. 1 (January 1939) page 1.
7. R. Anthony, "Atmospheric Absorption of Solar Infrared Radiation," *Physical Review*, Vol. 85, No. 4 (February 1952), page 674.
8. W. T. Roach and R. M. Goody, "Absorption and Emission in the Atmospheric Window from 770 to 1250 cm^{-1} ," *Quarterly Journal of the Royal Meteorological Society*, Vol. 84, (1958), page 319.
9. K. Bignell, F. Saiedy and P. A. Sheppard, "On the Atmospheric Infrared Continuum," *Journal of the Optical Society of America*, Vol. 53, No. 4 (April 1963), page 466.
10. J. H. McCoy, "Atmospheric Absorption of Carbon Dioxide Laser Radiation Near Ten Microns," Report 2476-2, 10 September 1968, The Ohio State University ElectroScience Laboratory, Department of Electrical Engineering; prepared under Contract F33615-67-C-1949 for Air Force Avionics Laboratory, Wright-Patterson Air Force Base, Ohio. (AD 839 938)
11. K. J. Bignell, *Quart. J. R. Met. Soc.*, 96, (1970) page 390.

12. G.L. Trusty, "Absorption Measurements of the 10.4 Micron Region Using a CO₂ Laser and a Spectrophone," Report 2819-4, The Ohio State University ElectroScience Laboratory (AFAL-TR-72-413) (AD 907 549) January 1973.
13. D. E. Burch, "Investigation of the Absorption of Infrared Radiation by Atmospheric Gases, Aeronutronic Report U-4784, January (1971).
14. P. S. Varanasi, S. Chou, and S. S. Penner, *J. Quant. Spectros. Radiat. Transfer* 8, page 1537 (1968).
15. H. R. Carlon, *Applied Optics*, Vol. 10, page 2297, October (1971).
16. J. U. White, *J. Opt. Soc. Am.* 32, page 285 (1942).
17. G. Herzberg, Molecular Spectra and Molecular Structure, Van Nostrand Reinhold Company, 1950.
18. V. Weisskopf, E. Wigner, *Zs. f. Phys.* 63 (1930), page 54 and 65 (1930) page 18.
19. D. Marcuse, Engineering Quantum Electrodynamics, Harcourt, Brace and World, Inc., 1970, page 200.
20. R. G. Breene, The Shift and Shape of Spectral Lines, Pergamon Press, 1961.
21. F. S. Mills, "Absorption of Deuterium Fluoride Laser Radiation by The Atmosphere," Report 4054-3, The Ohio State University Electro-Science Laboratory, Department of Electrical Engineering; prepared under Contract F30602-75-C-0029 for Rome Air Development Center. (RADC-TR-76-105) (AD/A 025 402)
22. A. Metropoulos, "Line Shape Parameters for H₂O in Air," M. S. Thesis, University of Maryland (1973)
23. C. Peach, "The Width of Spectral Lines," *Contemp. Phys.* 1975, Vol. 16, No. 1, page 17.
24. S. S. Penner, Addison-Wesley, Reading, Mass. (1959)
25. J. H. McCoy, "Atmospheric Absorption of Carbon Dioxide Laser Radiation Near Ten Microns," Report 2476-2, 10 September 1968, ElectroScience Laboratory, Department of Electrical Engineering, The Ohio State University; prepared under Contract F33615-67-C-1949 for Air Force Avionics Laboratory, Wright-Patterson Air Force Base, Ohio (AD 839 938)
26. D. E. Burch, "Radiative Properties of the Atmospheric Windows," presented at the Conference on Atmospheric Radiation sponsored by the American Meteorological Society, Ft. Collins, Colorado, August, 1972.

27. P. S. Varanasi, S. Chou, and S. S. Penner, *J. Quant. Spectros. Radiat. Transfer* 8 1937 (1968).
28. T. G. Adiks, V. N. Aref'ev, and V. I. Dianol-Klokov, *Jor. J. Quant. Electron.* 5, 481 (1975).
29. A. G. Bell. *Proc. Am. Assoc. Advance Sci.*, 29 (1880), page 115.
30. M. L. Viengerov, *Izv. Akad. Nauk, USSR, Fiz.* 4, (1940), p. 94.
31. E. L. Kerr and J. G. Atwood, *Appl Optics*, 7 (1968), p. 915.
32. L. B. Kreuzer, *J. Appl. Physics*, 42 (1971), page 2934.
33. C. F. Dewey, Jr., R. D. Kamm, and C. E. Hackett, *Appl. Phys. Lett.*, 23 (1973), page 633.
34. T. F. Deaton, D. A. Depatie, and T. W. Walker, *Appl. Phys. Lett.*, 26 (1975), page 300.
35. R. Gerlach and N. M. Amer, *Appl. Phys. Lett.*, Vol. 32, No. 4, (1970) page 228.
36. S. Shtrikman and M. Slatkine, *Appl. Phys. Lett.*, Vol. 31, No. 12 (1977) page 830.
37. P. D. Goldan and K. Goto, *Journal of Applied Physics*, Vol. 45, No. 10 (1974), page 4350.
38. L. B. Kreuzer and C. K. N. Patel, *Science*, Vol. 173, page 45 (1971).
39. W. Schnell and G. Fischer, *Optic Lett.*, Vol. 2, No. 3, page 67 (1978).
40. R.T. Menzies and M. S. Shumate, "Optoacoustic Measurements of Water Vapor Absorption at Selected CO Laser Wavelengths in the 5 μm Region," *Appl. Opt.* 15, page 2025 (1976).
41. M. S. Shumate, R. T. Menzies, J. S. Margolis and L. G. Rosengren, "Water Vapor Absorption of Carbon Dioxide Laser Radiation," *Applied Optics*, Vol. 15, No. 10, October 1976, page 2480.
42. V. E. Zuev, A. B. Antipov and V. A. Sapozhnikova, "Opto-acoustic Laser Measurements of $^{13}\text{CH}_4$ and $^{12}\text{CH}_4$ Absorption Spectra at 3.39 μm ," *J. Chem. Phys.* 68(3), page 1315 (1978).
43. E. K. Damon, J. C. Peterson, F. S. Mills and R. K. Long, "Spectrophone Measurements of the Water Vapor Continuum at DF Laser Frequencies," Report 4054-1, The Ohio State University Electro-Science Laboratory, July, 1975.

44. L. A. Farrow and R.E. Richton, "A More Complete Interpretation of Optoacoustic Data Taken with Fixed-Frequency Lasers," *J. Appl. Phys.* 48, page 4962 (1977).
45. T. L. Cottrell and McCoullrey, *Molecular Energy Transfer in Gases*, (Butterworths, London, 1961).
46. L. G. Rosengren, *Infrared Phys.* 13, page 109 (1973).
47. J. G. Parker, *Applied Optics*, 12 (1973), page 2974.
48. L. G. Rosengren, *Applied Optics*, 8 (1975) Page 1960.
49. C. Bruce, "Development of Spectrophones for cw and Pulsed Radiation Sources," (AD-A035 594), August 1976, ECOM-5802.
50. G. L. Trusty, "Absorption Measurements of the 10.4 Micron Region Using a CO₂ Laser and a Spectrophone," Report 2819-4, January 1973, The Ohio State University ElectroScience Laboratory, Department of Electrical Engineering; prepared under Contract No. F33615-69-C-1807 for Air Force Avionics Laboratory. (AD 907549) (AFAL-TR-72-413)
51. R. L. Abrams, *Applied Physics Letters*, 10 (1974) page 609.
52. C. K. N. Patel and R. J. Kerl, *Applied Physics Letters*, 11 (1977) page 578.
53. J. C. Peterson, "A Differential Spectrophone of Unique Design," Thesis, The Ohio State University, 1976.
54. J. C. Peterson, R. J. Nordstrom, and R. K. Long, *Applied Optics*, 12 (1976), page 2974.
55. W. H. Thomason and D. C. Elbers, "An Inexpensive Method to Stabilize the Frequency of a CO₂ Laser," 1974, Louisiana State University, Department of Chemistry, private communication.
56. F. S. Mills, "A Computer Controlled Data Acquisition System for Atmospheric Propagation Studies," Thesis and Report 2834-1, The Ohio State University ElectroScience Laboratory, Department of Electrical Engineering; prepared under Contract No. DAAG05-69-C-0782.
57. J. C. Peterson, R. J. Nordstrom and R. K. Long, "A Subtle Source of Contamination in Spectrophones," *Applied Optics*, Vol. 15, No. 12, December 1976, page 2974.

58. J. H. McCoy, "Atmospheric Absorption of Carbon Dioxide Laser Radiation Near Ten Microns," Report 2476-2, 10 September 1968, ElectroScience Laboratory, Department of Electrical Engineering, The Ohio State University; prepared under Contract F33615-67-C-1949 for Air Force Avionics Laboratory, Wright-Patterson Air Force Base, Ohio. (AD 839 938)
59. S. G. Wechter and F. Kramer, Jr., "Evaluation of Gas Phase Moisture Standards," paper presented at 21st National Symposium of the Analysis Instrument Division, Instrument Society of America, King of Prussia, PA on May 8, 1975.
60. H. R. Carlon, "Model for Infrared Emission of Water Vapor/Aerosol Mixtures," Applied Optics, Volume 10, page 2297, October 1971.
61. M. S. Shumate, R. T. Menzies, J. S. Margolis and L. G. Rosengren, "Water Vapor Absorption of Carbon Dioxide Laser Radiation," Applied Optics, Vol. 15, No. 10, October 1976, page 2480.
62. W. S. Benedict and L. D. Kaplan, J. Quant. Spectrosc. Radiat. Transfer Vol. 4, p. 453, (1964).
63. W. Braker and A. L. Mossman, "Matheson Gas Data Book," Matheson Gas Products (1971).
64. J. H. McCoy, "Atmospheric Absorption of Carbon Dioxide Laser Radiation Near Ten Microns," Report 2476-2, 10 September 1968, The Ohio State University ElectroScience Laboratory, Department of Electrical Engineering; prepared under Contract F33615-67-C-1949 for Air Force Avionics Laboratory, Wright-Patterson Air Force Base, Ohio. (AD 839 938)
65. J. E. A. Selby and R. A. McClatchey, "Atmospheric Transmittance from 0.25 to 28.5 μm Computer Code LOWTRAN 3," AFCRL-TR-75-0255, Air Force Cambridge Research Laboratories Environmental Research Papers, No. 513 (1975)
66. R. K. Long, F. S. Mills, and E. K. Damon, paper presented at the OSA Conference on Applications of Laser Spectroscopy, Anaheim, CA (March 19-21, 1975)
67. R. A. McClatchey, W. S. Benedict, S. A. Clough, D. E. Burch, R. F. Calfee, K. Fox, L. S. Rothman, and J. S. Garing, "AFCRL Atmospheric Absorption Line Parameters Compilation," Air Force Cambridge Research Laboratory, Technical Report AFCRL-TR-73-0096, January 1973.
68. M. S. Shumate, R. T. Menzies, J. S. Margolis and L. G. Rosengren, "Water Vapor Absorption of Carbon Dioxide Laser Radiation," Applied Optics, Vol. 15, No. 10, October 1976, page 2480.

69. J. H. McCoy, "Atmospheric Absorption of Carbon Dioxide Laser Radiation Near Ten Microns," Report 2476-2, 10 September 1978, The Ohio State University ElectroScience Laboratory, Department of Electrical Engineering; prepared under Contract F33615-67-C-1949 for Air Force Avionics Laboratory, Wright-Patterson Air Force base, Ohio. (AD 839 938)
70. R. S. Eng and K. W. Nill, paper presented at the OSA Conference on Applications of Laser Spectroscopy, Anaheim, CA (March 19-21, 1975)
71. W. S. Benedict and L. D. Kaplan, *J. Quant. Spectro. Rad. Transfer* 4, page 453 (1964)
72. R. J. Nordstrom, private communication, ElectroScience Laboratory, The Ohio State University, Columbus, Ohio.
73. M. E. Thomas, private communication, The Ohio State University ElectroScience Laboratory, Columbus, Ohio.
74. G. L. Trusty, "Absorption Measurements of the 10.4 Micon Region Using a CO₂ Laser and a Spectrophone," Report 2819-4, January 1973, The Ohio State University ElectroScience Laboratory, Department of Electrical Engineering; prepared under Contract No. F33615-69-C-1807 for Air Force Avionics Laboratory. (AD 907549) (AFAL-TR-72-413)
75. V. N. Arefev, V. I. Dianov-Klokov, *Opt. Spectrosc.* 42, page 488 (1977)
76. D. E. Burch, Aeronutronics Publication No. U-4784, "Semi-Annual Technical Report," Air Force Cambridge Research Laboratories, Contract No. F19628-69-C-0263, January 1970.
77. W. S. Benedict and L. D. Kaplan, *J. Quant. Spectros. Rad. Transfer* 4, page 453 (1964)
78. R. S. Eng and K. W. Nill, paper presented at the OSA Conference on Applications of Laser Spectroscopy, Anaheim, CA (March 19-21, 1975).
79. M. S. Shumate, R. T. Menzies, J. S. Margolis and L. G. Rosengren, "Water Vapor Absorption of Carbon Dioxide Laser Radiation," *Applied Optics*, Vol. 15, No. 10, October 1976, page 2430.
80. Arefev and Dianov-Klokov, *Opt. Spectrosc.* 42, page 488 (1977).